

Optimizing X-Ray Production with Nanosecond Laser Pulses by Two-Plasmon Decay

Optimierung der Röntgenerzeugung mit Nanosekunden-Laserpulsen durch Two-Plasmon Decay

Master thesis by Philipp Mathias Hesselbach

Date of submission: October 15, 2021

1. Review: Priv. Doz. Dr. Vincent Bagnoud

2. Review: Priv. Doz. Dr. Paul Neumayer

Darmstadt



TECHNISCHE
UNIVERSITÄT
DARMSTADT

Physics Department
Institute of Nuclear Physics
Working Group Bagnoud

Optimizing X-Ray Production with Nanosecond Laser Pulses by Two-Plasmon Decay
Optimierung der Röntgenerzeugung mit Nanosekunden-Laserpulsen durch Two-Plasmon Decay

Master thesis by Philipp Mathias Hesselbach

1. Review: Priv. Doz. Dr. Vincent Bagnoud
2. Review: Priv. Doz. Dr. Paul Neumayer

Date of submission: October 15, 2021

Darmstadt

Erklärung zur Abschlussarbeit gemäß §22 Abs. 7 und §23 Abs. 7 APB der TU Darmstadt

Hiermit versichere ich, Philipp Mathias Hesselbach, die vorliegende Master thesis ohne Hilfe Dritter und nur mit den angegebenen Quellen und Hilfsmitteln angefertigt zu haben. Alle Stellen, die Quellen entnommen wurden, sind als solche kenntlich gemacht worden. Diese Arbeit hat in gleicher oder ähnlicher Form noch keiner Prüfungsbehörde vorgelegen.

Mir ist bekannt, dass im Fall eines Plagiats (§38 Abs. 2 APB) ein Täuschungsversuch vorliegt, der dazu führt, dass die Arbeit mit 5,0 bewertet und damit ein Prüfungsversuch verbraucht wird. Abschlussarbeiten dürfen nur einmal wiederholt werden.

Bei der abgegebenen Thesis stimmen die schriftliche und die zur Archivierung eingereichte elektronische Fassung gemäß §23 Abs. 7 APB überein.

Bei einer Thesis des Fachbereichs Architektur entspricht die eingereichte elektronische Fassung dem vorgestellten Modell und den vorgelegten Plänen.

Darmstadt, 15. Oktober 2021

P. Hesselbach

Contents

1. Introduction	7
2. X-Ray Diffraction	11
3. Increasing Numbers of Photons From Higher-Energetic Line Emission by Two-Plasmon Decay	13
3.1. X-Ray Production Mechanisms	13
3.1.1. Bremsstrahlung	13
3.1.2. Recombination	13
3.1.3. Line Emission	14
3.2. Challenge of High Numbers of Photons From Higher-Energetic Line Emission	15
3.3. Experiment Idea	16
4. Two-Plasmon Decay	18
4.1. The Two Types of Waves Participating in the Two-Plasmon Decay	18
4.1.1. Electromagnetic Waves in a Plasma	18
4.1.2. Electron Plasma Waves	20
4.2. Introduction to the Two-Plasmon Decay	21
4.3. Derivation of the Coupling Equation in Homogeneous Media	25
4.4. Derivation of the Two-Plasmon Decay Growth Rate in Homogeneous Media	27
4.5. Discussion of the Two-Plasmon Decay Growth Rate in Homogeneous Media	32
4.5.1. Dependence of the Homogeneous Growth Rate on the Electron Plasma Wave Vectors	32
4.5.2. Influence of Damping Effects	34
4.5.3. Discussion of Assumptions	36
4.6. Electron Density Dependence of the Two-Plasmon Decay	38
4.7. Convective Two-Plasmon Decay Instability	41
4.7.1. Convective Two-Plasmon Decay Gain	41
4.7.2. Influence of Damping Effects	44
4.8. Electron Acceleration to Superthermal Energies and Propagation of Electron Plasma Waves	46
5. Experimental Setup and Design	49
5.1. Overview of Experimental Setup	49
5.2. Experimental Optimization of Two-Plasmon Decay Conditions	50
5.3. Diagnostic Setup	54
5.3.1. Hard X-Ray Detector	55
5.3.2. Highly Oriented Pyrolytic Graphite Crystal	56
5.3.3. Streak Camera and Spectrometer	57
6. Evaluation and Methods	58
6.1. Calculation of the Two-Plasmon Decay Strength From Streak Camera Data	58

6.2. Calculation of Line Emission Yield From Highly Oriented Pyrolytic Graphite Spectrometer Data	60
6.2.1. Energy Calibration	60
6.2.2. Different Types of Line Emission Observed	61
6.2.3. Calculation of K_{α} Yield	63
6.3. Fast Electron Analysis	65
6.3.1. Calculation of Hard X-Ray Detector Signal	66
6.3.2. Simulation of X-Ray Emission	66
6.3.3. Quantification of the Quality of Electron Fits to the Hard X-Ray Detector Data	68
6.3.4. Fitting Procedure to Hard X-Ray Detector Data With Monoenergetic Fast Electrons	69
6.3.5. Fitting Procedure to Hard X-Ray Detector Data With Temperature Distributed Fast Electrons	74
6.3.6. Calculation of Fast Electron Number From Highly Oriented Pyrolytic Graphite Spectrometer Data	78
7. Results and Discussion	81
7.1. Shots at Best Focus	81
7.1.1. Two-Plasmon Decay Strength and Convective Gain	81
7.1.2. Comparison of K_{α} Yield and Two-Plasmon Decay Strength	84
7.1.3. Comparison of K_{α} Yields for Different Coating Thicknesses	86
7.1.4. Comparison of K_{α} Yields for Different Target Materials	87
7.1.5. Fast Electron Conversion Efficiency for the Monoenergetic Model	89
7.1.6. Fast Electron Temperature Obtained With the Temperature Model	91
7.1.7. Fast Electron Conversion Efficiency for the Temperature Model	94
7.1.8. Relation Between K_{α} Yield and Fast Electron Conversion Efficiency for the Temperature Model	97
7.1.9. Potential Improvements on the Hard X-Ray Detector	99
7.2. Shots With Phase Plate	101
7.2.1. Two-Plasmon Decay Strength and Convective Gain	101
7.2.2. Line Emission Yield	105
7.2.3. Monoenergetic Fast Electrons	106
7.2.4. Temperature Distributed Fast Electrons	107
8. Conclusion and Outlook	110
Appendices	113
A. Intensity Calculation From Focus Images	113
A.1. Measurements of the Spatial Intensity Distribution	113
A.2. Calculation of the Spatial Average of the Intensity Distribution at Best Focus	115
A.3. Calculation of the Spatial Average of the Intensity Distribution With the Phase Plate	116
B. Identification of Lines for Uncoated Mo Targets	117

1. Introduction

The study of warm dense matter (WDM) is important for many different research subjects like astrophysics, planetary physics, geophysics and inertial confinement fusion [1–8]. Therefore, WDM is experimentally produced and researched. Still, phase diagrams and equations of state are barely known at the extreme states of WDM which are characterized by high temperatures, typically 0.1 – 100 eV, and high densities, typically from solid density to ten times above [5]. A large amount of energy needs to be deposited in the sample under investigation within a short period of time in order to heat it to WDM conditions. Among other methods, this can be implemented by irradiating a target with intense ion pulses (e.g., at GSI Helmholtz Center for Heavy Ion Research [9]) or X-ray pulses (e.g., at European X-ray Free Electron Laser XFEL [10]), and by the means of laser pulses (e.g., at National Ignition Facility NIF [11, 12]) or pulsed power discharges (e.g., at Sandia National Laboratories Z-machine [13]).

To probe WDM, novel diagnostic methods have been developed over the past two decades [14]. Among others, X-ray sources have been proven to be suitable [5, 15] because their short-wavelength photons have attenuation lengths long enough to penetrate targets of WDM experiments. In addition to sources such as synchrotrons or X-ray free electron lasers, a common way to provide X-ray sources is based on lasers. By means of intense laser pulses, hot plasmas can be produced resulting in the emission of radiation in the X-ray regime.

Depending on the specific diagnostic application, different requirements have to be fulfilled by the produced X-ray spectra. Continuous X-ray emission can be used, for example, for X-ray absorption spectroscopy [16] which allows to observe phase transitions in WDM and may even enable temperature determination in the future [17]. This diagnostic method requires broadband X-ray emission whose intensity is as constant as possible over a specific energy interval. The interval is determined by the absorption features which are to be observed in the sample under investigation. On the other hand, X-ray line emission is necessary, e.g., for X-ray Thomson scattering and X-ray diffraction. X-ray Thomson scattering is used to measure the dynamic structure factor that contains information about collective behavior of WDM [18, 19] and allows to draw conclusions on WDM properties such as temperature, density and ionization state [19, 20]. Furthermore, X-ray diffraction is utilized to detect crystallographic structures. This method was originally used within the research of solid-state physics [21] and later applied in the scope of WDM research to investigate phase transitions during the formation of WDM from crystal-like solids [22]. For both, X-ray Thomson scattering and X-ray diffraction in WDM, line emission is required to have high intensities in order to provide strong signals on the detector. Furthermore, higher photon energies are desirable, since they generally coincide with larger transmission through the sample. In other words, the larger the line emission intensity and the photon energy, the higher the densities, nuclear charges and thicknesses of WDM targets for which the absorption is within the feasible range of the diagnostic setup. Since a major characteristic of WDM is its high density, these requirements are of particular importance. In contrast to the diagnostic methods presented above, X-ray radiography does not require specific X-ray spectrum characteristics apart from highest possible photon energies and intensities for the same reasons as previously described.

My work focuses on the characterization and optimization of an X-ray source for X-ray Thomson scattering and X-ray diffraction. The X-ray emission is produced by focusing laser pulses on a target, more specifically the nanosecond pulse of the Petawatt High-Energy Laser for Heavy Ion Experiments (PHELIX) [23] located at the GSI Helmholtzzentrum für Schwerionenforschung GmbH in Darmstadt, Germany. The plasma physics group at GSI conducted a PHELIX experiment at the experimental place Z6 [24] at GSI. My work is centered around the activity of this team which I am part of. At the experimental station Z6, PHELIX ns-pulses can be focused down to a full width at half maximum (FWHM) of $25\text{ }\mu\text{m}$ and pulse energies up to 200 J at 2ω (527 nm) are available. In order to optimize the X-ray source, we aim to enhance conversion efficiencies from laser energy into photons of high-energetic line emission by exploiting the process of two-plasmon decay (TPD) [25]. TPD is a parametric instability arising from laser plasma interactions [26–31]. Under certain conditions, it produces fast electrons with superthermal energies which in turn produce K_{α} emission [32]. Usually, TPD is known from inertial confinement fusion experiments where it displays a disturbing effect that causes preheat of the fuel and should therefore be avoided [33–35]. Our aim was, however, to identify a regime accessible with the PHELIX parameters where TPD is enhanced as much as possible. We tested the capability of a special target design in terms of increasing TPD and thus line emission conversion efficiency. Our special target design involved coating a metallic layer with a material consisting of atoms with low nuclear mass. Based on the results of other groups using ns-laser pulses [32, 35–37], also combined with shorter pulses ($\sim 100\text{ ps}$) [25], we expect an improvement in comparison to bare metallic target designs.

Our research is of current interest because the experimental site of GSI recently allows for the worldwide unique possibility of combining high-energy heavy ion beams capable of producing WDM and high-energy laser pulses [38, 39]. This is achieved at the High energy, High Temperature (HHT) experimental station thanks to the new HHT laser beamline that has been commissioned in May 2021. The beamline guides the PHELIX ns-pulse from the laser building to the HHT experimental place where the light is frequency doubled to 527 nm and focused on a target. The specialty of the HHT beamline is that it allows the combination of PHELIX laser pulses and ion pulses that have been accelerated in the heavy ion synchrotron SIS-18, thus reaching velocities of $0.9c$ [40] and numbers of $\sim 4 \cdot 10^9$ ions (for U^{73+}) per FWHM = 100 ns bunch [38]. At the HHT experimental station, the ion pulses can be focused down to the millimeter range using normal conducting magnets. In the past, combined ion beam and PHELIX experiments were only possible at the experimental place Z6 after the UNIversal Linear ACcelerator (UNILAC) whose operational capability in terms of ion beam intensity and ion energy impedes to reach the WDM regime by ion heating [41]. During the commissioning of the HHT beamline, laser energies were limited to 100 J at 2ω , but we expect being able to reach 200 J once the beamline is fully optimized. Additionally, the focusing capabilities at HHT are similar as at Z6. Therefore, the results of our experiment at Z6, which was conducted before the commissioning, are valid for laser driven X-ray sources at HHT, as well.

Beyond this, the ongoing optimization of X-ray sources at PHELIX ns-pulse parameters constitutes preparatory work for the intended research at the Atomic, Plasma Physics and Applications (APPA) cave at the Facility for Antiproton and Ion Research (FAIR). FAIR will still be under construction for the next few years, but for its final stage, FAIR is designed to feature ion numbers of up to $\sim 5 \cdot 10^{11}$ ions (U^{28+}) per bunch accelerated in the synchrotron SIS-100 [42]. The APPA cave is foreseen to allow the combination of X-ray diagnostics and ion heating similar to the HHT cave but enables experiments at higher temperatures thanks to the increased ion numbers. Besides more advanced synchrotron capabilities, the design of the APPA cave itself contributes to the enhanced performance. This is due to the fact that superconducting magnets will be used for the ion focusing. Such magnets enable stronger magnetic fields and thus the focusing of smaller charge-to-mass ratios than normal conducting magnets. In particular, U^{28+} instead of U^{73+} can be used. The smaller charge-to-mass ratio coincides with less space charge in the synchrotron caused by the

ion pulses. This, in turn, allows to operate the accelerator at higher ion numbers. Similarly to the HHT cave, X-ray sources at the APPA experimental station will be provided by means of a laser system which will be newly built and feature comparable characteristics as the PHELIX ns-pulses.

In the following, I elaborate on why we prefer the PHELIX laser (or a similar laser system) for X-ray production over the implementation of other X-ray sources. Therefore, I will exemplarily compare X-ray sources produced by the PHELIX ns-pulse with the top-end pulsed X-ray tube manufactured by Specialised Imaging (S.I.) [43].

One major advantage of the PHELIX based approach is the short X-ray pulse duration that is similar to the laser pulse duration of ~ 1 ns so that an extensive time resolution of the ion beam heating which occurs on ~ 100 ns timescales [38] can be obtained. In contrast, the S.I. X-ray tube is characterized by much longer pulse lengths of ~ 25 ns which would cause temporal blurring. Another important quantity is the brilliance $B = d^2E/(d\Omega dA)$ of the X-ray source which correlates the emitted X-ray energy per solid angle $dE/d\Omega$ to the source size A . Generally, more X-ray energy is desired to obtain higher signals on the diagnostics, while small source sizes enable, e.g., better spatial resolution for X-ray radiography and better angular resolution for X-ray diffraction and Thomson scattering. Assuming an X-ray spot size of $50 \mu\text{m}$, slightly larger than the laser spot size, isotropic emission and an X-ray conversion efficiency of at least 10^{-3} [44], one obtains a brilliance $B \approx 6 \text{ J sr}^{-1} \text{ mm}^2$ for a 200 J PHELIX pulse. In contrast to that, the S.I. X-ray tube has a much larger X-ray source sizes of 2 mm . We estimate $dE/d\Omega$ from the dose 0.55 mSv in a distance of 1 m [43]. Considering a cube of 1000 cm^3 water, we get $dE/d\Omega \approx 0.7 \text{ J sr}^{-1}$ and thus $B \approx 0.2 \text{ J sr}^{-1} \text{ mm}^2$ which is roughly a factor of 30 less compared to the laser based approach. One limitation of the ns-laser based X-ray source is that the spectral intensity typically strongly decreases above energies of $\sim 10 \text{ keV}$. The X-ray tube, on the other hand, would easily allow for photon energies of $\sim 100 \text{ keV}$.

My work addresses this drawback of our laser generated X-ray source, especially with the goal to enhance diagnostic capabilities of X-ray diffraction based on PHELIX ns-pulses. A particular motivation of my work is that there are already experiments proposed and accepted that combine ion heating at HHT with this diagnostic method. One of those experiments deals with superheating of iron. Superheating is a phenomenon that can be observed in solid materials when heated so quickly past the melting point that solid state is still present. It was observed for laser-shocked iron in the past [45], whereas the current experiment proposal includes the heating up to few thousand K with the ion beam available at HHT. Meanwhile, solid-liquid phase transitions and possibly other solid-solid transitions corresponding to crystal structure changes are predicted and proposed to be detected by X-ray diffraction with the PHELIX ns-pulse.

This thesis is structured as follows. In chapter 2, I explain how X-ray diffraction works and the reason why it requires intense line emission at high photon energies. Chapter 3 summarizes X-ray production mechanisms and motivates why we intend to use TPD in order to optimize the X-ray sources for X-ray diffraction. The main idea of our experiment, using coated targets, is briefly introduced. In chapter 4, the theory of TPD is presented. The growth rate for a homogeneous plasma is derived and discussed. The derivation was developed as part of this thesis in cooperation with Vincent Bagnoud. Furthermore, the density dependence of TPD is explained and the TPD gain for a linear density profile is presented. Finally, I describe how TPD leads to the generation of fast electrons, the amount of which we try to enhance within the framework of this work. Chapter 5 is about our experimental setup and design. An overview of our setup is given and the advantages of our experimental design regarding TPD are discussed and connected to the previously presented theory. This concerns in particular our coated target design. Chapter 6 describes the calculations and evaluation algorithms which were used to analyze the data in terms of TPD, production of line emission and fast electrons. The evaluation is based on input from the working group, in particular from Paul Neumayer, Zsuzsanna Major and Vincent Bagnoud, and was implemented

and carried out mainly by myself. In chapter 7, I present the results that point out links between TPD, fast electrons and line emission and I compare different targets as well as the effect of different laser intensities and energies. The results are discussed based on my trains of thoughts, some of which evolved from conversations within the group. I will end with a conclusion and outlook in chapter 8 where my most important findings so far are summarized and further steps for future work are proposed.

2. X-Ray Diffraction

In this chapter, I explain how crystal structures can be determined by X-ray diffraction and why intense line emission at high photon energies is required for this purpose.

A scheme of a potential experimental setup for X-ray diffraction at HHT is shown in Fig. 2.1. The scheme is based on the design of X-ray diffraction experiments in campaigns at other laser facilities, e.g., at NIF [46]. In the first step, the PHELIX ns-pulse is incident on a target to produce X-rays, especially a large amount of monoenergetic photons from line emission. In the second step, the emitted photons are collimated, e.g., by using a pinhole, and reach the ion heated target afterwards. A prerequisite for the shown X-ray diffraction scheme is that this target has a polycrystalline structure, i.e., that it consists of crystallites, at least in the initial state, without heating. The incident X-rays are diffracted at the lattice planes of the different crystallites and constructive interference occurs when the Bragg condition [47]

$$n\lambda = 2d_{hkl} \sin(\theta) \quad (2.1)$$

is satisfied, where n is the diffraction order, θ the Bragg angle, λ the X-ray wavelength and d_{hkl} the lattice plane distance depending on the Miller indices h, k, l . The crystallites have random orientations such that the Bragg condition is fulfilled in different reflection directions depending on the specific crystallite. Taking into account the superposition from all crystallites, the reflection is rotationally symmetric around the axis set by the direction of the incident X-rays. Additionally, the Bragg condition can be fulfilled for different lattice plane distances. This situation is depicted in Fig. 2.1.

As third step of the setup, the diffracted X-rays need to be detected. Diffraction rings can be observed and from their Bragg angles the corresponding lattice plane distances d_{hkl} can be inferred. Since the dependence of d_{hkl} on the Miller indices is uniquely determined by the crystal lattice, this allows to draw conclusions on the crystal structure of the probed target. Furthermore, X-ray diffraction can be used to indicate phase transitions, in particular from solid to liquid when the diffraction signal vanishes.

Let us discuss the influence of a finite range of incidence angles, i.e., the case of an X-ray cone incident on the sample. For the different incidence angles, there exist different crystallites for which the Bragg condition is fulfilled and the detected diffraction rings are thus smeared out. In order to resolve different d_{hkl} , the rings need to be distinguishable, in other words, the opening angle of the cone needs to be sufficiently small. This is the reason why small X-ray sources are preferable for X-ray diffraction.

Similar considerations as for a finite range of incidence angles hold for the case that the spectral range of applied X-rays is broadened. In the Bragg condition 2.1, this can be seen from the dependence $\lambda \propto \sin(\theta)$. For the different wavelengths λ , there exist different crystallites for which the Bragg condition is fulfilled under different Bragg angles. This smears out the diffraction rings and therefore the X-ray source emission should be as spectrally narrow as possible.

Furthermore, high X-ray source intensities and photon energies are desired so that diffraction rings can still be observed for ion heated targets with high densities, nuclear charges and thicknesses. Let us consider

the influence of these parameters on the detected signal. High photon energies reduce the attenuation by photoelectric and Compton effect [48] within the ion heated target. This enhances the signal strength, as does higher X-ray source intensity. In contrast to that, high densities, nuclear charges and thicknesses of the sample under investigation increase the attenuation. Assuming that a certain signal strength is necessary for the observation of diffraction rings, an increase in photon energy or source intensity allows to increase target densities, nuclear charges and thicknesses. Another advantage of higher photon energies is that the Bragg condition is fulfilled for smaller Bragg angles which means that more diffraction rings can be imaged on a detector of a limited size. This in turn facilitates the determination of crystal structures.

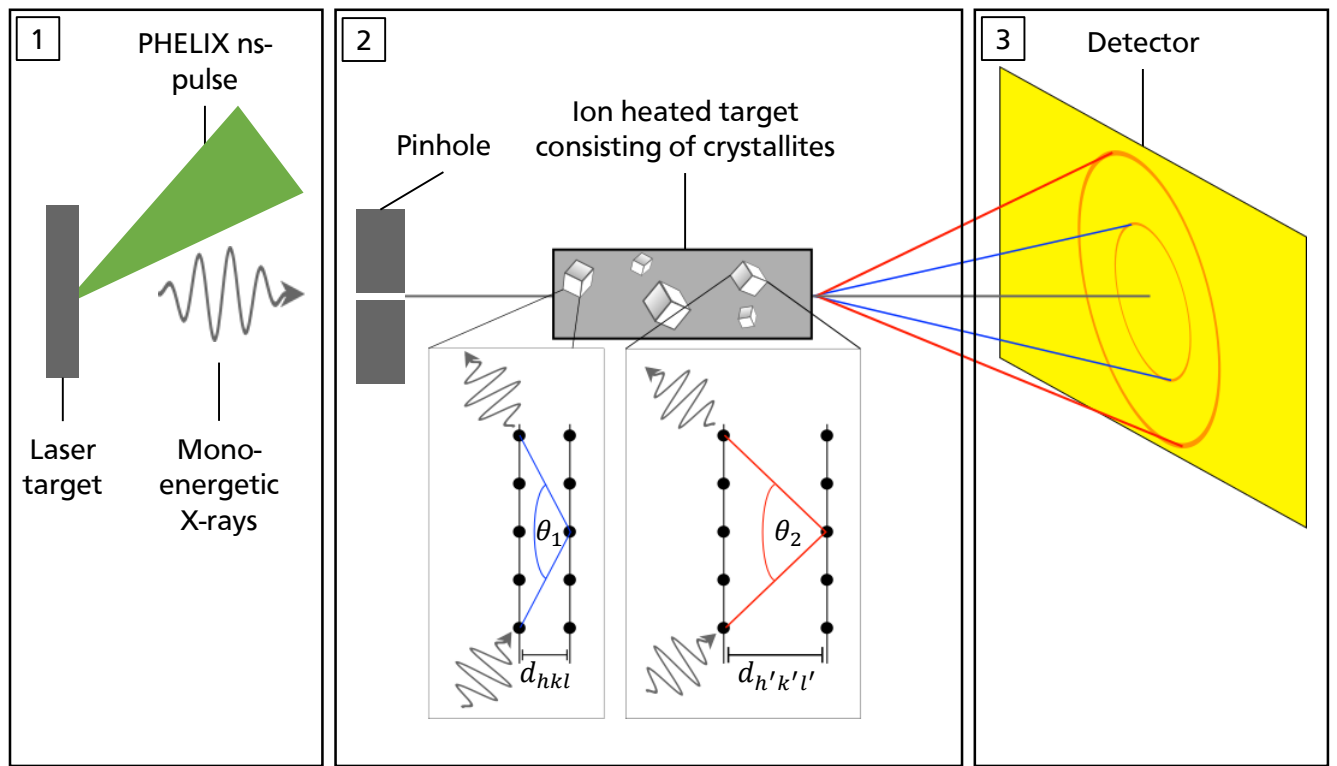


Figure 2.1.: A scheme of an X-ray diffraction setup is shown. 1: X-rays are generated by laser-matter interaction. 2: X-rays are diffracted at an ion heated target with crystallite structure. 3: Diffraction rings are detected.

3. Increasing Numbers of Photons From Higher-Energetic Line Emission by Two-Plasmon Decay

In section 3.1 of this chapter, I summarize X-ray production mechanisms. They build the theoretical foundation for the motivation why we intend to use the two-plasmon decay (TPD) in order to increase numbers of photons from higher-energetic line emission (above 10 keV). In section 3.2, this motivation is presented in detail and in section 3.3, our experiment idea of using coated targets is introduced.

3.1. X-Ray Production Mechanisms

There are three fundamental X-ray production mechanisms: bremsstrahlung, recombination and line emission [49]. The first is due to free-free interactions, the second to free-bound and the last to bound-bound interactions. The mechanisms are described in the following.

3.1.1. Bremsstrahlung

Bremsstrahlung occurs in general when a charged particle is accelerated. In case of a laser plasma, bremsstrahlung is mainly produced when free electrons are deflected while interacting with ions under emission of photons [50]. Each electron can produce photons up to a maximum frequency of $\nu_{\max} = mv^2/2h$ [49] where m is the electron mass, v the electron velocity and h the Planck constant. On average, the radiated energy per frequency is constant for electrons of the same velocity. This means that bremsstrahlung leads to a continuous emission spectrum, even for monoenergetic electrons. In a plasma, electrons have a continuous velocity distribution which influences the superimposed emission spectrum from all electrons. This means that detecting the bremsstrahlung spectrum of a plasma allows to draw conclusions on the electron spectrum.

3.1.2. Recombination

When an electron recombines with an ion, a photon is emitted. The photon energy

$$h\nu = \frac{1}{2}mv^2 + E_{Z_i}^n \quad (3.1)$$

consists of two terms: the initial kinetic energy and the electron binding energy $E_{Z_i}^n$ where Z_i is the ion charge and n the quantum number of the electron's bound state. It should be noted that the electron

binding energy typically includes the energy that is released by the transition of the electron from its initial bound state to the ground state. Equation 3.1 indicates that X-ray emission from electron recombination is in general not continuous. However, it is continuous if the electron velocity distribution is so. Note that for each combination of Z_i and n , X-ray emission only occurs for $h\nu > E_{Z_i}^n$ leading to steps in the emission spectrum, so called recombination edges [49]. As bremsstrahlung, recombination connects photon and electron energies.

3.1.3. Line Emission

Figure 3.1 schematically show the creation of line emission in a singly charged ion. Initially, there is a hole in an electron shell, in the case of Fig. 3.1 in the K-shell. A bound electron from a higher level can fill the vacancy under photon emission which is called spontaneous emission [51]. Holes in the K-shell result in highest photon energies and from all transitions to the K-shell, the one from the L-shell has the highest rate of spontaneous emission. For singly charged ions (only hole in K-shell), this emission is called K_α emission (see Fig. 3.1). In contrast, K_β photons correspond to the transition $M \rightarrow K$ -shell whose rate of spontaneous emission is smaller than the rate of K_α emission. For each element, the ratio of these two emission rates is fixed [52]. It is important to note that line emission, in contrast to bremsstrahlung and recombination, enables the production of many monoenergetic X-rays which is necessary for X-ray diffraction.

In the case of higher charged states, the binding energy of electrons increases because of decreased shielding of the nuclear charge by bound electrons. This influences the photon energies from line emission. In particular, the photon energies corresponding to transitions to the K-shell are shifted towards higher energies [52]. Note that this is due to the quantum mechanical nature of electrons which results in decreased K-shell shielding by removing more outward electrons, too.

If different ionization states are present in a plasma, multiple shifted lines corresponding to $L \rightarrow K$ -shell transitions can occur. Ions where only electrons from the M-shell and more outer shells are removed (in addition to the necessary vacancy in the K-shell) emit photons from $L \rightarrow K$ -shell transitions with only slightly increased energies compared to K_α photons from singly charged ions.

On the other hand, $L \rightarrow K$ -shell transitions in ions with only few electrons in the inner shells, i.e., with holes in the K- or L-shell in addition to the necessary vacancy in the K-shell, correspond to larger energy shifts and are therefore more characteristic concerning X-ray emission from a plasma. In Hydrogen-like, Helium-like, Lithium-like, ... up to Oxygen-like ions, the K- and L-shell (apart from the necessary vacancy in the K-shell for K-shell transitions) are never fully occupied. For this work, the so called He_α emission

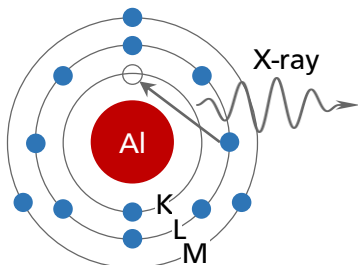


Figure 3.1.: K_α emission at $E^{ph}(K_\alpha) = 1.49$ keV in Al [52].

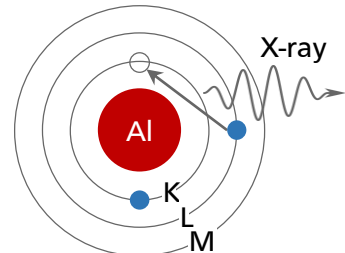


Figure 3.2.: He_α emission at $E^{ph}(He_\alpha) = 1.59$ keV in Al [52] with $E^{ph}(He_\alpha) > E^{ph}(K_\alpha)$.

from Helium-like ions is particularly important. The situation of this L → K-shell transition is depicted in Fig. 3.2.

Independent of the ionization state, higher nuclear charges Z result in higher photon energies from K-shell emission. The K_α photon energies $E^{\text{ph}}(K_\alpha)$ [52] and He α photon energies $E^{\text{ph}}(\text{He}_\alpha)$ [52] of different materials relevant for our experiment are shown in Table 3.1 to give an example of this behavior.

Table 3.1.: Ionization energies and photon energies from line emission of different materials (all data from [52] besides E_L^{ion} of ${}_6\text{C}$ [53]).

Material	${}_6\text{C}$	${}_{13}\text{Al}$	${}_{29}\text{Cu}$	${}_{42}\text{Mo}$	${}_{47}\text{Ag}$
$E^{\text{ph}}(K_\alpha)$ in keV	0.277	1.486	8.041	17.443	22.103
$E^{\text{ph}}(\text{He}_\alpha)$ in keV	0.392	1.593	8.370	17.982	22.730
E_K^{ion} in keV	0.284	1.560	8.979	20.000	25.514
E_L^{ion} in keV	0.011	0.118	1.097	2.866	3.806

3.2. Challenge of High Numbers of Photons From Higher-Energetic Line Emission

The reader should be reminded that our requirements to X-ray spectra for X-ray diffraction are high numbers of monoenergetic photons with high photon energies. To meet these requirements, line emission needs to be optimized or to be more precise, photon numbers from transitions to the K-shell in high-Z materials need to be enhanced. However, the maximum nuclear charge that can be used to efficiently produce line emission is limited by the electron temperature of the plasma. In the following, this dependence is explained and an estimate of the electron temperature for PHELIX ns-pulse parameters is used to investigate the limit in our case.

As described in section 3.1.3, the prerequisite for K-shell emission is to have a hole in the K-shell. In a plasma, such a hole can be caused by K-shell ionization from collisional processes involving unbound electrons or from radiative processes involving photons [54]. Besides ionization, a hole in the K-shell can also be caused by the excitation of a K-shell electron to another shell. For this case two conditions must be fulfilled: The final shell of the transition must not be fully occupied and the energy transferred from the electron or photon must match the transition.

To cause K-shell ionization, the electron or photon energy has to be higher than the K-shell ionization energy E_K^{ion} . To cause excitation of K-shell electrons, the lowest possible energy is $E^{\text{ph}}(K_\alpha)$ which corresponds to the transition from K-shell with lowest energy, namely the K → L-shell transition.

In the case of thermalized electrons, their Maxwell-Boltzmann energy distribution is determined by the electron temperature T_e . In contrast, photon energies can in principle be enlarged compared to electron energies by recombination, but the increase is only small (compared to E_K^{ion} and $E^{\text{ph}}(K_\alpha)$) if there are no holes present in the K-shell. The reason is that L-shell ionization energy E_L^{ion} is much smaller than E_K^{ion} and $E^{\text{ph}}(K_\alpha)$ (see Table 3.1). Altogether, this means that T_e has to be large enough to ensure that sufficient electrons and photons can cause K-shell ionization or excitation. In particular, higher T_e are necessary for materials with higher Z .

In the case of PHELIX ns-pulses with maximum intensities of few $10^{15} \text{ W cm}^{-2}$, we expect to reach $T_e \approx 1 - 2 \text{ keV}$. This value was estimated from findings of a previous work [44] where PHELIX ns-pulses were used. In that work, line emission spectra were analyzed with regard to the populated ionization states, and the corresponding temperatures were compared to hydrodynamic MULTI-2D [55] simulations and analytical calculations with the following equation [49]:

$$T_e \approx 3 \cdot 10^7 \left(\frac{I_{\text{abs}}(\text{W cm}^{-2})}{f n_e} \right)^{2/3} \text{ eV}, \quad (3.2)$$

where I_{abs} is the absorbed laser intensity, f the flux limiter and n_e the electron density.

In a previous work [44], it was observed that line emission from $L \rightarrow K$ -shell transitions can be produced with Ti, Fe, Ni and Cu. For each element, multiple highly charged ionization states, among others He-like states, were populated and contributed to the emission. The conversion efficiencies into overlapping emission lines around the He_α photon energy were found to be dropping with nuclear charge Z : from $\eta \sim 10^{-3}$ for Ti ($Z = 22$) and laser intensities of $I \sim 2 \cdot 10^{15} \text{ W cm}^{-2}$ to $\eta \sim 4 \cdot 10^{-5}$ for Cu ($Z = 29$) and $I \sim 5 \cdot 10^{15} \text{ W cm}^{-2}$. Furthermore, a strong dependence of the conversion efficiency on laser intensity, i.e., T_e , was observed. Altogether, there is a trade-off between increasing nuclear charges and thus photon energies from line emission on the one hand, and reaching larger conversion efficiencies on the other. In particular, we expect even lower conversion efficiencies for targets with considerably higher Z , e.g., Mo ($Z = 42$) or Ag ($Z = 49$), than observed in the previous work [44]. Our expectation is supported when comparing $T_e \approx 1 - 2 \text{ keV}$ with E_K^{ion} of Mo and Ag (see Table 3.1) which are at least a factor of 10 larger than T_e .

3.3. Experiment Idea

The main purpose of our experiment was to address the limitation of nuclear charges where line emission can be efficiently produced (cf. section 3.2). The basic idea to address this issue is explained subsequently.

Fundamentally, more electrons at energies above the K-shell ionization energy are required. Therefore, we tried to exploit a plasma absorption mechanism that produces fast electrons with energies much larger than the thermal electron temperature $T_e \approx 1 - 2 \text{ keV}$ of thermal electrons. The process we chose was the TPD which is one among several parametric instabilities arising from laser-plasma interactions [31, 56] and promising for our purpose. By TPD the incoming electromagnetic laser light couples to electron plasma waves which can in turn produce fast electrons with superthermal energies by collisionless damping. When exploiting TPD, one challenge is that the process only takes place in a small range of the electron density n_e and is very sensitive to laser parameters and plasma properties [27, 32–35, 57].

The optimal conditions for TPD can typically not be met when using materials with large nuclear charges like Mo or Ag [58] (cf. section 5.2), but these are essential for high photon energies from line emission. To solve this contradiction, we decided to decouple the processes of TPD and fast electron generation on the one hand, and the production of line emission on the other hand. We implemented a coated target design with a low-Z coating on a high-Z substrate. The low-Z coating enables to optimize TPD conditions and the high-Z substrate to produce line emission at high photon energies.

As shown in Fig. 3.3, the laser is incident on the low-Z coating, in our case the plastic C_3H_6 , producing a preplasma and driving the TPD instability. The generated fast electrons can in turn penetrate the coating and reach the high-Z substrate material where they ionize K-shell electrons and K_α emission with high

photon energies is produced. This coated target design is similar to the one used by LePape *et al.* during an experiment at NIF [25].

Note that when using our coated targets, the substrate is expected to be rather cold so that K_{α} emission from cold material but no emission from K \rightarrow L-shell transitions in higher charged ions is produced. In addition to increased diagnostic capabilities due to higher photon energies, the K_{α} emission from coated targets is spectrally much narrower than the overlap of different emission lines from highly charged ions with different charge states in uncoated targets. This enables the detection of more intense diffraction rings with less angular broadening and thus better Bragg angle resolution when applied to X-ray diagnostics.

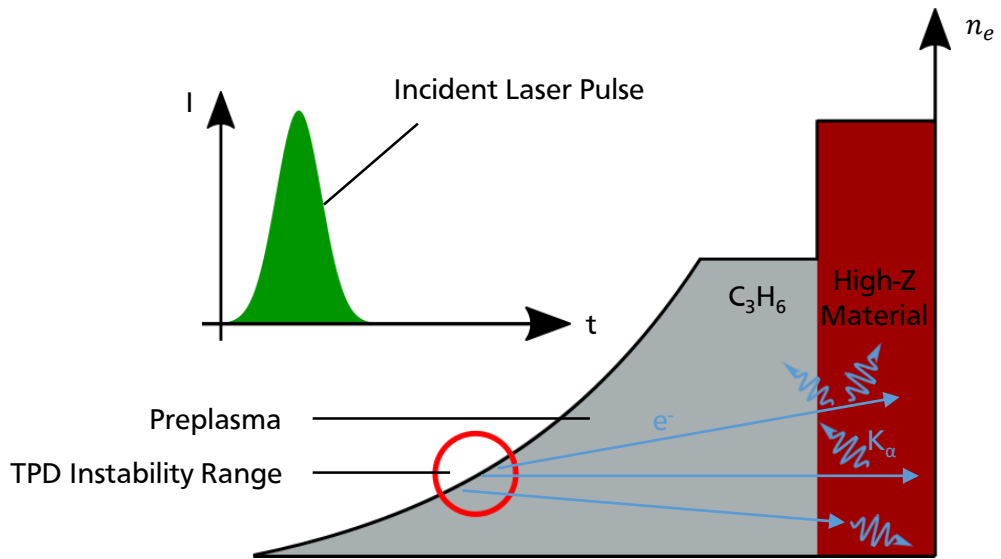


Figure 3.3.: Schematic of our coated target design with C_3H_6 as coating and a high-Z substrate material. The incident laser pulse produces a preplasma and drives the TPD instability.

4. Two-Plasmon Decay

In this chapter, I present the theory of TPD in detail. In section 4.1, I summarize the most important information about the two types of waves participating in TPD: electromagnetic waves in a plasma and electron plasma waves (EPWs). Afterwards, an introduction to TPD is given in section 4.2. The subsequent section 4.3 summarizes the derivation of a differential equation that describes the coupling of the incident laser field into EPWs. In section 4.4, the TPD growth rate is derived from that differential equation. In both sections 4.3 and 4.4, we limit ourselves to the case of homogeneous media. The derivations were developed in cooperation with Vincent Bagnoud. We did not find any comprehensive derivation of the TPD growth rate in the literature of which the results allowed for reasonable conclusions on the TPD instability.

Our result for the growth rate in homogeneous media is discussed and visualized in section 4.5 based on further investigations by myself. I present a quantitative example of the TPD growth rate for typical laser parameters and motivate in which directions EPWs are excited by TPD. Furthermore, the relevance of damping effects on the EPWs is discussed. In section 4.6 the dependence of TPD on the electron density is analyzed. Section 4.7 summarizes the most important information about the convective TPD instability in the case of a linear varying electron density. This includes the convective TPD gain as derived in the literature [27, 59, 60] and the influence of damping effects. The last section 4.8 describes how TPD generates fast electrons for which we try to exploit the process.

4.1. The Two Types of Waves Participating in the Two-Plasmon Decay

This section summarizes the most important characteristics of the waves participating in TPD: electromagnetic waves in a plasma and electron plasma waves. The equations needed later in this chapter are stated. Their derivations can be found in standard plasma physics books, e.g., in [56] and [50]. For our considerations, we assume the ions to be immobile and thus to constitute a homogeneous background.

4.1.1. Electromagnetic Waves in a Plasma

We make the ansatz of a transversal electromagnetic wave and choose the wave vector in x-direction as

$$\vec{k}_0 = \begin{pmatrix} k_0 \\ 0 \\ 0 \end{pmatrix} \quad (4.1)$$

and the electric field in y-direction as

$$\vec{E}_0 = E_0 e^{i(\omega_0 t - k_0 x)} \vec{e}_y, \quad (4.2)$$

where ω_0 , k_0 and E_0 are the angular frequency, wave number and field amplitude, respectively. The corresponding magnetic field is connected to the electric field via Faraday's law of induction

$$\vec{\nabla} \times \vec{E} = -\frac{\partial \vec{B}}{\partial t} \quad (4.3)$$

and it holds

$$\vec{B}_0 = \frac{k_0}{\omega_0} E_0 e^{i(\omega_0 t - k_0 x)} \vec{e}_z = \frac{1}{v_0^{\text{ph}}} E_0 e^{i(\omega_0 t - k_0 x)} \vec{e}_z, \quad (4.4)$$

where $v_0^{\text{ph}} = \frac{\omega_0}{k_0}$ is the phase velocity of the wave. Here, we only consider the wave in the situation without any background field. The velocity \vec{v}_0 of electrons in the plasma caused by the electromagnetic wave can then be calculated from the Lorentz force

$$m \frac{d\vec{v}_0}{dt} = -e(\vec{E}_0 + \vec{v}_0 \times \vec{B}_0) \approx -e\vec{E}_0, \quad (4.5)$$

where m is the electron mass, e the unit charge and the term with \vec{B}_0 can be neglected assuming that $|\vec{v}_0| \ll v_0^{\text{ph}}$. Due to this assumption, the electron movement in the wave is only in the direction of the electric field. Inserting Eq. 4.2 into Eq. 4.5 and integrating yields

$$\vec{v}_0 = i \frac{e}{m\omega_0} \vec{E}_0 = i \frac{eE_0}{m\omega_0} e^{i(\omega_0 t - k_0 x)} \vec{e}_y. \quad (4.6)$$

From Eqs. 4.3, 4.4 and 4.6, it is also possible to relate the magnetic field and the electrons' velocity in the wave by

$$\vec{B}_0 = \frac{m}{e} \vec{\nabla} \times \vec{v}_0. \quad (4.7)$$

It is important to point out that the movement of the electrons is perpendicular to the direction of \vec{k}_0 , i.e., the direction in which the phase of their movement varies (see Eq. 4.6). This means that the electron movement does not cause any temporal or spatial change in the electron density in homogeneous media. Considering the homogeneous ionic background, the electromagnetic wave is, in particular, source free, i.e., $\vec{\nabla} \cdot \vec{E}_0 = 0$.

The described interaction of the electrons and the wave changes the dispersion relation of the electromagnetic wave, i.e, the photons, compared to the vacuum. After some calculation [50, 56], one obtains the dispersion relation

$$\omega_0^2 = \omega_p^2 + c^2 k_0^2, \quad (4.8)$$

where ω_p is the plasma frequency and c the speed of light in vacuum. The plasma frequency depends on the electron density n_e and is given by

$$\omega_p = \sqrt{\frac{n_e e^2}{\epsilon_0 m}}, \quad (4.9)$$

where ϵ_0 is the dielectric constant. The plasma frequency is the eigenfrequency of the oscillation that occurs when electrons are displaced from the uniform background of ions. The electromagnetic wave forces the electrons to an oscillation with a modified frequency (see Eq. 4.8).

For the stated results, it was implicitly assumed that the electron density has no gradient, as the angular frequency, wave vector and thus the dispersion relation were not assumed to be space dependent. In the case of laser produced plasmas, the physical picture is more complete when taking a density gradient into account. We will discuss the most important extensions for that case using our previous results.

The dispersion relation implies that with increasing electron density, the wave number decreases, since the frequency ω_0 stays constant. From Eqs. 4.8 and 4.9 follows

$$k_0 = \sqrt{\frac{\omega_0^2 - \omega_p^2}{c^2}} = \frac{\omega_0}{c} \sqrt{1 - \frac{n_e}{n_c}} = k_{\text{vac}} \sqrt{1 - \frac{n_e}{n_c}}, \quad (4.10)$$

where $k_{\text{vac}} = \omega_0/c$ is the wave number in vacuum and n_c the critical density. The latter is defined as

$$n_c = \frac{\epsilon_0 m \omega_0^2}{e^2}, \quad (4.11)$$

such that $k_0(n_e = n_c) = 0$ which means that photons show a cut-off behavior at the critical density and cannot penetrate higher densities. The wave number k_0 (see Eq. 4.10) determines the phase velocity

$$v_0^{\text{ph}} = \frac{\omega_0}{k_0} = \frac{c}{\sqrt{1 - \frac{n_e}{n_c}}}, \quad (4.12)$$

which is larger in a plasma compared to the vacuum. Our aforementioned assumption $|\vec{v}_0| \ll v_0^{\text{ph}}$ is thus well justified for $|\vec{v}_0| \ll c$. The group velocity v_0^g follows from dispersion relation such that

$$v_0^g = \frac{\partial \omega_0}{\partial k_0} = \frac{k_0 c^2}{\omega_0} = c \cdot \sqrt{1 - \frac{n_e}{n_c}} \leq c. \quad (4.13)$$

Note that Eqs. 4.10 - 4.13 base on the derived dispersion relation (see Eq. 4.8) of the homogeneous case, but with the assumption of a variable density. The Eqs. 4.10 - 4.13 are thus also valid for the particular case of homogeneous density.

4.1.2. Electron Plasma Waves

In contrast to transversal electromagnetic waves, the EPWs correspond to a density variation which I explain in the following. The waves fulfill the definition of longitudinal waves

$$\vec{E}_L \parallel \vec{k}_L, \quad (4.14)$$

where \vec{E}_L and \vec{k}_L are the electric field and wave vector of the EPW, respectively. To fulfill Eq. 4.14, the typical ansatz made for the electric field is

$$\vec{E}_L = \frac{\vec{k}_L}{k_L} E_L e^{i(\omega_L t - \vec{k}_L \vec{r})}, \quad (4.15)$$

where ω_L , k_L and E_L are the angular frequency, wave number and field amplitude, respectively. From Faraday's law of induction (see Eq. 4.3), it follows that the wave is electrostatic, i.e., it does not coincide with any time varying magnetic field. Not considering any possible constant background field, it follows

$$\vec{B}_L = 0. \quad (4.16)$$

From the Lorentz force, the electrons' movement in the EPW can be calculated similar to Eq. 4.5 and 4.6 and it holds

$$\vec{v}_L = i \frac{e}{m \omega_L} \vec{E}_L = i \frac{e E_L}{m \omega_L} \frac{\vec{k}_L}{k_L} e^{i(\omega_L t - \vec{k}_L \vec{r})}. \quad (4.17)$$

The electrons move in the direction of the wave vector \vec{k}_L which is the reason for the electrostatic waves to cause a density variation n_L . From magnetohydrodynamics, it follows that n_L fulfills the differential equation [31]

$$-\frac{\partial^2}{\partial t^2} n_L = \frac{e^2 n_0}{m \epsilon_0} n_L - \frac{\zeta k_B T_e}{m} \vec{\nabla}^2 n_L, \quad (4.18)$$

where k_B is the Boltzmann constant, T_e the thermal electron temperature and ζ the adiabatic index. For the derivation of Eq. 4.18, it was assumed that the density variation n_L due to the EPWs only causes a small perturbation to the homogeneous electron density n_0 of free electrons in the plasma. Furthermore, no other wave besides the electrostatic wave was assumed to be present in the plasma.

From Eq. 4.18, it follows that

$$n_L = n e^{i(\omega_L t - \vec{k}_L \cdot \vec{r})}, \quad (4.19)$$

where n is the amplitude of the density variation. From the density variation, the dispersion relation of the EPWs or - put another way - the waves' quantized excitation states, the so-called plasmons, follows. It is given by

$$\omega_L^2 = \omega_p^2 + \frac{\zeta}{2} v_{th}^2 k_L^2, \quad (4.20)$$

where the thermal electron velocity is defined as

$$v_{th} = \sqrt{2k_B T_e / m}. \quad (4.21)$$

The dispersion relation implies the phase and group velocity,

$$v_L^{ph} = \frac{\omega_L}{k_L} = \sqrt{\frac{\omega_p^2}{k_L^2} + \frac{\zeta}{2} v_{th}^2} \quad (4.22)$$

and

$$v_L^g = \frac{\partial \omega_L}{\partial k_L} = \frac{\zeta v_{th}^2 k_L}{2 \omega_L}, \quad (4.23)$$

respectively.

For the previous considerations, we have assumed the electron density n_0 to have no density gradient and the thermal electron temperature not to be space dependent. Furthermore, no damping effects are included in the equations specified above. Note that the dispersion relation of both, photons (see Eq. 4.8) and plasmons (see Eq. 4.20), depends on the plasma frequency.

We can transfer our results to the case of a density gradient, similarly to section 4.1.1 by allowing for a variable density. From the dispersion relation 4.20, it follows that at a constant thermal electron temperature, a change of the electron density corresponds to a change of the EPW number, since the frequency ω_L stays constant.

4.2. Introduction to the Two-Plasmon Decay

TPD is the decay of a photon of an electromagnetic wave into two plasmons [26, 27, 29, 31]. It represents an absorption mechanism by which incident laser light can excite EPWs. TPD sets on if there is a perturbation δn_e in the electron density in the direction of the laser propagation [31]. Such a perturbation can arise

from noise and constitutes an EPW [31]. Since EPWs are in turn amplified by TPD, the onset for TPD growths and a feedback loop is created. On the other hand, there exist also damping effects counteracting the growth of EPWs by TPD. Above the resulting threshold, TPD causes an exponential amplification until saturation effects start playing a role.

This section first summarizes the early days of theoretical research regarding TPD. Afterwards, some special properties of the TPD instability are pointed out, including an easily measurable experimental proof for the occurrence of TPD. Furthermore, damping, saturation effects and the production of fast electrons are discussed.

The TPD instability was theoretically described in the 1960's for the first time. Goldman (supervised by DuBois) investigated the "coupling of external radiation to a pair of longitudinal modes" [26] by a Green's function approach including what is considered as TPD nowadays. He calculated the TPD growth rate slightly above threshold. Only little later, Jackson used the Vlasov equation to analyze "the parametric excitation of the modes of an infinite plasma by intense incident radiation" [61] (including TPD) which resulted in a more general description of the TPD growth rate. In the special case of low laser intensity, he reproduced the results of Goldman.

In 1972, Rosenbluth published a paper investigating parametric instabilities in inhomogeneous media [27]. Supposed there is an electron density gradient in one direction, for instance in x -direction, then the amplitude $E_0(x)$ of an electromagnetic wave propagating through the gradient changes with that coordinate. In order to simplify the description of this amplitude change, Rosenbluth used the WKB approximation $\frac{\partial E_0(x)}{\partial x} \ll kE_0(x)$, i.e., that the amplitude change is small over one wavelength. He obtained TPD to be a convective instability which amplifies EPWs arising from noise.

Convective means that the waves travel significantly through the interaction region during their amplification. In case of TPD, these are EPWs, eventually leaving the interaction region with a larger amplitude. In contrast to that, an *absolute* instability describes the situation when the amplification happens faster than the EPW propagates through the interaction region. In that case, the amplification occurs with time at a nearly fixed position until limited by saturation effects. The absolute instability coincides with a low group velocity of the EPW which is causal for the slow propagation of the density perturbation.

Based on the work of Drake and Lee for other parametric instabilities [62], Lee and Kaw [63] pointed out that Rosenbluth obtained TPD to be only convectively and not absolutely unstable because he used the WKB approximation. They calculated that TPD also shows an absolutely unstable behavior when no WKB approximation is used. In 1976, Liu and Rosenbluth published a more generalized analysis than Lee and Kaw where they extended Lee and Kaw's calculations to a wider range of EPW vectors [28]. New analytical approximations and numerical solutions to the differential equation in this paper of Liu and Rosenbluth describing the TPD instability were published by Simon *et al.* [29] in 1983.

After this historical overview, we will now look at the special characteristics that distinguish TPD from other parametric instabilities. Particularly important is that TPD only takes place in a small range around the quarter critical density of the laser photons [31]. The TPD condition $n_e \approx n_c/4$ can be derived from the dispersion relation of photons (transversal electromagnetic waves, see Eq. 4.8) and the dispersion relation of plasmons (longitudinal EPWs, see Eq. 4.20) as follows [31]. When the laser photon decays, energy must be conserved which is ensured by the equation

$$\begin{aligned} \omega_0 &= \omega_1 + \omega_2 \\ \Leftrightarrow \sqrt{\omega_p^2 + c^2 k_0^2} &= \sqrt{\omega_p^2 + \frac{\zeta}{2} v_{th}^2 k_1^2} + \sqrt{\omega_p^2 + \frac{\zeta}{2} v_{th}^2 k_2^2}, \end{aligned} \quad (4.24)$$

where the indices 1 and 2 denote the frequencies of the two produced plasmons. Since $c \gg v_{\text{th}}$ (at least at $T_e \approx 1 - 2 \text{ keV}$), we make the approximation $\omega_1 \approx \omega_2 \approx \omega_p$. Inserting the plasma frequency ω_p (see Eq. 4.9) and the critical density n_c (see Eq. 4.11) into Eq. 4.24 results in

$$\begin{aligned} \sqrt{\frac{n_c e^2}{\epsilon_0 m}} &= \omega_0 \approx 2\omega_p = 2\sqrt{\frac{n_e e^2}{\epsilon_0 m}} \\ \Rightarrow n_e &\approx n_c/4. \end{aligned} \quad (4.25)$$

More detailed analyses show that TPD typically occurs at density ranges $0.25 \gtrsim n_e/n_c > 0.2$ as a convective instability. Only over a much smaller range TPD is absolutely unstable [60], typically $0.25 \gtrsim n_e/n_c > 0.243$ [33]. For typical laser-driven TPD experiments, the convective instability behavior of TPD dominates the interaction, since it takes place in a much larger region of the plasma.

Nevertheless, the frequencies of the plasmons excited by TPD all lie in a small interval around $\omega_0/2$, since $\omega_1 \approx \omega_2 \approx \omega_p (n_e = n_c/4) = \omega_0/2$. This can be used for an indirect detection technique of TPD. The interaction of plasmons with laser photons, which have the frequency ω_0 , results in electron oscillations at a frequency of $\omega_0/2 + \omega_0 = 3/2 \omega_0$ (cf. section 4.4). Therefore, dipole radiation at $3/2 \omega_0$ occurs and constitutes a signature of TPD [64]. Usually, the $3/2 \omega_0$ radiation is easy to measure for typical wavelengths of high energy laser systems. The prescribed detection technique has been used since the 1970's [65, 66] and was also part of the experiment carried out in the context of this master thesis.

Electron plasma waves excited by TPD have a wave vector in the plane given by the electric field and wave vector of the incident electromagnetic wave. A specialty about TPD compared to stimulated Raman scattering and stimulated Brillouin scattering is that the EPW vectors cannot have vanishing components perpendicular to the photons' wave vector [31, 33].

There are two different types of damping processes counteracting the growth of the EPWs by TPD: collisional and Landau damping [28, 33]. Collisional damping means that an electron (moving in the EPW) makes a Coulomb collision with an ion which randomizes the electron's oscillatory motion. In particular, the electron cannot participate in the collective movement of the wave after colliding, thus the wave is damped. Collisional damping is often considered with respect to electromagnetic waves where it displays an important absorption mechanism and is also known as inverse Bremsstrahlung [30]. The process applies similarly to EPWs [31]. For a Maxwellian electron velocity distribution, the collisional wave *energy* damping rate is given by [31]

$$\Gamma_C = -\frac{\omega_p^2}{\omega_L^2} \nu_{ei}, \quad (4.26)$$

where ν_{ei} is the electron ion collision rate. For simplicity, we assume $\omega_L \approx \omega_p$, i.e., we neglect the thermal correction in the dispersion relation (see Eq. 4.20). For EPWs amplified by TPD ($\omega_L = \omega_1, \omega_2$), it is $\omega_1 \approx \omega_2 \approx \omega_p (n_e = n_c/4)$. Since $\omega_p^2 \propto n_e$, the collisional damping rate would actually be around 20% smaller at $n_e = 0.2n_c$ than with our assumption. The closer n_e gets to $0.25n_c$, the smaller the deviation. With the described simplification, the wave *amplitude* damping rate reads [31]

$$\gamma_C = \frac{\Gamma_C}{2} \approx -\frac{\nu_{ei}}{2} = -\frac{1}{6(\pi)^{1.5}} \frac{Z_i \omega_p^4}{n_e v_{\text{th}}^3} \ln(\Lambda_C), \quad (4.27)$$

where Z_i is the charge state of the ions and $\ln(\Lambda_C)$ the Coulomb Logarithm. In the case that the minimum impact parameter of the considered collisions is the distance of closest possible approach between electron and ion, it holds

$$\Lambda_C = 9N_D/Z_i, \quad (4.28)$$

where $N_D = 4/3 \pi n_e \lambda_D^3$ is the number of electrons in a Debye sphere. The Debye sphere has a radius of the Debye length

$$\lambda_D = \sqrt{\frac{\epsilon_0 k_B T_e}{n_e e^2}}. \quad (4.29)$$

It should be noted that for Eqs. 4.26 and 4.27 to be valid, it is necessary that the electron velocity distribution stays a Maxwellian while collisions occur. In other words, the electrons need to rethermalize faster than they loose energy. This is the case for $\nu_{ee} v_{th}^2 / 2 \gg \nu_{ei} v_L^2$ [31], where ν_{ee} is the electron-electron collision rate and v_L the electron velocity in the EPW. The thermal velocity v_{th} is related to the thermal electron temperature of the Maxwellian distribution. The dependence of Eq. 4.27 on Z_i indicates that $\nu_{ee} = \nu_{ei}/Z_i$ can be used as first approximation, since electrons are only singly charged. The rethermalizing condition can thus be written as $2Z_i v_L^2 / v_{th}^2 \ll 1$ [31].

On the other hand, Landau damping is a collisionless process where electrons with velocities near the plasma wave's phase velocity v_L^{ph} (see Eq. 4.22) are accelerated by the wave which in turn loses energy. For a Maxwellian electron velocity distribution and the case that the plasma wave's frequency is close to the plasma frequency, i.e., the thermal correction in the dispersion relation (see Eq. 4.20) is negligible, the damping rate is given by [31, 56]

$$\gamma_L = -0.22 \sqrt{\pi} \omega_p \frac{1}{(\sqrt{2} k_L \lambda_D)^3} e^{-\frac{1}{2k_L^2 \lambda_D^2}}. \quad (4.30)$$

For Eq. 4.30 to be valid, it is furthermore required that the damping is weak, i.e., the damping rate is small compared to the wave frequency, and that the EPW phase velocity is large compared to the thermal velocity related to the Maxwellian distribution. In formulas, this relates to $\gamma_L \ll \omega_L$ and $v_{th} \ll v_L^{ph} = \omega_L/k_L$.

In order that EPWs can be amplified by TPD, the growth due to the instability must overcome both damping effects, i.e., collisional and Landau damping.

Furthermore, there exist effects that lead to a saturation behavior of TPD when the EPW amplitude increases. These nonlinear effects and most obviously the depletion of the electromagnetic wave decrease the growth by TPD once large EPW amplitudes are reached. Another example of a saturation effect is the profile steepening of n_e at $n_c/4$ due to ponderomotive forces from the superposition of electromagnetic wave and EPWs. The profile steepening reduces the volume where TPD can occur and thus weakens the effect [31, 67].

The production of fast electrons by TPD occurs via collisionless damping of EPWs. Therefore, collisional damping reduces the amount of energy transferred to fast electrons. How large this influence is and thus how large the EPWs actually need to grow, given a certain amount of fast electrons, is the subject of recent research. The work of Turnbull *et al.* [37] indicates that collisional damping is the dominant process concerning the dissipation of energy of EPWs excited by TPD.

In typical TPD experiments, conversion efficiencies over 1 % from laser energy into fast electrons have been observed (see, e.g., [32, 35]). Furthermore, it has been reported that the temperatures of fast electrons produced by TPD increased with laser intensity. Values up to 90 keV were measured.

4.3. Derivation of the Coupling Equation in Homogeneous Media

This section deals with the derivation of a differential equation to describe the coupling of the incident laser field into EPWs in homogeneous media neglecting second order terms of the EPWs and their damping. The calculation is mainly based on two fundamental results from magnetohydrodynamics: the equation of continuity and the momentum equation which are summarized in the following. For this work, it is assumed that the reader is familiar with the concept of magnetohydrodynamics. Details can be found in standard plasma physics books, e.g., in [56] and [50].

The equation of continuity

$$\frac{\partial n_e}{\partial t} + \vec{\nabla}(n_e \vec{v}_e) = 0, \quad (4.31)$$

where \vec{v}_e and n_e are the mean electron velocity and electron density in a fluid element, respectively, refers to the concept of total mass conservation. In a descriptive way, the equation of continuity 4.31 means that the electron number N within a finite volume V can only be changed by the flux of electrons, $\vec{j}_e = n_e \vec{v}_e$, through the bounding surface ∂V .

The momentum equation is given by

$$m n_e \left[\frac{\partial \vec{v}_e}{\partial t} + (\vec{v}_e \vec{\nabla}) \vec{v}_e \right] = -e n_e (\vec{E} + \vec{v}_e \times \vec{B}) - \vec{\nabla} p, \quad (4.32)$$

where \vec{E} and \vec{B} are the electric and magnetic field, respectively, and $p \equiv n_e k_B T_e$ is the pressure. It describes the motion of a fluid element due to the forces on it. These forces are on the right hand side of Eq. 4.32. The left hand side of Eq. 4.32 incorporates a partial time and a space derivative. This is due to the so called Lagrangian fluid description in which fluid elements move along with the particles contained in the respective element. The Lagrangian description is commonly used when it comes to the momentum equation, since it is very intuitive to have particles and fluid elements moving together when one calculates their trajectories.

Assuming an equation of state of the form

$$p = C \rho^\zeta, \quad (4.33)$$

where C is a constant, ρ the mass density and ζ the adiabatic index, it holds $\vec{\nabla} p = \zeta k_B T_e \vec{\nabla} n_e$. Inserting into Eq. 4.32 and dividing by n_e results in

$$m \left[\frac{\partial \vec{v}_e}{\partial t} + (\vec{v}_e \vec{\nabla}) \vec{v}_e \right] = -e (\vec{E} + \vec{v}_e \times \vec{B}) - \frac{\zeta k_B T_e \vec{\nabla} n_e}{n_e}. \quad (4.34)$$

Equations 4.31 and 4.34 are the basis for the derivation of the growth rate. Note that in Eq. 4.34, there are no damping effects included. For the following analysis, we first neglect damping and consider it as counteracting effect of the growth afterwards, described in section 4.5.2. Together, Eqs. 4.31 and 4.34 are dependent on n_e , \vec{v}_e , \vec{E} and \vec{B} which all need to be considered during the calculation. On the other hand, T_e is assumed to be constant.

As a next step, we simplify the equations by superposing the electromagnetic wave and excited EPWs which will result in a coupling of them. We express the density, velocity, electric and magnetic field as

$$\begin{aligned} n_e &= n_0 + n_1, \\ \vec{v}_e &= \vec{v}_0 + \vec{v}_1, \\ \vec{E} &= \vec{E}_0 + \vec{E}_1, \\ \vec{B} &= \vec{B}_0, \end{aligned} \tag{4.35}$$

where index 0 and index 1 denote quantities corresponding to the electromagnetic wave and the EPWs, respectively. There is no field \vec{B}_1 , since the electrostatic EPWs do not coincide with any magnetic field (cf. section 4.1.2). To consider the two plasmons, we will later use $n_1 = n_{11} + n_{12}$ and $\vec{v}_1 = \vec{v}_{11} + \vec{v}_{12}$. We assume that the EPWs are only a small perturbation to the electron density, i.e., $n_1 \ll n_0$, and to the electron movement in the electromagnetic wave, i.e., $|\vec{v}_1| \ll |\vec{v}_0|$. Therefore, terms in second order of n_1 or \vec{v}_1 are neglected in the following and our analysis cannot reproduce nonlinear effects of growth such as saturation. For the transversal movement, it holds $\frac{\partial n_0}{\partial t} = 0$, $\vec{\nabla} n_0 = 0$ and $\vec{\nabla} \vec{v}_0 = 0$, since we consider a homogeneous medium. Inserting our ansatz 4.35 into the equation of continuity 4.31 and using the relations described above, yields

$$\begin{aligned} \cancel{\frac{\partial n_0}{\partial t}} + \frac{\partial n_1}{\partial t} + n_0(\vec{\nabla} \vec{v}_0) + \vec{v}_0(\vec{\nabla} n_0) + n_0(\vec{\nabla} \vec{v}_1) + \vec{v}_1(\vec{\nabla} n_0) + \vec{\nabla}(n_1 \vec{v}_0) + \vec{\nabla}(n_1 \vec{v}_1) &= 0 \\ \Leftrightarrow \quad \frac{\partial n_1}{\partial t} + n_0(\vec{\nabla} \vec{v}_1) + \vec{\nabla}(n_1 \vec{v}_0) &= 0. \end{aligned} \tag{4.36}$$

On the other hand, we simplify the momentum equation 4.34, additionally using $m \frac{\partial \vec{v}_0}{\partial t} = m \frac{d \vec{v}_0}{dt} = -e(\vec{E}_0 + \vec{v}_0 \times \vec{B}_0)$ (see Eq. 4.5), and get

$$\begin{aligned} m \left[\cancel{\frac{\partial \vec{v}_0}{\partial t}} + \frac{\partial \vec{v}_1}{\partial t} + (\vec{v}_e \vec{\nabla}) \vec{v}_e \right] &= -e(\vec{E}_1 + \vec{E}_0 + \vec{v}_0 \times \vec{B}_0 + \vec{v}_1 \times \vec{B}_0) - \frac{\zeta k_B T_e (\vec{\nabla} n_0 + \vec{\nabla} n_1)}{n_0 + \nu_T} \\ \Leftrightarrow \quad m \left[\frac{\partial \vec{v}_1}{\partial t} + (\vec{v}_e \vec{\nabla}) \vec{v}_e \right] &= -e(\vec{E}_1 + \vec{v}_1 \times \vec{B}_0) - \frac{\zeta k_B T_e \vec{\nabla} n_1}{n_0}. \end{aligned} \tag{4.37}$$

Note that $\partial \vec{v}_0 / \partial t = d \vec{v}_0 / dt$ because of $(\vec{v}_0 \vec{\nabla}) \vec{v}_0 = 0$ which is due to the fact that \vec{v}_0 only has a y -component and a spatial dependence of x . Furthermore, note that n_1 in the denominator of Eq. 4.37 was neglected because of $n_1 \ll n_0$.

Equations 4.36 and 4.37 can be combined by taking the divergence of the latter and inserting Eq. 4.36 for $\vec{\nabla} \vec{v}_1$. Furthermore, we insert Gauss's law $\vec{\nabla} \vec{E}_1 = -\frac{en_1}{\epsilon_0}$ which describes that the source of the electrostatic field \vec{E}_1 is the density variation n_1 . It holds

$$\begin{aligned} m \left[\frac{\partial}{\partial t} \vec{\nabla} \vec{v}_1 + \vec{\nabla}((\vec{v}_e \vec{\nabla}) \vec{v}_e) \right] &= -e(\vec{\nabla} \vec{E}_1 + \vec{\nabla}(\vec{v}_1 \times \vec{B}_0)) - \frac{\zeta k_B T_e \vec{\nabla}^2 n_1}{n_0} \\ \Leftrightarrow \quad m \left[\frac{\partial}{\partial t} \left(-\frac{1}{n_0} \left[\frac{\partial n_1}{\partial t} + \vec{\nabla}(n_1 \vec{v}_0) \right] \right) + \vec{\nabla}((\vec{v}_e \vec{\nabla}) \vec{v}_e) \right] &= -e \left[\frac{-en_1}{\epsilon_0} + \vec{\nabla}(\vec{v}_1 \times \vec{B}_0) \right] - \frac{\zeta k_B T_e \vec{\nabla}^2 n_1}{n_0} \\ \Leftrightarrow \quad m \left[-\frac{\partial^2 n_1}{\partial t^2} - \vec{\nabla} \frac{\partial}{\partial t} (n_1 \vec{v}_0) + n_0 \vec{\nabla}((\vec{v}_e \vec{\nabla}) \vec{v}_e) \right] &= -en_0 \left[\frac{-en_1}{\epsilon_0} + \vec{\nabla}(\vec{v}_1 \times \vec{B}_0) \right] - \zeta k_B T_e \vec{\nabla}^2 n_1. \end{aligned} \tag{4.38}$$

Rearranging the terms of Eq. 4.38 results in

$$-m \frac{\partial^2 n_1}{\partial t^2} + \zeta k_B T_e \vec{\nabla}^2 n_1 - \frac{e^2 n_0 n_1}{\epsilon_0} = \vec{\nabla} \left[m \frac{\partial}{\partial t} (n_1 \vec{v}_0) - m n_0 ((\vec{v}_e \vec{\nabla}) \vec{v}_e) - n_0 e (\vec{v}_1 \times \vec{B}_0) \right], \quad (4.39)$$

where we have used $\vec{\nabla} n_0 = 0$ to write n_0 inside the divergence. In Eq. 4.39, there is still the term $(\vec{v}_e \vec{\nabla}) \vec{v}_e$ which needs to be expressed by \vec{v}_0 and \vec{v}_1 (see Eq. 4.35). For that purpose, we use the relation $\vec{\nabla}(\vec{A}^2/2) = (\vec{A} \vec{\nabla}) \vec{A} - (\vec{\nabla} \times \vec{A}) \times \vec{A}$ which is valid for any vector \vec{A} . Applying to $(\vec{v}_e \vec{\nabla}) \vec{v}_e$, as suggested by Liu and Rosenbluth [28], yields

$$\begin{aligned} (\vec{v}_e \vec{\nabla}) \vec{v}_e &= \vec{\nabla} (\vec{v}_e^2 / 2) + (\vec{\nabla} \times \vec{v}_e) \times \vec{v}_e \\ &= \left(\vec{\nabla} (\vec{v}_0^2) + \vec{\nabla} (2\vec{v}_0 \vec{v}_1) + \vec{\nabla} (\vec{v}_1^2) \right) / 2 + (\vec{\nabla} \times \vec{v}_0) \times \vec{v}_0 + (\vec{\nabla} \times \vec{v}_0) \times \vec{v}_1 + (\vec{\nabla} \times \vec{v}_1) \times (\vec{v}_0 + \vec{v}_1). \end{aligned} \quad (4.40)$$

A few terms in Eq. 4.40 are zero. First, it holds $\nabla \times \vec{v}_1 = 0$, since EPWs are longitudinal. Second, for \vec{v}_0 belonging to the electromagnetic wave (see Eq. 4.6), one can calculate that $\vec{\nabla} (\vec{v}_0^2) / 2 + (\vec{\nabla} \times \vec{v}_0) \times \vec{v}_0 = 0$. Additionally, we insert $\vec{\nabla} \times \vec{v}_0 = \frac{e}{m} \vec{B}_0$ (see Eq. 4.7) and neglect $\vec{\nabla} (\vec{v}_1^2)$ as it is a term of second order. Altogether follows

$$(\vec{v}_e \vec{\nabla}) \vec{v}_e = \vec{\nabla} (\vec{v}_0 \vec{v}_1) + \frac{e}{m} \vec{B}_0 \times \vec{v}_1. \quad (4.41)$$

Inserting Eq. 4.41 into Eq. 4.39, we get the final result for the differential equation

$$\begin{aligned} -m \frac{\partial^2 n_1}{\partial t^2} + \zeta k_B T_e \vec{\nabla}^2 n_1 - \frac{e^2 n_0 n_1}{\epsilon_0} &= \vec{\nabla} \left[m \frac{\partial}{\partial t} (n_1 \vec{v}_0) - m n_0 \left(\vec{\nabla} (\vec{v}_0 \vec{v}_1) + \frac{e}{m} \vec{B}_0 \times \vec{v}_1 \right) - n_0 e (\vec{v}_1 \times \vec{B}_0) \right] \\ \Leftrightarrow -m \frac{\partial^2 n_1}{\partial t^2} + \zeta k_B T_e \vec{\nabla}^2 n_1 - \frac{e^2 n_0 n_1}{\epsilon_0} &= \vec{\nabla} \left[m \frac{\partial}{\partial t} (n_1 \vec{v}_0) - m n_0 (\vec{\nabla} (\vec{v}_0 \vec{v}_1)) \right] \end{aligned} \quad (4.42)$$

describing the coupling of the incident laser field into longitudinal EPWs. The left hand side of the equation represents the propagation of the EPWs (see Eq. 4.18) while the right hand side gives rise to their excitation. It therefore appears that the oscillation $\vec{v}_0 \neq 0$ of electrons in the transversal electromagnetic field is causal to the amplification of EPWs.

Our result for the coupling equation 4.42 is the same as derived in the textbook of Mulser [30] who used a different ansatz for his derivation.

4.4. Derivation of the Two-Plasmon Decay Growth Rate in Homogeneous Media

In this section, we solve the coupling equation 4.42 and calculate the growth rate of the TPD instability in homogeneous media. When making an ansatz for n_1 , we need to take into account that two EPWs are excited by TPD. Therefore, we consider $n_1 \equiv n_{11} + n_{12}$. We make the ansatz

$$n_{1j} = \frac{1}{2} \left(n_{1j}(t) e^{i(\omega_j t - \vec{k}_j \cdot \vec{r})} + C.C. \right) \equiv n_{1j}^+ + n_{1j}^-, \quad (4.43)$$

where $j = 1, 2$ distinguishes the two EPWs, ω_j and \vec{k}_j denote their angular frequencies and wave vectors, respectively, and $n_{1j}(t)$ are time dependent amplitudes. The excitation of the EPWs is represented by

the growth of these amplitudes. Later in our calculation, we will assume the coupling to be slow, i.e., $\frac{\partial}{\partial t} n_{1j}(t) \ll \omega_j n_{1j}(t)$.

For the electromagnetic wave, we assume that it is not weakened by the excitation of the EPWs. This assumption corresponds to the perturbation ansatz that we used in section 4.3. The movement of the electrons due to the electromagnetic field is then given by

$$\vec{v}_0 = \frac{1}{2} \left(i \frac{eE_0}{m\omega_0} \cdot \vec{e}_y \cdot e^{i(\omega_0 t - k_0 x)} + C.C. \right) \equiv \vec{v}_0^+ + \vec{v}_0^-, \quad (4.44)$$

where Eq. 4.6 was extended by its complex conjugate. Note that considering the complex conjugate in Eqs. 4.43 and 4.44 is necessary, since the product $n_1 \vec{v}_0$ appears in the coupling equation 4.42. In that equation, the product of $\vec{v}_0 \vec{v}_1$ occurs, as well. From the density variation due to the EPWs, we can derive an expression for the corresponding electron velocities \vec{v}_{1j} with $\vec{v}_1 = \vec{v}_{11} + \vec{v}_{12}$. Starting from the simplified continuity equation (see Eq. 4.36), we use $\vec{\nabla} \vec{v}_0 = 0$ and assume $\vec{v}_0 (\vec{\nabla} n_1) \ll n_0 (\vec{\nabla} \vec{v}_1)$, which will be proven justified later in section 4.5.3 for typical TPD experiments. One obtains

$$\begin{aligned} \frac{\partial n_1}{\partial t} + n_0 (\vec{\nabla} \vec{v}_1) + \cancel{\vec{v}_0 (\vec{\nabla} n_1)} + n_1 (\cancel{\vec{\nabla} \vec{v}_0}) &= 0 \\ \Leftrightarrow \quad \frac{\partial n_1}{\partial t} + n_0 (\vec{\nabla} \vec{v}_1) &= 0. \end{aligned} \quad (4.45)$$

Equation 4.45 should be fulfilled for each EPW separately, i.e., for $n_1 \rightarrow n_{1j}$ and $\vec{v}_1 \rightarrow \vec{v}_{1j}$. Inserting Eq. 4.43 into Eq. 4.45 and using $\frac{\partial}{\partial t} n_{1j}(t) \ll \omega_j n_{1j}(t)$ then yields

$$\vec{v}_{1j} = \frac{1}{2} \left(\frac{\omega_j}{n_0 k_j^2} \cdot \vec{k}_j \cdot n_{1j}(t) e^{i(\omega_j t - \vec{k}_j \vec{r})} + C.C. \right). \quad (4.46)$$

Having determined the ansatz of n_1 , \vec{v}_0 and \vec{v}_1 (see Eq. 4.43, 4.44 and 4.46, respectively), our aim is to insert them into the coupling equation 4.42. As one can easily see, this includes numerous terms that we consider separately for the sake of convenience. For the product $n_1 \vec{v}_0 = (n_{11} + n_{12}) \vec{v}_0$, we get

$$\begin{aligned} n_{1j} \vec{v}_0 &= \vec{v}_0^+ n_{1j} + \vec{v}_0^- n_{1j} = \vec{v}_0^+ n_{1j} + C.C. \\ &= i \frac{eE_0}{4m\omega_0} \cdot \vec{e}_y \cdot n_{1j}(t) e^{i(\omega_0 t - k_0 x)} \left(e^{i(\omega_j t - \vec{k}_j \vec{r})} + e^{-i(\omega_j t - \vec{k}_j \vec{r})} \right) + C.C. \\ &= i \frac{eE_0}{4m\omega_0} \cdot \vec{e}_y \cdot n_{1j}(t) \left(e^{i((\omega_0 + \omega_j)t - k_0 x - \vec{k}_j \vec{r})} + e^{i((\omega_0 - \omega_j)t - k_0 x + \vec{k}_j \vec{r})} \right) + C.C. \end{aligned} \quad (4.47)$$

Similarly, it holds

$$\begin{aligned} \vec{v}_0 \vec{v}_{1j} &= \vec{v}_0^+ \vec{v}_{1j} + C.C. \\ &= i \frac{eE_0}{4m\omega_0} \frac{\omega_j}{n_0 k_j^2} \cdot k_{jy} \cdot n_{1j}(t) \left(e^{i((\omega_0 + \omega_j)t - k_0 x - \vec{k}_j \vec{r})} + e^{i((\omega_0 - \omega_j)t - k_0 x + \vec{k}_j \vec{r})} \right) + C.C. \end{aligned} \quad (4.48)$$

Considering the derivatives of Eq. 4.47 according to the coupling equation 4.42, it follows with our

assumption $\frac{\partial}{\partial t} n_{1j}(t) \ll \omega_j n_{1j}(t)$ that

$$\begin{aligned}
\vec{\nabla} \frac{\partial}{\partial t} (n_{1j} \vec{v}_0) &= \vec{\nabla} \left(i \frac{eE_0}{4m\omega_0} \cdot \vec{e}_y \cdot \left[\left(\cancel{\frac{\partial n_{1j}(t)}{\partial t}} + i(\omega_0 + \omega_j) n_{1j}(t) \right) e^{i((\omega_0 + \omega_j)t - k_0 x - \vec{k}_j \vec{r})} \right. \right. \\
&\quad \left. \left. + \left(\cancel{\frac{\partial n_{1j}(t)}{\partial t}} + i(\omega_0 - \omega_j) n_{1j}(t) \right) e^{i((\omega_0 - \omega_j)t - k_0 x + \vec{k}_j \vec{r})} \right] + C.C. \right) \\
&= \frac{eE_0}{4m\omega_0} \cdot k_{jy} \cdot \left[\left(i(\omega_0 + \omega_j) n_{1j}(t) \right) e^{i((\omega_0 + \omega_j)t - k_0 x - \vec{k}_j \vec{r})} \right. \\
&\quad \left. - \left(i(\omega_0 - \omega_j) n_{1j}(t) \right) e^{i((\omega_0 - \omega_j)t - k_0 x + \vec{k}_j \vec{r})} \right] + C.C. \\
&\tag{4.49}
\end{aligned}$$

It should be noted that our assumption $\frac{\partial}{\partial t} n_{1j}(t) \ll \omega_j n_{1j}(t)$ allows for neglecting $\frac{\partial n_{1j}(t)}{\partial t}$ in the second line, since $\omega_0 - \omega_j \approx \omega_0/2 \approx \omega_j$. Next we calculate the derivatives of Eq. 4.48 occurring in the coupling equation 4.42. It follows

$$\begin{aligned}
\vec{\nabla}^2 (\vec{v}_0 \vec{v}_{1j}) &= \vec{\nabla} \left(i \frac{eE_0}{4m\omega_0} \frac{\omega_j}{n_0 k_j^2} \cdot k_{jy} \cdot n_{1j}(t) \left[i(-k_0 \vec{e}_x - \vec{k}_j) e^{i((\omega_0 + \omega_j)t - k_0 x - \vec{k}_j \vec{r})} \right. \right. \\
&\quad \left. \left. + i(-k_0 \vec{e}_x + \vec{k}_j) e^{i((\omega_0 - \omega_j)t - k_0 x + \vec{k}_j \vec{r})} \right] + C.C. \right) \\
&= -i \frac{eE_0}{4m\omega_0} \frac{\omega_j}{n_0 k_j^2} \cdot k_{jy} \cdot n_{1j}(t) \left[\left((k_{jx} + k_0)^2 + k_{jy}^2 \right) e^{i((\omega_0 + \omega_j)t - k_0 x - \vec{k}_j \vec{r})} \right. \\
&\quad \left. + \left((k_{jx} - k_0)^2 + k_{jy}^2 \right) e^{i((\omega_0 - \omega_j)t - k_0 x + \vec{k}_j \vec{r})} \right] + C.C., \\
&\tag{4.50}
\end{aligned}$$

where we used that \vec{k}_0 only has an x-component and that \vec{k}_j have no z-component, since the incident electromagnetic field propagates in x-direction and oscillates in y-direction. This means that no momentum transfer in z-direction is possible, i.e., the excited EPWs cannot propagate in z-direction.

Let us now insert our ansatz 4.43 into the left hand side of the coupling equation 4.42. It holds

$$\begin{aligned}
&= -m \frac{\partial^2 n_{1j}}{\partial t^2} + \zeta k_B T_e \vec{\nabla}^2 n_{1j} - \frac{e^2 n_0 n_{1j}}{\epsilon_0} \\
&= -\frac{m}{2} \left(\left[\frac{\partial^2}{\partial t^2} n_{1j}(t) \right] e^{i(\omega_j t - \vec{k}_j \vec{r})} + 2 \left[\frac{\partial}{\partial t} n_{1j}(t) \right] \left[\frac{\partial}{\partial t} e^{i(\omega_j t - \vec{k}_j \vec{r})} \right] \right) \\
&\quad - \frac{m}{2} n_{1j}(t) \left[\frac{\partial^2}{\partial t^2} e^{i(\omega_j t - \vec{k}_j \vec{r})} \right] + \zeta k_B T_e \vec{\nabla}^2 n_{1j} + -\frac{e^2 n_0 n_{1j}}{\epsilon_0} + C.C. \\
&= -\frac{m}{2} \left(\left[\cancel{\frac{\partial^2}{\partial t^2} n_{1j}(t)} + 2i\omega_j \frac{\partial}{\partial t} n_{1j}(t) \right] e^{i(\omega_j t - \vec{k}_j \vec{r})} \right) \\
&\quad + \frac{n_{1j}(t)}{2} \left(-m \left[\frac{\partial^2}{\partial t^2} e^{i(\omega_j t - \vec{k}_j \vec{r})} \right] + \zeta k_B T_e \left[\cancel{\vec{\nabla}^2} e^{i(\omega_j t - \vec{k}_j \vec{r})} \right] - \frac{e^2 n_0 e^{i(\omega_j t - \vec{k}_j \vec{r})}}{\epsilon_0} \right) + C.C., \\
&\tag{4.51}
\end{aligned}$$

of which the two simplifications are explained in the following. First, we assume $\frac{\partial^2}{\partial t^2} n_{1j}(t) \ll \omega_j \frac{\partial}{\partial t} n_{1j}(t)$ similar to $\frac{\partial}{\partial t} n_{1j}(t) \ll \omega_j n_{1j}(t)$. The second term vanishes as it is equivalent to Eq. 4.18 with the exponential $e^{i(\omega_j t - \vec{k}_j \vec{r})}$ describing a dimensionless density variation of the EPWs. Taking into account the terms of both EPWs, the coupling equation reads

$$-im\omega_1 \left[\frac{\partial}{\partial t} n_{11}(t) \right] e^{i(\omega_1 t - \vec{k}_1 \vec{r})} - im\omega_2 \left[\frac{\partial}{\partial t} n_{12}(t) \right] e^{i(\omega_2 t - \vec{k}_2 \vec{r})} + C.C. = \vec{\nabla} \left[m \frac{\partial}{\partial t} (n_1 \vec{v}_0) - mn_0 (\vec{\nabla}(\vec{v}_0 \vec{v}_1)) \right]. \quad (4.52)$$

Generally, the idea for the further calculation is to rearrange Eq. 4.52 to $\frac{\partial}{\partial t} n_{1j}(t)$ and integrate later on. Inserting Eq. 4.49 and 4.50 after rearranging yields numerous terms with different frequencies and wave vectors in the corresponding exponentials. Of these, many can be neglected as they are off-resonant for the TPD mechanism. The mathematical reason is that their exponentials oscillate for $\omega_0 \rightarrow \omega_1 \& \omega_2$, thus averaging to zero when integrating over a sufficiently long time interval. One example is the exponential $e^{i(\omega_0 + \omega_2 - \omega_1)t}$ which follows from multiplying Eq. 4.52 by $e^{-i(\omega_1 t - \vec{k}_1 \vec{r})}$ and would require $\omega_0 + \omega_2 = \omega_1$ in order to be resonant. Therefore, the exponential is not resonant when considering TPD.

On the other hand, the exponential $e^{i(\omega_0 + \omega_2 - \omega_1)t}$ indicates that the coupling of a photon at ω_0 and a plasmon at $\approx \omega_0/2$, produced from TPD, to a plasmon at $\approx 3/2 \omega_0$ is possible. The resulting electron oscillation at $\approx 3/2 \omega_0$ results in dipole radiation at that frequency. This radiation is a signature of TPD [64–66] (cf. section 4.2), since the plasmon at $\approx \omega_0/2$, produced from TPD, is a prerequisite for its generation. The mathematical analysis of the described process goes beyond the scope of this master thesis.

After this remark, let us continue with the derivation of the TPD growth rate. All terms in Eq. 4.52 off-resonant in the case of TPD have frequencies of the order $\sim \omega_0$ such that it is appropriate to neglect them when considering time intervals longer than some femtoseconds. Keeping only the resonant terms, the coupling equation 4.52 becomes

$$\begin{aligned} & \omega_1 \left[\frac{\partial}{\partial t} n_{11}(t) \right] e^{i(\omega_1 t - \vec{k}_1 \vec{r})} + \omega_2 \left[\frac{\partial}{\partial t} n_{12}(t) \right] e^{i(\omega_2 t - \vec{k}_2 \vec{r})} \\ &= \frac{eE_0}{4m\omega_0} \left[n_{11}(t) k_{1y} \left((\omega_0 - \omega_1) - \frac{\omega_1}{k_1^2} ((k_{1x} - k_0)^2 + k_{1y}^2) \right) e^{i((\omega_0 - \omega_1)t - k_0 x + \vec{k}_1 \vec{r})} \right. \\ & \quad \left. + n_{12}(t) k_{2y} \left((\omega_0 - \omega_2) - \frac{\omega_2}{k_2^2} ((k_{2x} - k_0)^2 + k_{2y}^2) \right) e^{i((\omega_0 - \omega_2)t - k_0 x + \vec{k}_2 \vec{r})} \right]. \end{aligned} \quad (4.53)$$

It can be shown that Eq. 4.53 translates to a system of two coupled differential equations

$$\text{I. } \omega_1 \left[\frac{\partial}{\partial t} n_{11}(t) \right] = \frac{eE_0}{4m\omega_0} n_{12}(t) k_{2y} \left((\omega_0 - \omega_2) - \frac{\omega_2}{k_2^2} ((k_{2x} - k_0)^2 + k_{2y}^2) \right) e^{i((\omega_0 - \omega_2 - \omega_1)t - k_0 x + (\vec{k}_2 + \vec{k}_1) \vec{r})} \quad (4.54a)$$

$$\text{II. } \omega_2 \left[\frac{\partial}{\partial t} n_{12}(t) \right] = \frac{eE_0}{4m\omega_0} n_{11}(t) k_{1y} \left((\omega_0 - \omega_1) - \frac{\omega_1}{k_1^2} ((k_{1x} - k_0)^2 + k_{1y}^2) \right) e^{i((\omega_0 - \omega_2 - \omega_1)t - k_0 x + (\vec{k}_2 + \vec{k}_1) \vec{r})}. \quad (4.54b)$$

We note that the growth of one EPW depends on the amplitude of the other, thus both EPWs grow together. Equations 4.54a and 4.54b still contain exponentials. From the condition that they do not oscillate and

therefore do not average out when integrating, it follows energy conservation

$$\omega_0 = \omega_1 + \omega_2. \quad (4.55)$$

Furthermore, we assumed the amplitudes $n_{1j}(t)$ of the EPWs to be only time and not space dependent. For that assumption to be fulfilled, the space dependence in the exponentials in Eq. 4.54a and 4.54b needs to vanish which yields momentum conservation

$$\vec{k}_0 = \vec{k}_1 + \vec{k}_2. \quad (4.56)$$

Note that Eqs. 4.55 and 4.56 both correspond to the situation of a photon decaying in two plasmons. The exact energy and momentum conservation, however, followed from a mathematical side of view. For each coordinate, the momentum conservation reads

$$\begin{pmatrix} k_{0x} \\ 0 \\ 0 \end{pmatrix} = \begin{pmatrix} k_{1x} + k_{2x} \\ k_{1y} + k_{2y} \\ 0 \end{pmatrix}, \quad (4.57)$$

because $k_{jz} = 0$. We drop the exponentials in Eqs. 4.54a and 4.54b, using energy conservation (see Eq. 4.55) and momentum conservation (see Eq. 4.57), and it follows

$$\text{I. } \left[\frac{\partial}{\partial t} n_{11}(t) \right] = \frac{eE_0}{4m\omega_0} n_{12}(t) k_{2y} \left(\frac{\omega_1 k_2^2 - \omega_2 k_1^2}{\omega_1 k_2^2} \right) \quad (4.58a)$$

$$\text{II. } \left[\frac{\partial}{\partial t} n_{12}(t) \right] = \frac{eE_0}{4m\omega_0} n_{11}(t) k_{1y} \left(\frac{\omega_2 k_1^2 - \omega_1 k_2^2}{\omega_2 k_1^2} \right). \quad (4.58b)$$

The system of equations 4.58a and 4.58b is solvable by usual approaches for linear systems of coupled differential equations. Here, we choose to take the time derivative of Eq. 4.58a, insert Eq. 4.58b and get

$$\frac{\partial^2}{\partial t^2} n_{11}(t) = \left(\frac{eE_0}{4m\omega_0} \right)^2 k_{2y} \left(\frac{\omega_1 k_2^2 - \omega_2 k_1^2}{\omega_1 k_2^2} \right) k_{1y} \left(\frac{\omega_2 k_1^2 - \omega_1 k_2^2}{\omega_2 k_1^2} \right) n_{11}(t) \equiv \gamma^2 n_{11}(t). \quad (4.59)$$

Similarly, we could get $\frac{\partial^2}{\partial t^2} n_{12}(t) = \gamma^2 n_{12}(t)$. For both $j = 1, 2$, the factor γ is the same. Clearly, we can see that the time dependent amplitudes

$$n_{1j}(t) = n_{1j}(0) \cdot e^{\gamma t} \quad (4.60)$$

solving the differential equations grow exponentially in time, since

$$\gamma = \frac{eE_0}{4m\omega_0} \sqrt{k_{2y} \left(\frac{\omega_1 k_2^2 - \omega_2 k_1^2}{\omega_1 k_2^2} \right) k_{1y} \left(\frac{\omega_2 k_1^2 - \omega_1 k_2^2}{\omega_2 k_1^2} \right)} = \frac{eE_0}{4m\omega_0} \sqrt{k_{1y}^2 \frac{(\omega_1 k_2^2 - \omega_2 k_1^2)^2}{\omega_1 k_2^2 \omega_2 k_1^2}} > 0. \quad (4.61)$$

For that reason, γ is called the TPD growth rate. Corresponding to γ being the same for both EPWs, Eq. 4.61 is invariant when interchanging the indices j . The factor

$$G = e^{\gamma t} \quad (4.62)$$

describes the gain of an initial electron density perturbation $n_{1j}(0)$ by TPD. The homogeneous growth rate stated in Eq. 4.61 is also used in the literature [59, 60].

If $v_{\text{th}} \ll c$, the growth rate can be further simplified using $\omega_1 \approx \omega_2$ (cf. section 4.2) to

$$\gamma = \frac{eE_0}{4m\omega_0} \sqrt{k_{1y}^2 \frac{(k_2^2 - k_1^2)^2}{k_2^2 k_1^2}}. \quad (4.63)$$

4.5. Discussion of the Two-Plasmon Decay Growth Rate in Homogeneous Media

In the following, our result for the TPD growth rate is discussed in more detail. In section 4.5.1, the dependence of γ on the EPW vectors is analyzed. The directions in which EPWs are excited are visualized and a condition for maximum TPD growth is calculated. Section 4.5.2 is about the influence of collisional and Landau damping. Each of the two sections 4.5.1 and 4.5.2 includes a quantitative example at typical laser parameters, the first for the growth rate and the second for the damping rates. In section 4.5.3, I discuss a few of our assumptions made during the derivation of the homogeneous growth rate (see sections 4.3 and 4.4) and assumptions regarding the collisional and Landau damping rates.

4.5.1. Dependence of the Homogeneous Growth Rate on the Electron Plasma Wave Vectors

In the following, the dependence of the TPD growth rate on the EPW vectors is analyzed. A condition for maximum TPD growth is calculated and a quantitative example of the growth rate is given.

We consider the growth rate given by Eq. 4.63 for the case of negligible thermal corrections in the dispersion relation of the plasmons (see Eq. 4.20), i.e., $\omega_1 \approx \omega_2$. Using momentum conservation (see Eq. 4.57), we make the growth rate dependent on the momentum of only one EPW. It follows

$$\gamma(k_x, k_y) = \frac{eE_0}{4m\omega_0} \sqrt{k_y^2 \frac{\left((k_0 - k_x)^2 + k_y^2 - (k_x^2 + k_y^2)\right)^2}{\left((k_0 - k_x)^2 + k_y^2\right)(k_x^2 + k_y^2)}} = \frac{eE_0}{4m\omega_0} \sqrt{k_y^2 \frac{\left(k_0^2 - 2k_0k_x\right)^2}{\left((k_0 - k_x)^2 + k_y^2\right)(k_x^2 + k_y^2)}}, \quad (4.64)$$

where we dropped the index j , since the result is the same nevertheless which index we use. Equation 4.64 enables to plot the growth rate over k_x and k_y as presented in Fig. 4.1. The laser intensity and vacuum wavelength were assumed to be $I = 1 \cdot 10^{15} \text{ W cm}^{-2}$ and $\lambda_{\text{vac}} = 527 \text{ nm}$, respectively. This corresponds to typical values in this work achieved with the PHELIX laser. From the intensity, the electric field amplitude was estimated by

$$E_0 = \sqrt{\frac{2I}{c\epsilon_0}}. \quad (4.65)$$

Note that here we consider TPD and thus E_0 in a homogeneous medium while the experimentally produced plasmas are strongly inhomogeneous. The intensity in Eq. 4.65 should actually be the intensity in the homogeneous medium, but here we consider the vacuum laser intensity neglecting absorption. In Eq. 4.65, we also neglect the influence of the electron density and thus group velocity (see Eq. 4.13) on the field amplitude. For a fixed intensity, $I = \langle W \rangle_t v_0^G$, where $\langle W \rangle_t$ is the time averaged energy density, it follows $E_0 \propto \sqrt{I} \propto \sqrt{v_0^G} \propto (1 - n_e/n_c)^{0.25}$. At quarter critical density, this corresponds to a factor of $0.75^{0.25}$ compared to the vacuum and the effect is thus only very small. In contrast to the previous considerations, we take the variation of the wave number of the electromagnetic wave in a plasma compared to the vacuum (see Eq. 4.10) into account. At quarter critical density, it holds $k_0 = \sqrt{0.75}k_{\text{vac}} = \sqrt{0.75} \frac{2\pi}{\lambda_{\text{vac}}}$.

In Fig. 4.1, it is neglected that TPD occurs only approximately at quarter critical density and the homogeneous medium does not necessarily have $n_0 = n_e/4$, but this constant value of k_0 is used. This corresponds to an approximation error of $((1 - n_e/n_c)/(1 - 0.25))^{0.5}$ in k_0 , which is only 3% at $n_e = 0.2n_c$.

Next, let us investigate the constellations (k_x, k_y^{\max}) where the TPD growth rate is maximized for each k_x . For that purpose,

$$\frac{\partial}{\partial k_x} \gamma(k_x, k_y^{\max}) \stackrel{!}{=} 0 \quad (4.66)$$

needs to be solved and from that, it is possible to calculate the y-components of the EPW vector k_y^{\max} that correspond to maximum growth rates for each k_x . For $k_x \leq 0$ or $k_x \geq 1$, it follows

$$k_y^{\max}(k_x) = \pm \sqrt{k_x(k_x - k_0)} \quad (4.67)$$

and the TPD growth rate reaches its global maximum

$$\gamma_{\max} = \frac{eE_0}{4m\omega_0} k_0. \quad (4.68)$$

Using E_0 (see Eq. 4.65) and k_0 as previously, this yields $\gamma_{\max} \approx 1.1 \cdot 10^{13} \text{ s}^{-1}$ and the approximation error of 3 % in $k_0 = \sqrt{0.75} \frac{2\pi}{\lambda_{\text{vac}}}$ is the same in γ_{\max} . This means that, our assumption to neglect off-resonant terms is justified (cf. section 4.4), since the growth occurs on longer timescales than the femtosecond range. It is worth to mention that Eq. 4.68 does actually not depend on the laser wavelength, since $k_0 \propto 1/\lambda_{\text{vac}}$ and $\omega_0 \propto 1/\lambda_{\text{vac}}$.

The curves of globally maximal growth given by Eq. 4.67 are indicated in Fig. 4.1 for $k_x \leq 0$ or $k_x \geq 1$. In contrast to that, the TPD growth rate does not reach the global maximum at $0 < k_x < k_0$. At the

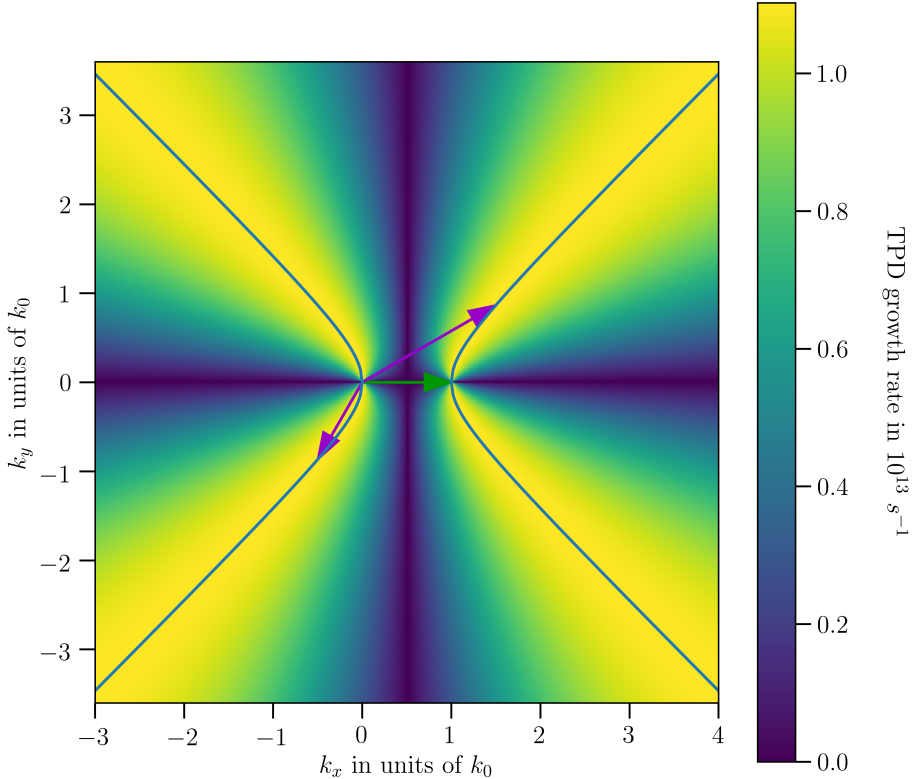


Figure 4.1.: TPD Growth rate in dependence of the EPW vector. The curves of maximum growth are shown in blue. A possible constellation with maximum growth is indicated with the electromagnetic wave vector in green and the EPW vectors in purple. For scaling the x - and y -axis, it was used $k_0 = \sqrt{0.75} k_{\text{vac}}$.

corresponding k_y^{\max} in this range, γ decreases linearly from $k_x = 0$ to $k_x = 0.5k_0$ from where it increases again. At $k_x = 0.5k_0$, the growth rate is zero for all k_y . More generally, we can see in Fig. 4.1 that the growth rate is axisymmetric around $k_x = 0.5k_0$. Furthermore, it is axisymmetric around $k_y = 0$. For two wave vectors fulfilling momentum conservation (see Eq. 4.57), this means that the TPD growth rate is the same for both waves. In Fig. 4.1, this is indicated for a combination of waves at maximum growth rate. Additionally, the wave vector of the incident electromagnetic wave is shown. Note that it is arbitrary which of the two EPWs has $k_y > 0$.

It is worth to point out that $\gamma(k_x, k_y)$ strongly influences in which directions EPWs are excited by TPD. Since the growth rate is in the exponent of the gain (see Eq. 4.62), almost only EPWs with maximum growth rate can grow to highest amplitudes. Simulations [59] show that these modes are indeed dominant in inhomogeneous media, too. Vectors $\vec{k} = (k_x, k_y)$ on the line of maximum growth rate in Fig. 4.1 directly point in the direction of propagation of these EPWs. The higher $|k_x|$ the more the angle relative to \vec{k}_0 approaches 45° .

On the other hand, the limit for smallest $|k_x|$ on the curve of maximum growth rate is $k_{1x} \rightarrow k_0$ and $k_{2x} \rightarrow 0$ with $k_{1y} = -k_{2y} \rightarrow 0$ (choice of indices is arbitrary). In Eq. 4.64, the growth rate is not defined for the exact limit values, but it can be evaluated from the system of differential equations 4.58a and 4.58b. Due to $\frac{\partial}{\partial t} n_{11}(t) \propto k_{2y} = 0$ and $\frac{\partial}{\partial t} n_{12}(t) \propto k_{1y} = 0$, there is actually no growth by TPD at the exact limit values. This indicates that the limit $k_{1x} \rightarrow k_0$ and $k_{2x} \rightarrow 0$ with $k_{1y} = -k_{2y} \rightarrow 0$ can only be reached asymptotically. For values close to the limit, one EPW nearly propagates in the direction of \vec{k}_0 while the other EPW vector is nearly at 90° to \vec{k}_0 .

4.5.2. Influence of Damping Effects

In this section, I describe the influence of damping effects on the TPD instability. Their damping rates counteract the TPD growth and need to be considered in order to get the total growth rate

$$\gamma_{\text{tot}} = \gamma + \gamma_C + \gamma_L, \quad (4.69)$$

where γ_C and γ_L are the collisional and Landau damping rate, respectively. Note that $\gamma_C < 0$ (see Eq. 4.27), $\gamma_L < 0$ (see Eq. 4.30) and that amplification of EPWs only occurs for $\gamma_{\text{tot}} > 0$.

Let us consider both damping effects separately starting with collisional damping. For an easier investigation, the damping rate with the simplification $\omega_j \approx \omega_p$ (see Eq. 4.27) is shown here once more with all dependencies inserted:

$$\gamma_C = -\frac{1}{6(\pi)^{1.5}} \frac{e^4}{\epsilon_0^2 m^{0.5}} \frac{Z_i n_e}{(2k_B T_e)^{1.5}} \ln \left(12\pi \left(\frac{\epsilon_0 k_B T_e}{e^2} \right)^{1.5} Z_i^{-1} n_e^{-0.5} \right). \quad (4.70)$$

At $n_e = 0.25n_c$ (for $\lambda_{\text{vac}} = 527 \text{ nm}$), $T_e = 1 \text{ keV}$ and for fully ionized carbon $Z_i = 6$, the damping rate is $\gamma_C \approx -0.22 \cdot 10^{13} \text{ s}^{-1}$. This is below the maximum TPD growth rate γ_{\max} calculated previously and allows for $\gamma_{\text{tot}} > 0$. In a plasma consisting of ions with higher charges, however, the damping rate increases significantly and becomes comparable to the the maximum TPD growth rate γ_{\max} . In the numerical example, we have only considered the quarter critical density. Neglecting the dependence in the logarithm, it holds $\gamma_C \propto n_e$ and therefore γ_C changes by the factor $n_e/(0.25n_c)$ from our calculated value. For a density of $n_e = 0.2n_c$, this corresponds to a reduction of 20 %. Another 20 % and thus a total reduction of 36 % is due to our simplification $\omega_j \approx \omega_p$ used in Eq. 4.70.

Next, we take a look at the impact of Landau damping on the TPD instability. From Eq. 4.30, we can see that Landau damping depends on $k\lambda_D$. Figure 4.2a shows γ_L against $k\lambda_D$ for a fixed plasma frequency at $n_e = 0.25n_c$ (for $\lambda_{\text{vac}} = 527 \text{ nm}$). We can see that γ_L is negligible for small $k\lambda_D$, but at some point the damping rate increases strongly with $k\lambda_D$. It overcomes the growth rate γ_{\max} (see Eq. 4.68) by TPD [31] which is indicated in Fig. 4.2a for $I = 1 \cdot 10^{15} \text{ W cm}^{-2}$ and $k_0 = \sqrt{0.75} \frac{2\pi}{\lambda_{\text{vac}}}$.

We calculate the intersection point of growth and damping by numerically solving $\gamma_{\max}^! = -\gamma_L$ for $k\lambda_D$. It follows

$$k\lambda_D \sim 0.27, \quad (4.71)$$

which is in good agreement to the typical value $k\lambda_D \sim 0.25$ found in the literature [33, 35, 36]. Due to the strong increase of γ_L with $k\lambda_D$, the intersection point is roughly the same even if plasma conditions and laser parameters vary.

In our numerical solution and in Fig. 4.2a, we have neglected the dependence of the plasma frequency on the density and thus the dependence $\gamma_L \propto n_e^{0.5}$ (see Eq. 4.30). Considering this dependence would alter the damping rate in our numerical calculation by a factor $\sqrt{n_e/(0.25n_c)}$ and reduce it by 10 % at $n_e = 0.2n_c$. Furthermore, we have neglected the approximation error in γ_{\max} (3 % at $n_e = 0.2n_c$). Due to the strong dependence of the Landau damping on $k\lambda_D$, these two approximations do, however, not significantly alter the result in Eq. 4.71.

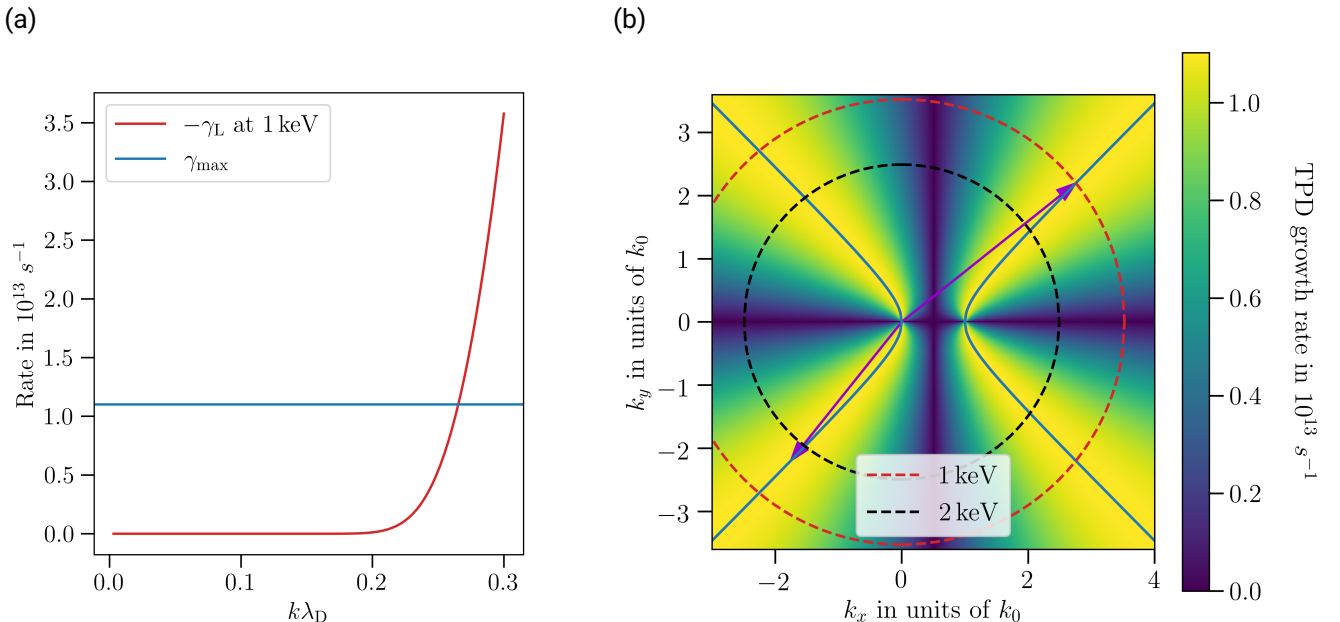


Figure 4.2.: Depiction of the relation between TPD and Landau damping. In (a), the damping rate is shown in comparison to the maximum TPD growth rate. In (b), the TPD growth rate and Landau cutoff at two different thermal electron temperatures (dashed circles) are shown. The curves of maximum growth are shown in blue. The constellation of largest EPW vectors at $T_e = 1 \text{ keV}$ and at maximum growth is indicated in purple. For scaling k_x and k_y , it was used $k_0 = \sqrt{0.75} k_{\text{vac}}$

If we neglect the density dependence $\lambda_D \propto n_e^{-0.5}$, as well, Eq. 4.71 directly denotes a condition for the wave number, above which EPWs cannot be excited by TPD. By this simplification, we overestimate the allowed values of k by approximately 10 % at $n_e = 0.2n_c$.

The influence of Landau damping on wave numbers below the limit denoted by Eq. 4.71 is small. Exemplarily, we calculate the damping rate at $k\lambda_D = 0.22$. Again neglecting the density dependence, it holds $\gamma_L = -0.077 \cdot 10^{13} \text{ s}^{-1}$ which is much smaller than γ_{\max} . Since Landau damping is only relevant to the highest wave numbers allowed, the term Landau cutoff is often used for condition 4.71. Above the Landau cutoff, no electron plasma waves can be amplified by TPD.

In Fig. 4.2b, the Landau cutoff at $T_e = 1 \text{ keV}$ is shown as a circle around the coordinate origin. Note that the cutoff was calculated for γ_{\max} and thus would actually limit already smaller wave numbers when the growth rate is not maximal. Due to the strong variation of γ_L with $k\lambda_D$, the difference would be small for most wave vectors. Figure 4.2b also includes a combination of EPW vectors with maximal wave numbers at $T_e = 1 \text{ keV}$ under the constraint to have the maximal TPD growth rate. From Fig. 4.2b, we can see that the condition 4.71 applies first to the EPW with $k_x > 0$, since that one has a larger wave number. Due to the coupling of the two EPWs (see Eqs. 4.58a and 4.58b), this hinders the growth of the other EPW, as well. Note that, it is again arbitrary which wave we choose to have $k_y > 0$.

Since $\lambda_D \propto T_e^{0.5}$, an increase in the thermal electron temperature shifts the Landau cutoff to smaller wave numbers. This is pictured in Fig. 4.2b, where the Landau cutoff is also shown for the temperature $T_e = 2 \text{ keV}$. If the temperature is increased further until the Landau cutoff applies for wave numbers below k_0 , the thermal electron temperature is too high in order to allow for any constellation of maximum TPD growth rate and therefore TPD is strongly suppressed.

4.5.3. Discussion of Assumptions

In the following, I discuss a few of our assumptions made during the derivation of the homogeneous TPD growth rate (see sections 4.3 and 4.4) and I discuss if using the typical formulas for collisional (see Eq. 4.70) and Landau damping (see Eq. 4.30) was justified.

First, let us investigate if $\vec{v}_0(\vec{\nabla}n_1) \ll n_0(\vec{\nabla}\vec{v}_1)$ is fulfilled which we used to derive Eq. 4.45. Using Eq. 4.46 and Eqs. 4.43, 4.44, we carry out the investigation for the two plasma waves separately. After some calculation, one obtains

$$\vec{v}_0(\vec{\nabla}n_{1j}) = -\frac{eE_0}{m\omega_0}n_{1j}(t)k_{jy} \sin(\omega_j t - \vec{k}_j \vec{r}) \sin(\omega_0 t - k_0 x) \quad (4.72)$$

and

$$n_0(\vec{\nabla}\vec{v}_{1j}) = n_{1j}(t)\omega_j \sin(\omega_j t - \vec{k}_j \vec{r}). \quad (4.73)$$

Only considering the amplitudes, we get

$$\frac{\vec{v}_0(\vec{\nabla}n_{1j})}{n_0(\vec{\nabla}\vec{v}_{1j})} \sim \frac{eE_0}{m\omega_0\omega_j} k_{jy} = \frac{2eE_0 k_0}{m\omega_0^2} \frac{k_{jy}}{k_0}, \quad (4.74)$$

where $\omega_j = \omega_0/2$ was used, neglecting the thermal correction in the dispersion relation of the EPWs (see Eq. 4.20). Furthermore, we multiplied by k_0/k_0 to be able to insert typical values k_{jy}/k_0 from Fig. 4.2b. Relating E_0 and k_0 to $I = 1 \cdot 10^{15} \text{ W cm}^{-2}$ and $\lambda_{\text{vac}} = 527 \text{ nm}$ as done above, it holds

$$\frac{\vec{v}_0(\vec{\nabla}n_{1j})}{n_0(\vec{\nabla}\vec{v}_{1j})} \sim 0.025 \frac{k_{jy}}{k_0} \quad (4.75)$$

and since typical values of k_{jy} are only up to three times k_0 , the assumption $\vec{v}_0(\vec{\nabla}n_{1j}) \ll n_0(\vec{\nabla}\vec{v}_{1j})$ is fulfilled.

Second, the assumption $|\vec{v}_1| \ll |\vec{v}_0|$ as part of our perturbation analysis (cf. section 4.3) is discussed. In Eq. 4.46, we made an ansatz for \vec{v}_{1j} which corresponds to

$$|\vec{v}_{1j}| \sim \frac{n_{1j}(t)}{n_0} \frac{\omega_j}{k_j} = \frac{n_{1j}(t)}{n_0} v_j^{\text{ph}}, \quad (4.76)$$

when only considering the amplitude. The phase velocity of the EPWs v_j^{ph} can be estimated using $\omega_j \approx \omega_0/2$ and typical values for k_j . In Fig. 4.2b, we can see that the latter are a few times k_0 . Making a quantitative example for $k_j = 2k_0$, we get

$$v_j^{\text{ph}} \sim \frac{\omega_0}{2k_0} = \frac{\omega_0}{2\sqrt{0.75}k_{\text{vac}}} \approx 0.58c. \quad (4.77)$$

Therefore, the phase velocities are actually very high and it strongly depends on $n_{1j}(t)/n_0$ if $|\vec{v}_{1j}| \ll |\vec{v}_0|$. For $I = 1 \cdot 10^{15} \text{ W cm}^{-2}$ and $\lambda_{\text{vac}} = 527 \text{ nm}$, it follows

$$|\vec{v}_0| \sim \frac{eE_0}{m\omega_0} = 0.014c, \quad (4.78)$$

when only considering the amplitude and relating E_0 and I as usual. Therefore, the assumption is only fulfilled when $n_{1j}(t)/n_0 \ll 0.014/0.58 = 0.024$ which is a much stronger condition compared our original assumption $n_{1j}/n_0 \ll 1$ (cf. section 4.3). In particular, EPWs with $k_x < 0$ can also have very small values k_j , thus increasing the phase velocity even further. Altogether, we conclude that our assumption $|\vec{v}_1| \ll |\vec{v}_0|$ is not necessarily fulfilled for all wave vector combinations and when the EPWs have grown. However, without this assumption the calculation would be much more complicated which goes beyond the scope of this master thesis.

Next, let us investigate if it is justified to approximate the electron velocity distribution as Maxwellian which is used for the derivation of the collisional damping rate (see Eqs. 4.26, 4.27, 4.70) and the Landau damping rate (see Eq. 4.30). We need to compare the electron velocities in the electromagnetic wave (see Eq. 4.44) and in the EPW (see Eq. 4.46) with the thermal electron velocity. From our previous consideration, we use Eq. 4.78 and note that this is smaller than

$$v_{\text{th}} = \sqrt{2k_B T_e/m} = 0.063c \quad (4.79)$$

at $T_e = 1 \text{ keV}$ (see Eq. 4.21). On the other hand, we estimated $|\vec{v}_{1j}| < |\vec{v}_0|$ for $n_{1j}(t)/n_0 < 0.024$ (at $k_j = 2k_0$). Therefore, the assumption of a Maxwellian velocity distribution seems to be valid at least for small EPW density oscillations and not too small wave numbers.

Concerning the collisional damping rate, it was also assumed that $2Z_i v_{1j}^2 / v_{\text{th}}^2 \ll 1$ (cf. section 4.2) in order that the electron velocity distribution stays a Maxwellian. Using Eqs. 4.76, 4.77 and 4.79, we note that this is the case if

$$\begin{aligned} 2Z_i \frac{v_{1j}^2}{v_{\text{th}}^2} &= 2Z_i \left(\frac{n_{1j}(t)}{n_0} \right)^2 \left(\frac{0.58c}{0.063c} \right)^2 \ll 1 \\ &\Leftrightarrow \sqrt{2Z_i} \frac{n_{1j}(t)}{n_0} \ll 0.11. \end{aligned} \quad (4.80)$$

Therefore, the assumption is only fulfilled for small Z_i or small $n_{1j}(t)/n_0$. However, also for larger Z_i , the EPWs should not contain too much energy as they are only a perturbation, thus the Maxwellian distribution

should not be altered much by their collisional damping. Concerning the electromagnetic waves, the situation might be different.

Equation 4.30 is valid for the case that the EPW phase velocity is large compared to the thermal velocity. By comparing Eq. 4.77 and Eq. 4.79, we can see that this condition is fulfilled. Furthermore, the requirement of weak Landau damping for Eq. 4.30 is met, since $\omega_j \approx \omega_0/2 = 1.8 \cdot 10^{15} \text{ s}^{-1}$ is much larger than the considered damping rates in the order of $1 \cdot 10^{13} \text{ s}^{-1}$.

4.6. Electron Density Dependence of the Two-Plasmon Decay

As mentioned in section 4.2, TPD approximately occurs at the quarter critical density. This approximation is based on neglecting the temperature correction in the dispersion relation of the EPWs (see Eq. 4.20). In this section, we calculate the electron density dependence of TPD more thoroughly including the effect of a finite temperature. We need to consider that the frequencies of the EPWs depend not only on the plasma frequency but also on their wave number. Let us derive a relation between the plasma frequency and wave numbers for which energy conservation of the TPD (see Eq. 4.55) is fulfilled.

Starting from Eq. 4.55, we insert the dispersion relation (see Eq. 4.20) and get

$$\omega_0 = \omega_1 + \omega_2 = \sqrt{\omega_p^2 + \frac{\zeta}{2} v_{th}^2 k_1^2} + \sqrt{\omega_p^2 + \frac{\zeta}{2} v_{th}^2 k_2^2}. \quad (4.81)$$

Rearranging to ω_p yields

$$\omega_p^2 = \frac{1}{4} \left(\omega_0 + \frac{\zeta v_{th}^2 (k_{1x}^2 + k_{1y}^2 - k_{2x}^2 - k_{2y}^2)}{2\omega_0} \right)^2 - \frac{\zeta}{2} v_{th}^2 (k_{1x}^2 + k_{1y}^2). \quad (4.82)$$

Inserting momentum conservation (see Eq. 4.57), we make the plasma frequency dependent of only one of the two EPWs. It follows

$$\omega_p^2(k_x, k_y) = \frac{1}{4} \left(\omega_0 + \frac{\zeta v_{th}^2 (2k_0 k_x - k_0^2)}{2\omega_0} \right)^2 - \frac{\zeta}{2} v_{th}^2 (k_x^2 + k_y^2), \quad (4.83)$$

where we dropped the index j , since the result is the same nevertheless which of the two EPWs is considered. Using the relation between plasma frequency and electron density (see Eq. 4.9), we find an expression for the density at which an EPW of a certain wave vector can be amplified. It holds

$$n_0(k_x, k_y) \approx \frac{\epsilon_0 m \omega_p^2(k_x, k_y)}{e^2} = \frac{\epsilon_0 m}{e^2} \left[\frac{1}{4} \left(\omega_0 + \frac{\zeta v_{th}^2 (2k_0 k_x - k_0^2)}{2\omega_0} \right)^2 - \frac{\zeta}{2} v_{th}^2 (k_x^2 + k_y^2) \right]. \quad (4.84)$$

Note that $n_0 \approx n_e$ was assumed, since $n_1 \ll n_0$. A plot of Eq. 4.84 for $\lambda_{vac} = 527 \text{ nm}$, $k_0 = \sqrt{0.75} \frac{2\pi}{\lambda_{vac}}$, $\zeta = 3$ and $T_e = 1 \text{ keV}$ can be found in Fig. 4.3. We can see that the density is axisymmetric around $k_x = 0.5k_0$ and $k_y = 0$. As a result of that, the density, where amplification occurs, is the same for two wave vectors fulfilling momentum conservation (see Eq. 4.57). This is consistent with the fact that we theoretically predicted TPD in homogeneous media. In fact, the density is rotationally symmetric around $k_x = 0.5k_0$. In Fig. 4.3, we can see that larger wave numbers (relative to $k_x = 0.5k_0$) correspond to smaller densities. This is due to the fact that the temperature terms in Eq. 4.81 increase with the wave numbers of the two EPWs. Since the photon frequency is constant, the plasma frequency and thus the density needs to decrease.

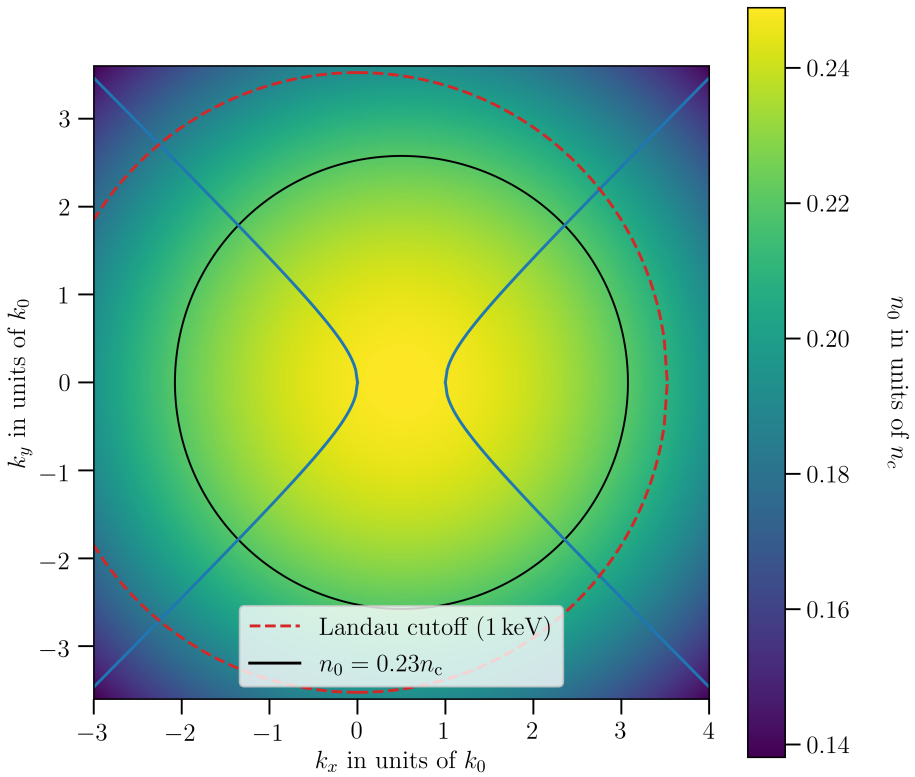


Figure 4.3.: TPD electron density in dependence of the EPW vector. The dashed red circle indicates the Landau cutoff at $T_e = 1 \text{ keV}$ and the black circle the constant density $n_0 = 0.23n_c$. The curves of maximum growth are shown in blue. For scaling the x - and y -axis, it was used $k_0 = \sqrt{0.75k_{\text{vac}}}$.

In particular, for a finite temperature all values of n_0 from Eq. 4.84 are below $0.25n_e$ and not even approaching this value asymptotically because the photon's momentum needs to be conserved (see Eq. 4.57). So, the densities where TPD occurs, are reduced compared to the case of neglecting the temperature terms.

In Fig. 4.3, there is also the Landau cutoff, from our calculation using the homogeneous growth rate, included (cf. section 4.5.2). If TPD can amplify EPWs at a certain density is mainly determined by whether the corresponding wave numbers are below or above the Landau cutoff. If the density is too small, Landau damping overcomes the TPD growth and thus Landau damping limits the density range where TPD can occur to a small region slightly below $n_0 = 0.25n_c$ (cf. section 4.2). In section 4.5.2, we have seen that the Landau cutoff limits wave vectors with $k_x > 0$ first. Similarly, the Landau cutoff limits the density range first due to the wave vectors with $k_x > 0$.

For deriving the density dependence (see Eq. 4.84), we did not assume a homogeneous medium. On the other hand, we derived the numerical value of the Landau cutoff $k\lambda_D \sim 0.27$ in the case of the growth rate in homogeneous media (cf. section 4.4). However, the strong dependence of γ_L on $k\lambda_D$ (see Eq. 4.30) justifies that we use this result as an approximation for inhomogeneous media, thus our previous considerations regarding the density are valid for both, homogeneous and inhomogeneous media. In the latter - and in particular in laser produced plasmas - Landau damping limits the volume of material where

TPD occurs. On the other hand, if the density scales from zero to solid density - as in laser produced plasmas - there is always a certain region susceptible to TPD.

Let us now investigate the behavior of TPD at different densities in more detail. At one density, only wave vectors on a circle around $k_x = k_0/2$ are allowed (see Fig. 4.3). The Landau cutoff determines whether these wave vector combinations and especially those with maximum growth rate (cf. section 4.4) are allowed. The latter are indicated in Fig. 4.3 and we can see that at a fixed density, there are only two combinations of a pair of EPWs, depending on the signs of k_x and k_y , that have maximum growth. In particular, the propagation direction of the EPWs with maximum growth changes with density. To give a better picture of this connection, we insert the condition for maximum growth $k_y = k_y^{\max}(k_x)$ given by Eq. 4.67 into Eq. 4.84 and get

$$n_0(k_x) \equiv n_0(k_x, k_y^{\max}(k_x)) = \frac{\epsilon_0 m}{e^2} \left[\frac{1}{4} \left(\omega_0 + \frac{\zeta v_{\text{th}}^2 (2k_0 k_x - k_0^2)}{2\omega_0} \right)^2 - \frac{\zeta}{2} v_{\text{th}}^2 (2k_x^2 - k_x k_0) \right], \quad (4.85)$$

which is plotted in Fig. 4.4a. We can see that for each density only two values of k_x allow for maximum growth rate - in accordance to our previous observation. We connect the 1D density plot (see Fig. 4.4a) with Fig. 4.4b, where the TPD growth rate in homogeneous media is shown. In Fig. 4.4b, the values of k_x at the intersection points of the Landau cutoff with the curves of maximum growth rate are marked by black dashed lines. These markings are also included in Fig. 4.4a for better orientation.

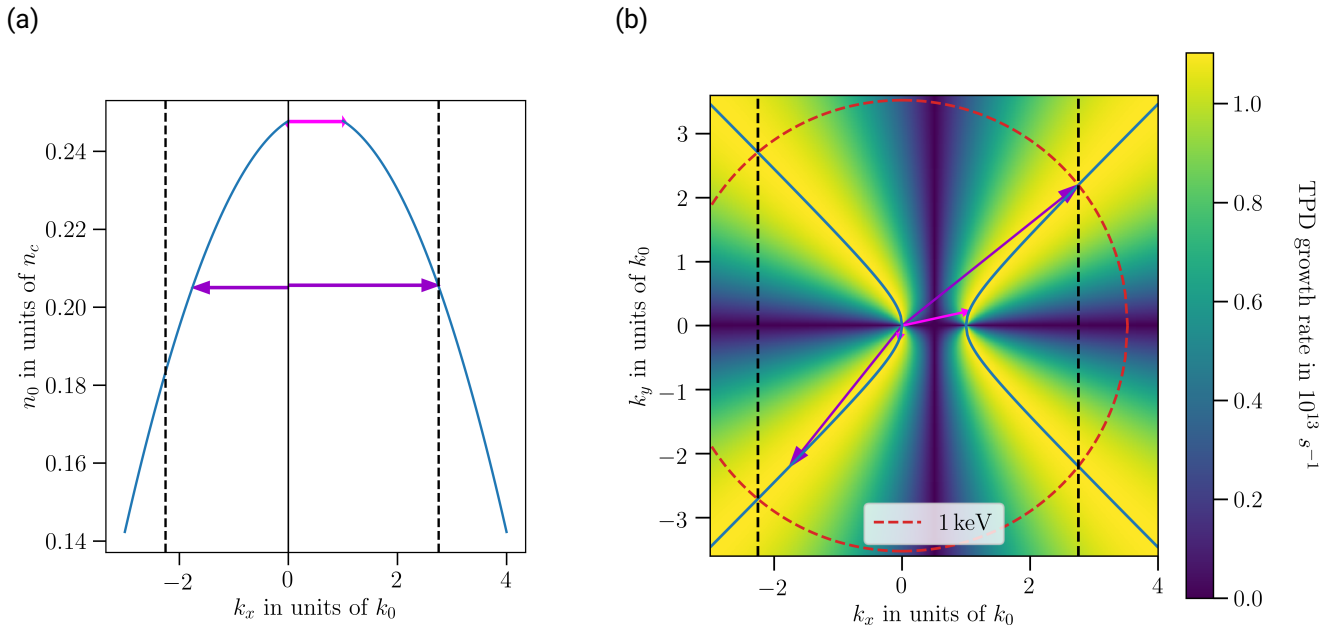


Figure 4.4.: Illustration of the connection between TPD density and growth rate. In (a), the density along the curves of maximum growth and in (b) the growth rate including the curves of maximum growth (blue) and the Landau cutoff are shown (red, dashed). The dashed black lines mark the intersection point of maximum growth and Landau cutoff. In (a) and (b), two combinations of EPW vectors are shown, each in pink or purple. For scaling the axes k_x and k_y , it was used $k_0 = \sqrt{0.75} k_{\text{vac}}$.

In both Figs. 4.4a and 4.4b, two combinations of EPWs (at maximum growth rate) are shown. First, a combination with small wave numbers, corresponding to a density relatively close to $n_0 = 0.25n_c$ (pink arrows). Second, a combination at Landau cutoff, corresponding to a density $n_0 \lesssim 0.22n_c$ (purple arrows). It becomes clear that close to the maximum of $n_0(k_x)$, i.e., at the possible values closest to $n_0 = 0.25n_c$, the EPWs propagate nearly in a right angle to each other (pink arrows). The wave vectors nearly point in the directions of $\vec{k}_0 \parallel \vec{e}_x$ and $\pm \vec{E}_0 \parallel \vec{e}_y$, respectively. On the other hand, at smallest possible densities, the EPWs propagate at nearly 180° to each other (purple arrows) and at angles of intersection of nearly 45° with \vec{k}_0 and \vec{E}_0 . This means that in inhomogeneous media many different pairs of EPWs are excited. Between different pairs of EPWs, the wave numbers and propagation directions change with density, even when only considering the most relevant constellations of maximum growth.

In our previous considerations, we have, however, neglected that a pair of EPWs excited at one density propagates from the starting point of the interaction to different densities. Taking this propagation into account, the wave vectors of a pair of EPWs also change during the propagation through the density gradient and effects besides the homogeneous growth rate need to be considered. More details about this convective instability behavior are presented in the following.

4.7. Convective Two-Plasmon Decay Instability

The reader should be reminded that the convective TPD instability typically dominates over the absolute instability during laser-plasma interactions. This is due to the fact that the first takes place over a much larger density range (cf. section 4.2), i.e., larger region of the plasma than the latter. Therefore, the absolute instability is not discussed further in this work but it is referred to the literature for more information [28, 29, 62, 63].

The quantitative results for the TPD gain from the convective instability are presented in section 4.7.1, based on different sources [27, 59, 60]. The density gradient is assumed to point in the same direction as the wave vector of the electromagnetic wave, this is in x -direction. Similar to our own calculation for homogeneous media (cf. section 4.3), nonlinear growth effects are neglected. Damping effects are discussed subsequent to the gain from the convective instability in section 4.7.2.

4.7.1. Convective Two-Plasmon Decay Gain

In the case of the convective instability, it is not sufficient to only consider a temporal growth rate because the electromagnetic and electron plasma waves propagate a significant distance through the density gradient during the amplification process. The resulting effects on the growth of the TPD instability are discussed in this section.

During the propagation of the waves through the density gradient, the wave numbers of all three waves change, since first $\omega_p^2 \propto n_e$ (see Eq. 4.9) and second $\omega_L = \sqrt{\omega_p^2 + \frac{3}{2}v_{th}^2k_L^2}$ (see Eq. 4.20 for an adiabatic index of $\zeta = 3$) and $\omega_0 = \sqrt{\omega_p^2 + c^2k_0^2}$ (see Eq. 4.8) stay constant. Due to the fact that the wave numbers do not change equally, a dephasing between the three waves occurs during the convective amplification. The dephasing can be quantified by [27, 59]

$$\kappa = k_0(x) - k_1(x) - k_2(x) - (k_0(0) - k_1(0) - k_2(0)), \quad (4.86)$$

where the indices 0 and 1, 2 denote the electromagnetic and EPWs, respectively. At the point $x = 0$, the waves are assumed to be in phase, i.e., $\kappa = 0$, and when propagating from this position, κ increases. Because of that, the time during which the EPWs can be effectively amplified, is limited. Not considering any damping effects, the total gain of the amplitude of an initial density perturbation δn was approximately calculated by Rosenbluth [27] as

$$G \sim e^{\frac{\pi \gamma^2}{|\kappa' v_1^g v_2^g|}}, \quad (4.87)$$

where for $j = 1, 2$

$$v_j^g = \partial \omega_j / \partial k_j = \frac{3v_{\text{th}}^2 k_j}{2\omega_j} \quad (4.88)$$

are the group velocities of the EPWs (see Eq. 4.23, here for an adiabatic index of $\zeta = 3$) and γ is the growth rate in a homogeneous medium (given by Eq. 4.61). The amplification takes place over a distance from $-x_t$ to x_t denoting the interaction region and the maximum amplitude is reached at x_t . During the propagation beyond x_t , the theory predicts an oscillation of the EPW amplitudes where energy is transferred back and forth between the EPWs and the electromagnetic wave. In this work, we only consider the amplification G until x_t .

The variations of γ and v_j^g due to the change of the EPW vectors with density, i.e., with x , were neglected during the calculation of Rosenbluth. In fact, the homogeneous growth rate γ is rather only the instantaneous growth rate at $x = 0$ given by the wave vectors at $x = 0$. Including the dependence of the growth rate on the changing wave vectors would, however, make the calculation much more complicated favoring simulations to target this problem. Therefore, it is not considered in this work. Another assumption of Rosenbluth to obtain Eq. 4.87 is that the dephasing of the electromagnetic and plasma waves is linear, i.e., $\kappa = \kappa' x$. Note that $v_j^g \propto k_j$ is the reason why the convective behavior of the TPD instability needs to be considered for larger wave numbers, i.e., smaller densities (cf. section 4.6) while the instability becomes absolute for lower wave numbers, i.e., densities closer to $n_e = n_c/4$ in the range $0.25 \gtrsim n_e/n_c > 0.243$ [33].

Let us now apply Eq. 4.87 to the case of a linear varying electron density

$$n_0(x) = N(1 + x/L), \quad (4.89)$$

where L corresponds to the density scale length $n_e/\vec{\nabla} n_e$ at $x = 0$. The linear profile is a Taylor expansion of the laser induced density profile, thus the density should be at (or slightly below) quarter critical density at $x = 0$ when considering TPD. We calculate the dephasing by the relation between wave numbers and density, given by the dispersion relations, for electromagnetic waves (see Eqs. 4.8 and 4.10) and EPWs (see Eq. 4.20). It holds

$$k_m(x) = \sqrt{\frac{\omega_m^2 - \omega_p^2}{C_m}} = \sqrt{\frac{\omega_m^2 - \omega_p^2(x=0)(1+x/L)}{C_m}}, \quad (4.90)$$

where $m = 0, 1, 2$ distinguishes electromagnetic and EPWs such that $C_0 = c^2$ and $C_{1,2} = \frac{3}{2}v_{\text{th}}^2$ (adiabatic index of $\zeta = 3$). Differentiating Eq. 4.90 yields

$$\frac{\partial k_m(x)}{\partial x} = 0.5 \left(\frac{\omega_m^2 - \omega_p^2(x=0)(1+x/L)}{C_m} \right)^{-0.5} \left(-\frac{\omega_p^2(x=0)}{LC_m} \right) = -\frac{\omega_p^2(x=0)}{2Lk_m(x)C_m} \quad (4.91)$$

and consequently

$$\kappa' = \frac{\partial \kappa}{\partial x} = \frac{\omega_p^2(x=0)}{L} \left(-\frac{1}{2k_0 c^2} + \frac{1}{3k_1 v_{th}^2} + \frac{1}{3k_2 v_{th}^2} \right), \quad (4.92)$$

where the space dependence of the wave numbers was neglected. This means that $\kappa = \kappa' x$ is a first order Taylor expansion in the case of a linear density profile. We simplify κ' further to

$$\kappa' \approx \frac{\omega_p^2(x=0)}{L} \left(\frac{1}{3k_1 v_{th}^2} + \frac{1}{3k_2 v_{th}^2} \right) = \frac{\omega_p^2(x=0)}{L} \left(\frac{k_1 + k_2}{3k_1 k_2 v_{th}^2} \right) = \frac{\omega_p^2(x=0)}{L} \left(\frac{k_0}{3k_1 k_2 v_{th}^2} \right), \quad (4.93)$$

where the term of the electromagnetic wave was neglected, since $c^2 \gg v_{th}^2$, and momentum conservation was used. The TPD convective gain can be calculated by inserting Eqs. 4.88 and 4.93 into Eq. 4.87 and it holds

$$G \sim \exp \left(\pi \gamma^2 \frac{L}{\omega_p^2(x=0) k_0} \cdot \frac{4\omega_1 \omega_2}{3v_{th}^2} \right). \quad (4.94)$$

Furthermore making the simplification $\omega_1 \approx \omega_2 \approx \omega_p(x=0)$, i.e., neglecting the temperature term in the EPW dispersion relations (see Eq. 4.20), the gain reads

$$G \sim \exp \left(\pi \gamma^2 \frac{4L}{3k_0 v_{th}^2} \right), \quad (4.95)$$

where the same assumption could be applied to γ which would then be given by Eq. 4.63. In section 4.5.1, we have calculated the maximum γ_{max} of Eq. 4.63 (see Eq. 4.68). Inserting γ_{max} and the thermal electron velocity (see Eq. 4.21) into Eq. 4.95 yields

$$G \sim \exp \left(\pi \frac{e^2 E_0^2 k_0}{4m\omega_0^2} \cdot \frac{L}{6k_B T_e} \right). \quad (4.96)$$

Most precisely, the electric field amplitude needs to be taken at the place where the amplification process occurs, i.e., roughly at quarter critical density. We neglect the decrease of the group velocity of the electromagnetic wave (cf. section 4.5.1) and relate the electric field with the intensity I by

$$E_0 = \sqrt{\frac{2I}{c\epsilon_0}}. \quad (4.97)$$

If the intensity is known at quarter critical density, then that value should be used for I . However, neglecting the absorption of laser light, it is also possible to use the vacuum intensity as approximation of I similar to section 4.5.1. Furthermore, we insert $k_0/\omega_0 = \frac{\sqrt{0.75}}{c}$ which follows for quarter critical density from Eq. 4.12, $\omega_0 = 2\pi c/\lambda_{vac}$ and get

$$G \sim \exp \left(\frac{\sqrt{0.75} e^2}{24m\epsilon_0 c^3} \cdot \frac{\lambda_{vac} I L}{k_B T_e} \right). \quad (4.98)$$

In practical units this is equivalent to

$$G \sim \exp \left(0.0266 \frac{I_{14} \lambda_\mu L_\mu}{T_{keV}} \right), \quad (4.99)$$

where I_{14} is the intensity in $1 \cdot 10^{14} \text{ W cm}^{-2}$, λ_μ and L_μ are the vacuum wave length and scale length in μm , respectively, and T_{keV} is the thermal electron temperature in keV. Note that T_e (T_{keV}) needs to be

taken at the quarter critical density which is the case for L (L_μ), too, due to linearizing the density profile. For $L \rightarrow \infty$, we get $G \rightarrow \infty$ which corresponds to having homogeneous growth for infinite time since no dephasing occurs. Our result in Eq. 4.99 reproduces the leading term of the formula given by Yan *et. al* [59]

$$G \sim \exp \left(0.0263 \frac{I_{14} \lambda_\mu L_\mu}{T_{\text{keV}}} \left[1 - 0.00881 T_{\text{keV}} - 0.0470 T_{\text{keV}} \left(\frac{k_y c}{\omega_0} \right)^2 \right] \right). \quad (4.100)$$

The calculation of κ' presented beforehand was carried out in a similar way as by Yan *et. al* [59] and Xiao *et. al* [60], but a major difference is that they defined the phase mismatch $\tilde{\kappa} = k_0(x) - k_{1x}(x) - k_{2x}(x)$ to be only dependent on the x -coordinates of the wave vectors. Note that it is $k_0(x) \equiv k_{0x}(x)$, by the definition that the electromagnetic wave propagates in x -direction, and that the constant term of our definition Eq. 4.86 vanishes due to momentum conservation (see Eq. 4.57) when considering only the x -coordinates. Furthermore, they considered only the x -component of the group velocity $\tilde{v}_j^g = \partial \omega_j / \partial k_{jx}$ which also alters the gain (see Eq. 4.87). In our opinion, the calculation of the TPD gain by Rosenbluth [27] is better reflected when considering the absolute values of the vectors from both, the x and y -component. The additional terms in Eq. 4.100 compared to our result (see Eq. 4.99) are expected to be, on the one hand, due to the fact that Yan *et al.* [59] did not neglect the term of the electromagnetic wave in $\tilde{\kappa}'$ (see Eqs. 4.92 and 4.93 for our approximation). On the other hand, they considered the maximum homogeneous growth rate for each k_y , but without the simplification $\omega_1 = \omega_2 = \omega_p(x=0)$.

Rosenbluth [27] calculated the threshold of the convective TPD instability due to the density gradient as

$$\frac{e^2}{12m\epsilon_0 c^3} \cdot \frac{\lambda_{\text{vac}} I L}{k_B T_e} \gg 1. \quad (4.101)$$

Below this threshold, the dephasing of the waves is too fast compared to the (homogeneous) growth rate to allow for substantial gain. Equation 4.101 follows directly from Eq. 4.98 when neglecting the change of the wave number compared to the vacuum, i.e., neglecting the factor $\sqrt{0.75}$, and applying the condition $G \gg e^{0.5}$. Note that Rosenbluth set the exponent of the right-hand side to 0.5 and not 1 because he considered the Gain of the wave intensity (and not amplitude) to be $G^2 \gg e$. In practical units, the threshold can be stated as

$$\frac{I_{14} \lambda_\mu L_\mu}{T_{\text{keV}}} \gg 16.3. \quad (4.102)$$

For $I = 10 \cdot 10^{14} \text{ W cm}^{-2}$, $T_e = 1 \text{ keV}$, $\lambda_{\text{vac}} = 0.527 \mu\text{m}$ and assuming a scale length of $L = 100 \mu\text{m}$, it holds $\frac{I_{14} \lambda_\mu L_\mu}{T_{\text{keV}}} = 527$ which clearly fulfills the threshold condition. For these parameters, the theory predicts a gain of $G \sim \exp(0.0266 \cdot 527) = \exp(14) \approx 1 \cdot 10^6$ when using Eq. 4.99 such that nonlinear growth effects and saturation are expected to limit the experimentally observed gain of the convective instability. Note that the time corresponding to the theoretically predicted gain is of the order $t \sim \ln(G)/\gamma_{\text{max}} = 14/(1.1 \cdot 10^{13} \text{ s}^{-1}) = 1.3 \text{ ps}$ when assuming the growth rate during the convective amplification to be similar to the maximum of the homogeneous case despite dephasing. This assumption implies that $t \sim 1.3 \text{ ps}$ is rather a lower limit, but for ns-laser pulses as used within the framework of this work, we still expect the growth time of TPD to be much smaller than the laser pulse duration.

4.7.2. Influence of Damping Effects

In addition to nonlinear growth effects and saturation, the damping of EPWs limits the gain compared to the theory described above. The implications of the damping on the convective TPD instability are described in this section.

First, it is important to note that the gain G is not directly comparable to the collisional (see Eq. 4.27) and Landau (see Eq. 4.30) damping rates, since G corresponds to the gain over a certain distance. To make a comparison, the basic gain length $L_0 = \sqrt{|v_1^g v_2^g|/\gamma}$ is compared to the absorption length $L_a = (\nu_1/|v_1^g| + \nu_2/|v_2^g|)^{-1}$ by the TPD damping coefficient

$$\beta = L_0/L_a = \left(\nu_1 \sqrt{\left| \frac{v_2^g}{v_1^g} \right|} + \nu_2 \sqrt{\left| \frac{v_1^g}{v_2^g} \right|} \right) / \gamma, \quad (4.103)$$

where $\nu_j = -\gamma_{Cj} - \gamma_{Lj} > 0$ are the damping rates of a pair of EPWs ($j = 1, 2$) due to the sum of both, collisional and Landau damping. The basic gain length approximates how far the EPWs propagate during the amplification of their amplitudes by a factor of e . Similarly, the absorption length corresponds to a reduction of the amplitudes by a factor of e . The group velocities and growth/damping rates are approximated to be constant over the respective length. Let us quantitatively estimate the basic gain length L_0 in order to understand on which scales the convective amplification of EPWs by TPD takes place. Using $\omega_j \approx \omega_0/2$, $k_j \sim 2k_0$ (cf. section 4.5.2) and $k_0 \approx \sqrt{0.75}k_{\text{vac}}$, the group velocity (see Eq. 4.88) becomes $v_j^g \sim 6v_{\text{th}}^2 k_0 / \omega_0 \approx 6\sqrt{0.75}v_{\text{th}}^2/c$. For $T_e = 1 \text{ keV}$, this equals $v_j^g \sim 0.020c$. Additionally using the maximum homogeneous growth rate $\gamma_{\max} = 1.1 \cdot 10^{13} \text{ s}^{-1}$ obtained for $I = 1 \cdot 10^{15} \text{ W cm}^{-2}$ and $\lambda_{\text{vac}} = 527 \text{ nm}$ (cf. section 4.5.1), it follows $L_0 = 0.55 \mu\text{m}$. For n times e -folding, the corresponding gain length increases to $n \cdot L_0$ when still neglecting damping and dephasing. Still, the few micrometer range seems to be an appropriate estimation and is small enough to allow TPD to take place in laser focus spots of tens of micrometers. The scale length of the plasma also needs to be in the range of tens of micrometers, since the density values where EPWs can be amplified by TPD only span a range varying by 20 %. This variation occurs already over a distance of 20 % of the scale length.

Let us now continue our discussion of the damping effects. The threshold due to damping is given by $\beta = 2$ [60] and amplification of EPWs by TPD only occurs for $\beta < 2$. In a descriptive way a smaller damping coefficient means that while propagating the absorption length, the basic gain length is covered more often, thus the net gain is larger. Note that the damping threshold is an additional condition to the threshold caused by the density gradient (see Eq. 4.102). Here, we consider again the absolute value of the group velocity from both components, x and y , while Xiao *et al.* [60] only considered the x -component in their definitions $\tilde{L}_0 = \sqrt{|\tilde{v}_1^g \tilde{v}_2^g|/\gamma}$ and $\tilde{L}_a = (\nu_1/|\tilde{v}_1^g| + \nu_2/|\tilde{v}_2^g|)^{-1}$.

In Fig. 4.5, the damping coefficient of our definition (see Eq. 4.103) is plotted using the assumption $\omega_1 \approx \omega_2$ for calculating v_j^g and γ in β (γ is then given by Eq. 4.63). Furthermore, $I = 1 \cdot 10^{15} \text{ W cm}^{-2}$ and $\lambda_{\text{vac}} = 527 \text{ nm}$ are used to calculate γ analogously to section 4.5.1. A thermal electron temperature of $T_e = 1 \text{ keV}$ is assumed for calculating the Landau and collisional damping (cf. section 4.5.2). For the latter, we exemplarily investigate fully ionized carbon. Here, the dependence of γ_C (see Eq. 4.70) and γ_L (see Eq. 4.30) on the density and thus on (k_x, k_y) is considered (only the approximation $\omega_j = \omega_p$ for Eq. 4.70 is still applied). For simplicity, only damping coefficients $\beta < 2$ are shown in Fig. 4.5, where EPWs can be amplified by TPD. The damping coefficient is axisymmetric around $k_x = 0.5k_0$ and $k_y = 0$ which means that if $\beta < 2$ for one EPW vector, the other wave vector fulfilling momentum conservation (see Eq. 4.57) has $\beta < 2$, as well. Comparing with the homogeneous growth rate (see, e.g., Fig. 4.1), we find that damping overcomes the growth in the regions of small growth rate. This is due to collisional damping whose dependence on the wave vector can be and was neglected (cf. section 4.5.2), thus it displays a constant threshold to the necessary homogeneous growth rate. Landau damping, on the other hand, limits the maximum possible k -vectors rather independent of the exact value of the growth rate (cf. section 4.5.2). In an inhomogeneous medium, this corresponds to limiting the electron densities, i.e., the volume, where

TPD occurs. For comparing the effect of Landau damping to the homogeneous case, the Landau cutoff as discussed in section 4.5.2 is included in Fig. 4.5, as well. Taking into account that the wave vector with $k_x > 0$ is limited first by Landau damping, the behavior of the damping coefficient β is similar to the homogeneous Landau cutoff.

Altogether, we conclude that the EPW vectors which are allowed when considering damping effects in inhomogeneous media are similar to homogeneous media. In particular, for the typical laser and plasma parameters we investigated, numerous different pairs of wave vectors are excited by TPD in an inhomogeneous medium.

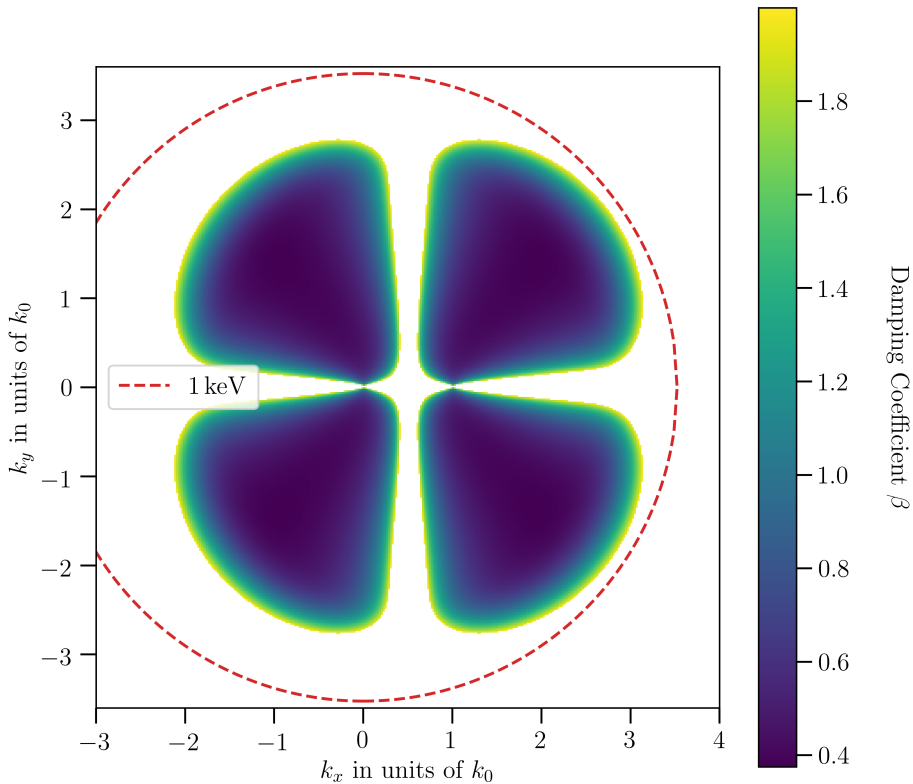


Figure 4.5.: TPD damping coefficient β of the convective instability. For simplicity, only values $\beta < 2$, and for comparison the homogeneous Landau cutoff are shown. For scaling the x - and y -axis, it was used $k_0 = \sqrt{0.75}k_{\text{vac}}$.

4.8. Electron Acceleration to Superthermal Energies and Propagation of Electron Plasma Waves

The following section presents in a descriptive way how electrons can be accelerated to superthermal energies by EPWs from TPD. To understand the mechanism, we need to take the behavior of EPWs during their propagation through the density gradient in an inhomogeneous medium into account.

Each EPW exerts a force on electrons by its electric field. At a fixed position, this field oscillates which prevents an effective net-acceleration. In contrast, if an electron moves roughly with the phase velocity v_L^{ph}

of an EPW, the electron moves at the same speed as the wave crest and thus is subject to the same electric field over a longer period of time. This is a collisionless acceleration mechanism until the electron speed has become too large compared to the phase velocity. A specialty about TPD in inhomogeneous media is that it offers the potential that the phase velocity of some EPWs increases during the acceleration process, therefore enabling to reach much higher energies than for a constant phase velocity [57].

Let us investigate this behavior in detail focusing on the EPWs with maximum growth rate. For such a pair, one EPW has $k_x > 0$ while the other has $k_x < 0$ (cf. section 4.5.1). Considering the linear density profile of Eq. 4.89, $k_x > 0$ and $k_x < 0$ correspond to propagating to higher and lower densities, respectively. At increased density, i.e., increased x , the wave number of the EPW with $k_x > 0$ has decreased, since first $\omega_p^2 \propto n_e$ (see Eq. 4.9) and second $\omega_L = \sqrt{\omega_p^2 + \frac{3}{2}v_{th}^2 k_L^2}$ (see Eq. 4.20 for an adiabatic index of $\zeta = 3$) stays constant. The change of the wave number has also been described in section 4.7.1 by Eq. 4.91.

The smaller wave numbers at higher densities correspond to higher phase velocities. Therefore, an electron being initially accelerated by an EPW with $k_x > 0$ can be accelerated to continuously higher velocities when propagating (together with the wave) to higher densities. Simultaneously, the group velocity of the EPW decreases (see Eq. 4.88) and the electron density where the wave will turn is dependent on the EPW frequency [57]. Note that one prerequisite of the presented acceleration mechanism is the presence of a density gradient. Furthermore, the increase of electron speed needs to match the increase of phase velocity. Generally, the electrons cannot keep track with a wave crest when the phase velocity increases too fast or the electric field of the EPW, i.e., the accelerating force, is too weak. For a more detailed analysis, a quantitative treatment of the acceleration process would be necessary, most probably using simulations as in [34, 57, 58], but this goes beyond the frame of this master thesis. In contrast to the electrons being accelerated up the density gradient, the acceleration in EPWs with $k_x < 0$ corresponds to a continuous decrease of the phase velocity, thus not enabling the advanced acceleration scheme. These EPWs propagate until reaching the Landau cutoff and being Landau damped.

Besides the described behavior of an electron in a single EPW, the electron encounters other EPWs while being accelerated. The tendency of their wave number dependence on density is the same which we investigated in section 4.6 where no convection was considered and density and wave number were simply related for the resonant case. Therefore, the basic idea of the acceleration mechanism is also applicable to a combination of different EPWs. The excitation of different EPWs, their interplay and propagation is best investigated using simulations. In particle-in-cell (PIC) simulations, the effect of TPD is naturally taken into account [34]. They require considerable computation power which is the reason that also dedicated TPD simulation tools are used [57, 58]. Simulations implied that the fast electron temperature scales with IL/T_e , where T_e is the thermal electron temperature [57]. Experimentally, an increase of the temperature with intensity and therefore also with IL/T_e was observed [32, 35].

Here, we just make a simple estimation to get an idea of the relevant phase velocities. We exemplarily calculate the highest and lowest phase velocities of EPWs with maximum growth and $k_x > 0$ for their resonant excitation, i.e., without considering their propagation. The smallest phase velocity (largest wave number) corresponds to smallest density which can be approximated by the Landau cutoff (cf. section 4.5.2). For $T_e = 1$ keV, it follows $n_{cutoff} = 0.205n_c$, $k_{cutoff} = 3.5k_0$ and $v_{L,cutoff}^{ph} \approx \omega_0/7k_0 = c/7$. On the other hand, the highest phase velocity just corresponds to the limit $k \rightarrow k_0^+$ (limit from above) which yields $v_{L,max}^{ph} \approx \omega_0/2k_0 = c/2$. The density then corresponds to $n_{max} = 0.248n_c$ and thus already the region of

absolute instability. Using the relativistic formula

$$E_{\text{kin}} = mc^2 \left(\frac{1}{\sqrt{1 - (\frac{v}{c})^2}} - 1 \right), \quad (4.104)$$

where E_{kin} , m and v are the kinetic energy, rest mass and velocity of an electron, respectively, we calculate which energies electrons have at the minimum and maximum phase velocity.

It follows $E_{\text{min}} = 5.3 \text{ keV}$ and $E_{\text{max}} = 79 \text{ keV}$. Around E_{min} , there are many thermal electrons in the Maxwellian temperature distribution - even at $T_e = 1 \text{ keV}$ - which can be principally accelerated to higher energies, namely E_{max} in our simple estimation. At E_{max} , the contribution of thermal electrons is negligibly small, therefore, the increase of electron energies is significant. Note that also electrons with higher initial energies than E_{min} can be accelerated starting the process at larger densities than n_{cutoff} . Furthermore note that due to rethermalization, there are always electrons available to being accelerated. It is worth to point out that our estimation $E_{\text{max}} = 79 \text{ keV}$ fits well with the experimentally observed fast electron temperatures of up to 90 keV [32, 35] even though we did not consider convection. However, our simple estimation does not indicate a dependence of the maximum energy on IL/T_e . Furthermore, if convection is considered, arbitrary low wave numbers can be reached, thus the minimum value of the wave numbers would not denote a limit to the maximum energy anymore. It is then rather the fact that the wave numbers decrease too fast for the electrons to keep track with a wave crest that limits the maximum energies [57].

It is worth to mention that collisional damping dissipates energy from EPWs which is then not available for the described acceleration mechanism, anymore. In order to maximize the fast electron output, collisional damping should be minimized. The work of Turnbull *et al.* [37] indicates that collisional damping is actually the dominant process concerning the dissipation of energy of EPWs excited by TPD, thus this optimization is of great importance.

5. Experimental Setup and Design

In this chapter, I will give the reader an overview of our experimental setup and design. I start in section 5.1 by introducing the individual components. The following section 5.2 gives more detailed and theoretically founded information about how we experimentally optimized TPD. This concerns the coated target design and the laser setting. In section 5.3, I present the diagnostics we used more comprehensively.

5.1. Overview of Experimental Setup

For our experiment, we used the experimental station Z6 at GSI. Figure 5.1 shows a schematic of the experimental arrangement in- and outside the target chamber. Here the PHELIX ns-laser pulse is shown entering the target chamber from the left-hand side. Not included in Fig. 5.1 is the frequency doubling of the laser pulse to $\lambda_{\text{vac}} = 527 \text{ nm}$ and the focusing by a lens which are both implemented within the PHELIX beamline to Z6.

For our experiment, we used 1.5 ns long PHELIX pulses. Most of the time during the experiment, we used the PHELIX beam in best focus with a focal spot size of $d_{\text{FWHM}} = (25 \pm 5) \mu\text{m}$ reaching intensities of $I = (5.9 \pm 2.6) \cdot 10^{15} \text{ W cm}^{-2}$ (at the maximum nominal laser energy of 200 J). Additionally, we performed shots using a phase plate [68] that produces a spot size of $d = 500 \mu\text{m}$ corresponding to intensities of $I = (1.07 \pm 0.02) \cdot 10^{14} \text{ W cm}^{-2}$ for highest laser energies. Details of our intensity calculation are given in appendix A.

For each laser shot, we positioned a target (number 1 in Fig. 5.1) at the center of the target chamber to produce a plasma by laser-matter interaction. From the plasma, photons were emitted in a large spectral range from the optical to the hard X-ray regime. We detected this radiation with four different diagnostics to collect information about the plasma, especially its X-ray emission and the TPD.

To track TPD, we used a combination of a *Hamamatsu Universal streak camera C10910-01* (number 12 in Fig. 5.1, see [69] for data sheet) with a spectrometer (number 11 in Fig. 5.1). This combination was used to measure UV-radiation around $3/2 \omega_0$, where $\omega_0 = 2\pi c/\lambda_{\text{vac}}$, as TPD signature (cf. section 4.2).

Furthermore, we used a hard X-ray detector (numbers 6 & 7 in Fig. 5.1), a highly oriented pyrolytic graphite spectrometer (numbers 4 & 5 in Fig. 5.1) and a pinhole camera (numbers 2 & 3 in Fig. 5.1). These diagnostics were used for X-ray detection which we implemented using *Cytiva BAS IP SR 2040 E* imaging plates (see [70] for data sheet). The hard X-ray detector (HXRD) allowed us to measure the total yield of hard X-rays (several tens of keV) and the highly oriented pyrolytic graphite (HOPG) spectrometer was used to spectrally resolve X-ray line emission. Both, HXRD and HOPG spectrometer, also allowed us to track fast electrons indirectly, since fast electrons cause bremsstrahlung, recombination and line emission. We used the pinhole camera to measure the X-ray source size which influences the source brightness. In the

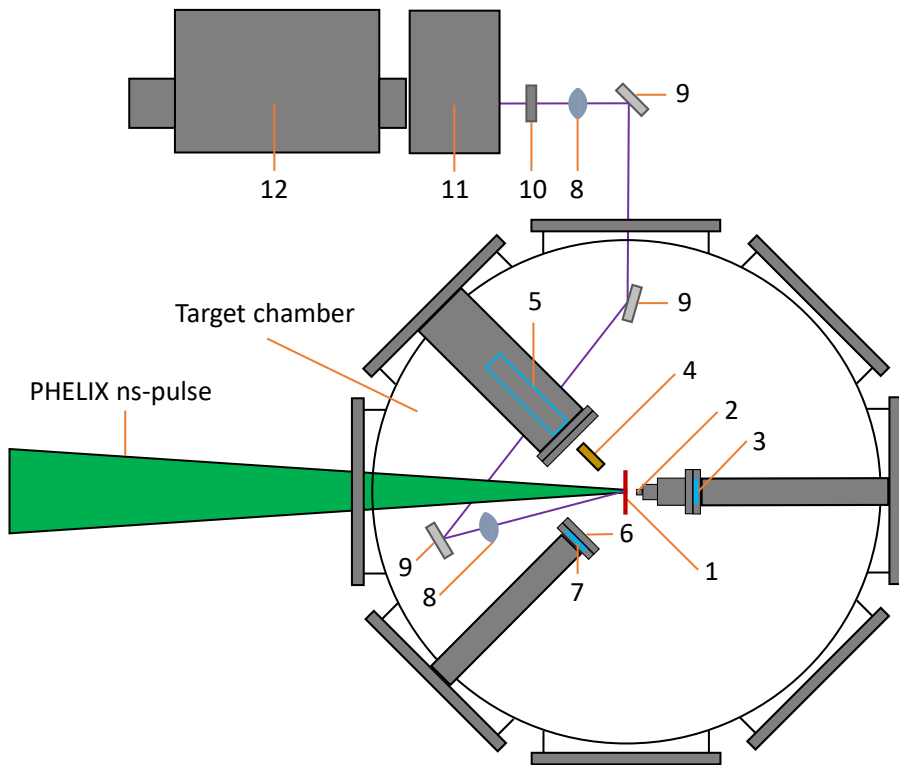


Figure 5.1.: Schematic of the setup of our experiment (not to scale). 1: Target; 2: Pinhole; 3: Pinhole camera imaging plate position; 4: Highly oriented pyrolytic graphite (HOPG) crystal; 5: HOPG spectrometer imaging plate position; 6: Hard X-ray detector (HXRD) filter array; 7: HXRD imaging plate position; 8: Lenses; 9: Mirrors; 10: Filter; 11: Spectrometer; 12: Streak camera. Each imaging plate is positioned in a re-entrant tube. The $3/2 \omega_0$ beam path from target to spectrometer is indicated in purple. Note that the laser beam comes in at an angle of 9° to the drawing plane.

frame of this master thesis, the pinhole camera data was not analyzed and the diagnostics will therefore not be considered in this work.

In order to place the imaging plates without venting the target chamber between different shots, we used re-entrant tubes each with a 0.5 mm thick polymethyl methacrylate (PMMA) window. The imaging plates of all X-ray diagnostics were placed in the re-entrant tubes before each shot. 10 min after each shot, they were scanned with a *Cytiva Amersham Typhoon IP Biomolecular Imager* (see [71] for data sheet) and with a pixel size of $50 \mu\text{m}$. The spatially resolved signal obtained from the scanning process is called photostimulated luminescence. Over a large dynamic range, it is proportional to the energy that had been deposited in the imaging plates.

5.2. Experimental Optimization of Two-Plasmon Decay Conditions

In order to experimentally optimize TPD, we divided the production of line emission into two subprocesses using a coated target design (cf. section 3.3). First, the conditions for generating fast electrons by TPD are

optimized in the coating and second the substrate is chosen suitable for the production of high-energetic K_{α} photons. In this section, I motivate our choices of plastic as coating and Mo or Ag as substrate material and present the different target types tested in the scope of our experiment. I will estimate that using coated Mo or Ag targets has the potential of considerably increasing diagnostic capabilities of X-ray diffraction. At the end of this section, I will furthermore discuss the laser setting in order to enhance TPD.

The coating material plastic - more specifically we used polypropylene (C_3H_6) - has the key attribute of consisting of atoms with low nuclear charges Z and thus low ion charge numbers Z_i . First, this results in a faster ion sound speed and thus larger scale length which is important for both increasing the convective TPD gain (cf. section 4.7.1) and increasing the volume where TPD is possible and thus the total amount of EPWs excited by TPD. Second, low ion charge numbers result in little collisional damping (see Eq. 4.70). This is important, since less collisional damping means faster growth of the EPWs and since collisional damping dissipates energy of EPWs which is not available for accelerating electrons to superthermal energies, anymore (cf. section 4.8).

Let us exemplarily compare the expected scale lengths between C_3H_6 and Mo. Assuming an isothermal expansion, charge neutrality and a single ionic species, the electron density can be estimated by a simple model presented by Samir *et al.* [72] which yields

$$n_e = Z_i n_i \exp[-(\xi + 1)], \quad (5.1)$$

where n_i is the ion density and $\xi = x/c_s t$ relates space and time. The ion sound speed c_s reads [31, 56]

$$c_s \approx \sqrt{\frac{\zeta Z_i k_B T_e}{M}}, \quad (5.2)$$

where M is the ion mass and ζ the electron adiabatic index. We estimate the ion sound speeds in C_3H_6 and Mo at $T_e = 1 \text{ keV}$ and assuming $\zeta = 1$ (in correspondence to the isothermal expansion in the Samir model). Concerning C_3H_6 , carbon and hydrogen are each fully ionized at that thermal electron temperature and we simply consider the mean ion charge and mass of the two elements weighted by their abundances to use the Samir expansion model [72]. It follows $Z_i^{C_3H_6} = 2.67$, $M^{C_3H_6} \approx 4.67 \text{ u}$ and thus

$$c_s^{C_3H_6} = 235 \mu\text{m ns}^{-1}. \quad (5.3)$$

In the case of Mo, we use FLYCHK [73] simulations to determine the mean ion charge $Z_i^{\text{Mo}} \approx 30$ at the quarter critical density $n_e = n_c/4 = 1 \cdot 10^{21} \text{ cm}^{-3}$ of the $\lambda_{\text{vac}} = 527 \text{ nm}$ PHELIX pulse. The ion mass of Mo is $M^{\text{Mo}} \approx 96 \text{ u}$ and therefore one gets

$$c_s^{\text{Mo}} = \sqrt{\frac{Z_i^{\text{Mo}} M^{C_3H_6}}{M^{\text{Mo}} Z_i^{C_3H_6}}} \cdot c_s^{C_3H_6} = 0.74 \cdot c_s^{C_3H_6}. \quad (5.4)$$

The Samir model [72] enables to relate the scale length

$$L = n_e / \vec{\nabla} n_e \quad (5.5)$$

to the ion sound speed. Inserting Eq. 5.1 from the Samir model into Eq. 5.5 yields

$$L = c_s t. \quad (5.6)$$

This is valid for all x due to the exponential density profile in Eq. 5.1. The ratio between the scale lengths of C_3H_6 and Mo is only dependent on the ratio of their ion sound speeds. Using Eq. 5.4, it holds

$$\frac{L^{\text{Mo}}}{L^{C_3H_6}} = 0.74 \quad \Leftrightarrow \quad L^{C_3H_6} = 1.35 L^{\text{Mo}}. \quad (5.7)$$

We note that the increase of the scale length of C_3H_6 compared to Mo is due to the increase of the ratio Z_i/M since first plastic is fully ionized and second the elements hydrogen and carbon have higher proton to neutron ratios than Mo. Even though the increase seems relatively small, it may be relevant because the scale length is in the exponent of the convective TPD gain (see Eq. 4.99). At an exemplary amplification of $G \sim \exp 5 = 150$ with Mo, this would mean an increase by the factor 5.7 for C_3H_6 to $G \sim \exp 5 \cdot 1.35 = 850$. This is, however, mainly relevant when the convective TPD instability is not driven to saturation. Furthermore, there is the advantage of an increased region susceptible to TPD and thus more EPWs. If the EPWs have the same amplitudes as with a smaller scale length, this generally allows for more fast electrons. From another point of view, more EPWs could also mean that for the same total energy in EPWs, their amplitudes are lower which would indicate that only a smaller gain is necessary and that less nonlinear and saturation effects occur.

Concerning collisional damping, we compare the damping rates between C_3H_6 and Mo (see Eq. 4.70) at $T_e = 1\text{ keV}$ and $n_e = 1 \cdot 10^{21} \text{ cm}^{-3}$. It follows that the damping rate $\gamma_C^{\text{Mo}} = -8.6 \cdot 10^{12} \text{ s}^{-1}$ is nearly one order of magnitude larger than $\gamma_C^{C_3H_6} = -1.06 \cdot 10^{12} \text{ s}^{-1}$. It is important to note that γ_C^{Mo} is comparable to the maximum TPD growth rate $\gamma_{\max} = 1.1 \cdot 10^{13} \text{ s}^{-1}$ at $I = 1 \cdot 10^{15} \text{ W cm}^{-2}$ (cf. section 4.2). Therefore, at the considered laser and plasma conditions, collisional damping would significantly decrease the growth of EPWs by TPD in Mo compared to C_3H_6 . Note that we have not even taken the absorption of laser light until quarter critical density into account which would reduce the intensity reaching quarter critical density and thus the TPD growth rate (cf. section 4.5.1). The influence of collisional damping depending on the ion charge state has also been noted by Myatt *et al.* based on simulations where they compared $Z_i = 14$ against $Z_i = 5.3$ [58], even a smaller difference than in our case. Additionally to hindering the growth of EPWs, collisional damping dissipates energy of grown EPWs which is then not available for producing fast electrons, anymore [37]. Note that the first effect of hindering the growth of EPWs goes beyond loosing energy that is already in an EPW because EPWs are amplified exponentially by TPD, i.e., proportional to their amplitude (see Eqs. 4.58a and 4.58b). The previous considerations confirm that uncoated high-Z targets are not ideal in order to maximize TPD and the resulting fast electron production. However, we should not forget that the ratio between maximum growth and collisional damping rate is strongly dependent on the laser and plasma parameters. Using the maximum intensities $I = (5.9 \pm 2.6) \cdot 10^{15} \text{ W cm}^{-2}$ (neglecting absorption) during our experiment (cf. section A), the maximum growth rate increases to $\gamma_{\max}^{2\text{keV}} = 2.7 \cdot 10^{13} \text{ s}^{-1}$. On the other hand, at potentially higher thermal electron temperatures of $T_e = 2\text{ keV}$, the collisional damping in Mo decreases to $\gamma_C^{\text{Mo}, 2\text{keV}} = -3.8 \cdot 10^{12} \text{ s}^{-1}$ ($Z_i = 32$) which is then a few times smaller than $\gamma_{\max}^{2\text{keV}}$.

In the following, we confirm the choices of Mo and Ag as substrates of our coated targets. First, these elements have K_α photon energies 2 and 2.6 times the Cu He_α photon energy, respectively. The production of line emission around the He_α photon energy, by highly charged Cu ions in uncoated targets, denotes the baseline situation in terms of high photon energies as it has been demonstrated in a previous work at PHELIX [44] (cf. section 3.2). Second, typical temperatures of fast electrons from TPD are reported to reach from 20 keV up to 90 keV [32, 35]. Assuming comparable temperatures for our experiment, there are many fast electrons in the energy distribution that can cause K-shell ionization in Mo and Ag, even at a temperature of 20 keV. One could argue that at 90 keV even K-shells of materials with higher nuclear charge could possibly be ionized. However, if the electron energy is not far above the K-shell ionization energy, the K-shell ionization cross section by electron impact increases with electron energy. The exact electron energy up to which this behavior can be observed, depends on the specific material. As rule of thumb, a local maximum in ionization cross section occurs at roughly 2 to 3 times the K-shell ionization energy (see [74] for data and analysis of K-shell cross section in several materials). For Mo and Ag, this corresponds to an electron energy of 40 – 60 keV and 51 – 77 keV, respectively, which is well comparable with typical TPD fast electron temperatures. Depending on fast electron temperatures achievable with the

PHELIX ns-pulse, we might consider using substrates with different nuclear charges than $Z = 42, 47$ (Mo, Ag) in future experiments. In particular, an option is to forego optimal K-shell ionization cross section and K_α conversion efficiency in order to further increase the nuclear charge of the laser target and thus the photon energy from line emission. It should be noted that line emission is also produced in the coating at areas where it is not fully ionized but this is not considered because of the low photon energy.

TPD experiments with coated targets have already been implemented by other groups with ns-laser pulses [32, 35–37], also combined with shorter pulses (~ 100 ps) [25], at different laser facilities, e.g., Omega and NIF. They report conversion efficiencies from laser energy into fast electrons up to over 1%. The conversion from fast electrons to K_α emission generally depends on target properties such as the metallic material. The group around Yaakobi *et al.* [32] has measured a conversion efficiency from laser energy to K_α emission of $\gtrsim 10^{-5}$ for coated Mo targets during an experiment at the Omega laser facility. Similar targets were also used within our experiment. If we could reach a similar conversion efficiency with those targets, this would be comparable to the efficiency $\eta \sim 4 \cdot 10^{-5}$ of the baseline situation (line emission from highly charged Cu ions in uncoated targets [44], cf. section 3.2), but with roughly twice the photon energy.

An overview over all target types tested during our experiment is given in Table 5.1. For each metal material, we compared coated and uncoated targets to investigate the effects of the coating on TPD and line emission. Additionally to Mo and Ag, we chose Cu as a metal material, since using the line emission from highly charged Cu ions in uncoated targets represents the baseline situation [44] (cf. section 3.2) for X-ray diffraction. The reason that we used uncoated Cu targets of two different thicknesses is that there were not enough targets of a single thickness available. Nevertheless, the difference is rather small so that we expect the results of these two targets to differ only slightly. For Cu, we additionally performed shots on targets with two different coating thicknesses to investigate its influence on line emission.

The coating thickness has two counteracting effects on K_α production via TPD. On the one hand, a thicker coating decreases the amount of fast electrons reaching the metallic layer to produce K_α emission. On the other hand, a coating that is too thin has the disadvantage that the shock wave driven by laser-matter interaction and propagating through the target could reach the metallic layer before the end of the laser pulse. This would, in turn, reduce K_α production capabilities, since metallic material is blown-off. We decided to test the two coating thicknesses 10 μm and 25 μm , since typical shock wave velocities are of the order 10 km s^{-1} and the PHELIX pulse we used had a duration of 1.5 ns. We confirmed such shock wave velocities by 1D HELIOS [75, 76] simulations in advance of our experiment. Additionally, our simulations confirmed our coatings to be thick enough to prevent the laser from burning through. Concerning the transmission of electrons through the coating, Monte-Carlo FLUKA [77, 78] simulations indicated that electrons with energies of tens of keV can penetrate the coating layer. All in all, the coating thicknesses we have chosen are similar to the 30 μm used by Yaakobi *et al.* [32].

The following estimation demonstrates the relevance of an increase of photon energies for diagnostic capabilities even by a factor of only 2 (Mo) or 2.6 (Ag). Let us assume that the ion-heated target consists

Table 5.1.: Different targets investigated during our experiment.

Target type	1	2	3	4	5	6	7	8
Metal type	Cu	Cu	Mo	Ag	Cu	Cu	Mo	Ag
Metal thickness in μm	12.7	12.7	10.07	10.05	10	12.7	10.07	10.05
Coating thickness in μm	25	10	25	25	-	-	-	-

of iron and should be diagnosed at solid density. Furthermore, we assume the attenuation to be the same as for cold iron. This is justified, since ion heating to temperatures of $\sim 0.1 - 10$ eV will almost only ionize electrons from outer shells. The binding energies of which are, however, small compared to X-ray photon energies, thus their ionization does not alter the attenuation. From photon energies of Cu He $_{\alpha}$ over Mo K $_{\alpha}$ to Ag K $_{\alpha}$, the attenuation length of cold iron (corresponding to a transmission of 1/e) increases from 4.7 μm over 35 μm to 68 μm [48]. The attenuation length constitutes the typical distance that can be penetrated by the X-rays. This roughly constrains the target size to the attenuation length in the direction X-rays penetrate the target for X-ray diffraction diagnostics which constitutes a strong restriction in possible ion target designs. The transmission of Cu He $_{\alpha}$ photons through 35 μm iron is only $e^{-35/4.7} \approx 5.8 \cdot 10^{-4}$ and through 68 μm even only $e^{-68/4.7} \approx 5.2 \cdot 10^{-7}$, which stresses that Cu He $_{\alpha}$ photons are not suitable for X-ray diffraction in targets of that thickness.

Concerning the TPD convective gain (see Eq. 4.99), the interplay between the laser and plasma parameters I , L and T_e is important. On the one hand, the smaller the laser spot the higher the intensity, but on the other hand there exists a limit to the scale length which decreases for smaller laser spots due to 2D plasma expansion effects [32, 35]. It should be noted that this behavior cannot be investigated by the 1D Samir model [72]. Furthermore, the intensity influences the thermal electron temperature T_e whose analytical dependence is $T_e \propto I^{2/3}$ (see Eq. 3.2). The exact experimental dependence of T_e on I is more complicated and scales more weakly in most cases [49]. At the same intensity, a larger laser spot generally results in higher thermal electron temperatures. During our experiment, we used PHELIX in best focus and also with a phase plate to vary the relations of I , L and T_e and search for a sweet spot of TPD conditions for PHELIX parameters. Note that a larger scale length using the phase plate also indicates a larger region where TPD is possible and thus more EPWs as discussed above.

Using the phase plate, maximum laser intensities during our experiment were $I = (1.07 \pm 0.02) \cdot 10^{14} \text{ W cm}^{-2}$. This results in a lower maximum TPD growth rate of $\gamma_{\max}^{\text{PP}} = 3.6 \cdot 10^{12} \text{ s}^{-1}$ compared to the best focus setting. If we assume the lower intensity but larger laser spot results in a similar temperature around $T_e = 1 \text{ keV}$ as for the best focus, the influence of collisional damping is thus expected to be even more relevant.

It should be noted that the phase plate setting is expected to increase the X-ray source size and therefore to decrease its brilliance compared to the best focus. Concerning X-ray diffraction (cf. chapter 2), this reduces the X-ray yield after collimation or smears out the detected diffraction rings. Therefore, it depends on the specific application of the X-ray diagnostics if the phase plate setting can be used. One of the proposed experiments at HHT foresees the generation of WDM by irradiating an iron foil with a size of 500 $\mu\text{m} \times 500 \mu\text{m}$ with ion pulses. Among other methods, this sample should be diagnosed by X-ray diffraction without collimation. Assuming as a first approximation the X-ray source size to be comparable to the 500 μm laser spot, the resulting angular spread is not larger than due to the sample size itself, such that the phase plate setting seems suitable. Using the pinhole camera (cf. section 5.1) data, the source size needs to be analyzed quantitatively in the future.

5.3. Diagnostic Setup

In this section, I present in more detail how our diagnostics worked and for which purposes they are used. Section 5.3.1 describes our hard X-ray detector, in section 5.3.2 our highly oriented pyrolytic graphite spectrometer is discussed and section 5.3.3 is about our combination of streak camera and spectrometer.

5.3.1. Hard X-Ray Detector

For the HXRD, we used Al filters with thicknesses of 100 µm, 250 µm, 350 µm, 450 µm, 600 µm and 700 µm, respectively, that we glued on a 0.5 mm thick PMMA sheet. Our filter array design is schematically shown in Fig. 5.2a. In our setup, it was mounted on a re-entrant tube. Directly behind the re-entrant tube window, we positioned an imaging plate (IP) to detect the X-ray yield behind the different filters.

The X-ray yield behind different filters gives rise to information on the shape of the incident hard X-ray spectrum. This is due to the fact that $T(E)$, where T is the transmission through a filter in dependence of the photon energy E , changes its shape with filter thickness. Exemplarily, the transmission is shown in Fig. 5.2b through 100 µm and 700 µm Al [48].

The difference between the X-ray yield behind a thinner and thicker filter is mostly due to photons with energies where the transmission differs significantly between the filters. If the filter transmissions were perfect step functions, the spectral interval of such photons would be unambiguously known. Due to the real shape of the transmission increasing over a large energy range, the X-ray yield behind different filters contains this information only implicitly and typically ambiguously. In particular, the use of more than two different filter thicknesses is necessary.

The detected hard X-ray signal behind different filters contains, furthermore, information about fast electrons, since X-ray emission and electrons are related by the processes of bremsstrahlung (cf. section 3.1.1) and recombination (cf. section 3.1.2).

We expect the chosen filter thicknesses of our HXRD to strongly suppress thermal X-ray emission - especially for thicker filters - and to enable us to distinguish X-ray energies in the regime of several tens of keV corresponding to typical electron energies from TPD.

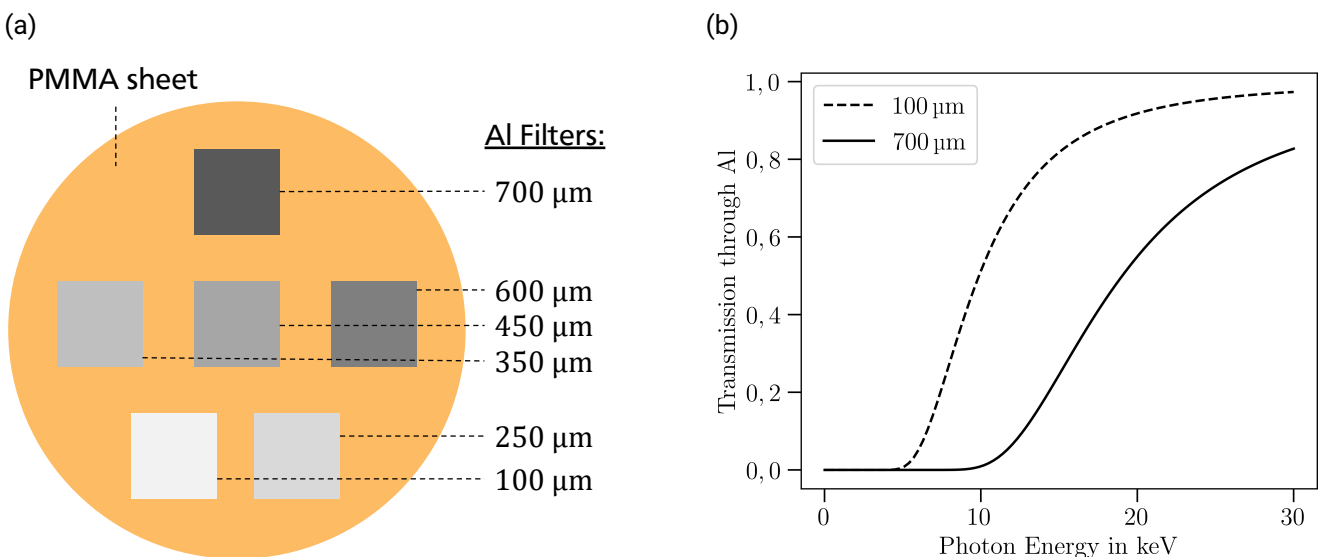


Figure 5.2.: The HXRD filter setup is shown. In (a), a schematic indicates the design of our filter array. Each filter covered an area of roughly 4 mm × 4 mm. In (b), the transmissions through our thinnest and thickest Al filters are plotted.

5.3.2. Highly Oriented Pyrolytic Graphite Crystal

We used a HOPG crystal to spectrally resolve different X-ray emission lines from the plasma. This diagnostic method is well known [79] and I will explain it briefly in the following.

Let us consider X-rays emitted from the target that reach our HOPG crystal. The X-rays are reflected at different lattice planes of the crystal which have a spacing of $d = 0.3354 \text{ nm}$, so that diffraction occurs. Photons with different energies or rather wavelengths λ fulfill the Bragg condition

$$n\lambda = 2d \sin(\theta) \quad (5.8)$$

for constructive interference in n^{th} order under different Bragg angles θ . We detected the resulting spatial separation of photons of different energies with an IP positioned in a re-entrant tube (see Fig 5.1). Note that we covered the HOPG crystal with a layer of Al foil as blast shield against debris.

A specialty about the HOPG is its mosaic structure with a certain mosaic spread ($\phi_{\text{FWHM}} = (0.25 \pm 0.05)^\circ$ for our crystal). Even though this spread decreases the energy resolution, it is useful for X-ray detection in our case. The reason is that the mosaic spread increases the integrated reflectivity of the crystal so that even weak line emission from the target can be detected with the HOPG spectrometer. Figure 5.3 shows the reflection at the HOPG crystal schematically.

During our experiment, we had to change the height H of the HOPG crystal for each target material to be able to detect K_α lines. Originally, we planned to detect K_α line emission of copper (molybdenum) [silver] in first (second) [third] diffraction order. The Bragg angles of which would have allowed to keep the HOPG crystal in the same position to display the lines on the IP. However, in this initial crystal position, we were not able to see any K_α line in the case of molybdenum and silver. After moving the HOPG crystal so that K_α lines could be reflected in the first diffraction order, the lines were clearly visible. This may be due to a strong decrease of the HOPG reflectivity with increasing diffraction order.

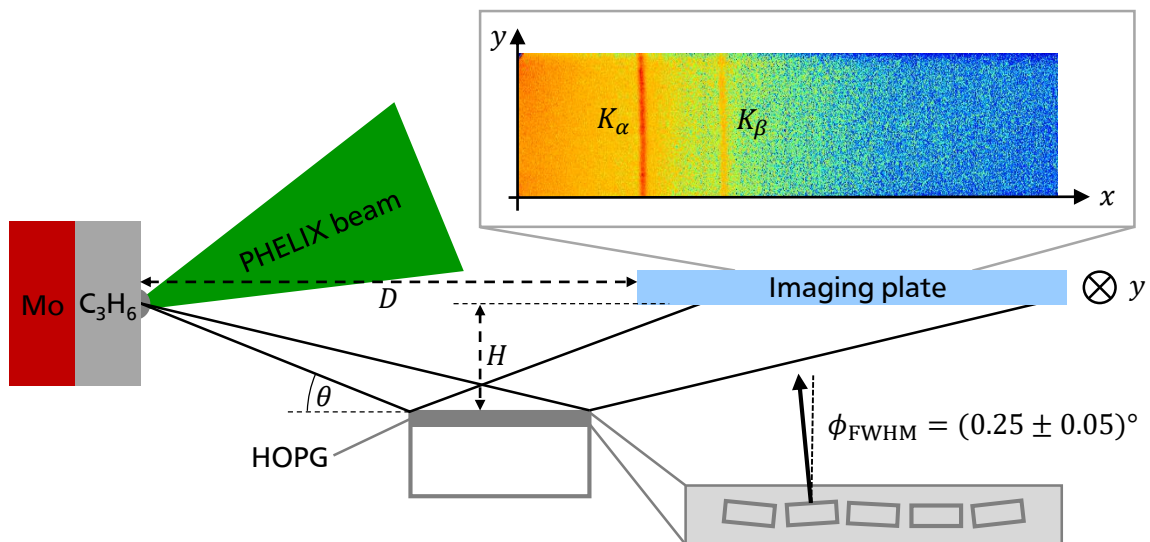


Figure 5.3.: A schematic of the X-ray reflection off the HOPG crystal is shown. As illustrative example, the detected photostimulated luminescence of one shot is included. In x -direction, X-ray emission is spectrally resolved. K_α and K_β lines are clearly visible.

5.3.3. Streak Camera and Spectrometer

We used a combination of streak camera and spectrometer to measure the $3/2 \omega_0$ signature from TPD (cf. section 4.2). The spectrometer dispersed photons in a narrow spectral window around $3/2 \omega_0$ which were then temporally resolved by the streak camera. To reach these diagnostics, the $3/2 \omega_0$ emission was guided from the target out of the chamber by a combination of lenses (number 8 in Fig. 5.1) and mirrors (number 9 in Fig. 5.1).

We adjusted the spectrometer with another laser at $\lambda_{\text{adj}} = 355$ nm to map a frequency range around $3/2 \omega_0$ on the entrance slit of the streak camera. The streak camera was triggered with an electrical pulse delivered from the PHELIX facility and its internal delay was set to compensate for the time difference between the trigger signal and the actual time when the plasma emission reached our diagnostic. This timing was taken care of at the start of the experiment with low-energy pulses from the PHELIX ns-frontend while the spectrometer was set to the ω_0 regime. We set the streak camera's sweep time to 20 ns as the best compromise between temporal resolution and total measuring time window. To prevent the streak camera signal from saturation, we placed filters (number 10 in Fig. 5.1) in front of the spectrometer.

6. Evaluation and Methods

In this chapter, I present the evaluation of the raw data, explain the methods used for extracting the quantities of interest and the simulations performed for that purpose. The analysis is based on input from the working group, in particular from Paul Neumayer, Zsuzsanna Major and Vincent Bagnoud, and was implemented and carried out mainly by myself. Monte-Carlo simulations in FLUKA [77, 78] (cf. section 6.3.2) were performed with the help of Xiao Yu.

In section 6.1, I present how we obtained the $3/2\omega_0$ signal, indicating the TPD strength, from the streak camera data. Section 6.2 shows the analysis of the HOPG data for the X-ray line emission and in section 6.3 the evaluation of both, the HXRD and HOPG data, is described in terms of the fast electron yield for which FLUKA simulations were used.

6.1. Calculation of the Two-Plasmon Decay Strength From Streak Camera Data

Here, I start with presenting how we calculated the TPD strength S from the raw data of the streak camera images. We assume the TPD strength to be given by the strength of the $3/2\omega_0$ signal, the TPD signature (cf. section 4.2). Figure 6.1 shows exemplarily an image for a shot on a coated target. We can clearly see a signal peak due to $3/2\omega_0$ emission. In order to determine its strength, we manually defined a time interval that contains this peak. Afterwards, we integrated the signal over the area A_{signal} determined by the time interval and without limitations in spectral range. We additionally subtracted the background that we determined by the mean signal in an area $A_{\text{background}}$ over the same time interval as previously, but only over a small spectral range set by pixel numbers 40 to 60. When choosing that spectral range we ensured that no features, e.g., pedestals, of the main peak were contained in the background calculation. Furthermore, we ensured that we were away far enough from marginal pixels where we observed nonuniform illumination in some cases. Despite the small spectral range, the pixel number for the background calculation is ~ 1000 which allows for good statistics. In Fig. 6.1, the areas used for our analysis are indicated.

For each shot, we set the time interval defining A_{signal} and $A_{\text{background}}$. As a further example, I show a typical streak camera image for a shot on an uncoated target in Fig. 6.2 together with the areas A_{signal} and $A_{\text{background}}$. Since the background increases at the time when the $3/2\omega_0$ peak occurs, it is important that we limited $A_{\text{background}}$ to the same time interval as A_{signal} .

Due to the fact that the manual choices of A_{signal} and $A_{\text{background}}$ are somewhat ambiguous, the areas were varied from their defined values in order to determine the error ΔS for each shot. The pixel numbers limiting the spectral range for the background calculation were each varied in integer steps up to ± 5 pixels. Furthermore, the time interval concerning both, the signal and background calculation, was varied. The upper limit of the time interval was increased by up to $+5$ pixels and the lower limit of the time interval

was decreased by up to -5 pixels. This corresponds to only increasing the considered period of time - a decrease would not make sense, since part of the signal would be rejected. For each shot, the TPD strength S_i was calculated for the $i = 1, \dots, 4356 (11^2 \cdot 6^2)$ different combinations and the standard deviation was used as error ΔS .

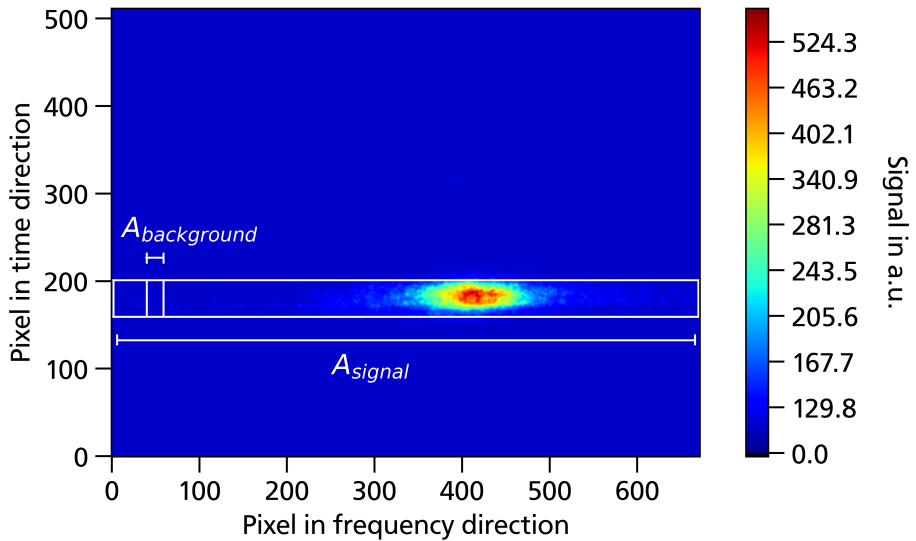


Figure 6.1.: Streak camera image of a shot (ID 19657 in PHELIX Shot Database PSDB) on $12.7\text{ }\mu\text{m}$ Cu with $10\text{ }\mu\text{m}$ C_3H_6 coating. A_{signal} and $A_{background}$ used for processing the raw data are shown.

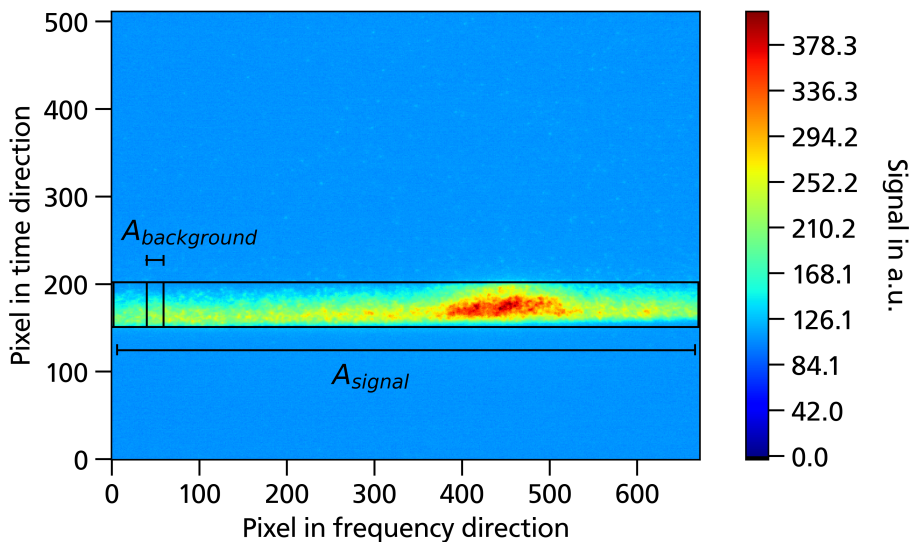


Figure 6.2.: Streak camera image of a shot (ID 19630 in PSDB) on uncoated $10\text{ }\mu\text{m}$ Cu. A_{signal} and $A_{background}$ used for processing the raw data are shown.

6.2. Calculation of Line Emission Yield From Highly Oriented Pyrolytic Graphite Spectrometer Data

With the HOPG spectrometer (cf. section 5.3.2), we detected characteristic X-ray emission lines such as K_α and K_β . In section 6.2.1 the energy calibration of the HOPG spectrometer data is described, in section 6.2.2 I show which emission lines were observed and in section 6.2.3 our calculation of the K_α emission strength is discussed.

6.2.1. Energy Calibration

A typical image obtained by a scan of the HOPG spectrometer IP is shown in Fig. 6.3. Through the Bragg condition

$$n\lambda = 2d \sin(\theta), \quad (6.1)$$

the x -axis of such an image can be transformed into an axis indicating the photon energy E (cf. section 5.3.2). The X-ray wavelength λ is related to the photon energy E by

$$E = hc/\lambda. \quad (6.2)$$

The Bragg angles θ are connected to the x -positions on the IP depending on the geometry of the HOPG spectrometer. With the crystal height H and the distance D between target and IP (see Fig. 5.3), it holds

$$\theta = \arctan\left(\frac{2H}{D+x}\right). \quad (6.3)$$

We insert Eqs. 6.2, 6.3 and the diffraction order $n = 1$ (cf. section 5.3.2) in Eq. 6.1 and obtain the transformation from position x to energy E :

$$E = \frac{hc}{2d \cdot \sin\left(\arctan\left(\frac{2H}{D+x}\right)\right)}. \quad (6.4)$$

The parameters D and H were measured when setting up the HOPG spectrometer. However, we determined their values from the detected signals, since this allowed for a more precise energy calibration. We clearly determined D and H by inserting the x -positions of K_α and K_β lines and the corresponding photon energies in Eq. 6.4 and solving the obtained system of equations. The x -position of each line was determined by a Gaussian fit with a linear function accounting for the background. The linear function was allowed to vary between K_α and K_β lines to account for nonlinear variations of the background.

We carried out the described calibration procedure for each HOPG crystal position set during the experiment. For each position, we used a shot on a coated target to extract the positions of the K_α and K_β lines and the resulting values for the crystal height H and the distance between target and IP D . Using these values, we calibrated all shots in the respective HOPG crystal position. The transformation of the horizontal axis from location x to photon energy E included the transformation of photostimulated luminescence (PSL) values according to $PSL(E) = |\frac{dx}{dE}| \cdot PSL(x(E))$, as well.

It should be noted that the IP data was averaged in y -direction over an interval of 200 pixels, i.e., a distance of 1 cm, for each x -value to obtain more statistics and higher accuracy. This was important, since single

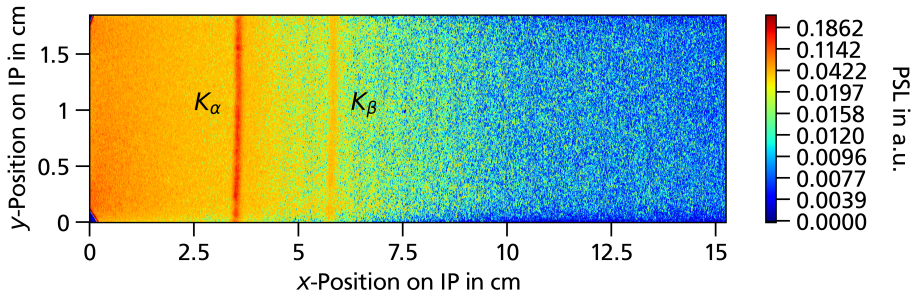


Figure 6.3.: Image of a HOPG spectrometer IP scan of a shot (ID 19612) on 12.7 μm Cu with 10 μm coating. K_α and K_β emission lines can be clearly identified.

pixels of the IP scan images often displayed only single photon events. The averaging was justified because the detected line emission features are, in good approximation, independent of the y -position (see Fig. 6.3). More precisely, our HOPG setup (cf. section 5.3.2) was such that each line emission feature on the IP was the sector of a circle in the xy -plane with a radius equal to the distance $D + x$ to the target. Since $D + x \approx 0.2 \text{ m} \gg 1 \text{ cm}$, the curvature was negligible.

6.2.2. Different Types of Line Emission Observed

Before the analysis of line emission strength is described in more detail, this section gives an overview over different types of line emission we observed from both coated and uncoated targets. In order to identify lines, we used the transition energies provided by the X-ray data booklet of Thompson *et al.* [52].

In the case of targets with C₃H₆ coating, the situation is similar for all metal substrates. Fast electrons are generated in the CH plasma and travel to the metallic material that has barely been heated yet. This leads to the production of K_α and K_β emission without emission from higher charged metal ions (cf. section 3.3). An example is shown in Fig. 6.4, where linear backgrounds are subtracted. For each of the two emission lines, an individual linear background was used. This can be seen by the apparent increase of the data at $E \approx 8.5 \text{ keV}$. Since linear backgrounds already had to be considered during the energy calibration (cf. section 6.2.1), the backgrounds of each shot were actually removed in the space-regime before calibrating the energy.

It should be noted that line emission produced from fast electrons while they travel through the coating has significantly lower energy and is not considered in the following because a major goal was to increase photon energies (cf. section 5.2). The same holds true for line emission from thermal electrons in the CH plasma.

For uncoated targets, the observed line emission is more complicated and depends on the target material. In principle, the emission line spectra consist of two different components. The first is caused by fast electrons which penetrate the target until they reach only barely heated material, comparable to the case of coated targets. This leads to line emission from cold atoms, especially K_α and K_β emission. Second, K-shell emission occurs in the hot laser-produced plasma. In comparison to neutral atoms, ions in the hot plasma produce K-shell emission with higher photon energies (cf. section 3.2). How far the corresponding lines are shifted, depends on the ionization states present in the hot plasma. The strength of these lines depends on the relation between K-shell ionization energy and the temperature of thermal electrons.

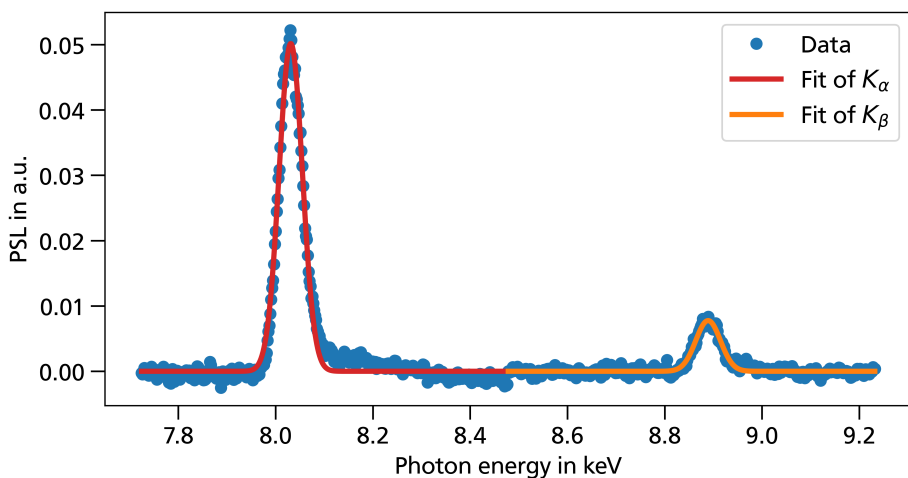


Figure 6.4.: Emission lines of a shot (ID 19612 in PSDB) on 12.7 μm Cu with 10 μm coating.

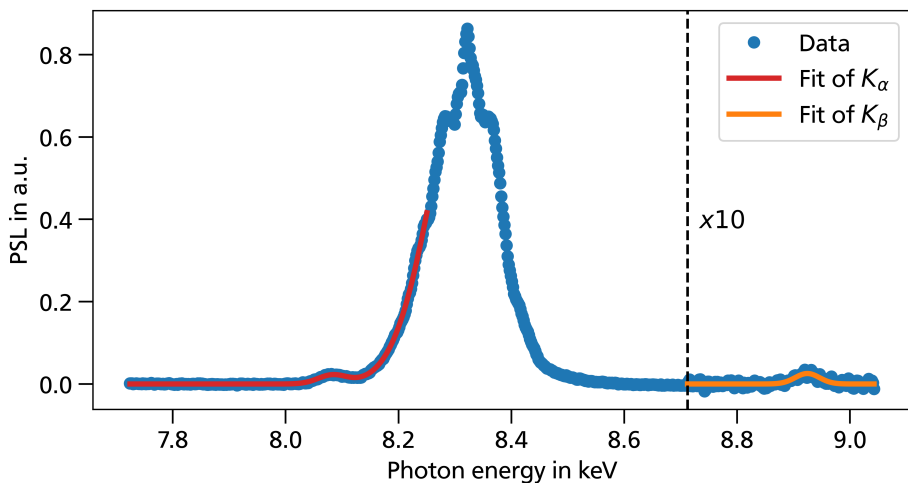


Figure 6.5.: Emission lines of a shot (ID 19567 in PSDB) on uncoated 10 μm Cu.

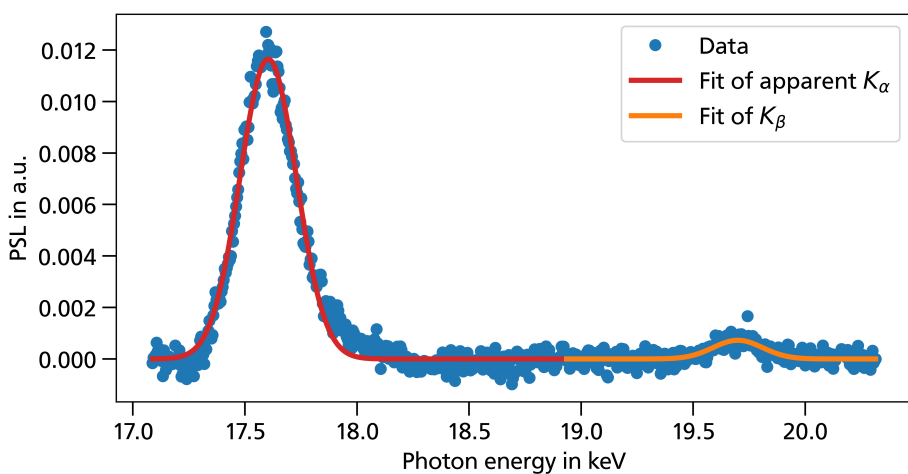


Figure 6.6.: Emission lines of a shot (ID 19660 in PSDB) on uncoated 10.07 μm Mo.

In Fig. 6.5, the situation is shown for uncoated Cu. In that case, there exist numerous electrons in the Boltzmann tail of the thermal distribution that have sufficiently high energies to cause K-shell ionization or excitation. Furthermore, the thermal electron temperature is so high that Helium-like, Lithium-like, ... ionization states are populated. As a result, line emission from transitions to the K-shell in highly charged ions is observed as in a previous work [44] (cf. section 3.2). The K_α emission line displays only a small bump on the lower-energy side of the line emission from $K \rightarrow L$ -shell transitions in highly charged ions. Future work might include to analyze the populations of different ionization states corresponding to the detected emission and to compare them with those observed in [44]. The populated ionization states could be furthermore used to estimate the electron temperature similar to [44]. However, this is not the main goal of our work, since we focus more on coated and Mo/Ag targets that have not been used within the work of [44], yet.

To make K_β emission visible in Fig. 6.5, the signal is multiplied by a factor of 10 on the right side of the dashed vertical line. We also observed emission lines from $M \rightarrow K$ -shell transitions in higher charged ions, but did not analyze them in more detail. Note that they are not shown in Fig. 6.5. Similar to the coated targets, two linear backgrounds were subtracted to obtain Fig. 6.5: one around the emission lines from highly charged ions and the K_α line, the other around the K_β line. The background subtraction of each shot was again already carried out before the energy calibration.

In contrast to Cu, the K-shell ionization energy of Mo and Ag is significantly higher which drastically reduces the number of electrons in the thermal distribution to produce K-shell emission. Furthermore, there are ionization states populated where more bound electrons are left. The result can be seen in Fig. 6.6 (exemplarily for Mo) where no strong line emission from higher charged ions can be observed. In fact, there is only a single line from $L \rightarrow K$ shell transitions visible. Our hypothesis is that this detected K_α line is an overlap of K_α emission from cold Mo and slightly shifted emission from higher charged ions. This hypothesis is supported by FLYCHK [73] simulations at the critical density $n_e = 4 \cdot 10^{21} \text{ cm}^{-3}$. Assuming $T_e = 1 \text{ keV}$, the simulations indicate that below 0.03 % of the populated ionization states are Oxygen-like or higher charged and therefore the emission from $L \rightarrow K$ transitions is expected to have only small energy shifts. An analysis of the detected emission lines which supports our hypothesis is shown in appendix B. The background subtraction for shots on uncoated Mo and Ag targets was similar as for coated targets and uncoated Cu. For each shot, linear backgrounds were subtracted around the detected K_α and K_β lines, respectively, before the energy calibration.

6.2.3. Calculation of K_α Yield

After transforming the HOPG spectrometer data into the energy-regime (cf. section 6.2.1) and identifying the different emission lines (cf. section 6.2.2), the lines were analyzed in more detail. In this section, I describe how we calculated the K_α and K_β line emission strength of the produced X-ray sources.

First, we fitted the K_α and K_β emission lines by Gaussian functions which have already been included in Figs. 6.4 - 6.6. In the case of uncoated Cu targets, the K_α line was already on the rising edge of a line from highly charged ions which we compensated by using the rising edge of a second Gaussian function as background. From the Gaussian fits, we calculated the K_α and K_β line emission strengths. Note that for potential application of coated targets for X-ray diffraction, the K_α emission strength will be relevant so that this quantity is mostly of relevance for this work. For our considerations in appendix B, the K_β emission strength is also necessary. For simplicity, the further description in this section is labeled for K_α emission but each step is analogously valid for K_β emission.

Table 6.1.: IP luminescence decay constants [80]. A_m and τ_m are the relative strengths and decay constants of the two ($m = 1, 2$) decays in our IPs.

A_1	τ_1 in min	A_2	τ_2 in min
0.56 ± 0.03	21.32 ± 2.77	0.43 ± 0.02	3282.92 ± 597.53

We integrated over the Gaussian fits of the K_α emission lines which provided the total PSL from K_α photons detected in an area on the HOPG IP that extends over the whole energy (x) direction and over a single pixel in y -direction. This quantity is called PSL_{line} in the following. Next, we calculated the number of K_α photons N_{line} corresponding to PSL_{line} by

$$N_{\text{line}} = \frac{a \cdot PSL_{\text{line}}(t = 0 \text{ min})}{\eta(E^{\text{ph}}(K_\alpha)) \cdot T(E^{\text{ph}}(K_\alpha)) \cdot E^{\text{ph}}(K_\alpha)}, \quad (6.5)$$

of which the different quantities are explained in the following. First, we need the conversion factor from PSL into deposited energy $a = (0.622 \pm 0.058) \text{ MeV PSL}^{-1}$. This value depends on the particular device used for scanning the IPs. For a previous scanner, $a_{\text{old}} = (0.926 \pm 0.065) \text{ MeV PSL}^{-1}$ has been determined in a systematic study [80]. The relative calibration between the scanner used for the here presented work and the old device resulted in a factor $f = 0.671 \pm 0.04$ [81] which gives the value $a = f \cdot a_{\text{old}}$.

To calculate N_{line} , we furthermore simulated the energy-dependent IP response $\eta(E)$, i.e., efficiency of energy deposition in the active layer of the IP, with the 3D Monte-Carlo simulation tool FLUKA [77, 78]. Data for K_α photon energy $E^{\text{ph}}(K_\alpha)$ was taken from the X-ray data booklet of Thompson *et al.* [52] and data for the energy-dependent X-ray transmission of the HOPG crystal blast shield and re-entrant tube window $T(E)$ was taken from the CXRO database [48] and the XCOM database [82]. Additionally, we had to take the time delay between a PHELIX shot and the IP scan into account because of decays of meta stable states in the IP. This results in a rescaling of PSL from scanning time $t = 10 \text{ min}$ to shot time $t = 0 \text{ min}$ by

$$PSL(t = 0 \text{ min}) = \frac{PSL(t = 10 \text{ min})}{A_1 \cdot e^{-10 \text{ min}/\tau_1} + A_2 \cdot e^{-10 \text{ min}/\tau_2}}. \quad (6.6)$$

The same rescaling holds true for $PSL_{\text{line}}(t = 10 \text{ min})$ and $PSL_{\text{line}}(t = 0 \text{ min})$. The decay constants and their relative strengths are summarized in Table 6.1.

From the quantity N_{line} (see Eq. 6.5), we calculated the total number of K_α photons $N(K_\alpha)$ emitted from the target (similar to [83]) by

$$N(K_\alpha) = \frac{4\pi \cdot 2F \cdot N_{\text{line}}}{R_{\text{int}} \cdot \Delta y_{\text{pixel}}}. \quad (6.7)$$

In particular, Eq. 6.7 takes the collection efficiency of the HOPG spectrometer into account. This efficiency is dependent on the integrated reflectivity of the HOPG crystal R_{int} , the distance a K_α photon travels from the target to its reflection point on the HOPG crystal $F = ((D + x)^2/4 + (H)^2)^{0.5}$ (see Eq. 6.1 and Fig. 5.3) and the pixel size in y -direction Δy_{pixel} of the scanned IP images. We made the approximation of an isotropic emitting X-ray source which we have accounted for in Eq. 6.7 by the factor 4π .

In fact, there exists an angular dependence which is due to re-absorption within the target. The re-absorption increases with the path length photons travel in the target material. Therefore, the X-ray source brightness is expected to be highest in target normal direction $\theta = 0^\circ$ and to decrease for increasing θ .

However, we do not expect the angular dependence to dramatically change our results as can be exemplarily estimated for the $12.7\text{ }\mu\text{m}$ thick Cu targets.

The transmission through cold, $12.7\text{ }\mu\text{m}$ thick Cu is $T > 0.5$ for $E^{\text{ph}}(K_\alpha)$ [48]. Even if the emission of K_α photons occurs at the backside of the target, an additional path length of $12.7\text{ }\mu\text{m}$ compared to target normal direction corresponds to an angle of $\theta = 60^\circ$ so that we do not expect the emission per solid angle to change by more than a factor of 2 from $\theta = 0^\circ$ to $\theta = 60^\circ$. In the case of Mo and Ag, the transmission is even higher for their K_α photons. Furthermore, the coatings are not important for our estimation because of their generally smaller absorption.

Still, an angular dependence could be simulated in the future to calculate $N(K_\alpha)$ more precisely and to estimate how much stronger the emission per solid angle is in target normal direction compared to its average.

Based on photon numbers $N(K_\alpha)$, we furthermore calculated the conversion efficiency $\frac{E(K_\alpha)}{E_{\text{Laser}}}$ from on-shot measured laser energy E_{Laser} at $\lambda_{\text{vac}} = 527\text{ nm}$ (cf. section 5.1) into K_α photons which will allow for easier comparison with other experiments and between shots at different laser energies. Here $E(K_\alpha) = N(K_\alpha) \cdot E^{\text{ph}}(K_\alpha)$ is the total energy of K_α photons.

During our calculations, we considered errors for $PSL_{\text{line}}(t = 0)$ that are given by uncertainties of the Gaussian fits of each emission line and the translation from IP scanning time $t = 10\text{ min}$ to $t = 0\text{ min}$ due to decays in the IP (see Eq. 6.6). Furthermore, we propagated the errors $\Delta R_{\text{int}} = 0.0001$ and $\Delta a = 0.058\text{ MeV PSL}^{-1}$ and assumed an error of $\Delta\eta(E^{\text{ph}}(K_\alpha))/\eta(E^{\text{ph}}(K_\alpha)) = 5\%$ which is an upper limit for all considered K_α energies. We neglected errors in $T(E^{\text{ph}}(K_\alpha))$ due to uncertainties in the thicknesses of the re-entrant tube window and blast shield and neglected errors in F , since they were estimated to be each below 2 %. Furthermore, we did not assume any error for the scanner's pixel size Δy_{pixel} and the laser energy E_{Laser} , since they were expected to be small, as well.

I point out that Δa and the translation of IP scanning time display systematic errors that are uncertainties in the calibration of absolute numbers $N(K_\alpha)$ and $\frac{E(K_\alpha)}{E_{\text{Laser}}}$, but not in terms of relative (shot-to-shot) numbers. The two systematic errors add up to $\sim 10\%$.

Furthermore, I would like to make some remarks concerning Eq. 6.7. First, the integrated reflectivity of our HOPG crystal was only known for Cu K_α where it has the value $R_{\text{int}} = 0.0025 \pm 0.0001$. The same value was assumed for Mo and Ag K_α , since no experimentally determined values were available for these cases. Second, we used the whole detected K_α line of uncoated Mo and Ag for calculating the K_α yield because no quantitative separation between K_α emission from cold material and from higher charged ions had been made. Nevertheless, the two contributions are comparably strong (see appendix B) so that our results are still meaningful.

6.3. Fast Electron Analysis

After calculating the K_α line emission strength as discussed in section 6.2, we analyzed the fast electrons produced in our experiment, since they were essential for generating K_α emission. We were interested in how many fast electrons of which energy corresponded to the detected X-ray yield, in terms of not only K_α , but also hard X-ray emission. The diagnostics we used to measure the latter was the HXRD and actually only the HXRD data allows to draw conclusions on the spectral shape of the fast electrons. To do so, we simulated the X-ray yield of electrons of different energies with FLUKA [77, 78] and fitted the electrons to match the

HXRД data. This analysis underlies the challenge and ambiguity that the HXRД does not directly detect data spectrally resolved (cf. section 5.3.1), thus assumptions about the spectral shape of the fast electrons need to be made. We tried two different models: first, the simplest possible of monoenergetic fast electrons and second, the one typically found in the literature [35, 84] using temperature distributed fast electrons. During the fit procedure, the HXRД data did not only allow for determining the energy/temperature, but also for scaling the number of fast electrons in accordance to the detected signal strength. Additionally, the scaling of the fast electron number was implemented by fitting the detected K_{α} emission strength with the simulated X-ray yield of electrons with the energy/temperature determined from the HXRД data. In the literature, the latter method is chosen for scaling, since the HXRД is usually not absolutely calibrated [32, 35, 36].

In section 6.3.1, I describe how the HXRД signal is calculated from the raw data. Section 6.3.2 is about the FLUKA simulations we performed for the respective targets and section 6.3.3 presents how we generally measured the quality of an electron fit to the HXRД data. In sections 6.3.4 and 6.3.5, the fitting procedure is explained in more detail for the monoenergetic and temperature distributed fast electron model, respectively, and applied to the data of exemplary shots. Section 6.3.6 describes the procedure how we scaled the fast electron numbers using our HOPG spectrometer data for both the monoenergetic and temperature distributed electron models.

6.3.1. Calculation of Hard X-Ray Detector Signal

The HXRД incorporates different filters (cf. section 5.3.1) behind which the X-ray yield was detected with IPs. For each shot, the data $PSL_j^{\text{data}}(t = 10 \text{ min})$ was determined by averaging the detected PSL over pixels within a manually chosen area behind each filter $j = 1, \dots, 6$. Due to the delay between a shot and the IP scanning time, the data corresponds to the PSL 10 min after a shot. To calculate $\Delta PSL_j^{\text{data}}(t = 10 \text{ min})$, we split the chosen areas into $n = 1, \dots, 25$ subareas and calculated the mean PSL value $PSL_j^{\text{data},n}(t = 10 \text{ min})$ for each subarea. We estimated the error as:

$$\Delta PSL_j^{\text{data}}(t = 10 \text{ min}) = \max_{n=1, \dots, 25} |PSL_j^{\text{data},n}(t = 10 \text{ min}) - PSL_j^{\text{data}}(t = 10 \text{ min})|. \quad (6.8)$$

This takes statistical variations and potential gradients in the signal behind each filter j into account. In Fig. 6.7, the PSL of the HXRД IP scan of an exemplary shot is shown. I marked the areas and subareas used for calculating $PSL_j^{\text{data}}(t = 10 \text{ min})$ and $\Delta PSL_j^{\text{data}}(t = 10 \text{ min})$. Note that the shadows of the six filters can be clearly identified by their different PSL levels.

6.3.2. Simulation of X-Ray Emission

To relate electrons and X-ray yield, we performed simulations with FLUKA [77, 78] in which monoenergetic electrons hit the respective solid target and the simulated X-ray yield was detected. In FLUKA, each electron individually hits the cold target so that no heating occurs and no plasma is produced. For our temperature distributed electron model, we did typically not assume temperature distributed electrons within FLUKA, but superimposed the X-ray yield of different monoenergetic electrons according to a temperature distribution. This was advantageous in terms of computing time and flexibility of the analysis, since it allows to replicate the X-ray yield of arbitrary electron temperatures.

The simulation geometry is shown in Fig. 6.8. The X-ray detection cone within FLUKA corresponded to the location of the HOPG spectrometer and HXRД with respect to the target when assuming cylindrical

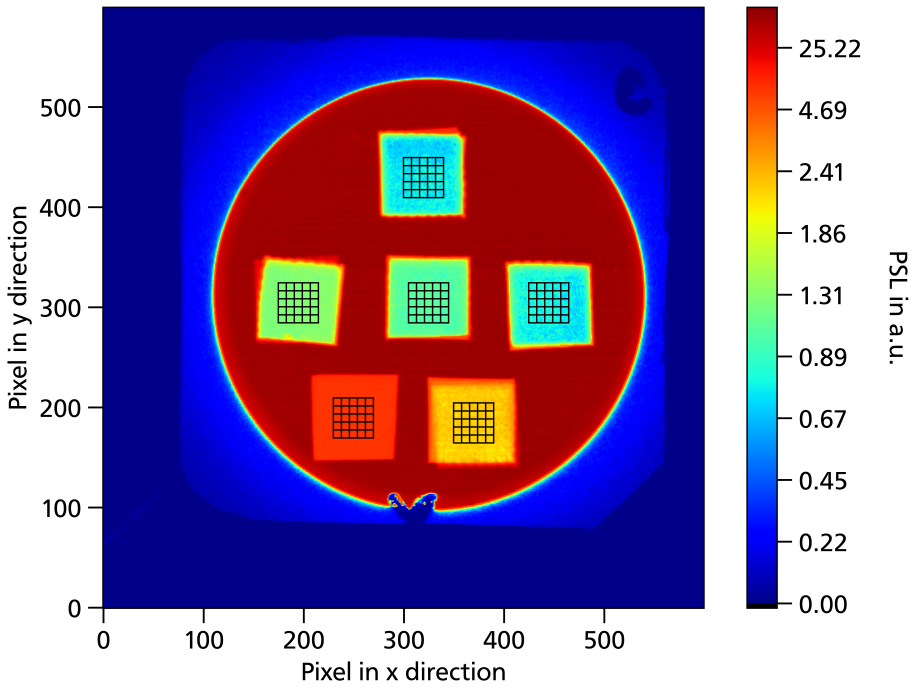


Figure 6.7.: PSL of HXRD IP scan of a shot (ID 19567 in PSDB) on 10 μm Cu. For each filter, the large square was used to calculate $PSL_j^{\text{data}}(t = 10 \text{ min})$ and the small squares to calculate $PSL_j^{\text{data},n}(t = 10 \text{ min})$.

symmetry. To maintain this symmetry, we assumed the electrons to hit the target in normal incidence. This is, of course, a simplification compared to the experiment where electron plasma waves are amplified in different directions by TPD (cf. sections 4.5.1 and 4.7.2) resulting in multi-directional electron acceleration. Nevertheless, all electron plasma waves relevant for the acceleration process have a wave vector component pointing to increasing electron densities (cf. section 4.8) and therefore the normal incidence is a first order approximation. The dependence of X-ray yield on the angle of incoming electrons is expected to be small, anyway.

We performed simulations for the Cu target with 10 μm coating, the coated Mo and Ag targets, and the bare Cu target with 10 μm thickness. For each target, various electron energies (see Tab. 6.2) were simulated. We chose a bin size of 25 eV for the simulated X-ray spectra in the case of electron energies below 100 keV and a bin size of 200 eV for electron energies from 100 keV on. The cutoff below which electrons and X-rays were not tracked anymore was set to 1 keV and 2 keV, respectively. Both values are small enough with respect to the production of K_{α} emission in the metallic layer and the X-ray energies relevant for the HXRD.

Table 6.2.: Electron energies E_i simulated in FLUKA. The energy spacing was increased from 2.5 keV to 5 keV, 10 keV, 20 keV and 50 keV with increasing E_i .

E_i in keV	5	7.5	...	20	25	...	50	60	...	100	120	...	200	250	300	350
--------------	---	-----	-----	----	----	-----	----	----	-----	-----	-----	-----	-----	-----	-----	-----

FLUKA outputs its data as spectral photon number per solid angle and per primary electron $\frac{dN_{ph,i}(E_{bin})}{dE \cdot \Omega \cdot \text{primary}}$ for each bin. The index i denotes the X-ray spectrum corresponding to the electron energy E_i . Of course, the spectra change between different target types, but no corresponding index is used for simplicity. Multiplying the output of FLUKA with the bin size of the simulation yields the number of photons in each bin per solid angle and primary electron $\frac{N_{ph,i}(E_{bin})}{\Omega \cdot \text{primary}}$.

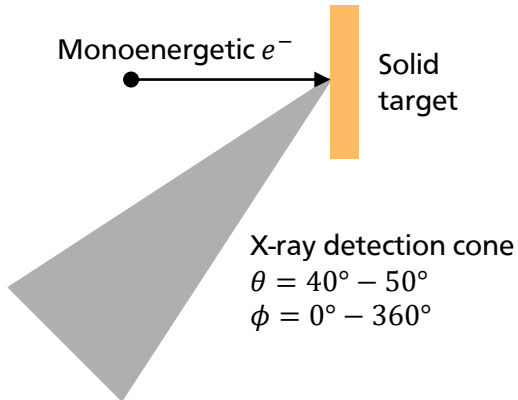


Figure 6.8.: Geometry used for FLUKA simulations.

6.3.3. Quantification of the Quality of Electron Fits to the Hard X-Ray Detector Data

The main principle of evaluating the HXRD data was to search for an electron composition of which the produced X-ray spectral distribution is consistent with the detected PSL values behind different filters simultaneously. For both our models, the monoenergetic and temperature distributed fast electrons, it was necessary to be able to quantify how good an electron composition fits the HXRD data. In the following, I present this measure for arbitrary superpositions of electrons of different energies which was applied to the monoenergetic and temperature distributed case.

To calculate the energy $E_{Dep,j}(E_{ph})$ that a photon with energy E_{ph} deposited in average behind filter j in the IP, the energy dependent transmission $T_j(E_{ph})$ and the energy dependent IP response $\eta(E_{ph})$ need to be considered. It holds

$$E_{Dep,j}(E_{ph}) = E_{ph} \cdot T_j(E_{ph}) \cdot \eta(E_{ph}). \quad (6.9)$$

Note that $T_j(E_{bin})$ includes not only the filter transmission but also the transmission through the re-entrant tube window, the PMMA sheet of the filter array and additional Al foil layers that were used to reduce the signal.

From a FLUKA spectrum corresponding to the electron energy E_i , one obtains the amount of energy $\frac{E_{Dep,j}^{\text{sim}}(E_i)}{\Omega \cdot \text{primary}}$ that was deposited in the IP per solid angle and primary electron. For that purpose, the simulated X-ray spectrum is integrated weighting each photon energy according to Eq. 6.9. Assuming each photon within a bin has the energy E_{bin} at the center of the bin, it follows

$$\frac{E_{Dep,j}^{\text{sim}}(E_i)}{\Omega \cdot \text{primary}} = \sum_{\text{bin}} \frac{N_{ph,i}(E_{bin})}{\Omega \cdot \text{primary}} \cdot E_{Dep,j}(E_{bin}) = \sum_{\text{bin}} \frac{N_{ph,i}(E_{bin})}{\Omega \cdot \text{primary}} \cdot T_j(E_{bin}) \cdot \eta(E_{bin}) \cdot E_{bin}. \quad (6.10)$$

For electron compositions of different energies, the total amount of energy $\frac{E_{\text{Dep},j}^{\text{sim}}}{\Omega}$ deposited in the IP per solid angle is calculated by the sum over the c_i electrons at each energy E_i . One obtains

$$\frac{E_{\text{Dep},j}^{\text{sim}}}{\Omega} = \sum_i c_i(t = 10 \text{ min}) \frac{E_{\text{Dep},j}^{\text{sim}}(E_i)}{\Omega \cdot \text{primary}} = \sum_i c_i(t = 10 \text{ min}) \sum_{\text{bin}} \frac{N_{\text{ph},i}(E_{\text{bin}})}{\Omega \cdot \text{primary}} \cdot T_j(E_{\text{bin}}) \cdot \eta(E_{\text{bin}}) \cdot E_{\text{bin}}. \quad (6.11)$$

Note that the electron numbers are labeled by $c_i(t = 10 \text{ min})$, since when fitting the data $PSL_j^{\text{data}}(t = 10 \text{ min})$, an electron number corresponding to the signal strength scanned 10 min after a shot is obtained. Of course, this electron number has no physical meaning but needs to be transferred to the point of time $t = 0 \text{ min}$ using the decay constants given in Tab. 6.1. The translation reads

$$c_i(t = 0 \text{ min}) = \frac{c_i(t = 10 \text{ min})}{A_1 \cdot e^{-10 \text{ min}/\tau_1} + A_2 \cdot e^{-10 \text{ min}/\tau_2}}. \quad (6.12)$$

The simulated $PSL_j^{\text{sim}}(t = 10 \text{ min})$ in a pixel of the IP scan image follow from $\frac{E_{\text{Dep},j}^{\text{sim}}}{\Omega}$. Taking into account the solid angle $(\Delta y_{\text{pixel}})^2/r^2$ a pixel covers at the HXRD IP position in the distance r from the target and using the conversion factor a from PSL into deposited energy (cf. section 6.2.3), it holds

$$PSL_j^{\text{sim}}(t = 10 \text{ min}) = \frac{E_{\text{Dep},j}^{\text{sim}}}{\Omega} \cdot \frac{(\Delta y_{\text{pixel}})^2}{r^2 \cdot a}. \quad (6.13)$$

To quantify the quality of a fit, we use the reduced chi-square

$$\chi_{\nu}^2 = \frac{1}{\nu} \sum_j \frac{(PSL_j^{\text{sim}}(t = 10 \text{ min}) - PSL_j^{\text{data}}(t = 10 \text{ min}))^2}{(\Delta PSL_j^{\text{data}}(t = 10 \text{ min}))^2}, \quad (6.14)$$

where the number of degrees of freedom $\nu = n_{\text{data}} - n_{\text{fit}}$ depends on the number of data points n_{data} and fit parameters n_{fit} . The smaller χ_{ν}^2 , the better the fit quality, in particular $\chi_{\nu}^2 < 1$ is considered a good fit. When fitting the HXRD data by our fast electron models, we thus tried to minimize χ_{ν}^2 .

Note that the definition of χ_{ν}^2 only makes sense for $n_{\text{data}} > n_{\text{fit}}$ and that, in our case, n_{data} corresponds to the number of filters behind which the data was fitted. The indices j over which the sum in Eq. 6.14 is taken also depends on the choice of fitted filters. Furthermore, note that n_{fit} depends on the considered electron model.

6.3.4. Fitting Procedure to Hard X-Ray Detector Data With Monoenergetic Fast Electrons

In this section, I present how we fitted the HXRD data with monoenergetic fast electrons. I will also discuss relevant errors to the results of the fitting procedure. First coated and then uncoated targets are considered.

Coated Targets

As the monoenergetic model is the simplest approach, we also kept the fitting procedure as simple as possible in order to obtain easily accessible results. This means that we manually tested different electron energies and did not use an algorithm to systematically test which energies agree with the data. For a fixed electron energy, the equation of the simulated energy deposition behind each filter in the IP (see Eq. 6.11) simplifies, since the sum vanishes. Eq. 6.11 becomes

$$\frac{E_{\text{Dep},j}^{\text{sim}}}{\Omega} = c_i(t = 10 \text{ min}) \frac{E_{\text{Dep},j}^{\text{sim}}(E_i)}{\Omega \cdot \text{primary}} = c_i(t = 10 \text{ min}) \sum_{\text{bin}} \frac{N_{\text{ph},i}(E_{\text{bin}})}{\Omega \cdot \text{primary}} \cdot T_j(E_{\text{bin}}) \cdot \eta(E_{\text{bin}}) \cdot E_{\text{bin}}. \quad (6.15)$$

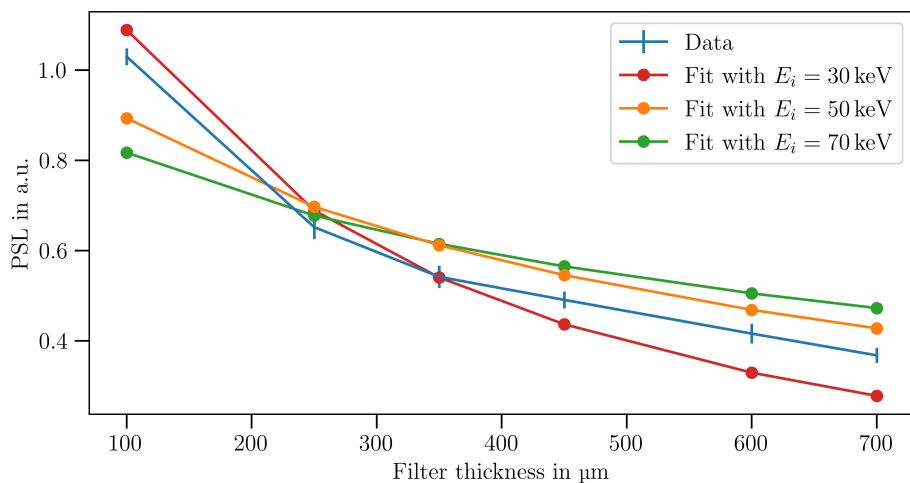
In particular, only one fit parameter $n_{\text{fit}} = 1$, namely the number of fast electrons c_i with energy E_i , is left which we optimized for each considered electron energy in order to minimize χ^2_ν . The obtained electron numbers c_i correspond to a global minimum of this convex optimization problem.

In Fig. 6.9a, the $PSL_j^{\text{sim}}(t = 10 \text{ min})$ corresponding to the best fits to the data behind all six filters are shown for different electron energies along with the data $PSL_j^{\text{data}}(t = 10 \text{ min})$ for a shot on coated Cu (ID 19612 in PSDB). None of the plotted energies can fit the data. In case of $E_i = 30 \text{ keV}$, the simulated PSL decrease too strongly with increasing filter thickness indicating that the X-ray spectrum simulated for $E_i = 30 \text{ keV}$ is too soft to fit the thick filters. On the other hand, at $E_i = 50 \text{ keV}$ and $E_i = 70 \text{ keV}$, the simulated PSL increase too weakly with decreasing filter thickness indicating that the simulated X-ray spectra are too hard to fit the thin filters. Exemplarily, it is $\chi^2_\nu = 18.1$ for the $E_i = 50 \text{ keV}$ fit. In fact, the outcome was similar when considering any simulated electron energy (cf. Tab. 6.2) and none of the energies thus corresponds to a good fit.

Let us discuss the reason for this issue. The thinnest filter has already a transmission of $T = 0.1$ at a photon energy of $E_{\text{ph}} = 6.6 \text{ keV}$. Therefore, it may be that behind thin filters, the origin of the HXRD signal is ambiguous. For these filters, the contribution of thermal X-ray emission to the signal could be comparable to the contribution from the harder but less intense X-ray emission of fast electrons. In contrast, the transmitted fraction of photons decreases stronger at lower compared to higher photon energies when increasing the filter thickness. Therefore, the hard X-ray emission is more relevant to the signal behind the thicker filters. The fact that the different filters weigh the two X-ray contributions differently prevents a single electron energy to fit the data behind all filters simultaneously. Since we are interested in the fast electrons and not the thermal X-ray emission, we exemplarily drop the two thinnest filters for the fitting procedure. The PSL corresponding to the best fits at different energies to only the four thickest filters are shown in Fig. 6.9b along with the data of all filters. The data behind the four thickest filters is fitted well with an electron energy of 50 keV which results in a best fit of $\chi^2_\nu = 0.196$. The other shown electron energies, 30 keV and 70 keV , result in contrast both in $\chi^2_\nu > 1$ and correspond to a too soft and too hard X-ray spectrum, respectively. For the fit with 50 keV fast electrons, the two thinnest filters cannot be replicated well (see Fig. 6.9b). This justifies the choice to drop them representing a good compromise of reducing the influence of thermal X-ray emission while keeping the number of fitted data points as high as possible. Note that the number of degrees of freedom needed to be adjusted in the definition of χ^2_ν (see Eq. 6.14) when considering different numbers of filters.

We analyzed all shots on Cu targets with the $10 \mu\text{m}$ coating and on coated Mo and Ag targets and it turned out that in (nearly) all cases, an electron energy of 50 keV was suitable to fit the data behind the four thickest filters with $\chi^2_\nu < 1$ (when obviously calculating c_i for each shot individually). Therefore, a fixed fast electron energy of 50 keV is considered for the monoenergetic model in the following of this work when investigating shots on coated targets.

(a)



(b)

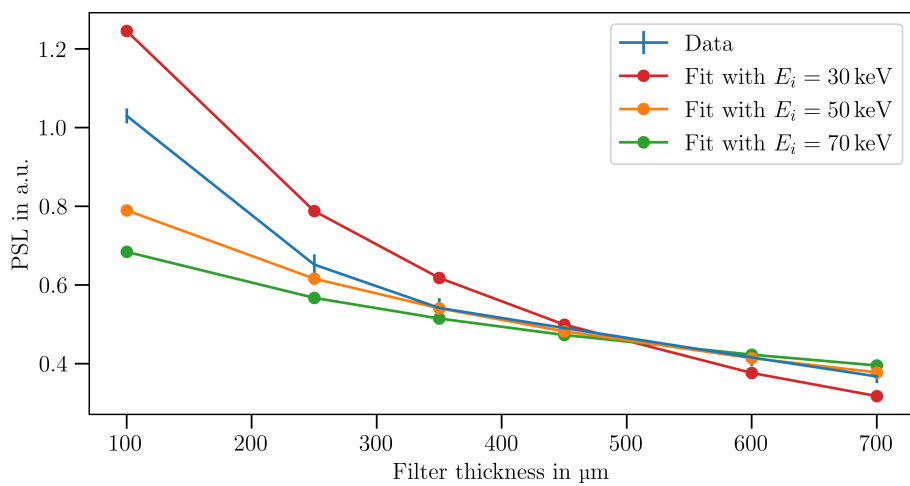


Figure 6.9.: PSL from best fits at different E_i and HXRD data of a shot (ID 19612 in PSDB) on 12.7 μm Cu with 10 μm coating. In (a), the data behind all six filters and in (b) only the four thickest filters are considered.

For each shot, the best fit coefficient directly denotes the number of fast electrons $N^{\text{HXRD}}(\text{e}^-) \equiv c_i(t = 0 \text{ min})$ necessary to reproduce the HXRD data. This allows to calculate the total energy in fast electrons $E_{\text{Electrons}}^{\text{HXRD}} = E_i \cdot N^{\text{HXRD}}(\text{e}^-)$, where $E_i = 50 \text{ keV}$, and thus the conversion efficiency $E_{\text{Electrons}}^{\text{HXRD}}/E_{\text{laser}}$ from laser energy into fast electrons. The index i is skipped in the newly defined variables, since i is taken such that 50 keV electrons are considered.

To determine an error of each electron number and conversion efficiency, we took the uncertainties Δa and those of the time translation from $c_i(t = 10 \text{ min})$ to $c_i(t = 0 \text{ min})$ into account. As well as in section 6.2.3, they add up to a systematic error of $\sim 10 \%$. Note that this systematic error would alter the fitted PSL behind all filters by the same factor, thus the same fit quality as without a systematic error could be obtained by adjusting c_i . Because of that, we did not consider this systematic error during the fitting procedure, but only for extracting the absolute values of fast electron numbers and conversion efficiencies. Furthermore, we estimated the error $\Delta c_i(t = 10 \text{ min})|_{\chi_{\nu}^2 < 1}$ that accounts for the fact that each fit with $\chi_{\nu}^2 < 1$ is considered a good fit to the data. To estimate this error, we varied $c_i^{\text{var}}(t = 10 \text{ min})$ for each

shot over a range of values around $c_i(t = 10 \text{ min})$ and calculated χ^2_ν for each $c_i^{\text{var}}(t = 10 \text{ min})$. We defined the error $\Delta c_i(t = 10 \text{ min})|_{\chi^2_\nu < 1}$ by the maximum possible variation of $c_i^{\text{var}}(t = 10 \text{ min})$ under the condition $\chi^2_\nu < 1$:

$$\Delta c_i(t = 10 \text{ min})|_{\chi^2_\nu < 1} = \max_{\chi^2_\nu(c_i^{\text{var}}(t = 10 \text{ min})) < 1} |c_i^{\text{var}}(t = 10 \text{ min}) - c_i(t = 10 \text{ min})|. \quad (6.16)$$

We propagated this error through to the electron number and conversion efficiency for each shot. On the other hand, we neglected uncertainties in r , since they were estimated to be below 2 % and uncertainties of the simulated photon number per bin $\frac{N_{\text{ph},i}(E_{\text{bin}})}{\Omega \cdot \text{primary}}$ because they are expected to cancel out when summing up over different bins. The same holds true for the IP response $\eta(E_{\text{bin}})$.

To estimate the influence of uncertainties in the filter thicknesses, we made the following analysis. We randomly selected each filter thickness from a probability distribution given by a Gaussian function centered at the nominal thickness and with a standard deviation of 5 %. With updated filter transmissions (depending on the drawn thicknesses), we repeated fitting 50 keV electrons to the data behind the (nominal) four thickest filters. We carried out the procedure exemplarily for one typical shot (ID 19612) and repeated it 1000 times for this shot. The standard deviation of the thousand corresponding fast electron numbers was only 1.5 %, therefore we neglected uncertainties of filter thicknesses for all shots. We noted that among the 1000 fitting procedures, there were several filter thickness combinations that resulted in $\chi^2_\nu > 1$ even though the fit was much better for the nominal filter thicknesses.

This indicates that such a kind of procedure could also be used to estimate an error of the fast electron energy, since with a different energy $\chi^2_\nu < 1$ might be possible again. However, for the simple monoenergetic model, we did not analyze the error of the electron energy. Another, possibly easier approach for estimating this error would be to simply test which electron energies can fit the data with $\chi^2_\nu < 1$ using the nominal filter thicknesses. To do so, it would be helpful to simulate more electron energies around the fixed energy of 50 keV with small energy spacings, e.g. 1 keV.

The overall findings using all our analyzed HXRD data with the method just described will be presented in chapter 7.

Uncoated Targets

This section deals with the fitting procedure for shots on 10 μm thick bare Cu targets. In that case, the quality of the fit was bad, i.e., $\chi^2_\nu > 1$ for (nearly) all shots on such targets, when fitting the data with monoenergetic electrons of any simulated energy. This outcome was independent of whether all or only the four thickest filters were considered. To improve the fit quality but stay to our model of monoenergetic electrons, we added a further, electron-independent component to the X-ray spectrum. This was an emission line at the energy of He_α photons to account for the strong line emission from highly charged ions that we observed for bare Cu targets (cf. section 6.2.2). FLUKA simulations did not produce any emission from highly charged ions because the simulated target was not heated so that it makes sense to consider this line emission separately. With the fit coefficient d denoting the number of He_α photons per solid angle, we modified $E_{\text{Dep},j}^{\text{sim}}/\Omega$ of Eq. 6.15 to

$$\begin{aligned} \frac{E_{\text{Dep},j}^{\text{sim}}}{\Omega} = & c_i(t = 10 \text{ min}) \sum_{\text{bin}} \frac{N_{\text{ph},i}(E_{\text{bin}})}{\Omega \cdot \text{primary}} \cdot T_j(E_{\text{bin}}) \cdot \eta(E_{\text{bin}}) \cdot E_{\text{bin}} \\ & + d \cdot T_j(E(\text{He}_\alpha)) \cdot \eta(E(\text{He}_\alpha)) \cdot E(\text{He}_\alpha), \end{aligned} \quad (6.17)$$

where $E_{\text{Dep},j}(E(\text{He}_\alpha)) = T_j(E(\text{He}_\alpha)) \cdot \eta(E(\text{He}_\alpha)) \cdot E(\text{He}_\alpha)$ is the energy deposited by a single He_α photon in the IP (see Eq. 6.9). This improved the fit qualities so that $\chi_\nu^2 < 1$ for at least about half the shots on $10 \mu\text{m}$ bare Cu targets when fitting the four thickest filters with monoenergetic 50 keV electrons and the He_α component (and obviously fitting the two coefficients for each shot individually). Seemingly, the photon energies and photon numbers due to line emission from highly charged ions were too high in order not to contribute to the detected signal behind the four thickest filters. It should be noted that the number of degrees of freedom needed to be adjusted in the definition of χ_ν^2 (see Eq. 6.14) when additionally fitting the coefficient d of the He_α component, i.e., $n_{\text{fit}} = 2$.

In Fig. 6.10, the simulated $PSL_j^{\text{sim}}(t = 10 \text{ min})$ corresponding to the best fit with the previously described method is shown along with the data $PSL_j^{\text{data}}(t = 10 \text{ min})$ for a shot on bare Cu (ID 19606). It is presented how the best fit is composed by the PSL due to $E_i = 50 \text{ keV}$ electrons and due to He_α photons. While the He_α photons account for 27 % of the total PSL behind the fourth thickest filter, the proportion is reduced to 1 % for the thickest filter. Therefore, the He_α component does not significantly alter the result concerning the coefficient $c_i(t = 10 \text{ min})$ of the fast electron component.

For the specific shot in Fig. 6.10, it is $\chi_\nu^2 = 2.40$ despite the fit looks quite accurate (for the four thickest filters). It should be noted that the generally higher HXRD signals with uncoated targets result in lower relative uncertainties in the data compared to coated targets, thus enlarging χ_ν^2 for the same relative deviation between the simulated PSL and the data (see Eq. 6.14). In the case of the shown shot, the relative error of the data behind the thickest filter is only 2.3 % which might be an underestimation leading to an overestimation of χ_ν^2 . Furthermore, it might be that only considering transmissions of the filters is a too strong simplification to reproduce the detected PSL within such a small error margin. Regarding Compton scattering, the transmission takes only the cross section of that process into account. This means it is only taken into account that scattering events occur, but the corresponding energy changes and scattering angles cannot be treated in a scalar quantity like the transmission. Typically, as in the case of the XCOM database [82], a scattered photon is considered as attenuated. In Al, the cross section of Compton scattering is already as large as 4.4 % of the cross section of photoabsorption, at a photon energy of 20 keV. Furthermore, the transmission through the thickest filter is $T = 0.55$ at that energy indicating that a more precise treatment

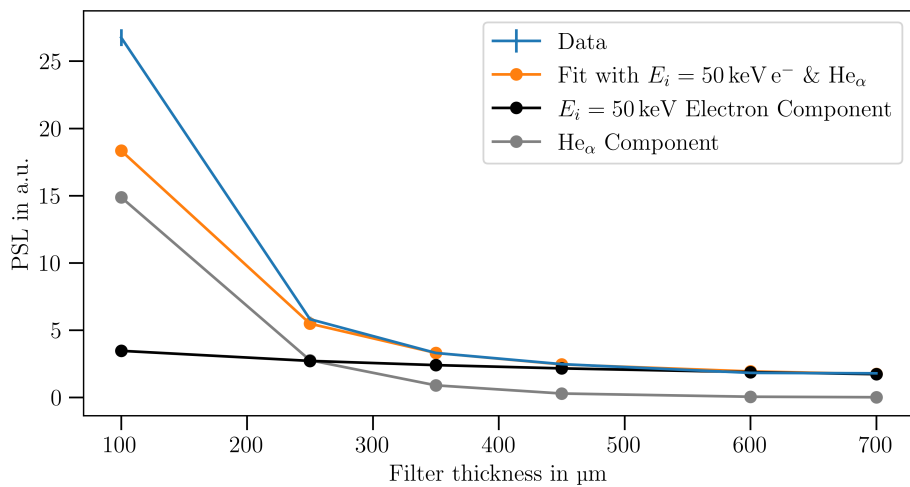


Figure 6.10.: HXRD data of a shot (ID 19606 in PSDB) on $10 \mu\text{m}$ Cu and best fit at $E_i = 50 \text{ keV}$ with an additional He_α component. The total PSL of the fit and those of each component are shown.

of Compton scattering might significantly alter the simulated PSL compared to the data uncertainty. To consider the PSL due to scattered photons, the behavior of the filters would need to be simulated which is time consuming and goes beyond the scope of this master thesis. Nevertheless, we conclude that even though $\chi^2_\nu \gtrsim 1$ for some shots, our model with 50 keV fast electrons and additional Cu He $_\alpha$ photons is suitable to reproduce the HXRD data of uncoated targets.

Fitting this model to each shot on 10 μm bare Cu targets, the coefficients $c_i(t = 0 \text{ min})$ directly denote the number of fast electrons $N^{\text{HXRD}}(\text{e}^-)$ and allow for calculating the conversion efficiencies $E_{\text{Electrons}}^{\text{HXRD}}/E_{\text{Laser}}$ similarly to the analysis of coated targets. Obviously, it is advantageous to use 50 keV electrons for both, coated and uncoated targets, with respect to the comparability of fast electron numbers and conversion efficiencies.

Uncertainties to the electron numbers and conversion efficiencies with uncoated targets were determined similarly to coated targets. However, it should be noted that no determination of $\Delta c_i(t = 10 \text{ min})|_{\chi^2_\nu < 1}$ was possible when the best fit already corresponded to $\chi^2_\nu > 1$. On the other hand, when the best fit corresponded to $\chi^2_\nu < 1$, the determination of χ^2_ν for a value $c_i^{\text{var}}(t = 10 \text{ min})$ additionally involved fitting d , i.e., the He $_\alpha$ component, in order to minimize χ^2_ν for this specific $c_i^{\text{var}}(t = 10 \text{ min})$. The uncertainty in fast electron numbers due to errors of filter thicknesses was exemplarily determined for one shot (ID 19606) to 2.6 % and thus neglected for all shots on 10 μm thick bare Cu targets.

At present, shots on the 12.7 μm Cu targets without coating and on uncoated Mo and Ag targets have not been simulated and not analyzed in terms of their fast electron yield, yet.

6.3.5. Fitting Procedure to Hard X-Ray Detector Data With Temperature Distributed Fast Electrons

In this section, the fitting is described for the model of temperature-distributed fast electrons. This model was applied to coated but not to uncoated targets. For the first, it is of greater importance, since it allows the comparison with the results with coated targets presented in the literature [32, 35, 84]. Typically, there is a single temperature Maxwellian distribution assumed which we also implement for our analysis.

Using a single temperature keeps the number of fit parameters low. More precisely, there are two fitting parameters $n_{\text{fit}} = 2$: the fast electron temperature $T(\text{e}^-)$ and the total fast electron number $N^{\text{HXRD}, \text{T}}(\text{e}^-)$. The latter displays a scaling factor and the temperature, on the other hand, determines the weights of different electron energies E by the continuous distribution (a 3D Maxwellian distribution normalized to one electron)

$$\frac{dN_{e^-}}{dE}(E, T(\text{e}^-)) = \frac{2}{\sqrt{\pi}T(\text{e}^-)^{1.5}} \sqrt{E} e^{-E/T(\text{e}^-)}. \quad (6.18)$$

We discretized this temperature distribution by superimposing electrons of the different simulated energies E_i by different weights f_i . For the electron numbers $c_i(t = 0 \text{ min})$ at energy E_i , this means

$$c_i(t = 0 \text{ min}) = N^{\text{HXRD}, \text{T}}(\text{e}^-) \cdot f_i^T. \quad (6.19)$$

The weights f_i^T are calculated by integrating $\frac{dN_{e^-}}{dE}(E, T(\text{e}^-))$ over an interval of electron energies

$$f_i^T = \int_{E_{i,\text{low}}}^{E_{i,\text{high}}} \frac{dN_{e^-}}{dE}(E, T(\text{e}^-)) dE, \quad (6.20)$$

where the interval $[E_{i,\text{low}}, E_{i,\text{high}}]$ denotes the energies of continuously distributed fast electrons that are assumed to cause the same X-ray emission spectrum as the simulated energy E_i .

To perform a translation to "electron numbers at $t = 10 \text{ min}$ " $c_i(t = 10 \text{ min})$ which are relevant for the fitting procedure (see Eq. 6.11), the translation in Eq. 6.12 is used. We write

$$c_i(t = 10 \text{ min}) = \tilde{N}^{\text{HXRD}, \text{T}}(\text{e}^-) \cdot f_i^T, \quad (6.21)$$

where $\tilde{N}^{\text{HXRD}, \text{T}} = N^{\text{HXRD}, \text{T}}(\text{e}^-) \cdot (A_1 \cdot e^{-10 \text{ min}/\tau_1} + A_2 \cdot e^{-10 \text{ min}/\tau_2})$. To emphasize that the "electron numbers at $t = 10 \text{ min}$ " do not have a physical meaning (cf. section 6.3.4), we use the tilde instead of a time dependence for labeling the total electron number. Inserting Eq. 6.21 into the simulated energy deposition in the IP behind the filters (see Eq. 6.11) yields

$$\frac{E_{\text{Dep},j}^{\text{sim}}}{\Omega} = \sum_i c_i(t = 10 \text{ min}) \frac{E_{\text{Dep},j}(E_i)}{\Omega \cdot \text{primary}} = \sum_i \tilde{N}^{\text{HXRD}, \text{T}}(\text{e}^-) \cdot f_i^T \sum_{\text{bin}} \frac{N_{\text{ph},i}(E_{\text{bin}})}{\Omega \cdot \text{primary}} \cdot T_j(E_{\text{bin}}) \cdot \eta(E_{\text{bin}}) \cdot E_{\text{bin}}. \quad (6.22)$$

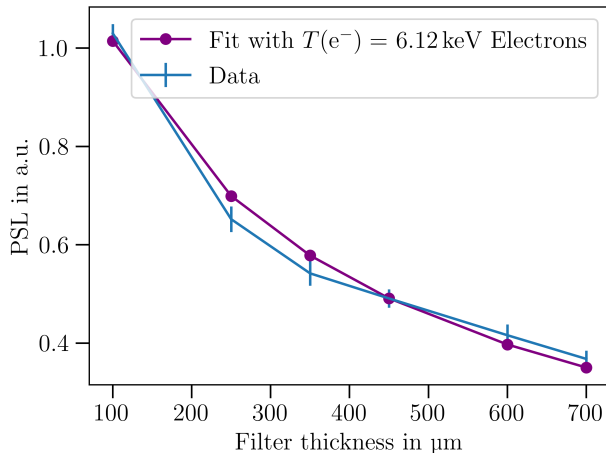
An overview of the intervals $[E_{i,\text{low}}, E_{i,\text{high}}]$ used for each simulated energy E_i is given in Tab. 6.3. Electron energies below 2.5 keV are neglected for calculating the weights f_i^T at $E_i = 5 \text{ keV}$, since all photons with energies below 2.5 keV have transmissions below 10^{-5} even for the thinnest filter. Note that the simulated energies are chosen such that a continuous fast electron energy distribution (see Eq. 6.18) can be efficiently sampled over a large range of electron temperatures, in particular at tens of keV. Thanks to increasing the energy spacing of the simulations with increasing electron energy, it was simultaneously possible to keep the number of necessary simulations and thus the needed overall computation time in a reasonable range. Since we used different bin sizes for the FLUKA simulations below and above 100 keV (cf. section 6.3.2), we post-processed the simulations to a unified bin size of 200 eV for all simulated energies.

The optimization problem with temperature-distributed energies is nonlinear due to the exponential dependence on $T(\text{e}^-)$. At a constant temperature, however, it becomes linear and is easily solvable. Because of that, we varied $T(\text{e}^-)$ over a large range of values in 20 eV steps and minimized χ^2_ν in terms of $N^{\text{HXRD}, \text{T}}(\text{e}^-)$ for each temperature value. Similarly to the case of monoenergetic fast electrons, we first tried to fit the data behind all six filters simultaneously. In Fig. 6.11a, the simulated PSL corresponding to the best fit are shown along with the data for a shot (ID 19612) on coated Cu. At the temperature $T(\text{e}^-) = 6.12 \text{ keV}$ of the best fit, the X-ray spectrum is too hard for reproducing the data behind the thin filters and at the same time too soft for the thick filters. It is $\chi^2_\nu = 1.97 > 1$, but we note that the fit generally represents the data better than when fitting monoenergetic electrons to the data behind all six

Table 6.3.: Simulated electron energies and corresponding integration intervals in order to replicate temperature-distributed fast electrons.

E_i in keV	5	7.5	...	20	25	...	50	60	...	90
$E_{i,\text{low}}$ in keV	2.5	6.25	...	18.75	22.5	...	47.5	55	...	85
$E_{i,\text{high}}$ in keV	6.25	8.75	...	22.5	27.5	...	55	65	...	95
E_i in keV	100	120	...	200	250	300	350			
$E_{i,\text{low}}$ in keV	95	110	...	190	225	275	325			
$E_{i,\text{high}}$ in keV	110	130	...	225	275	325	∞			

(a)



(b)

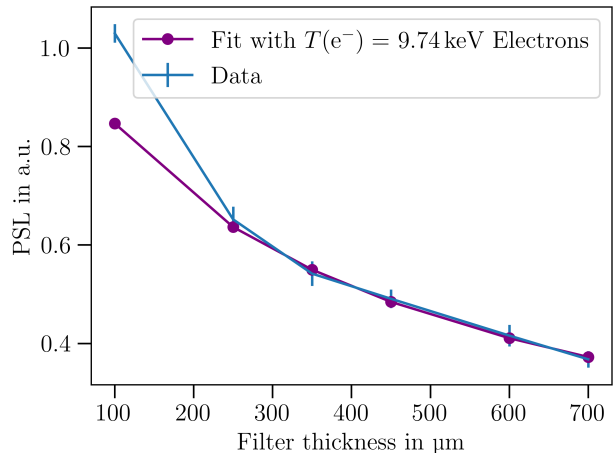


Figure 6.11.: Fitted PSL using temperature distributed fast electrons and data of a shot (ID 19612 in PSDB) on 12.7 μm Cu with 10 μm coating. In (a), the data behind all filters and in (b), the data behind the four thickest filters is fitted.

filters (cf. section 6.3.4 and see Fig. 6.9a for comparison). This is due to the fact that electrons at different energies are superimposed within the temperature model. Electrons at low energies enhance the simulated signal behind the thinner filters while the signal behind the thicker filters is nearly not altered, since the energy of a produced photon is limited by the energy of the electron.

However, in order to increase the fit quality, to make sure that the influence of thermal X-ray emission is reduced and for better comparability to the monoenergetic model, we dropped the two thinnest filters for the fitting procedure and only fitted the data behind the four thickest filters with temperature distributed fast electrons. The best fit with $\chi^2_\nu = 0.175 < 1$ and $T(\text{e}^-) = 9.74 \text{ keV}$ for the same shot as previously (ID 19612) is shown in Fig. 6.11b along with the data. Compared to when all six filters were fitted, the electron temperature increased corresponding to a harder X-ray spectrum. Similarly to the monoenergetic model, the number of degrees of freedom needed to be adjusted in the definition of χ^2_ν (see Eq. 6.14) when reducing the number of fitted data points.

In contrast to the electron energy in the monoenergetic model, we determined an error of the fast electron temperature. This is easily possible because we varied the electron temperature over a large range of values during the fitting procedure. Generally speaking, all combinations of $T(\text{e}^-)$ and $N^{\text{HXRD}}, T(\text{e}^-)$ with $\chi^2_\nu < 1$ are good fits and thus determine the uncertainty of these parameters within the uncertainty of our data. This means that the values of $T(\text{e}^-)$ where $N^{\text{HXRD}}, T(\text{e}^-)$ can be optimized in order to get $\chi^2_\nu < 1$ determine the temperature uncertainty interval. Since at different temperatures, different electron numbers correspond to $\chi^2_\nu < 1$, the temperature uncertainty also results in an error to the fast electron number. Such a behavior was not taken into account in the monoenergetic model and Fig. 6.12 helps to assess the impact of this new consideration. In Fig. 6.12, χ^2_ν is calculated for various combinations of $T(\text{e}^-)$ and $N^{\text{HXRD}}, T(\text{e}^-)$. The best fit with smallest χ^2_ν is marked with a red cross and all combinations with $\chi^2_\nu < 1$ are colored white for simplicity. We can see that the fast electron temperature uncertainty interval ranges from $T(\text{e}^-) = 6.96 \text{ keV}$ to $T(\text{e}^-) = 15.46 \text{ keV}$. On the other hand, the uncertainty interval of $N^{\text{HXRD}}, T(\text{e}^-)$ (defined by the values where $T(\text{e}^-)$ can be optimized to get $\chi^2_\nu < 1$) ranges from $N^{\text{HXRD}}, T(\text{e}^-) = 1.25 \cdot 10^{13}$ to $N^{\text{HXRD}}, T(\text{e}^-) = 2.41 \cdot 10^{14}$. This spans more than one order of magnitude due to the fact that different

temperatures are considered. In comparison, the uncertainty of $N^{\text{HXRD}, T}(e^-)$ at a fixed temperature, i.e., the range of values of $N^{\text{HXRD}, T}(e^-)$ with $\chi_\nu^2 < 1$ at a fixed temperature, is much smaller. The latter was the only fit uncertainty taken into account for the monoenergetic model (see Eq. 6.16) and thus we expect the errors in fast electron numbers to be much higher when we use the temperature model and consider the influence of the temperature uncertainty. In that case, further uncertainties to the electron number, such as the systematic error due to Δa and the rescaling from $t = 10 \text{ min}$ to $t = 0 \text{ min}$ (cf. section 6.3.4) are negligible.

There is an intuitive reason why the fast electron number is so sensitive on the fast electron temperature. An increase of the latter results in a harder bremsstrahlung emission. Photon energies around $E_{\text{ph}} = 10 \text{ keV}$ are just at the onset of X-ray transmission through the fourth thickest filter. The transmission increases strongly with photon energy from $T(E_{\text{ph}} = 10 \text{ keV}) \approx 0.1$ to $T(E_{\text{ph}} = 15 \text{ keV}) \approx 0.5$. Therefore, changing the electron temperature significantly alters how many photons and thus electrons are necessary to reproduce the HXRD signal. The dependence gets weaker for higher temperatures, as can be seen in Fig. 6.12.

From the fast electron number and temperature of the best fit, we calculated the conversion efficiency $E_{\text{Electrons}}^{\text{HXRD}, T}/E_{\text{Laser}}$ from laser energy into fast electrons, where $E_{\text{Electrons}}^{\text{HXRD}, T} = N^{\text{HXRD}, T}(e^-) \cdot \langle E \rangle = N^{\text{HXRD}, T}(e^-) \cdot 1.5k_B T(e^-)$. Furthermore, we estimated the error of the conversion efficiency. Since the electron number and temperature depend on each other, their uncertainties cannot be treated separately. Instead, the error of $E_{\text{Electrons}}^{\text{HXRD}, T}/E_{\text{Laser}}$ is given by the obtained range of values $E_{\text{Electrons}}^{\text{HXRD}, T}/E_{\text{Laser}}$ when inserting all combinations ($T(e^-)$, $N^{\text{HXRD}, T}(e^-)$) with $\chi_\nu^2 < 1$. It should be mentioned that the uncertainties of electron number and temperature are generally asymmetric around the best fit and therefore the same holds true for the conversion efficiency.

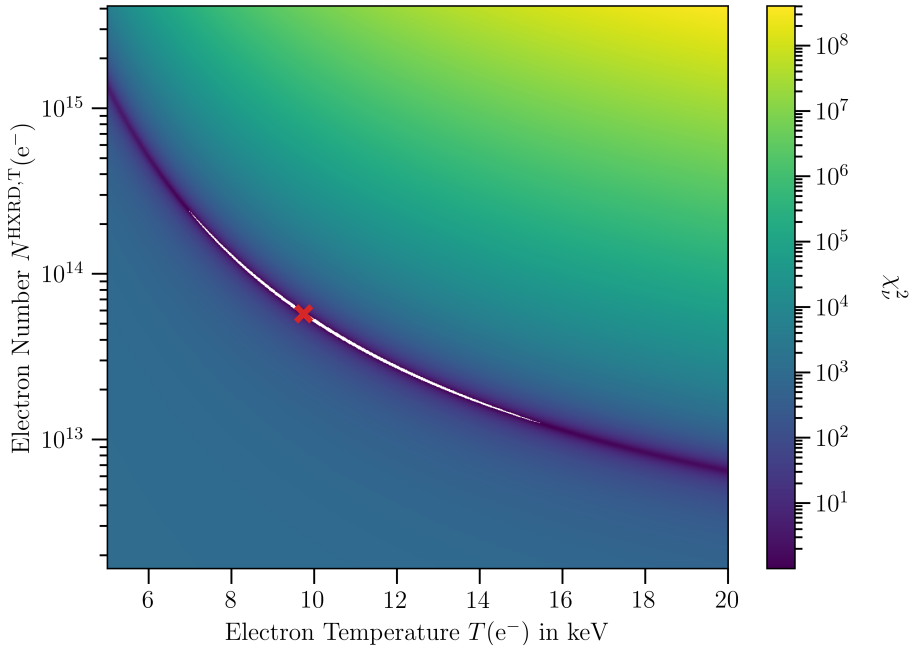


Figure 6.12.: Reduced chi-square map for a shot (ID 19612) on $12.7 \mu\text{m}$ Cu with $10 \mu\text{m}$ fitting temperature distributed fast electrons to the four thickest filters. All combinations of $T(e^-)$ and $N^{\text{HXRD}, T}(e^-)$ with $\chi_\nu^2 < 1$ are plotted in white for better illustration. The best fit combination is marked with a red cross.

We carried out the procedure described above for all shots on Cu targets with the 10 µm coating and on coated Mo/Ag. For each shot, an individual fast electron temperature and error were fitted. This, in turn, influences the results concerning electron numbers and conversion efficiencies from shot to shot differently.

For a better comparison between different shots independent of the temperature variation, we additionally fixed the fast electron temperature T^{fix} for all shots on coated targets and without considering a temperature error. This is similar to the monoenergetic model (cf. section 6.3.4), but now for temperature-distributed fast electrons and not discrete electron energies. For shots at the best focus setting and with the phase plate, we fixed the temperature to $T(e^-) = 10 \text{ keV}$ which turned out to be in the uncertainty range of nearly all shots on coated targets (cf. sections 7.1.6 and 7.2.4).

In the case of a fixed temperature, the systematic uncertainties due to the rescaling from $t = 10 \text{ min}$ to $t = 0 \text{ min}$ and in Δa , which add up to $\sim 10\%$, are relevant uncertainties for the fitted fast electron numbers $N^{\text{HXRD}, T^{\text{fix}}}(e^-)$ and calculated conversion efficiencies $E_{\text{Electrons}}^{\text{HXRD}, T^{\text{fix}}} / E_{\text{Laser}}$. Furthermore, the fit uncertainty of the electron number needs to be considered. For each shot, it is given by how far the electron number can be varied at the fixed temperature under the condition that $\chi_\nu^2 < 1$ still holds. In the definition of χ_ν^2 , it is most convenient to still use $n_{\text{fit}} = 2$ in order to keep the fit quality at T^{fix} equal to the temperature fitting procedure. Other errors to the electron number and conversion efficiency are neglected, similarly to section 6.3.4.

We end this section by pointing out that both the monoenergetic and temperature distributed fast electron model fit the HXRD data well. Therefore, in terms of this aspect, they are equally valid although the energy of the first model was fixed to $E_i = 50 \text{ keV}$ and the latter model suggests temperatures which are in agreement with $T(e^-) = 10 \text{ keV}$. The implications of the different models on the overall findings concerning electron numbers and conversion efficiencies are discussed in chapter 7.

6.3.6. Calculation of Fast Electron Number From Highly Oriented Pyrolytic Graphite Spectrometer Data

In this section, I describe how we scaled the fast electron number using the HOPG spectrometer data, i.e., $N(K_\alpha)$ (cf. section 6.2.3) for both monoenergetic and temperature distributed fast electrons. It should be noted that the HOPG spectrometer data does not allow for determining the fast electron energies/temperatures. Because of that, we based our analysis upon the results that we had obtained from the HXRD data (cf. sections 6.3.4 and 6.3.5).

For each simulated electron energy and target type (cf. section 6.3.2), we calculated the number of K_α photons per solid angle and primary fast electron $\frac{N_{\text{ph}}^i(E^{\text{ph}}(K_\alpha))}{\Omega \cdot \text{primary}}$ from the simulated X-ray spectrum. We scaled the number of fast electrons so that the simulated K_α yield matched the detected HOPG spectrometer data. The procedure is explained first for monoenergetic electrons and afterwards generalized to temperature distributed ones.

In the case of monoenergetic fast electrons, the K_α photon number of only one simulated energy, namely $E_i = 50 \text{ keV}$, is relevant for each target type. The number of fast electrons $N^{\text{HOPG}}(e^-)$ matching the HOPG spectrometer data $N(K_\alpha)$ can then be calculated by

$$\frac{N(K_\alpha)}{4\pi} = N^{\text{HOPG}}(e^-) \frac{N_{\text{ph}}^i(E^{\text{ph}}(K_\alpha))}{\Omega \cdot \text{primary}} \Leftrightarrow N^{\text{HOPG}}(e^-) = \frac{N(K_\alpha)}{4\pi \cdot \frac{N_{\text{ph}}^i(E^{\text{ph}}(K_\alpha))}{\Omega \cdot \text{primary}}}, \quad (6.23)$$

where we converted $N(K_\alpha)$ into photons per solid angle by the factor 4π . For calculating the error $\Delta N^{\text{HOPG}}(e^-)$, we considered the error $\Delta N(K_\alpha)$ (cf. section 6.2.3) and the uncertainty of K_α photon numbers in the simulated FLUKA spectra. It should be noted that Eq. 6.23 only results in a rescaling of $N(K_\alpha)$ for shots on the same target type, since the same fast electron energy and thus the same simulated X-ray spectra were used. From the fast electron numbers obtained with the HOPG data, we furthermore calculated the conversion efficiency $E_{\text{Electrons}}^{\text{HOPG}}/E_{\text{Laser}}$ from laser energy into monoenergetic fast electrons, where $E_{\text{Electrons}}^{\text{HOPG}} = E(e^-) \cdot N^{\text{HOPG}}(e^-)$ with $E(e^-) = 50 \text{ keV}$.

In the case of temperature distributed fast electrons, Eq. 6.23 needs to be modified by superimposing the simulated K_α photon numbers of different electron energies. To do that, the weights f_i^T given by Eq. 6.20 are used. It follows

$$N^{\text{HOPG}, T}(e^-) = \frac{N(K_\alpha)}{4\pi \cdot \sum_i f_i^T \frac{N_{\text{ph}}^i(E^{\text{ph}}(K_\alpha))}{\Omega \cdot \text{primary}}}. \quad (6.24)$$

From the number of temperature distributed electrons, we also calculated the conversion efficiency $E_{\text{Electrons}}^{\text{HOPG}, T}/E_{\text{Laser}}$, where $E_{\text{Electrons}}^{\text{HOPG}, T} = N^{\text{HOPG}, T}(e^-) \cdot 1.5k_B T(e^-)$.

The scaling with the HOPG data and temperature distributed fast electrons was carried out for all shots on coated targets. Let us first consider the case where Eq. 6.24 is applied to the shot dependent temperatures and corresponding uncertainties from the electron fit to the HXRD data (cf. section 6.3.5). This is not only a rescaling of $N(K_\alpha)$ anymore, since the temperature varies between different shots. Furthermore, the temperature uncertainty is an additional uncertainty compared to the case of monoenergetic electrons and propagated through to $N^{\text{HOPG}, T}(e^-)$ by inserting all temperatures that allowed for $\chi_\nu^2 < 1$. In Fig. 6.13, the resulting fast electron numbers are shown for an exemplary shot (ID 19612). The temperature interval corresponding to $\chi_\nu^2 < 1$ between $T(e^-) = 6.96 \text{ keV}$ and $T(e^-) = 15.46 \text{ keV}$ yields $N^{\text{HOPG}, T}(e^-) = 1.78 \cdot 10^{15}$ to $N^{\text{HOPG}, T}(e^-) = 1.51 \cdot 10^{14}$. Similarly to scaling with the HXRD data (cf. section 6.3.5), the electron number depends strongly on the temperature. For the considered example, this is intuitively understandable because the temperatures and thus the energies of most electrons are just around the K-shell ionization energy. Therefore, an increase in temperature increases the efficiency of K_α production. Due to the large uncertainty of one order of magnitude in $N^{\text{HOPG}, T}(e^-)$, the uncertainty $\Delta N(K_\alpha)$ and the uncertainty of the simulated K_α photon numbers can be neglected when considering the temperature error.

The uncertainty of $E_{\text{Electrons}}^{\text{HOPG}, T}/E_{\text{Laser}}$ was, in turn, calculated by inserting all tuples $(T(e^-), N^{\text{HOPG}, T}(e^-))$ for temperatures with $\chi_\nu^2 < 1$. Similar to section 6.3.5, the uncertainty of the conversion efficiency is generally asymmetric around the value obtained with the temperature corresponding to the best HXRD fit.

In order to better compare the conversion efficiencies between different shots despite the large temperature uncertainty, we additionally fixed the fast electron temperature to one value for all shots on coated targets similar to the HXRD analysis (cf. section 6.3.5). In that case, the uncertainty of the electron number and thus conversion efficiency is calculated from the error $\Delta N(K_\alpha)$ and the uncertainty in K_α photon numbers from the simulated FLUKA spectra. For each target type, the electron numbers are simply a rescaling of the detected K_α photon numbers $N(K_\alpha)$ when fixing the temperature, similar to the case of monoenergetic fast electrons.

We have applied these data analysis procedures on the data collected during our experiment. The outcome is presented and discussed in chapter 7.

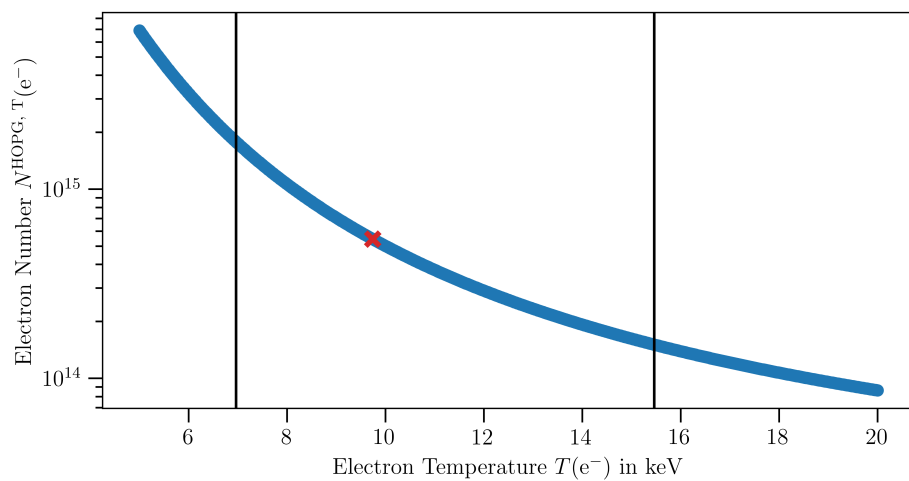


Figure 6.13.: Fast electron number inferred from the HOPG data for a shot (ID 19612) on 12.7 μm Cu with 10 μm C_3H_6 coating. The fast electron temperature interval corresponding to $\chi^2_\nu < 1$ in the temperature fit to the four thickest filters is marked by vertical lines. The electron number at the best HXRD fit temperature is marked with a red cross.

7. Results and Discussion

In this chapter, I present and discuss the results of our analysis. The discussion is based on my trains of thoughts, some of which evolved from conversations within the group, in particular with Paul Neumayer, Zsuzsanna Major and Vincent Bagnoud. In section 7.1, only shots at best focus, i.e., without phase plate, are considered. Section 7.2 is about our results for shots using the phase plate.

7.1. Shots at Best Focus

In section 7.1.1, I show our findings about the TPD strength of bare and coated targets and analyze the convective TPD gain for coated ones. I compare TPD strength with K_α yield in section 7.1.2, and K_α yields in dependence of the two different coating thicknesses and of the different metal materials in sections 7.1.3 and 7.1.4, respectively. In section 7.1.5, our results regarding the fast electron conversion efficiency with the monoenergetic model are presented. Sections 7.1.6 and 7.1.7 are about our results concerning the fast electron temperature fitted to each shot individually and the conversion efficiencies from the temperature model. The relation between K_α yield and fast electron conversion efficiency is analyzed in section 7.1.8. Finally, potential improvements for the HXRD design are discussed in section 7.1.9.

7.1.1. Two-Plasmon Decay Strength and Convective Gain

Our results regarding TPD strength are important to verify if TPD was enhanced by our coated target design. In Fig. 7.1, the normalized TPD strength S is shown against the laser intensity I . The uncertainties of the TPD strength are below 10% and the error bars are thus contained in the data points. The intensity of a shot was obtained by scaling the laser energy at $\lambda_{\text{vac}} = 527 \text{ nm}$, whose measurement is provided by the PHELIX infrastructure, according to a calibration (see appendix A). This method causes some statistical error in the inferred intensity. First, there are uncertainties in the measured laser energy. Second, there are shot-to-shot variations in the wavefront of the laser pulse resulting in different intensity distributions at the focal position for a given energy. Since the focal intensity distribution cannot be measured on-shot at the target position, there is no shot-dependent correction of the calibrated intensity possible. The overall effects on the relative statistical error of the calibrated intensity are estimated to be around 10%, based on experience.

The data in Fig. 7.1 is divided into shots on coated and uncoated targets, respectively. No further distinction between different target types is made because we did not observe any dependency of S on the metal material or coating thickness. In the case of coated targets, this is explained by the fact that TPD only occurs in the underdense C_3H_6 plasma. In the case of uncoated targets, two considerations may explain the similarity between the different materials.

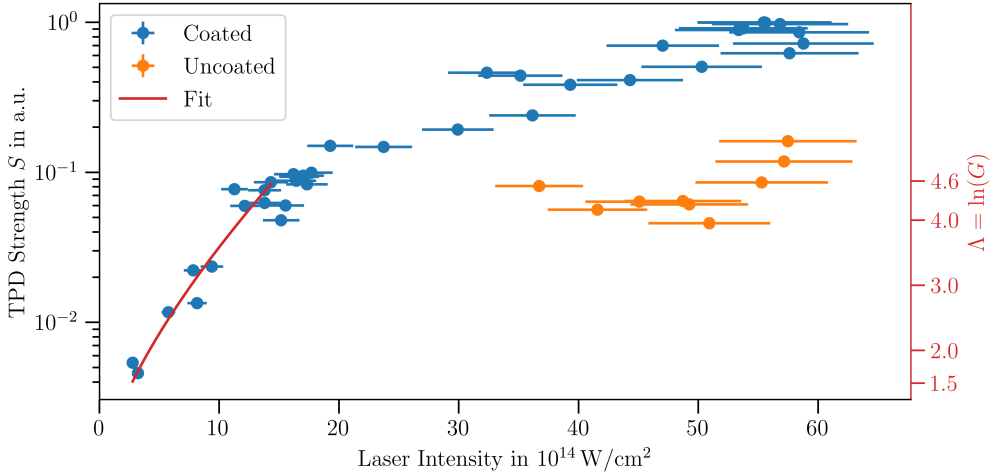


Figure 7.1.: TPD strength in dependence of laser intensity for shots on coated and uncoated targets in the best focus setting up to a maximum laser energy of 199.2 J. A fit to the data at $I \leq 15 \cdot 10^{14} \text{ W cm}^{-2}$ is included and the values of the natural logarithm of the TPD gain $\Lambda = \ln(G)$ corresponding to the fit are indicated.

First, their mean ion charge states do not vary too much at $T_e = 1 \text{ keV}$ and $n_e = 1 \cdot 10^{21} \text{ cm}^{-3}$ (Cu: $Z_i = 23$; Mo: $Z_i = 30$; Ag: $Z_i = 31$; simulated with FLYCHK [73]), therefore the effect of collisional damping is comparable (cf. sections 4.2 and 5.2). Second, the ion charge to mass ratios are nearly equal (Cu: $Z_i/M = 0.36 \text{ u}^{-1}$; Mo: $Z_i/M = 0.31 \text{ u}^{-1}$; Ag: $Z_i/M = 0.29 \text{ u}^{-1}$) and the scale length is thus not expected to change much between the different materials (cf. section 5.2).

Comparing coated and uncoated targets leads to the expected conclusion that S , i.e., TPD, is stronger for coated targets, by up to one order of magnitude. This proves the coated targets to be suitable to enhance TPD and confirms our experimental approach for the optimization of TPD (cf. section 5.2).

With coated targets, we performed shots over a large range of different intensities to better understand how TPD depends on I . We observed a strong increase of TPD with laser intensity I which is due to the fact that the convective TPD gain G increases exponentially with intensity (see Eq. 4.98). Most precisely the intensity at quarter critical density would be considered for the TPD gain G in Eq. 4.98, but due to the fact that this quantity is not easily measurable, we consider the *vacuum* laser intensity I as first approximation here. From Fig. 7.1, we can infer some qualitative findings about the TPD regimes at different intensities I . We can see that the laser intensity is above the TPD threshold, even at low intensities of $I \approx 3 \cdot 10^{14} \text{ W cm}^{-2}$, because of the strong increase of S . On the other hand, the flattening of S above $I \approx 15 \cdot 10^{14} \text{ W cm}^{-2}$ can be attributed to saturation effects.

In the unsaturated regime of S , i.e., below $I \approx 15 \cdot 10^{14} \text{ W cm}^{-2}$, the measured TPD strength of different shots allows to estimate the convective TPD gain as follows.

Provided that saturation effects play a minor role, we assume the TPD strength to be proportional to the convective TPD gain G and therefore write $S = A \cdot G$, where A is an unknown proportionality constant. The reader should be reminded that the convective TPD gain (see Eq. 4.98) reads $G \sim \exp(\Lambda)$ with $\Lambda = C \frac{IL}{k_B T_e}$ and the constant $C = \frac{\sqrt{0.75} e^2 \lambda_{\text{vac}}}{24 m_e c^3}$. We have not measured or systematically simulated L and T_e so that we consider the two quantities as intensity dependent. From the Samir model [72] (cf. section 5.2), it

follows $L \propto c_s \propto \sqrt{T_e}$. Furthermore, we insert the analytical dependence $T_e \propto I_{\text{abs}}^{2/3}$ (see Eq. 3.2), assuming $I_{\text{abs}} \propto I$ and thus $T_e \propto I^{2/3}$. Altogether, it follows

$$S = A \cdot G \sim A \cdot \exp(\Lambda) \quad \text{with} \quad \Lambda = C' I^{2/3}, \quad (7.1)$$

where C' is another proportionality constant. Note that the value of C' is not only determined by natural and fixed experimental constants, but is actually dependent on the time t , the ion charge to mass ratio Z_i/M (both in L), the flux limiter f and the ratio of absorbed laser intensity (both in T_e). However, we do not allow the proportionality constant C' to vary between the different fitted shots. Furthermore, note that the proportionality constant C' allows the value of C to vary from that in Eq. 4.98.

In addition, it should be mentioned that different physical properties and processes influence the quantity A : the relation between the gain G and the amplitudes of EPWs, the conversion of EPWs to $3/2 \omega_0$ emission, the collection efficiency and calibration of our streak camera setup. In particular, the streak camera setup collects the $3/2 \omega_0$ radiation only under a certain angle. In contrast to that, the angles of maximum TPD growth rate (cf. section 4.5.1) and smallest damping coefficient (cf. section 4.7.2) are dependent on plasma parameters such as the electron density, indicating a possible shot-to-shot dependence of A . For the presented analysis such a dependence is not considered.

Eq. 7.1 was fitted to the TPD strength in the unsaturated regime, i.e., to the data for $I \leq 15 \cdot 10^{14} \text{ W cm}^{-2}$. The fitting procedure was based on minimizing the mean squared difference between the fit and the data, weighting the difference to each data point by the inverse of the signal strength S . In Fig. 7.1, the best fit with the parameters $C' = 0.77 \cdot (10^{14} \text{ W cm}^{-2})^{-2/3}$ and $\log(A) = -3.06$ is included. It should be noted that the fit agrees well with the data, considering the intensity uncertainty, even though we only used analytical dependencies from simple models to estimate $\frac{IL}{k_B T_e} \propto I^{2/3}$. From the best fit parameter $C' = 0.77 \cdot (10^{14} \text{ W cm}^{-2})^{-2/3}$, the convective TPD gain $G \sim \exp(\Lambda)$ and $\Lambda = C' I^{2/3}$ are obtained. In Fig. 7.1, the resulting values of Λ are shown by an additional ordinate. The Λ -axis is related to the axis of TPD strength, since Λ is linear to $\log(S)$. The minimum and maximum values obtained for the fitted intensity range are $\Lambda_{\min} = 1.5$ and $\Lambda_{\max} = 4.6$. Note that the obtained values of Λ are given by the fit such that the described relation between the Λ - and S -axis is only valid for TPD strengths in the fitted, i.e., unsaturated, regime corresponding to $1.5 \leq \Lambda \leq 4.6$.

To better assess the quantitative values of Λ , we carry out a comparison with the study of Froula *et al.* [35]. While the experimental setup of Froula *et al.* differs from our best focus setting in many aspects, e.g., by the usage of multiple laser beams with phase plates, a comparison between the values of Λ at which saturation sets in is nevertheless instructive. Froula *et al.* simulated the scale length, thermal electron temperature and overlapped intensity I_q at quarter critical density for their experimental conditions. They experimentally investigated the fast electron conversion efficiency and their data shows a saturation behavior starting from $I_q L/T_e = 300 \cdot 10^{14} \text{ W } \mu\text{m} \text{ cm}^{-2} \text{ keV}^{-1}$, corresponding to intensities above $I = 3 \cdot 10^{14} \text{ W cm}^{-2}$. For a comparison with our work, we assume that the saturation in fast electron conversion efficiency coincides with a saturation in TPD strength. Using the wavelength $\lambda_{\text{vac}} = 0.35 \mu\text{m}$ of Froula *et al.* and Eq. 4.98, it follows that $\Lambda \approx 2.8$ when saturation sets in in their case. This value is smaller than our value $\Lambda_{\max} = 4.6$ at the onset of saturation ($I \approx 15 \cdot 10^{14} \text{ W cm}^{-2}$). However, the deviation is only by a factor of 1.6 which can be considered as small because only two onsets of saturation are compared without knowing the reasons for each saturation. Furthermore, there are methodical differences regarding the calculation of the two values of Λ as discussed in the following.

The value $\Lambda \approx 2.8$ was calculated with Eq. 4.98 for the convective TPD gain from $I_q L/T_e = 300 \cdot 10^{14} \text{ W } \mu\text{m} \text{ cm}^{-2} \text{ keV}^{-1}$ which Froula *et al.* obtained from hydro simulations. On the contrary, we used

the intensity dependent signal of the TPD strength for our analysis and implicitly allowed the proportionality factor C in $\Lambda = C \frac{IL}{k_B T_e}$ to vary from that in Eq. 4.98. Roughly estimating the expected Λ with Eq. 4.98 for our parameters yields $\Lambda \approx 5.2$ for the exemplary values $I = 15 \cdot 10^{14} \text{ W cm}^{-2}$, $L = 25 \mu\text{m}$ (laser spot size as first approximation; see appendix A for calculation of spot size) and $T_e = 1 \text{ keV}$. This is still very close to the value $\Lambda_{\max} = 4.6$ but very sensitive to the assumed values.

Altogether, our analysis suggests that our TPD gain at the onset of saturation is comparable to or possibly slightly larger than the value obtained from the study of Froula *et al.* at their onset of saturation. Concerning this comparison, it must be taken into account that Froula *et al.* used phase plates producing a much larger laser spot and potentially longer scale lengths than our best focus setting. In their case, TPD occurs over a larger area and involves more EPWs. Therefore, our gain comparable to the value of Froula *et al.* does not necessarily lead to a comparable large amount of energy in EPWs and fast electrons.

As part of future work, the presented fit to our data in the unsaturated regime needs to be investigated in more detail. In particular, uncertainties to the fit parameters must be determined and the exponent $\beta = 2/3$ of the dependence $\frac{IL}{k_B T_e} \propto I^\beta$ should be generalized to a fit parameter. For example, Froula *et al.* obtained $\beta = 0.85$ from their simulations. As further extension of the presented analysis, hydro simulations need to be carried out for our experimental parameters in order to estimate L , T_e and the intensity at quarter critical density. The simulation results can be used for both, estimating β and calculating the TPD gain with Eq. 4.98, similarly to the study of Froula *et al.* In particular, the obtained TPD gain needs to be compared to the value of Froula *et al.* and the differences between the two methods for the calculation of the TPD gain need to be investigated. Since T_e and L depend on expansion effects, it is necessary to carry out simulations at least in 2D.

For a potentially following experiment on TPD, I suggest to measure the scale length and thermal electron temperature on shot, in order to estimate Λ more precisely when using Eq. 4.98. Furthermore, the intensity scaling with β could also be inferred directly from the experimental data. If the on-shot intensity could be determined with better accuracy, shot-to-shot variations could be partly removed and the precision of our analysis could be increased, as well. To end this section, it should be emphasized that the data from our experiment proves the suitability of our coated target design to enhance TPD despite the issues regarding the determination of the TPD gain.

7.1.2. Comparison of K_α Yield and Two-Plasmon Decay Strength

One goal of our experiment was to optimize TPD using coated targets in order to increase the line emission yield. In coated targets, K_α emission from the cold substrate material, caused by fast electrons, is the relevant line emission process. Therefore, I will compare K_α photon numbers with TPD strength for the coated targets. Concerning uncoated targets, we additionally observed line emission from highly charged ions in the case of Cu, but no separate lines due to highly charged ions were detected in the case of Mo or Ag. Therefore and to investigate the line emission caused by fast electrons in uncoated targets (cf. section 6.2.2), I will also consider the K_α emission of these targets. A comparison to the corresponding TPD strength will be carried out, as well. Furthermore, I will show which K_α conversion efficiencies we were able to reach during our experiment for both, coated and uncoated targets.

In the case of coated targets, we can observe a similar behavior of S and $N(K_\alpha)$ (see Fig. 7.2 compared to 7.1). Qualitatively, both quantities S and $N(K_\alpha)$, increase with intensity. Quantitatively, the photon number increased from $N(K_\alpha) = (1.66 \pm 0.36) \cdot 10^7$ for a shot at $I = 2.77 \cdot 10^{14} \text{ W cm}^{-2}$ (ID 19691)

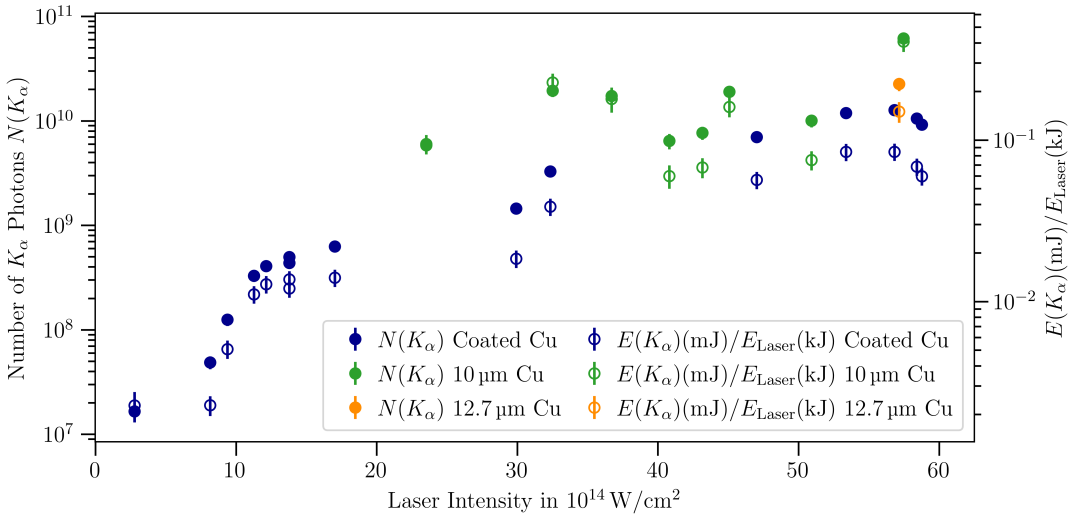


Figure 7.2.: K_α line emission strength for $12.7\text{ }\mu\text{m}$ Cu with $10\text{ }\mu\text{m}$ coating and uncoated Cu targets with $12.7\text{ }\mu\text{m}$ and $10\text{ }\mu\text{m}$ thicknesses. Intensity uncertainties are not shown for better visualization.

to $N(K_\alpha) = (1.27 \pm 0.16) \cdot 10^{10}$ for a shot at $I = 56.8 \cdot 10^{14} \text{ W cm}^{-2}$ (ID 19612). This corresponds to an increase of $N(K_\alpha)$ by a factor of 770 ± 200 . On the other hand, the TPD strength increased from $S = 0.00538 \pm 0.00032$ to 0.973 ± 0.013 for the same shots which corresponds to a factor of 181 ± 12 . While in both cases, this constitutes an increase by two orders of magnitude, a discrepancy of a factor of 4.3 ± 1.2 remains. A possible explanation is that the two quantities are not directly comparable, but additional effects must be considered. In particular, it is not obvious if the two quantities are expected to scale linearly with each other. One additional effect might be a potential increase of the TPD fast electron temperature with laser intensity [32, 35] which would result in an additional enhancement of $N(K_\alpha)$. However, our fast electron analysis does not indicate such a behavior as we will see in section 7.1.6.

Taking a closer look at the shape of the curves $N(K_\alpha)$ and S (see Figs. 7.2 and 7.1), we can find the saturation observed for TPD strength again in $N(K_\alpha)$ by a flattening above $I \approx 15 \cdot 10^{14} \text{ W cm}^{-2}$. All in all, the qualitative similarities between the curves of $N(K_\alpha)$ and S are a strong indication that the increase of $N(K_\alpha)$ is caused by fast electrons from TPD. Here, the comparison was exemplarily made for $12.7\text{ }\mu\text{m}$ Cu coated with $10\text{ }\mu\text{m}$ C_3H_6 , since the K_α yield of different target types will be discussed in sections 7.1.3 and 7.1.4.

Let us now look at the results for uncoated targets. In those targets, K_α emission is caused by fast electrons (cf. section 6.2.2). So, we can use $N(K_\alpha)$ as indication on how many fast electrons were produced. In Fig. 7.2, the results are shown for uncoated Cu of $12.7\text{ }\mu\text{m}$ and $10\text{ }\mu\text{m}$ thicknesses. We can observe that $N(K_\alpha)$ is larger than for coated targets. From the shot (ID 19612, $I = 56.8 \cdot 10^{14} \text{ W cm}^{-2}$) with maximum yield for coated targets to the shot (ID 19630, $I = 57.5 \cdot 10^{14} \text{ W cm}^{-2}$) with maximum yield for uncoated targets, the K_α photon number increased by a factor of 4.85 ± 0.91 . This behavior is very opposite to our observations for TPD strength S (see Fig. 7.1), where we observed enhanced TPD for coated targets. It indicates that other effects than TPD producing fast electrons play an important role in the case of uncoated targets and overcome the lack of fast electrons from weaker TPD. Possible effects include resonance absorption or stimulated Raman scattering which is in competition with TPD [67].

Nevertheless, we had expected $N(K_\alpha)$ to be higher for coated targets compared to uncoated ones. However, our maximum K_α conversion efficiency achieved with a coated target is only $\frac{E(K_\alpha)(\text{mJ})}{E_{\text{Laser}}(\text{kJ})} = 0.085 \pm 0.011$ (ID

19612, $I = 56.8 \cdot 10^{14} \text{ W cm}^{-2}$). This is two orders of magnitude below the maximum value $\frac{E(K_\alpha)(\text{mJ})}{E_{\text{Laser}}(\text{kJ})} \gtrsim 10$ reported by Yaakobi *et al.* [32] for coated Mo targets. The deviation is so large that $N(K_\alpha)$ of coated targets was not enhanced compared to uncoated ones in our experiment. Note that our coated Cu targets were compared with coated Mo targets used by Yaakobi *et al.* However, we do not expect the usage of Cu instead of Mo to be a reason for decreasing K_α conversion efficiency as shown in section 7.1.4. An explanation for the lower K_α conversion efficiency in our case is given in sections 7.1.6 and 7.1.8.

7.1.3. Comparison of K_α Yields for Different Coating Thicknesses

In order to optimize K_α production during our experiment, we tested two different coating thicknesses (cf. section 5.2) which are compared in this section. We make the comparison for K_α yields and not TPD strengths, since TPD was only a means to enhance line emission. Furthermore, more effects are involved when comparing K_α yields due to the fact that TPD occurs first and K_α emission is then produced by TPD fast electrons which, e.g., need to penetrate the coatings of different thicknesses.

In Fig. 7.3, the K_α emission strength is plotted for Cu targets with $10 \mu\text{m}$ and $25 \mu\text{m}$ thick coatings, respectively. At high intensities $I > 45 \cdot 10^{14} \text{ W cm}^{-2}$, the conversion efficiency with the thick coating is below that with the thin coating. A possible explanation for a smaller K_α conversion efficiency with the thicker coating is the stronger absorption of electrons in the plastic layer. However, this effect is not expected to increase with intensity.

For a quantitative analysis, we compare the shots with maximum conversion efficiency for the $25 \mu\text{m}$ coating (ID 19608, $I = 49.3 \text{ W cm}^{-2}$) and for the $10 \mu\text{m}$ coating (ID 19612, $I = 56.8 \text{ W cm}^{-2}$). The second has $\frac{E(K_\alpha)(\text{mJ})}{E_{\text{Laser}}(\text{kJ})} = 0.085 \pm 0.011$ (cf. section 7.1.2), whereas the first has $\frac{E(K_\alpha)(\text{mJ})}{E_{\text{Laser}}(\text{kJ})} = 0.052 \pm 0.007$. This represents a deviation by only a factor of 1.63 ± 0.51 such that the two values nearly coincide within their uncertainty intervals. This quantitative comparison indicates that the lower conversion efficiencies of shots on targets with the thicker coating at $I > 45 \cdot 10^{14} \text{ W cm}^{-2}$ could also only be due to shot-to-shot variations. Large shot-to-shot variations can also be observed for both coatings at intensities of $I < 20 \cdot 10^{14} \text{ W cm}^{-2}$.

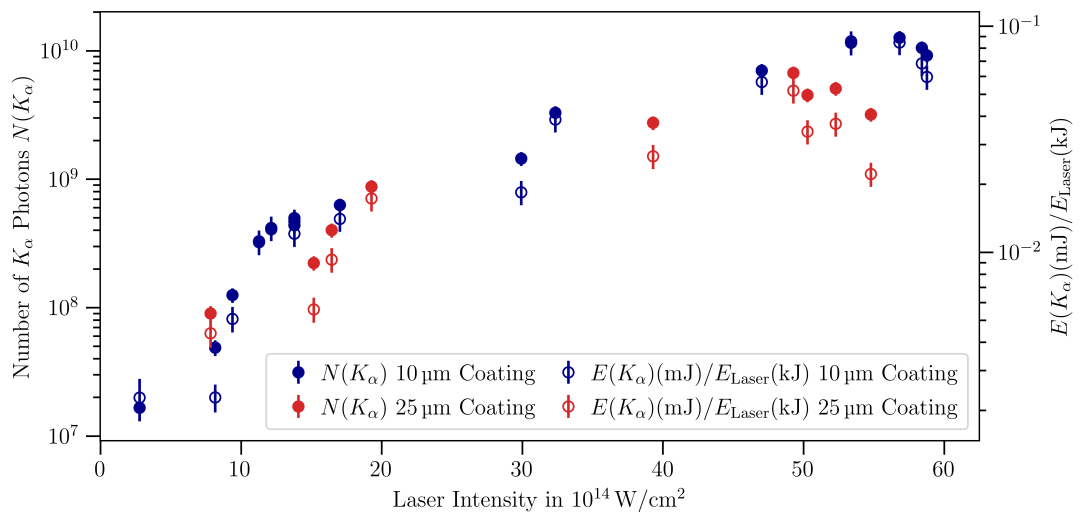


Figure 7.3.: K_α line emission strength for Cu targets with $10 \mu\text{m}$ and $25 \mu\text{m}$ thick coatings. Intensity uncertainties are not shown for better visualization.

As part of future work, a more detailed comparison of the two coating thicknesses needs to be carried out. The data must be compared taking different shots systematically into account. Furthermore, it needs to be investigated how much the absorption of electrons increases from 10 µm to 25 µm C₃H₆ in dependence of the fast electron energy/temperature. This might include to simulate and investigate the fast electrons for the Cu targets with 25 µm coating.

7.1.4. Comparison of K_α Yields for Different Target Materials

The major motivation for optimizing TPD conditions was to increase the numbers of photons from line emission in high-Z materials. Therefore, we tested coated Mo and coated Ag targets to verify that TPD electrons enable K-shell ionization, i.e., K_α emission, in Mo and Ag. Furthermore, we performed shots on uncoated Mo and Ag targets for comparison. Our results are presented in the following.

Figures 7.4a and 7.4b show the K_α yield for coated and bare Mo and for coated and bare Ag, respectively. In both cases, the coating was 25 µm thick. Additionally, the K_α yield of Cu targets with the 25 µm coating is shown for comparison purpose.

Let us take a look at the conversion efficiencies of the coated targets. The maximum value reached with coated Cu is $\frac{E(K_\alpha)(\text{mJ})}{E_{\text{Laser}}(\text{kJ})} = 0.052 \pm 0.007$ (cf. section 7.1.3) for a shot at $I = 49.3 \cdot 10^{14} \text{ W cm}^{-2}$ (ID 19608). This is larger than for the other materials, since the maximum conversion efficiencies achieved with coated Mo and Ag are $\frac{E(K_\alpha)(\text{mJ})}{E_{\text{Laser}}(\text{kJ})} = 0.032 \pm 0.004$ (ID 19666, $I = 53.7 \cdot 10^{14} \text{ W cm}^{-2}$) and $\frac{E(K_\alpha)(\text{mJ})}{E_{\text{Laser}}(\text{kJ})} = 0.015 \pm 0.002$ (ID 19676, $I = 55.5 \cdot 10^{14} \text{ W cm}^{-2}$), respectively. We can summarize that these calculated conversion efficiencies decrease with increasing nuclear charge, but this may be due to a systematic error in our analysis which is explained in the following.

During our analysis, we assumed the value $R_{\text{int}} = 0.0025 \pm 0.0001$ for the integrated reflectivity of the HOPG crystal for all K_α photon energies (cf. section 6.2.3). In fact, this value is only valid for Cu K_α. We do not know how R_{int} quantitatively changes for Mo and Ag K_α, but it is expected to decrease with increasing photon energy due to decreasing Bragg angles. Since $N(K_\alpha) \propto 1/R_{\text{int}}$, we expect to systematically underestimate N(K_α) for Mo and even more for Ag. To estimate this systematic error, we refer to the work of Döppner *et al.* [83] who investigated the change of the reflectivity of a HOPG crystal with photon energy. A change by a factor of 2 to 2.5 was reported from 12.6 keV photons to 22.2 keV photons (in second diffraction order). From our experiment, we calculated a decrease of the maximum K_α conversion efficiency by a factor of 1.6 ± 0.3 from coated Cu ($E^{\text{ph}}(K_\alpha) \approx 8.0 \text{ keV}$) to coated Mo ($E^{\text{ph}}(K_\alpha) \approx 17.4 \text{ keV}$) and by a factor of 3.5 ± 0.7 from coated Cu to coated Ag ($E^{\text{ph}}(K_\alpha) \approx 22.1 \text{ keV}$). Assuming a similar behavior for the reflectivity of our HOPG crystal (in first order) as for the HOPG crystal investigated by Döppner *et al.* (in second order), the difference between the calculated conversion efficiencies could only be due to the change of R_{int} . Based on this assumption, we would conclude that, in fact, (nearly) no difference between K_α conversion efficiencies of coated Cu, Mo and Ag targets was observed and that exploiting TPD is suitable to generate K_α emission in higher-Z targets with similar efficiency.

Future work might include to measure reflectivities of our HOPG crystal for Mo and Ag K_α photons to determine more precise K_α photon numbers and conversion efficiencies for these metal materials. Then, a more quantitative conclusion on the reason for the decrease of the calculated K_α conversion efficiencies within this work would be possible.

Let us now consider uncoated Mo and Ag targets. For those targets, we can observe the same behavior as described in section 7.1.2 for uncoated Cu targets. Even though the TPD strength decreased (see Fig. 7.1),

K_α conversion efficiencies were slightly higher than for the respective coated targets. In the case of a shot on uncoated Mo (ID 19660, $I = 55.3 \cdot 10^{14} \text{ W cm}^{-2}$), the conversion efficiency was larger by a factor of 2.0 ± 0.4 than the maximum conversion efficiency on the respective coated target. In the case of a shot on uncoated Ag (ID 19698, $I = 45.0 \cdot 10^{14} \text{ W cm}^{-2}$), it was larger by a factor of 1.8 ± 0.4 . I would like to remark that the detected K_α lines of uncoated Mo and Ag also contained emission from higher charged ions (cf. section 6.2.2 and appendix B). However, the strength of the emission from higher charged ions was comparable to the K_α emission from cold material.

From another point of view, the calculated K_α strengths and conversion efficiencies of uncoated Mo and Ag contain the whole line emission that could be used for X-ray diffraction with these targets, since no separate lines from higher ionized states were observed. This emphasizes the theoretical potential of optimizing TPD,

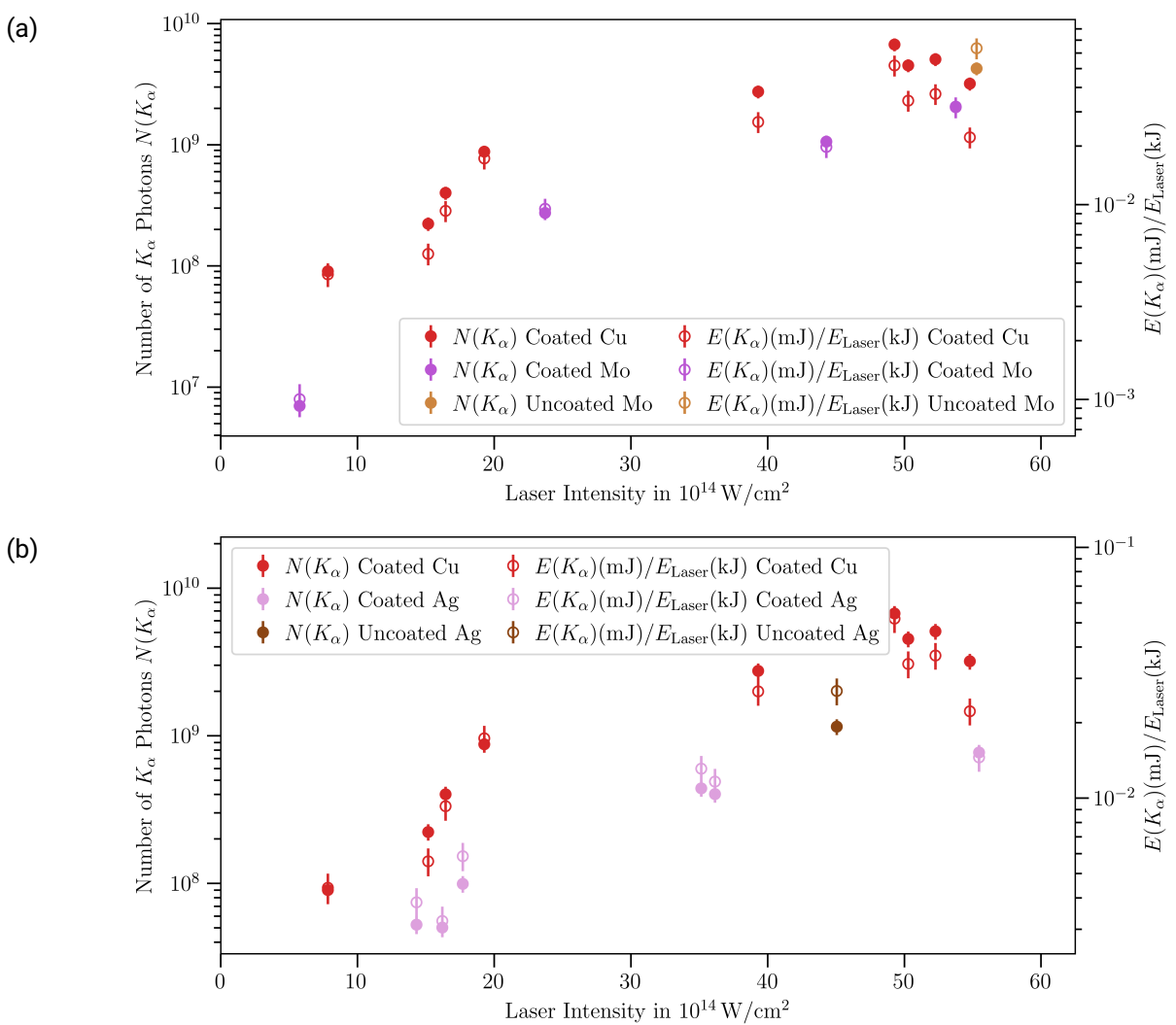


Figure 7.4.: K_α yield of coated and bare (a) Mo and (b) Ag targets in comparison to Cu targets with $25 \mu\text{m}$ coating. In the case of uncoated (a) Mo and (b) Ag targets, the strength of the whole detected K_α line is included (cf. section 6.2.2). Intensity uncertainties are not shown for better visualization.

if conversion efficiencies of $\frac{E(K_\alpha)(\text{mJ})}{E_{\text{Laser}}(\text{kJ})} \gtrsim 10$, as reported by Yaakobi *et al.* [32], could actually be reached. However, we must conclude that at the best focus setting, enhanced TPD of coated targets does not allow for increasing line emission conversion efficiencies in high-Z targets. An explanation for the lower K_α conversion efficiency in our case is given in sections 7.1.6 and 7.1.8.

7.1.5. Fast Electron Conversion Efficiency for the Monoenergetic Model

Our aim was to understand which fast electron distribution in terms of energies and electron numbers caused the observed X-ray emission. In section 6.3, I described two methods for this analysis: first, assuming monoenergetic fast electrons and second, assuming temperature distributed fast electrons. This section is about our results regarding the fast electron analysis with the monoenergetic model. In section 6.3.4, it was described that the fast electron energy was fixed to 50 keV for all investigated shots. It remains to present and discuss the findings concerning electron numbers and conversion efficiencies $E_{\text{Electrons}}^i/E_{\text{Laser}}$ for both diagnostics $i = \text{HXRD}, \text{HOPG}$.

With the monoenergetic model, shots on targets of the types 2-5 (see Table 5.1) were analyzed. We have not simulated the other targets in FLUKA, but the results are expected to be similar.

The fast electron conversion efficiencies for shots on coated and bare Cu targets are shown in Fig. 7.5a and Fig. 7.5b, respectively. For some shots on bare targets, the underlying best fit of the HXRD data had $\chi_\nu^2 > 1$ (cf. section 6.3.4). Since this inhibits to take the influence of the fit uncertainty for the error of the conversion efficiency into account, the shots are marked with an error bar of 100 % in Fig. 7.5b.

We can observe a good qualitative agreement between HXRD and HOPG spectrometer data in terms of increasing $N^i(e^-)$ and $E_{\text{Electrons}}^i/E_{\text{Laser}}$ with laser intensity for coated targets ($i = \text{HOPG}, \text{HXRD}$). For both diagnostics, the conversion efficiency increases by over one order of magnitude with laser intensity. In the case of uncoated targets, the variation from shot to shot also correlates between $N^i(e^-)$ and $E_{\text{Electrons}}^i/E_{\text{Laser}}$ ($i = \text{HOPG}, \text{HXRD}$). On the other hand, the absolute numbers differ quite strongly between $i = \text{HOPG}, \text{HXRD}$ for both coated and bare targets. For example, we calculated $N^{\text{HOPG}}(e^-) = (3.83 \pm 0.47) \cdot 10^{13}$ and $N^{\text{HXRD}}(e^-) = (3.38 \pm 0.38) \cdot 10^{12}$ for a shot at $I = 56.8 \cdot 10^{14} \text{ W cm}^{-2}$ on a coated target (ID 19612). This is a significant difference by more than one order of magnitude. A possible explanation is that the FLUKA model (cf. section 6.3.2) is too simple to reproduce both diagnostics equally well, since no plasma is simulated and no collective behavior of the electrons such as the creation of sheath fields is taken into account. The deviation between the two diagnostics needs to be investigated in the future.

Let us now compare the fast electron yield between coated and uncoated targets. With both diagnostics, i.e., HXRD and HOPG spectrometer, we can observe that the uncoated targets obtain higher fast electron conversion efficiencies. For example, the maximum conversion efficiency for coated targets is $E_{\text{Electrons}}^{\text{HOPG}}/E_{\text{Laser}} = (0.160 \pm 0.020) \%$ (ID 19612), whereas it is $E_{\text{Electrons}}^{\text{HOPG}}/E_{\text{Laser}} = (0.581 \pm 0.080) \%$ (ID 19630) for uncoated targets. The result is similar to section 7.1.2 where the comparison was made for K_α photon numbers. This is not surprising, since K_α photons are produced by fast electrons and confirms our presumption that other mechanisms than TPD produce fast electrons in the case of uncoated targets.

Concerning coated targets, the intensity dependence of $N^{\text{HOPG}}(e^-)$ and $N^{\text{HXRD}}(e^-)$ is similar to that of TPD strength (cf. section 7.1.1) and K_α yield (cf. section 7.1.2). The electron numbers indicate the same saturation behavior by a decreased slope above $I \approx 15 \cdot 10^{14} \text{ W cm}^{-2}$ for both $i = \text{HOPG}, \text{HXRD}$. In section 7.1.2, we compared shots at low and high intensity in terms of increasing K_α conversion efficiency and TPD strength and obtained increases by factors of 770 ± 200 and 181 ± 12 , respectively. For the same shots,

$N^{\text{HXRD}}(e^-)$ increases by a factor of 199 ± 63 from $N^{\text{HXRD}}(e^-) = (1.70 \pm 0.51) \cdot 10^{10}$ at $I = 2.77 \cdot 10^{14} \text{ W cm}^{-2}$ (ID 19691) to $N^{\text{HXRD}}(e^-) = (3.38 \pm 0.37) \cdot 10^{12}$ at $I = 56.8 \cdot 10^{14} \text{ W cm}^{-2}$ (ID 19612). This underlines the connection between TPD and the production of fast electrons. The deviation to the increase of K_α photon numbers might be due to additional effects, e.g., the electrons need to penetrate the coating which might have different plasma conditions depending on the intensity. Generally our data implies, the stronger TPD, the higher the electron and K_α conversion efficiency.

At this point, the plots of the fast electron conversion efficiencies for coated Mo and Ag targets are not shown because the results are very similar to Cu targets. This is not surprising, since we have already concluded the same for K_α conversion efficiencies (cf. section 7.1.4).

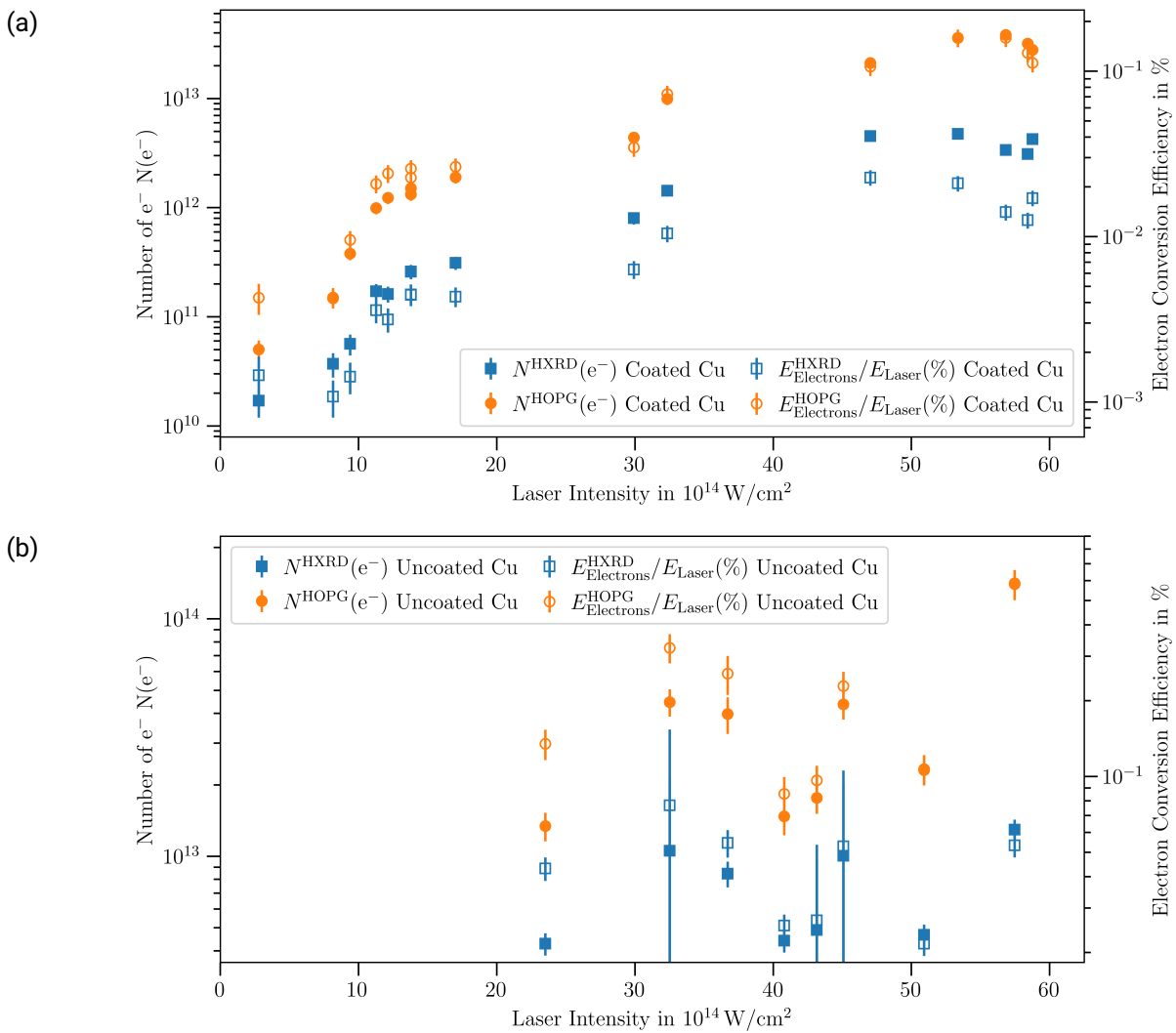


Figure 7.5.: Fast electron number and conversion efficiency calculated from HXRD and HOPG spectrometer data for (a) 12.7 μm Cu targets with 10 μm coating and (b) uncoated 10 μm Cu targets. Intensity uncertainties are not shown for better visualization.

7.1.6. Fast Electron Temperature Obtained With the Temperature Model

The evaluation method of temperature distributed fast electrons was applied to all shots on coated targets. As described in section 6.3.5, the temperature influences the electron conversion efficiency which is why the temperatures fitted individually to the different shots are discussed beforehand in this section. In contrast to the monoenergetic model, the results can be compared to the literature where the method of temperature distributed fast electrons is typically used [32, 35, 84, 85].

In Fig. 7.6, the fitted fast electron temperature is shown against laser intensity for shots on coated Cu targets. We notice that the uncertainties are large. In the case of some shots, in particular at lower intensities, the uncertainty interval exceeds the boundaries of the plotted temperature range from $T(e^-) = 5 \text{ keV}$ to $T(e^-) = 50 \text{ keV}$. At the end of this section, it is justified why we limit the considered temperature range in this way, but first the unlimited uncertainty intervals obtained from our analysis are discussed.

It is important to note that the large errors are not due to bad fits with $\chi^2_\nu > 1$. On the contrary, all temperatures within the uncertainty range correspond to $\chi^2_\nu < 1$ (cf. section 6.3.5). This is due to the fact that the relative error of the HXRD data increases when the intensity and thus the signal decreases. Exemplarily, Fig. 7.7 shows the detected PSL of a shot (ID 19649) at an intensity of $I = 12 \cdot 10^{14} \text{ W cm}^{-2}$ along with the fitted PSL for the best fit temperature of $T(e^-) = 19.5 \text{ keV}$. Taking a look at the data and uncertainties of the four thickest filters, it becomes clear that fitted PSL with very different slopes with respect to the filter thickness result in $\chi^2_\nu < 1$ and thus a large temperature uncertainty interval is obtained. In fact, for the considered shot, even *monoenergetic* electrons with $E_i = 350 \text{ keV}$ still fit the data with $\chi^2_\nu < 1$ (see Fig. 7.7). A further investigation of an upper limit of the temperatures fitting the data does not seem useful, since this value is physically unrealistic. Furthermore, temperatures in the few 100 keV regime cannot be effectively sampled, since we simulated electron energies only up to $E_i = 350 \text{ keV}$ (cf. section 6.3.5). Similar conclusions hold for the other shots where the temperature uncertainty reaches the upper plot limit of 50 keV. It should be noted that for the shot (ID 19615) at highest intensity $I = 59 \cdot 10^{14} \text{ W cm}^{-2}$ the large

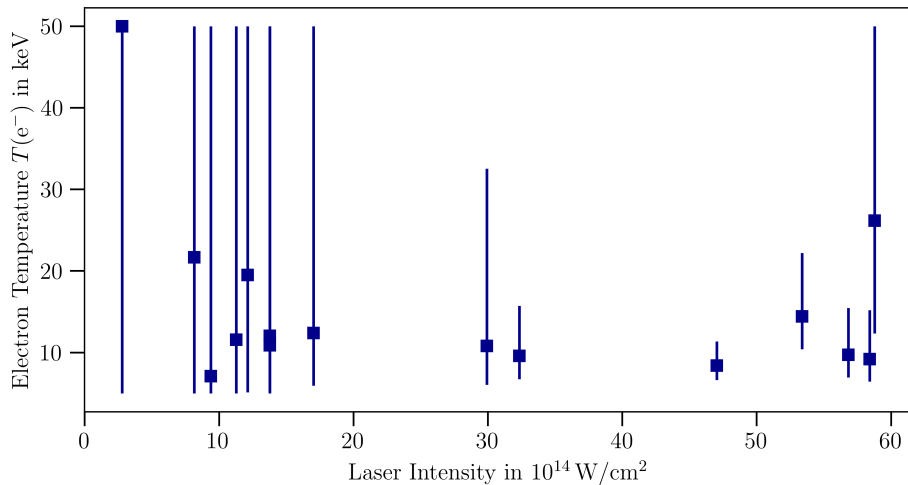


Figure 7.6.: Fast electron temperatures fitted individually to each shot on $12.7 \mu\text{m}$ Cu targets with $10 \mu\text{m}$ coating are presented. The shown uncertainty interval is limited to the range from 5 keV to 50 keV . For the fitting procedure, the HXRD data of the four thickest filters was considered. Intensity uncertainties are not shown for better visualization.

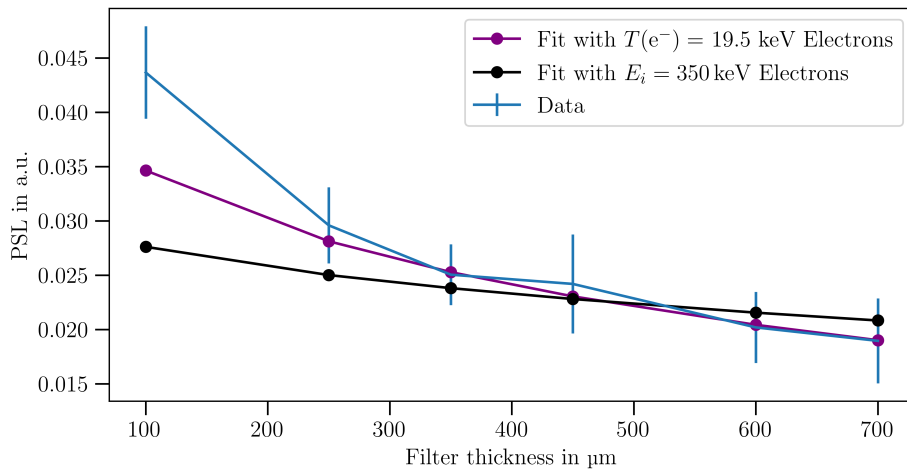


Figure 7.7.: The HXRD data of an exemplary shot (ID 19649) at $I = 12 \cdot 10^{14} \text{ W cm}^{-2}$ on a $12.7 \mu\text{m}$ Cu target with $10 \mu\text{m}$ coating is shown. The best temperature fit and a fit with *monoenergetic* electrons with $E_i = 350 \text{ keV}$ are included. For the fitting procedure, the HXRD data of the four thickest filters was considered.

temperature uncertainty is due to the fact that the detected PSL behind the fourth and third thickest filters were nearly equal. Considering the transmission, one would always expect the signal to decrease with increasing filter thickness which means that additional effects seem to influence the signal behind the third thickest filter in case of that shot.

Concerning the lower limit of the temperature uncertainty, our analysis showed that for some shots at low intensities even temperatures below the plot limit of 5 keV down to $T(e^-) = 3 \text{ keV}$ fitted the data with $\chi^2_\nu < 1$. Electrons at this temperature would not be considered as fast electrons, anymore. Furthermore, the simulated energies are not suitable to sample an electron distribution with $T(e^-) = 3 \text{ keV}$.

We conclude that the HXRD has significant limitations concerning the fast electron temperature determination, especially at low intensities. The uncertainty of the data compared to the variation of the signal between the considered four thickest filters is too large in order to distinguish between different temperatures. Possible improvements to the HXRD design are discussed later in section 7.1.9.

From Fig. 7.6, we can see that reasonable results with respect to the temperature uncertainty are obtained for shots at $I \gtrsim 30 \cdot 10^{14} \text{ W cm}^{-2}$ (including the shot at $I = 29.9 \cdot 10^{14} \text{ W cm}^{-2}$ and excluding the shot at highest intensity).

Considering the data of these six shots $l = 1, \dots, 6$, a fast electron temperature of $T^{\text{fix}} \approx 10 \text{ keV}$ is found to minimize the normalized chi-square

$$\chi^2_\nu(T) = \frac{1}{l_{\max} - 1} \sum_l \frac{(T^{\text{fix}} - T_l(e^-))^2}{(\Delta T_l(e^-))^2}, \quad (7.2)$$

where $l_{\max} = 6$ is the number of fitted, shot dependent temperatures $T_l(e^-)$. It is $\chi^2_\nu(T) = 0.31$ which means that the constant fast electron temperature $T^{\text{fix}} \approx 10 \text{ keV}$ agrees with the data of the six fitted shots.

This result is in contrast to what can be found in the literature with regard to fast electron temperatures from TPD. Froula *et al.* [35] and Yaakobi *et al.* [32] observed fast electron temperatures to increase from

20 keV up to 90 keV when the intensity was increased from $2 \cdot 10^{14} \text{ W cm}^{-2}$ to $7 \cdot 10^{14} \text{ W cm}^{-2}$. In our case we are at even higher intensities, but nevertheless we obtain a smaller temperature. Furthermore, we do not observe an intensity dependence of the temperature. However, the simulative expected increase with $\frac{IL}{k_B T_e}$ [57], which can be estimated as $\frac{IL}{k_B T_e} \propto I^{2/3}$ (cf. section 7.1.1), would correspond to a factor of only $2^{2/3} = 1.6$ over the range of reasonable temperature uncertainties, from $I \approx 30 \cdot 10^{14} \text{ W cm}^{-2}$ to $I \approx 60 \cdot 10^{14} \text{ W cm}^{-2}$. It might be that the intensity range is just too small in order to be sensitive to a temperature increase. Another effect decreasing the sensitivity is the fluctuation of the on-shot laser intensity.

Naively, we have not expected our experiment to result in reduced fast electron temperatures. Assuming the scaling of the fast electron temperature can be estimated by $\frac{IL}{k_B T_e}$ [57] for the experiments of Froula *et al.* [35] and Yaakobi *et al.* [32], on the one hand, and our experiment, on the other hand, the larger intensity of our setup seems to be counteracted by a larger thermal electron temperature or smaller scale length. Thermal electron temperatures in the experiment of Froula *et al.* were simulated to be around 1.4 keV to 2.5 keV which is comparable to the expected values in our case. In contrast to our best focus with $d_{\text{FWHM}} = 25 \mu\text{m}$, Froula *et al.* and Yaakobi *et al.* used multiple laser beams with phase plates generating an overlapped super-Gaussian laser spot with a diameter of nearly 1 mm. Considering that there is a limit to the scale length decreasing with a smaller laser spot size [32, 35], our small laser focus is expected to generate smaller scale lengths which might explain the lower fast electron temperatures.

Shorter scale lengths result in different conditions for the electron acceleration (cf. section 4.8), since electron plasma waves change their phase velocity faster when propagating through the steeper density gradient. An explanation for a decreased temperature in our case could be that the electrons cannot keep track to the phase velocity during the acceleration process. As part of future work, 2D or 3D hydrodynamic simulations need to be carried out to estimate the scale length for our experimental parameters. Furthermore, dedicated TPD simulation tools [57, 58] or PIC simulations [34] need to be used to investigate the effects on TPD and the electron acceleration.

Due to the large uncertainty of the data at lower intensities $I < 20 \cdot 10^{14} \text{ W cm}^{-2}$, it is unclear if the fast electron temperature was actually higher than at larger intensities and possibly in the range observed by Froula *et al.* [35] and Yaakobi *et al.* [32]. Nevertheless, my explanatory approach based on the scale length would also apply to shots at $I < 20 \cdot 10^{14} \text{ W cm}^{-2}$ and therefore I generally do not expect such a behavior. Furthermore, this would contradict the expectation of increasing temperatures with intensity.

Concerning the comparison of our temperatures to those obtained by Froula *et al.* and Yaakobi *et al.* at the Omega facility, some methodical differences need to be discussed. First, the HXRD of the Omega facility incorporates filters which are only penetrated by much higher photon energies compared to our design [84]. This means that a larger contribution of X-ray emission from thermal electrons to our data cannot be ruled out. As seen in section 6.3.5, including all six of our filters to the electron fitting procedure resulted in lower fast electron temperatures than in the case of excluding the two thinnest filters. This is expected to be due to the contribution of thermal electrons. For the results presented in this work, the two thinnest filters were excluded in order to reduce that contribution. Still, an influence of thermal electrons to the signal behind the four thickest filters might affect our analysis and might result in lower electron temperatures compared to a potential measurement with filters which are only sensitive to higher photon energies. In the future, the influence of thermal electrons on the signal behind different filters needs to be investigated more thoroughly.

Furthermore, Froula *et al.* and Yaakobi *et al.* inferred their fast electron temperatures by fitting exponential X-ray spectra with spectral energies proportional to $\exp(\frac{E_{\text{ph}}}{T(e^-)})$ and assuming that $T(e^-)$ is the fast electron

temperature, as suggested in [84, 85]. By performing Monte-Carlo simulations, Yaakobi *et al.* confirmed the agreement between exponential X-ray spectra and X-ray spectra from Maxwell distributed electrons with the same temperature for their setup up to a temperature of $T(e^-) = 80$ keV, i.e., in the relevant range. Even though they did not state the dimensionality of their Maxwell distribution, this indicates that the temperature is not sensitive on whether exponential X-ray or Maxwell distributed electron spectra are fitted. A first test of fitting the data of one shot of our experiment (ID 19612) with exponential X-ray spectra showed only little differences in the temperatures compared to our electron fitting procedure (cf. section 6.3.5). The best fit value with exponential X-ray spectra corresponded to a temperature of 12 keV instead of 10 keV for the electron fit. Future work needs to include a more systematic comparison between the two fitting methods, but the choice of fitting exponential X-ray spectra or X-ray spectra caused by electron distributions is not expected to significantly alter our results.

In principle, another possible explanation for the deviation of the temperatures could be that the fast electrons are not mainly produced by TPD in our case. However, the similar behavior of TPD strength, fast electron numbers from the monoenergetic model and numbers of K_α photons (cf. section 7.1.5) is a strong argument against it.

For the further analysis of our experiment presented in this work, we stick to the temperatures determined by our method of fitting electrons. When considering the temperature uncertainty, only the limited range from 5 keV to 50 keV as shown in Fig. 7.6 is applied. This constitutes a compromise between taking the huge uncertainty into account and staying to values which are realistic in comparison to the $l = 1, \dots, 6$ shots with reasonable temperature uncertainties. Note that the shot dependent best fit temperatures are contained in the considered uncertainty range apart from the shot at lowest intensity.

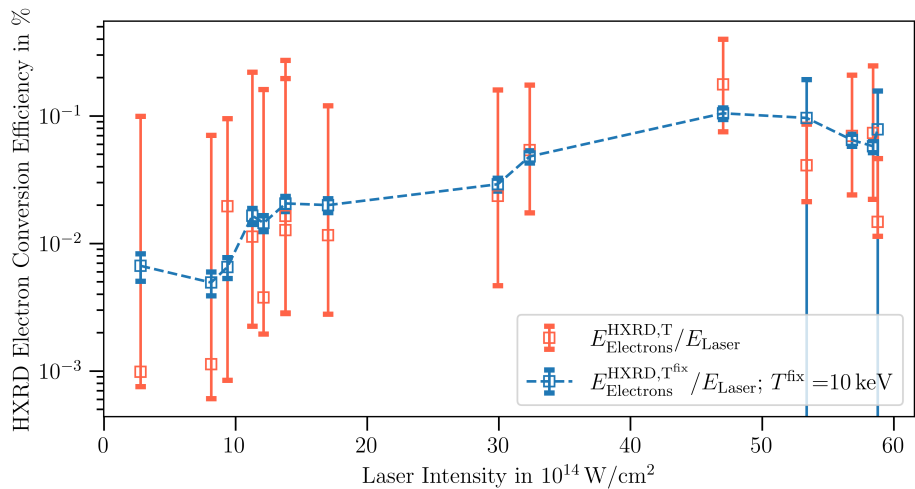
7.1.7. Fast Electron Conversion Efficiency for the Temperature Model

Concerning the results of fast electron conversion efficiencies from the temperature model, two different modes are presented. First, we allow the fast electron temperature to vary within the limited uncertainty range as shown in Fig. 7.6. Second, we fix the fast electron temperature for all shots to $T^{\text{fix}} = 10$ keV.

The fast electron conversion efficiency when scaling the electron number with the HXRD data is shown in Fig. 7.8a. In case of the data where the temperature uncertainty is considered, the intensity dependence observed with $E_i = 50$ keV monoenergetic electrons (cf. section 7.1.5) cannot be confirmed due to too large uncertainties. It should be noted that not the temperature model itself causes the uncertainties of the fast electron conversion efficiency to be much larger than in the monoenergetic case, instead, this is attributed to the fact that the HXRD did not allow for a temperature determination with small uncertainties. For a fixed fast electron temperature, the intensity dependence of the monoenergetic model is generally replicated and the conversion efficiency increases by more than one order of magnitude with intensity (see Fig. 7.8a).

In Fig. 7.8b, the conversion efficiency is shown in the case of scaling the fast electron number with the HOPG spectrometer data (cf. section 6.3.6). An increase of the conversion efficiency with laser intensity can even be observed when considering the temperature uncertainty. First, this is due to smaller errors in the uncertainty of the conversion efficiency than in the case of scaling the electron number with the HXRD data. In particular at low intensities, the difference is significant. Second, the data at higher intensities shows less outliers to lower conversion efficiencies. With the fixed fast electron temperature of $T^{\text{fix}} = 10$ keV, the increase of fast electron conversion efficiency by more than one order of magnitude is similar to the monoenergetic model.

(a)



(b)

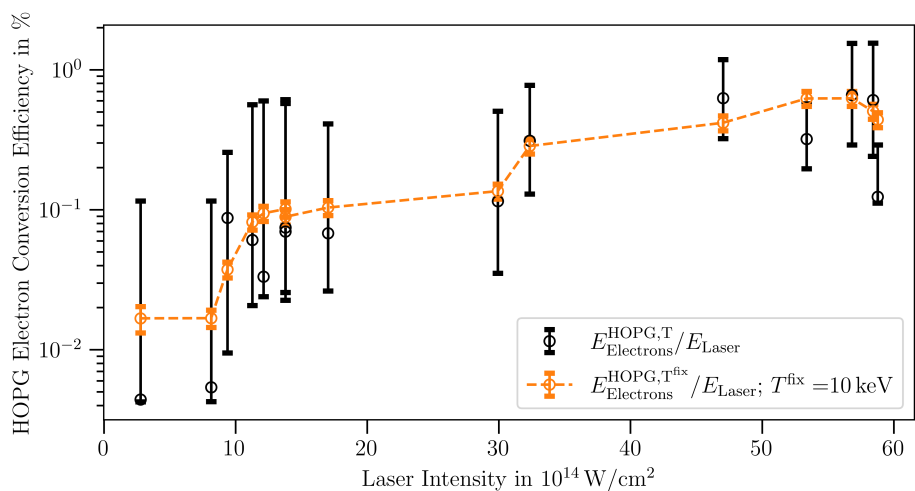


Figure 7.8.: Fast electron conversion efficiency for shots on $12.7\text{ }\mu\text{m}$ Cu targets with $10\text{ }\mu\text{m}$ coating when scaling the electron numbers by (a) the HXRD data and (b) the HOPG data. Each of (a) and (b) shows the results when considering temperature uncertainties (limited by 5 keV and 50 keV) from the HXRD fit and when using a fixed fast electron temperature of $T^{\text{fix}} = 10\text{ keV}$. In (a), an error of 100 % is used as indication for the shots where T^{fix} is not within the temperature uncertainty interval. Intensity uncertainties are not shown for better visualization.

The conversion efficiencies from scaling the electron number with the HOPG data are larger by around one order of magnitude than those from the HXRD data which we already concluded for the case of monoenergetic fast electrons (cf. section 7.1.5). The maximum of the conversion efficiency scaled by the HOPG data is $E_{\text{Electrons}}^{\text{HOPG},\text{T}^{\text{fix}}} / E_{\text{Laser}} = (0.626 \pm 0.077)\%$ for a shot at $I = 56.8\text{ W cm}^{-2}$ (ID 19612), while it only is $E_{\text{Electrons}}^{\text{HXRD},\text{T}^{\text{fix}}} / E_{\text{Laser}} = (0.0648 \pm 0.0070)\%$ for the same shot. The ratio 9.7 ± 1.6 between these two values is in agreement with the ratio 11.3 ± 1.9 between the conversion efficiencies of the two diagnostics obtained with the monoenergetic model for this shot. The issue of this deviation has already been discussed in section 7.1.5. Comparing the monoenergetic and temperature distributed model, a difference in the absolute numbers of the conversion efficiencies can be observed, since we only had a maximum of $E_{\text{Electrons}}^{\text{HOPG}} / E_{\text{Laser}} = (0.160 \pm 0.020)\%$ for $E_i = 50\text{ keV}$ monoenergetic electrons (ID 19612).

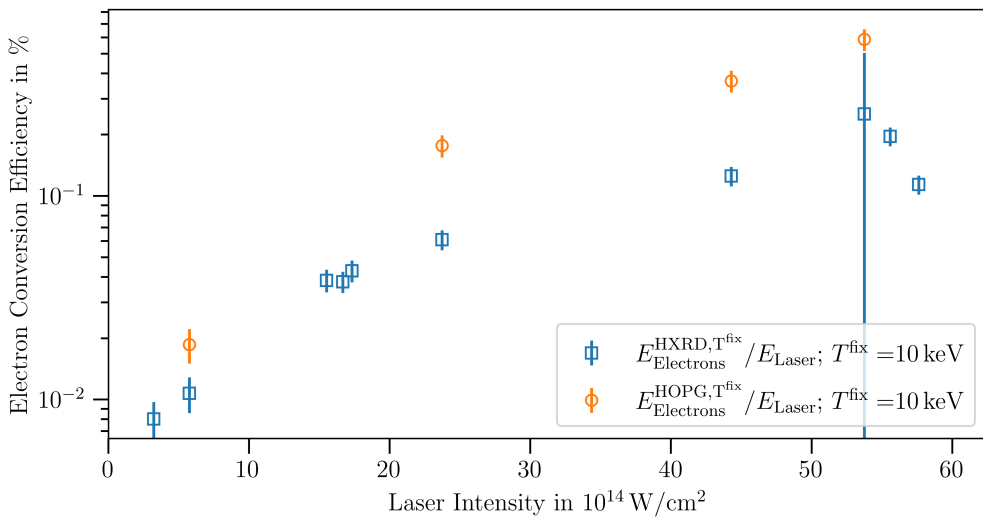


Figure 7.9.: Fast electron conversion efficiency for shots on $10.07 \mu\text{m}$ Mo targets with $25 \mu\text{m}$ coating when scaling the electron numbers by both the HXRD and HOPG data. The fast electron temperature is fixed to $T^{\text{fix}} = 10 \text{ keV}$. For the HXRD data, an error of 100 % indicates that T^{fix} is not within the temperature uncertainty interval. Intensity uncertainties are not shown for better visualization.

This is roughly a quarter of the value for temperature distributed fast electrons at $T^{\text{fix}} = 10 \text{ keV}$. The deviation is expected to be in that direction and not vice versa, since a fast electron temperature of $T^{\text{fix}} = 10 \text{ keV}$ results mostly in electrons with worse K-shell ionization cross section than at electron energies of 50 keV . However, this intuitive explanation is a huge simplification, since not only the incident electron energy is important, but also the energy modulation within the target. The corresponding effects are discussed in more detail in section 7.1.8.

In the literature, the fast electron conversion efficiency is usually determined by using the HOPG spectrometer data for scaling the electron number. The maximum values obtained by Froula *et al.* [35] and Yaakobi *et al.* [32] are up to a few percent and thus within one order of magnitude compared to our value $E_{\text{Electrons}}^{\text{HOPG}, T^{\text{fix}}} / E_{\text{Laser}} = (0.626 \pm 0.077) \%$. The deviation seems larger when comparing to our conversion efficiency from the HXRD scaling. However, conversion efficiencies calculated in such a way are not stated in the literature. Even though HXRDs are used to determine fast electron temperatures, they are usually not absolutely calibrated.

Until this point, I have not discussed the results with our coated Mo and Ag targets when analyzing with the temperature model. To summarize, the obtained fast electron temperatures are similar to those of coated Cu (cf. section 7.1.6) in terms of the quantitative values and the issue of large errors due to large uncertainties in the HXRD data, in particular at low intensities. Furthermore, the findings concerning the conversion efficiencies are similar. Exemplarily, the conversion efficiencies of shots on coated Mo are shown in Fig. 7.9. Both, the HXRD and HOPG scalings, are carried out at the same fixed temperature $T^{\text{fix}} = 10 \text{ keV}$ as previously, for comparison purpose. The number of data points from the HOPG scaling is smaller because we tried to use the HOPG crystal in second diffraction order, but no signal was detected in that setting (cf. section 5.3.2).

The maximum conversion efficiency $E_{\text{Electrons}}^{\text{HOPG}, T^{\text{fix}}} / E_{\text{Laser}} = (0.588 \pm 0.072) \%$ (ID 19666) of coated Mo is,

within the uncertainty, the same as $E_{\text{Electrons}}^{\text{HOPG}, \text{T}^{\text{fix}}} / E_{\text{Laser}} = (0.626 \pm 0.077) \%$ of coated Cu. Simultaneously, the deviation of the values from the two diagnostics, HXRD and HOPG spectrometer, has decreased. A possible explanation is the systematic error of using the HOPG reflectivity at the Cu K_α photon energy (cf. sections 7.1.4 and 6.2.3) when analyzing Mo K_α emission. If the reflectivity at Mo K_α was known, the amount of calculated K_α photon numbers and therefore $E_{\text{Electrons}}^{\text{HOPG}, \text{T}^{\text{fix}}} / E_{\text{Laser}}$ would be expected to increase such that the deviation of the two diagnostics would be similar to the case of coated Cu. Then, the maximum conversion efficiency $E_{\text{Electrons}}^{\text{HOPG}, \text{T}^{\text{fix}}} / E_{\text{Laser}}$ of coated Mo would agree even better with the literature. In the case of coated Ag, the maximum calculated value $E_{\text{Electrons}}^{\text{HOPG}, \text{T}^{\text{fix}}} / E_{\text{Laser}} = (0.369 \pm 0.046) \%$ (ID 19676) is below those of Cu and Mo. Simultaneously, the deviation between the two diagnostics, HXRD and HOPG, decreased even more and the systematic error due to the unknown reflectivity is expected to increase.

7.1.8. Relation Between K_α Yield and Fast Electron Conversion Efficiency for the Temperature Model

In our experiment, we have observed K_α conversion efficiencies two orders of magnitude below the maximum value $\frac{E(K_\alpha)(\text{mJ})}{E_{\text{Laser}}(\text{kJ})} \gtrsim 10$ reported by Yaakobi *et al.* [32]. Our fast electron conversion efficiency, in contrast, agrees much better with the literature. This holds, in particular, when comparing $E_{\text{Electrons}}^{\text{HOPG}, \text{T}^{\text{fix}}} / E_{\text{Laser}} = (0.588 \pm 0.072) \%$ obtained with coated Mo, which is expected to be systematically underestimated, to the value $E_{\text{Electrons}}^{\text{HOPG}, \text{T}} / E_{\text{Laser}} \approx 1.5 \%$ reported by Yaakobi *et al.* The apparent contradiction between the K_α and fast electron conversion efficiencies, i.e., the reason why the electrons produce K_α emission less efficiently in our case, is investigated in more detail in this section.

To do so, we analyze the K_α production efficiency $E(K_\alpha) / E_{\text{Electrons}}^{\text{HOPG}, \text{T}}$ which relates the detected energy in K_α photons to the calculated total energy of fast electrons with temperature T necessary to reproduce that K_α emission. The smaller the K_α production efficiency, the larger the electron numbers and thus electron conversion efficiencies that are necessary for a certain K_α conversion efficiency.

It is important to note that we determined $E_{\text{Electrons}}^{\text{HOPG}, \text{T}}$ by scaling the electron number such that the total energy of their K_α emission obtained from FLUKA simulations equals the detected energy in K_α photons $E(K_\alpha)$ (cf. section 6.3.6). Therefore $E_{\text{Electrons}}^{\text{HOPG}, \text{T}}$ and $E(K_\alpha)$ are not independent. For a given temperature, the quantity $E(K_\alpha) / E_{\text{Electrons}}^{\text{HOPG}, \text{T}}$, apart from its uncertainties, does not depend on experimental data, but directly results from the FLUKA simulations of the respective target. Consequently, in the following we consider the equivalent ratio

$$\frac{E(K_\alpha)}{E_{\text{Electrons}}^{\text{HOPG}, \text{T}}} \equiv \frac{N^{\text{HOPG}, \text{T}}(e^-) \cdot E_{\text{simu}}^{\text{T}}(K_\alpha)}{N^{\text{HOPG}, \text{T}}(e^-) \cdot 1.5k_{\text{B}}T(e^-)}, \quad (7.3)$$

where $N^{\text{HOPG}, \text{T}}(e^-)$ is the determined fast electron number (cf. section 6.3.6), $E_{\text{simu}}^{\text{T}}(K_\alpha)$ is the simulated mean energy in K_α emission per electron from the temperature distribution and $1.5k_{\text{B}}T(e^-)$ the mean energy of such electrons. Assuming isotropic emission, it holds

$$E_{\text{simu}}^{\text{T}}(K_\alpha) = \sum_i f_i^T \frac{N_{\text{ph}}^i(E^{\text{ph}}(K_\alpha))}{\Omega \cdot \text{primary}} \cdot 4\pi \cdot 1 \text{ primary} \cdot E^{\text{ph}}(K_\alpha), \quad (7.4)$$

where $E^{\text{ph}}(K_\alpha)$ is the K_α photon energy, $\frac{N_{\text{ph}}^i(E^{\text{ph}}(K_\alpha))}{\Omega \cdot \text{primary}}$ is obtained from the simulations (cf. sections 6.3.2) and f_i^T weighs the different electron energies E_i according to the temperature (cf. section 6.3.3).

In Fig. 7.10, the K_α production efficiency is plotted against temperature for different targets. Taking a look at the curve corresponding to our Cu target with 12.7 μm substrate and 10 μm coating thickness, we can observe that the K_α production efficiency is temperature dependent. One reason is that the K-shell ionization cross section reaches its maximum at around 2-3 times the K-shell ionization energy (cf. section 5.2). At our best fit fast electron temperature $T^{\text{fix}} = 10 \text{ keV}$, the K_α production efficiency is only $E_{\text{simu}}^T(K_\alpha)/1.5k_B T^{\text{fix}} \approx 1.4 \cdot 10^{-5}$ and not optimal due to too low temperature. Figure 7.10 also shows the K_α production efficiency of our coated Mo and Ag targets. The curves differ from those of the aforementioned coated Cu target due to a different coating thickness and a different substrate layer. Comparing different temperatures, we can see that higher temperatures than $T^{\text{fix}} = 10 \text{ keV}$ would be even more beneficial for K_α production than with the coated Cu target which is consistent with the higher K-shell ionization energies of Mo and Ag. This implies that the higher temperatures up to 90 keV reported by Yaakobi *et al.* [32] are a main reason for their higher K_α production efficiencies.

Additionally, the target design used by Yaakobi *et al.* [32] was different. Their Mo layer was 30 μm thick and sandwiched between two plastic layers of 30 μm thickness each. Yaakobi *et al.* simulated a K_α production efficiency of $\frac{dE_{\text{simu}}^T(K_\alpha)}{d\Omega \cdot 1.5k_B T(e^-)} \approx 7 \cdot 10^{-5} \text{ sr}^{-1}$ for their design in target normal direction and at 80 keV which we use as representative for their maximum fast electron temperatures. Assuming isotropic emission, this results in $E_{\text{simu}}^T(K_\alpha)/1.5k_B T(e^-) \approx 9 \cdot 10^{-4}$. Even when accounting for the fact that they simulated the target normal direction and not at 45° as in our case, their value would not decrease by more than a factor of 2 [32], i.e., not below $E_{\text{simu}}^T(K_\alpha)/1.5k_B T(e^-) \approx 4.5 \cdot 10^{-4}$.

This means that their K_α production efficiency at 80 keV is at least 6 times larger than $E_{\text{simu}}^T(K_\alpha)/1.5k_B T(e^-) \approx 7.5 \cdot 10^{-5}$ for our coated Mo targets at 80 keV. Comparing to the K_α production efficiency of our coated Cu targets at $T^{\text{fix}} = 10 \text{ keV}$, their value is at least 32 times larger. In comparison to the K_α production efficiency of $E_{\text{simu}}^T(K_\alpha)/1.5k_B T^{\text{fix}} \approx 5.4 \cdot 10^{-6}$ of our coated Mo targets at $T^{\text{fix}} = 10 \text{ keV}$, the difference increases even to a factor around 83. Therefore, the generated electrons can produce K_α emission more efficiently in the case of Yaakobi *et al.* and a smaller K_α conversion efficiency in our experiment corresponds to a comparable electron conversion efficiency. The difference in electron conversion efficiency would decrease if we reached higher temperatures.

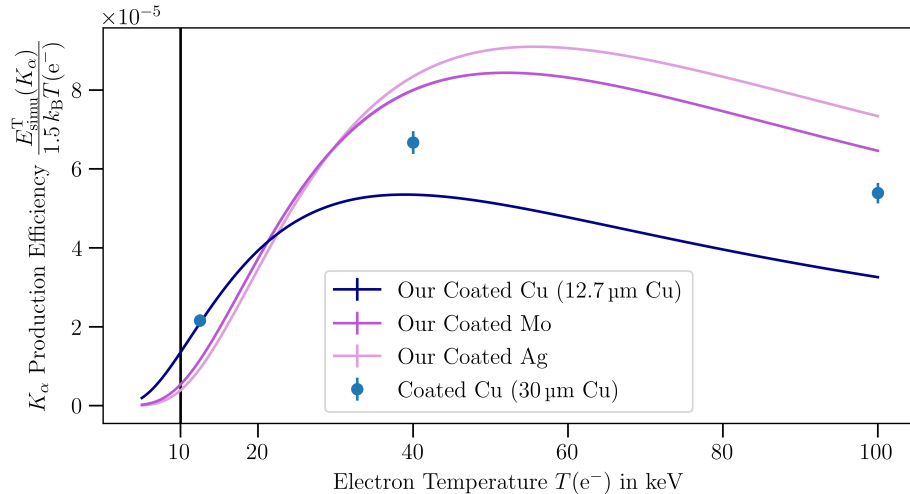


Figure 7.10.: K_α production efficiency in dependence of the electron temperature for different targets. For Cu, a coating thickness of 10 μm and for Mo and Ag a coating thickness of 25 μm is considered.

The fact that the K_α production efficiency of the coated Mo target of Yaakobi *et al.* is larger than the one of our coated Mo target at the same temperature of 80 keV points out that the difference in K_α production efficiency is due to the combination of both, larger temperatures and a different target design. While the coating at the backside of the targets of Yaakobi *et al.* is not expected to significantly alter the K_α production efficiency, their larger substrate thickness seems beneficial. Generally, a thicker substrate is always expected to produce more K_α emission, at least for front-side detection, due to the increased amount of material that can stop electrons. To investigate the influence of the substrate thickness separately from other effects, we simulated the K_α production efficiency for a target consisting of a 30 μm Cu substrate and a 10 μm coating which is compared to our coated Cu target with a substrate thickness of 12.7 μm . Figure 7.10 shows the results of FLUKA simulations at different temperatures. At low temperatures the added substrate material is not beneficial, since the amount of electrons penetrating the thinner substrate is negligible. In contrast, the K_α production efficiency increases at higher temperatures with the thicker substrate.

If and how much a thicker substrate increases the K_α production efficiency is dependent on several effects as follows. Electrons at initially too high energies to efficiently produce K-shell emission lose energy while penetrating the target and, supposed the substrate is thick enough, automatically reach an optimized energy range in terms of K-shell ionization cross section. Still, the amount of energy an electron loses due to bremsstrahlung during the deceleration, before ionizing K-shells, decreases the conversion efficiency. Furthermore, the produced K_α photons need to penetrate the target until reaching the front side in order to yield a signal. If the distance is too long, re-absorption of the X-rays dominates. Due to the dependence on K-shell ionization and K_α photon energy, the implications of different substrate thicknesses depend on the substrate material. An additional effect that generally needs to be taken into account for the efficiency of K_α production is the attenuation and energy loss of electrons in the coating. At high energies, the influence of the coating decreases. The situation gets even more complicated when the superposition of electrons at different energies in the temperature distribution is considered.

To conclude, the small fast electron temperature determined from our HXRD analysis is the explanation why we calculated similar electron conversion efficiencies as Yaakobi *et al.* [32] despite much smaller K_α conversion efficiencies. If our electron temperature was higher (cf. section 7.1.6 for methodical uncertainties), the calculated fast electron conversion efficiency would decrease. For a potential follow-up experiment on TPD, the processes behind the differences in K_α production efficiency due to different substrate materials and different thicknesses of the coating and substrate layer need to be investigated more systematically by FLUKA simulations. If higher temperatures than $T^{\text{fix}} = 10 \text{ keV}$ could be reached in such an experiment, thicker substrate layers than in this work are expected to be beneficial for K_α production.

7.1.9. Potential Improvements on the Hard X-Ray Detector

In section 7.1.6, we have seen that the HXRD data from our experiment has significant limitations with respect to the determination of the fast electron temperature. In particular for shots at low intensity and thus weak HXRD signals, the analysis suffered from large temperature uncertainties which, in turn, propagated to the fast electron conversion efficiency. Furthermore there are possibly methodical differences in our HXRD measurement compared to the literature [32, 35, 84]. This section is about potential improvements to our HXRD design in order to increase the data quality for potential future experiments.

A major issue of the temperature determination was that the signal behind filters of different thicknesses changed too little compared to the data uncertainty (cf. section 7.1.6). To obtain a larger signal change,

I suggest to use additional filters with smaller transmissions. Higher photon energies are necessary to penetrate those filters and thus the filters enable to distinguish them. For the implementation, thicker filters or materials with higher Z , e.g., Cu, can be used. The benefit of the latter is that the transmission rises over a smaller interval of photon energies which should facilitate the temperature reconstruction (cf. section 5.3.1). It can also be advantageous to combine different materials to one filter. For example, Al can be used to suppress the transmission through thin Cu layers, e.g., with a thickness of 50 μm , below the Cu K-shell ionization energy. Using filters with much smaller transmission would increase the comparability of the determined temperatures to the literature (cf. section 7.1.6). The HXRD at Omega [84] incorporates four filters cutting off photons at energies below $\sim 20\text{ keV}$, $\sim 40\text{ keV}$, $\sim 60\text{ keV}$ and $\sim 80\text{ keV}$, respectively. This ensures a much stronger suppression of the contribution from X-ray emission from thermal electrons compared to our HXRD design. For example, the filter with a cutoff at $\sim 20\text{ keV}$ has a transmission of $T = 0.5$ at a photon energy of 34 keV in comparison to a photon energy of 19 keV for our thickest filter (data from [82]).

A drawback of filters with less transmission is that the HXRD signal decreases and therefore the relative error increases. The signal decrease is even worse than only due to the decreased transmission, since the sensitivity of the imaging plate (IP) generally decreases with photon energy. At a photon energy of 34 keV, only 25 % of the incident energy is deposited in the sensitive layer of the IP. At 50 keV and 100 keV, this proportion decreases to 21 % and 6 %, respectively. A HXRD design developed by Williams *et al.* [86] at the Lawrence Livermore National Laboratory addresses this issue by installing a Ta fluorescence plate behind the IP. Photons with energies above the K-shell ionization energy of Ta, that have penetrated the IP, produce Ta K_α emission and are thus converted to lower energies. The K_α photons can be detected by the IP, subsequently.

In the case of Ta, the K-shell ionization energy is $E_K^{\text{ion}} = 67\text{ keV}$ and the K_α photon energy is $E^{\text{ph}}(K_\alpha) = 57\text{ keV}$ [52]. These energies seem suitable if fast electron temperatures up to 90 keV as reported by Froula *et al.* [35] and Yaakobi *et al.* [32] are reached, but not if the fast electron temperatures are around $T(e^-) \approx 10\text{ keV}$ as indicated by our HXRD analysis. An adaption of the design of Williams *et al.* [86] to lower photon energies by using a material with lower nuclear charge than Ta needs to be investigated in the future. However, a limit for this adaptation is set by the transmission through the IP which is at only $T = 0.1$ at 40 keV according to FLUKA simulations of the IP used in our experiment (*Cytiva BAS IP SR 2040 E*). It should be noted that this transmission also includes substrate layers and not only the sensitive layer of the IP.

Another advantage of the HXRD design of Williams *et al.* [86] is that it enables to determine a space dependent background of the HXRD signal. The filter channels are separated by Ta with a thickness of more than one centimeter in the direction of the direct line of sight to the target. Therefore, the direct line of sight does not contribute to the signal behind the Ta separations, but the signal due to high-angle scattering and fluorescence in the filters can be detected. Williams *et al.* [86] implemented their filter array by layering laser cut foils where different filter thicknesses are realized by cutting away material in different layers. The channel separations are automatically obtained by not cutting away material at the corresponding positions. In total, their filter array consisted of 36 separate channels. This number is much higher than in our case. We expect that increasing the number of channels of our HXRD while keeping each filter area fixed would facilitate the temperature determination, as well.

In front of their filter array, Williams *et al.* [86] additionally placed a low-Z filter (in their case Al) to decrease the amount of electrons that reaches the filter array and thus to reduce the effect of fluorescence at all. Concerning the reduction of X-ray scattering, implementing an array of filters with high nuclear charges generally improves the HXRD. The reason is that the ratio of the cross section of Compton scattering to

the cross section of photoelectric absorption increases for energies above the K-shell ionization energy. In particular, the filter material Al chosen for the experiment carried out in the frame of this master thesis has potential for improvement. For example, the ratio of the cross section of Compton scattering to the cross section of photoelectric absorption is 0.044 and 0.88 for Al at 20 keV and 50 keV photon energy, respectively, while it is only 0.0033 and 0.056 in the case of Cu at the same photon energies.

Generally, another possibility to resolve the problem of low IP sensitivity is to implement a HXRD in a cannon like design [87]. This means that the different filter channels are stacked behind and not next to each other. Filter layers and IPs alternate so that the subsequent decrease of the signal behind each filter layer can be detected. In contrast to the previously presented design, cannon like HXRD do inherently not allow for filter dependent background determination. Furthermore, cannon like HXRD are rather applied to X-rays with higher energies than in our case, e.g., in the MeV regime [87]. At energies in the range of few tens to hundred keV, the transmission through the first few layers of filters and IPs is too small. Nevertheless, an idea based on the cannon like design in order to improve our HXRD for our application is to stack two IPs instead of one IP behind the channel-separated filter array. This increases the amount of collected data while keeping the number of separate channels fixed.

Further investigations and FLUKA simulations need to be carried out in order to quantify how large the optimization potential of our HXRD by the aforementioned design adaptations is at photon energies relevant for our application. On the contrary to improving an IP-based HXRD, another possibility is to implement a HXRD with a different detection method than using IPs. The HXRD design at Omega [84] is based on scintillators and suitable for the operation with the four filters at cutoff energies of \sim 20 keV, \sim 40 keV, \sim 60 keV and \sim 80 keV. At NIF, the Filter-Fluorescer Diagnostic System (FFLEX) [85, 88], a HXRD which is also based on scintillators, has an operating range of photon energies from 20 keV to 500 keV. Using scintillators instead of IPs, no spatial resolution of the detected signal is implemented, but this is no drawback in the case of the HXRD, since only the different channels need to be distinguished. To conclude, a scintillator based HXRD promises high sensitivity to a large range of photon energies produced by fast electrons from TPD. The option of designing such a detector system for the PHELIX facility needs to be considered in the future.

7.2. Shots With Phase Plate

This section is about the results of our analysis of shots where the phase plate was used. In section 7.2.1, I compare the TPD strength of bare with coated targets and calculate the convective TPD gain. Section 7.2.2 is about the comparison of TPD strength with K_α yield and in section 7.2.3, the fast electron conversion efficiency from the monoenergetic model is presented. Finally, the temperatures and conversion efficiencies obtained with the model of temperature distributed fast electrons are discussed in section 7.2.4. For each topic, I point out similarities and differences between the best focus and phase plate setting. With the phase plate, we were only able to test two different target types: uncoated 12.7 μm thick Cu and Cu with the 10 μm coating. Therefore, I will not compare different coating thicknesses and metal materials as in the case of the best focus setting (cf. sections 7.1.3 and 7.1.4).

7.2.1. Two-Plasmon Decay Strength and Convective Gain

In Fig. 7.11, the TPD strength S is shown against laser intensity I for shots on 12.7 μm Cu with and without 10 μm coating. The intensity was obtained by scaling the measured laser energy at $\lambda_{\text{vac}} = 527 \text{ nm}$ according

to a calibration that estimates the mean intensity in the laser spot (see appendix A). A statistical error of 10 % is assumed for the calibrated intensity (see appendix A and cf. section 7.1.1). Lower laser energies were not tested when using the phase plate.

As in the case of shots at best focus (cf. section 7.1.1), TPD is stronger for coated than uncoated targets. Furthermore, the laser intensity is again above the TPD threshold in the case of coated targets, even at the lowest tested intensity of $I = 0.28 \cdot 10^{14} \text{ W cm}^{-2}$ corresponding to a laser energy of $E_{\text{Laser}} = 52.9 \text{ J}$ (ID 19734). This laser energy is, however, much larger than the values for which TPD was found to be above the threshold in the best focus setting.

Quantitatively considering the enhancement of TPD thanks to the coating, we observe an increase of the TPD strength by a factor of 58 ± 9 from the shot on bare Cu (ID 19721, $E_{\text{Laser}} = 195.4 \text{ J}$) to the shot on coated Cu with highest TPD strength (ID 19723, $E_{\text{Laser}} = 213.2 \text{ J}$). This is larger than the increase from shots on bare targets to shots on coated targets in the best focus setting (cf. section 7.1.1). The latter corresponds to only a factor of 10 for most shots which are comparable in terms of similar laser energy. There are some explanatory approaches for the larger effect of the coating on TPD when using the phase plate. First, the homogeneous growth rate (cf. section 4.4) is smaller at the lower laser intensities with phase plate and, in turn, the relevance of collisional damping as a countereffect to TPD is enhanced (cf. section 4.5.2). This holds also true for the convective TPD instability, where the damping coefficient is inversely proportional to the homogeneous growth rate (cf. section 4.7.2). Since collisional damping is stronger in Cu compared to the plastic coating (cf. section 5.2 for the comparison between Mo and the coating), the TPD strength of uncoated targets is decreased compared to coated ones. Second, it may be that only with the phase plate, there is actually an increase of the scale length for coated compared to bare targets, which was one of the reasons to use the coating (cf. section 5.2). Considering that there is a limit to the scale length decreasing with a smaller laser spot size [32, 35], the limit may be reached for both, coated and bare targets, in the best focus setting. This consideration is supported by the high laser intensities of the best focus which result in high thermal electron temperatures and therefore fast preplasma expansion.

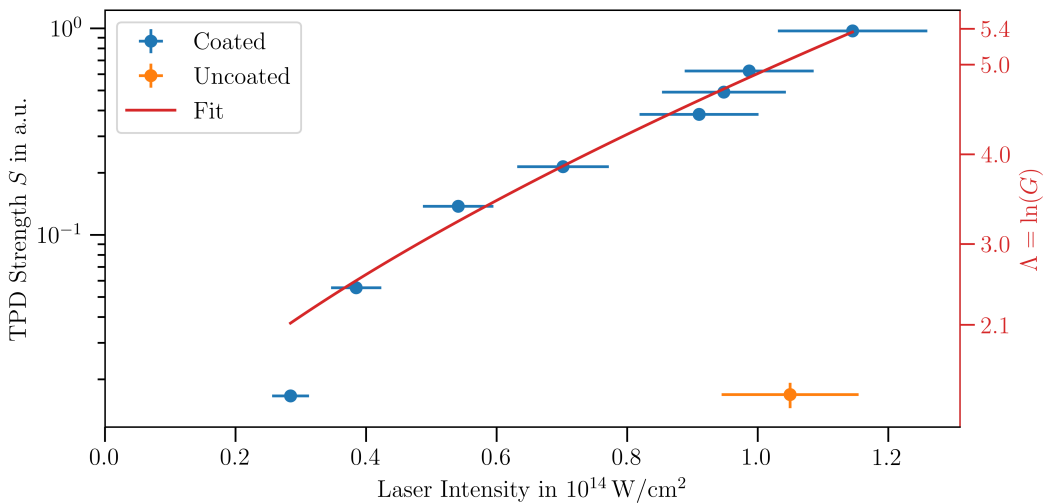


Figure 7.11.: TPD strength in dependence of laser intensity for shots with phase plate up to a maximum laser energy of 213.2 J. The data from coated targets is fitted and both, the fit and the resulting values $\Lambda = \ln(G)$ are shown.

With the phase plate on the other hand, the limit of the scale length is higher and the intensities are smaller. The potential increase of the scale length for coated compared to bare targets would result in a larger convective TPD gain $G \sim \exp\left(0.0266 \frac{I_{14} \lambda_\mu L_\mu}{T_{\text{keV}}}\right)$ (cf. section 4.7.1) for the first compared to the second. This would explain the increased difference in TPD strength between coated and bare targets. Froula *et al.* [35], who used a super-Gaussian laser spot with a diameter of nearly 1 mm, obtained an intensity scaling of $L_n = 250 \mu\text{m} (I_{14})^{0.25}$ for the scale length of their coating after 1.5 ns from simulations in the intensity range from $2 \cdot 10^{14} \text{ W cm}^{-2}$ to $7 \cdot 10^{14} \text{ W cm}^{-2}$. This indicates that the scale length of our coating, using a slightly smaller laser spot of $d = 500 \mu\text{m}$ but also slightly smaller intensities than Froula *et al.*, is not or only barely limited and our previous consideration is supported. In the future, simulations need to be performed to further investigate the different hypotheses. Two- or three-dimensional hydro simulations can be used to estimate the scale length. Concerning the influence on TPD, dedicated TPD simulation tools [57, 58] need to be used or PIC simulations [34] can be carried out. For a potentially following experiment on TPD, I suggest to measure the scale length on-shot, e.g., by interferometric methods.

It should be mentioned that the arbitrary units of the TPD strength in Fig. 7.11 are the same as in Fig. 7.1 (for the best focus) with respect to the fact that the signal strengths obtained from the streak camera images (cf. section 6.1) were normalized by the same factor. Assuming that the collection efficiency of the streak camera setup is the same, we can compare the TPD strengths between the phase plate and the best focus setting. At the best focus, the maximum TPD strength was $S = 1 \pm 0.011$ (for a shot at $E_{\text{Laser}} = 188.0 \text{ J}$, ID 19676). With the phase plate on the other hand, we reached the maximum value of $S = 0.972 \pm 0.019$ (for a shot at $E_{\text{Laser}} = 213.2 \text{ J}$, ID 19723). The two TPD strengths coincide even within the small uncertainties of the streak camera data. Considering the convective TPD gain, the lower intensity seems to be compensated by the larger laser spot size. First, a larger scale length might be reached. Second, the thermal electron temperature is expected to be lower for the phase plate compared to the best focus setting at the same laser energy, thus increasing the convective TPD gain. Third, the volume, at which TPD occurs, is larger in case of the phase plate so that we expect more electron plasma wave modes to get amplified. The comparison of the two laser settings demonstrates the importance of the interplay between I , L , T_e and the laser spot size for the convective TPD gain (see Eq. 4.98). To summarize, the regimes of TPD are very different between the two settings even though the TPD strength is comparable. To better understand these regimes, we need to carry out 2D or 3D hydro simulations to estimate L and T_e . Based on the results of the hydro simulations, the effects on TPD must be investigated by separate simulations.

Similarly to the best focus setting, we fitted the TPD strength of shots on coated targets in order to calculate the TPD gain G and $\Lambda = \ln(G)$ (cf. section 7.1.1). Here, we fitted all data points assuming that saturation effects are negligible. This assumption seems consistent with the results of Froula *et al.* [35], whose data indicates an onset of saturation in the fast electron conversion efficiency at $I = 3 \cdot 10^{14} \text{ W cm}^{-2}$. This is above our intensity range while the 1 mm diameter of their super-Gaussian laser spot is comparable to the spot size of 500 μm in our phase plate setting.

The obtained fit to the data is included in Fig. 7.11. Besides the data point at lowest laser intensity, the data is fitted well. Due to the small number of performed shots, it cannot be evaluated if this is a single shot exception or a trend. A possible explanation for a trend is that the intensity actually approaches the TPD threshold. Apart from this data point, shot-to-shot variations are of less relevance compared to the best focus setting. This could mean that the assumed statistical error of 10 % in the calibrated intensity is an overestimation. In fact, the uncertainty in the calculation of the averaged intensity for calibration pulses from the PHELIX ns-frontend was smaller (cf. appendix A). Together this may indicate that TPD is rather insensitive on spatial shot-to-shot variations in the speckled intensity distribution of the phase plate. Furthermore, the spatial intensity distribution with the phase plate is expected to be less sensitive

to the laser output which would support the observation of smaller shot-to-shot variations. In the future, the effects of the speckles on TPD need to be investigated in more detail. Generally, they depend on the relation between the propagation distance of plasmons and the distance between different speckles. In the literature, contradicting findings are reported. While some studies indicate the TPD instability to be dominated by a few intense speckles [37], in particular near the threshold, others find that the averaged intensity determines the TPD behavior [33].

The potential influence of speckles indicates that we must be careful about the comparison of intensities between our experiment and the experiments of Froula *et al.* [35] and Yaakobi *et al.* [32]. It is not clear how the spatial intensity distribution of their super-Gaussian laser spot looked like, how speckles influenced TPD in their case and how they were considered in the calculation of the intensity. Our intensity values, on the other hand, were determined by averaging over the whole laser spot. If only hot speckles of the intensity distribution had been taken into account, the intensities of our study were higher, up to a factor around 3 to 5 depending on which speckles are taken into account (see appendix A).

Another issue about the intensity comparison is that Froula *et al.* [35] and Yaakobi *et al.* [32] overlapped four laser beams. The study of Michel *et al.* [36] conducted at the Omega facility indicates a shift of the fast electron conversion efficiency to higher intensities when multiple beams under different incidence angles are used. For a setup mostly comparable to those of Froula *et al.* [35] and Yaakobi *et al.* [32], the intensity necessary for the same fast electron conversion efficiency was found to be smaller for a single beam than the four beam configuration. A quantitative comparison is strongly influenced by variations from shot to shot, but from the plot presented by Michel *et al.*, a factor around 2 seems to be a good estimate.

It should be noted that the discussed uncertainty concerning the comparability of intensities is mainly relevant for the phase plate setting. In contrast, the best focus setting is expected to correspond to larger intensities (at maximum laser energy) compared to the studies of Froula *et al.* and Yaakobi *et al.*, independently from how they calculated their intensity and if the effect of overlapping laser beams is taken into account. The latter would even decrease the intensity effectively relevant for TPD in the overlapped beam setting. Michel *et al.* [36] did not present data concerning the fast electron temperature and K_α conversion efficiency for the different settings, such that the studies of Froula *et al.* [35] and Yaakobi *et al.* [32] are still better suitable for a comparison to our work.

Let us continue the discussion of the fit to the TPD strength shown in Fig. 7.11. The best fit parameters are $\log(A) = -2.35$ and $C' = 4.90 \cdot (10^{14} \text{ W cm}^{-2})^{-2/3}$. In contrast, the best fit for the best focus setting corresponded to a smaller value $C' = 0.77 \cdot (10^{14} \text{ W cm}^{-2})^{-2/3}$ (cf. section 7.1.1). Therefore, the dependence of $\Lambda = C' I^{2/3}$ on laser intensity is much larger in case of the phase plate. Note that the dependence of the convective TPD gain $G = \exp(\Lambda)$ on laser intensity is even greater. This indicates that the TPD strength S could be significantly increased if higher laser intensities were available. This conclusion is also true if saturation effects were already present for the collected data.

To give a numerical example, a further increase of laser intensity from $I = 1.15 \cdot 10^{14} \text{ W cm}^{-2}$ to $I = 2 \cdot 10^{14} \text{ W cm}^{-2}$ would result in over 11 times the TPD strength, assuming the correlation with the convective TPD gain still holds and the relevance of saturation does not increase significantly. However, we have already used the maximum PHELIX laser energy during our experiment so that higher intensities could only be reached by using a phase plate that produces a smaller spot size.

7.2.2. Line Emission Yield

In this section, I present the results of our analysis of K_α emission strength regarding shots with the phase plate. The results will be compared with the TPD strength and the K_α yield at best focus.

The K_α emission strength of all shots we performed with the phase plate is shown in Fig. 7.12. First, we take a look at the data of coated Cu targets. As we have already observed when no phase plate was used (cf. section 7.1.2), the dependence of $N(K_\alpha)$ on laser intensity I is very similar to that of the TPD strength (see Fig. 7.11). The maximum conversion efficiency achieved with the phase plate is $\frac{E(K_\alpha)(\text{mJ})}{E_{\text{Laser}}(\text{kJ})} = 0.057 \pm 0.007$ (ID 19723) which is close to the one reached at best focus $\frac{E(K_\alpha)(\text{mJ})}{E_{\text{Laser}}(\text{kJ})} = 0.085 \pm 0.011$ (cf. section 7.1.2). The minor difference may be due to shot-to-shot variations. The similarity of conversion efficiencies with the phase plate and at best focus is consistent with our observation of similar TPD strengths (cf. section 7.2.1).

Concerning uncoated targets, we can observe that the K_α yield (see Fig. 7.12) is comparable to that of the coated targets despite much weaker TPD strength (see Fig. 7.11). Quantitatively, a shot (ID 19721) on a bare target had a K_α conversion efficiency of $\frac{E(K_\alpha)(\text{mJ})}{E_{\text{Laser}}(\text{kJ})} = 0.028 \pm 0.007$ which is only a factor of 2.0 ± 0.4 less than the maximum conversion efficiency with coated targets (ID 19723). In contrast to that, the TPD strength was smaller by a factor of 58 ± 9 (cf. section 7.2.1). A mismatch between K_α conversion efficiency and TPD strength was already observed for the laser setting at best focus (cf. section 7.1.2). Similar to that case, we think that other processes than TPD producing fast electrons are relevant when using uncoated targets.

I would like to make a comment about our observations concerning the K-shell emission from highly charged ions with the phase plate which have not been discussed elsewhere in this work. Owing to lower intensities and thermal electron temperatures with the phase plate, the strength of line emission from highly charged Cu ions in bare targets was reduced by over an order of magnitude compared to the best focus setting. However, these emission lines were still much stronger than K_α emission. Because of slightly lower ionization states, the line emission from highly charged ions was shifted towards slightly smaller

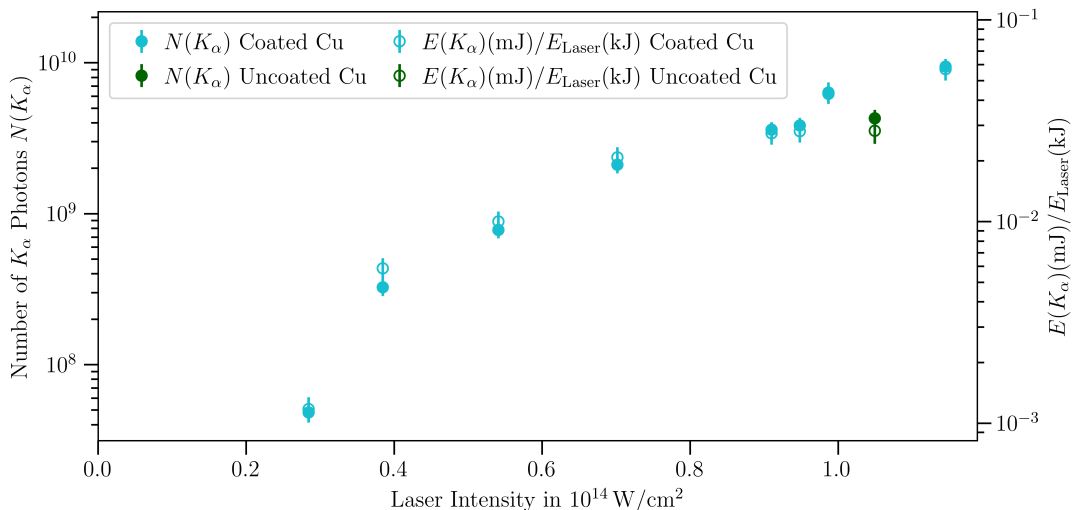


Figure 7.12.: K_α emission strength for $12.7 \mu\text{m}$ Cu with $10 \mu\text{m}$ coating and uncoated Cu with $12.7 \mu\text{m}$ thickness. Intensity uncertainties are not shown for better visualization.

energies. Future work might include to analyze the emission lines from highly charged ions regarding the corresponding thermal electron temperature in the phase plate setting.

To conclude, our findings about K_α emission with the phase plate are similar to those at best focus. It is striking that the K_α yield of coated targets did not change much despite quite different laser conditions and the different TPD regime. On the contrary, line emission from highly charged ions in bare targets was weakened by the phase plate because of lower thermal electron temperatures.

7.2.3. Monoenergetic Fast Electrons

In this section, I present the results of our fast electron analysis with the monoenergetic model. Note that this analysis was only carried out for shots on Cu targets with 10 μm coating, since other target types were either not tested with the phase plate or not simulated in FLUKA.

Figure 7.13 shows our results regarding the fast electron conversion efficiency from both scalings of the electron number, with the HXRD and HOPG data. Our findings are comparable to those without the phase plate. First, we can observe again that the dependence of $N^{\text{HOPG}}(\text{e}^-)$ and $N^{\text{HXRD}}(\text{e}^-)$ on laser intensity is similar to that of the TPD strength (see Fig. 7.11) and the K_α yield (see Fig. 7.12). Furthermore, the absolute numbers of $N^{\text{HOPG}}(\text{e}^-)$ are still about one order of magnitude above $N^{\text{HXRD}}(\text{e}^-)$. We obtained a maximum conversion efficiency of $E_{\text{Electrons}}^{\text{HOPG}}/E_{\text{Laser}} = (0.107 \pm 0.014)\%$ for the shot at highest intensity $I = 1.14 \cdot 10^{14} \text{ W cm}^{-2}$ (ID 19723) which is close to the maximum conversion efficiency $E_{\text{Electrons}}^{\text{HOPG}}/E_{\text{Laser}} = (0.160 \pm 0.020)\%$ (ID 19612) for shots on coated Cu in the best focus setting (cf. section 7.1.5).

Good fits with $\chi^2_\nu < 1$ to the four thickest filters (cf. section 6.3.4) were obtained using the same fast electron energy of 50 keV as at the best focus. In addition to our observations described above, this implies similarities between shots on coated targets in the best focus and phase plate setting despite completely different laser conditions.

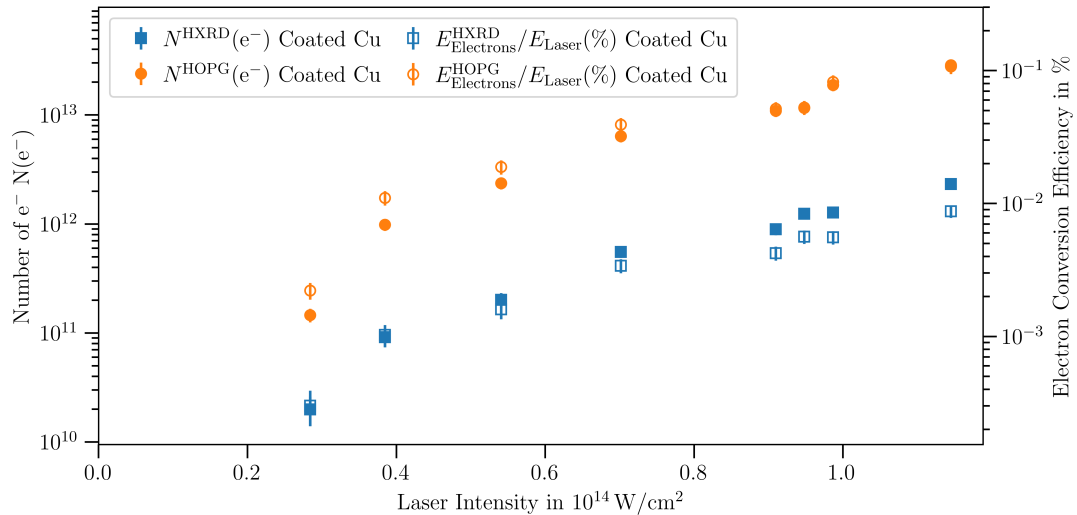


Figure 7.13.: Fast electron number and conversion efficiency calculated from the HXRD and HOPG data for shots on 12.7 μm Cu with 10 μm coating. Intensity uncertainties are not shown for better visualization.

7.2.4. Temperature Distributed Fast Electrons

This section is about the temperature distributed fast electron model applied to shots on coated Cu in the phase plate setting. First the obtained temperatures and second the conversion efficiencies from both scalings are discussed.

The fast electron temperatures from fitting the HXRD data behind the four thickest filters (cf. section 6.3.5) are presented in Fig. 7.14. Similarly to the best focus setting, the range of investigated temperatures was limited between 5 keV and 50 keV (cf. section 7.1.6). At lower intensities, in particular for the three shots with lowest intensity, the issue about the large temperature uncertainty is the same.

Fitting a fast electron temperature analogously to Eq. 7.2 to the $l = 1, \dots, 5$ ($l_{\max} = 5$) shots with reasonable temperature error, a best fit temperature of $T^{\text{fix}} = 9 \text{ keV}$ is found. This value is very similar to the 10 keV in the best focus setting. The methodical issues discussed in section 7.1.6 are also relevant for the phase plate setting. However, the influence of thermal electrons on the HXRD signal behind the four thickest filters is expected to decrease due to smaller thermal electron temperatures.

As for the best focus setting, we carry out a comparison with the studies of Froula *et al.* [35] and Yaakobi *et al.* [32] who observed an increase of the fast electron temperature from 20 keV to 80 keV in the intensity range from $2 \cdot 10^{14} \text{ W cm}^{-2}$ to $7 \cdot 10^{14} \text{ W cm}^{-2}$. Comparing to our intensities around $1 \cdot 10^{14} \text{ W cm}^{-2}$, the temperature $T^{\text{fix}} = 9 \text{ keV}$ from our analysis is in better agreement with their data than at the best focus setting. This suggests that we could reach higher temperatures if larger intensities were available in the phase plate setting. However, we must be careful about this conclusion due to methodical differences (cf. section 7.1.6) and uncertainties in the comparability of intensities (cf. section 7.2.1).

In Fig. 7.15a, the conversion efficiency when scaling the fast electron number with the HXRD data is presented. There is no clear intensity dependence within the uncertainty of the data if the *shot dependent* temperatures and uncertainties are considered (red data). However, if neglecting the uncertainties (still red data), we can observe an increase of the conversion efficiency with intensity. It seems like the uncertainties of the shot dependent temperatures and thus of the efficiencies are overestimated when using the phase

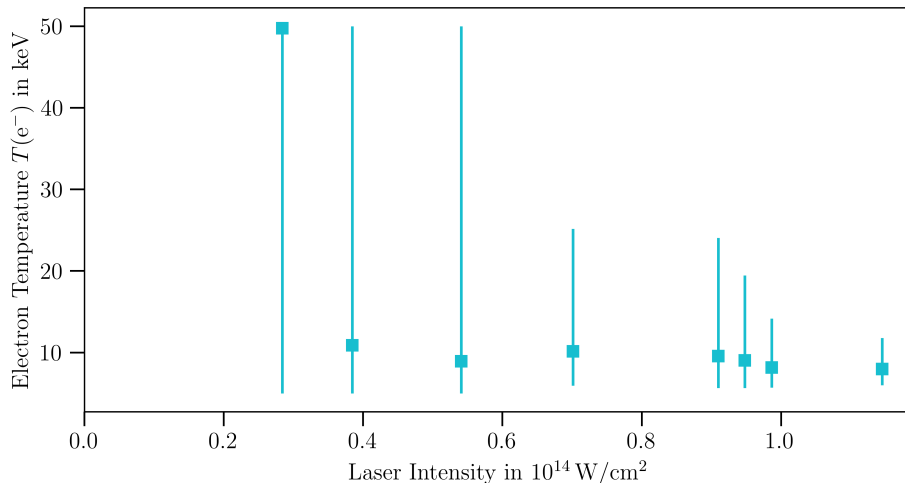


Figure 7.14.: Fast electron temperatures obtained from fitting the HXRD data behind the four thickest filters for shots on $12.7 \mu\text{m}$ Cu targets with $10 \mu\text{m}$ coating in the phase plate setting. Intensity uncertainties are not shown for better visualization.

plate. These results are in contrast to the case at best focus (see Fig. 7.8a) where no intensity dependence can be observed for the shot dependent best fit temperatures. A possible explanation is the decrease of shot-to-shot variations when using the phase plate which was already discussed concerning the TPD strength (cf. section 7.2.1).

Our results of the fast electron conversion efficiency from the HXRD data, but for a fixed fast electron temperature, are included in Fig. 7.15a, too. Even though $T^{\text{fix}} = 9 \text{ keV}$ was calculated for the phase plate setting, we use the value $T^{\text{fix}} = 10 \text{ keV}$ in order to get results which are comparable to the best focus setting. Nevertheless, the shot-to-shot variations and temperature uncertainties are too large in both settings to significantly distinguish between 9 keV and 10 keV (see Figs. 7.14 and 7.6). The trend of increasing electron conversion efficiency in the investigated intensity range can be clearly identified, similarly to the TPD strength (cf. section 7.2.1) and K_{α} conversion efficiency (cf. section 7.2.2). The increase is larger than

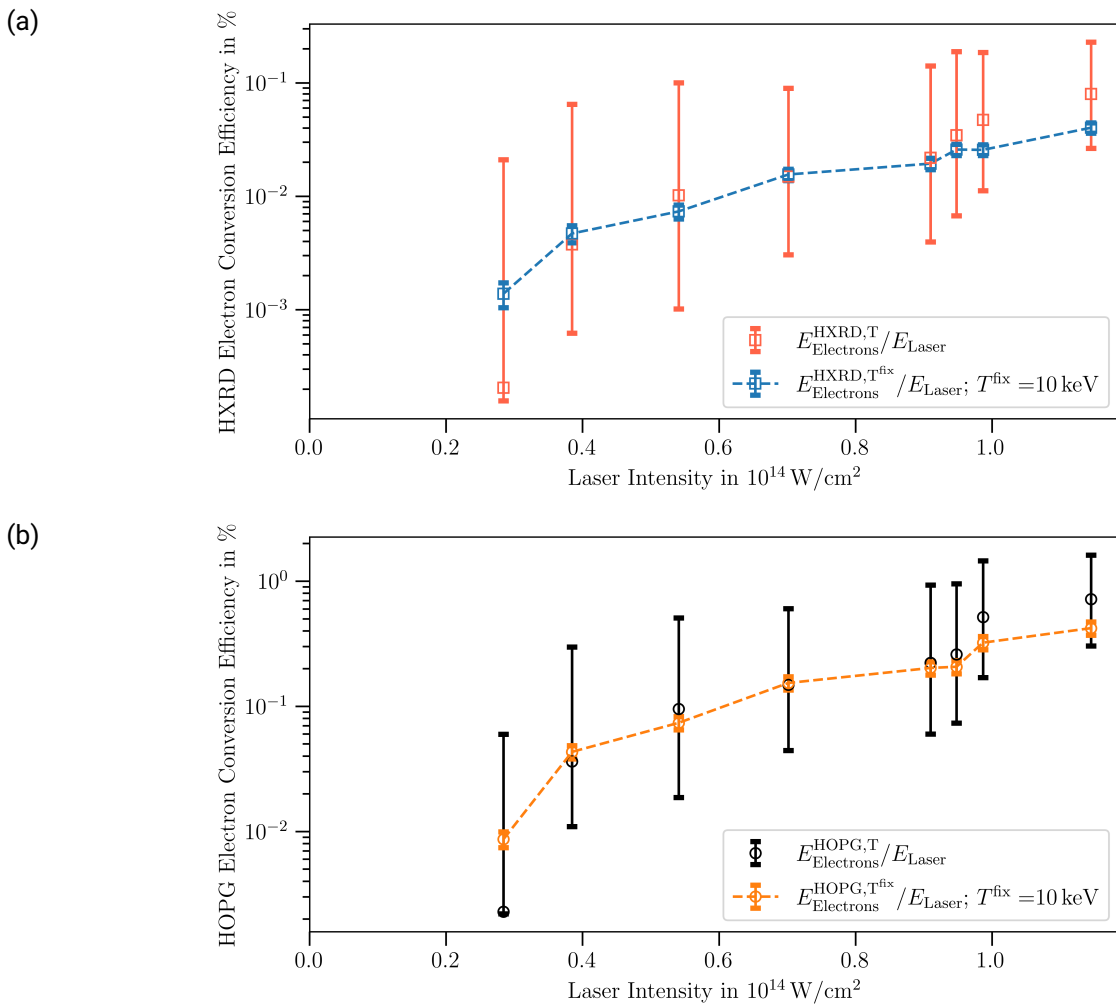


Figure 7.15.: Fast electron conversion efficiency for shots on $12.7 \mu\text{m}$ Cu targets with $10 \mu\text{m}$ coating in the phase plate setting when scaling the electron numbers by (a) the HXRD data and (b) the HOPG data. Each of (a) and (b) shows the results when considering temperature uncertainties (limited by 5 keV and 50 keV) from the HXRD fit and when using a fixed fast electron temperature of $T^{\text{fix}} = 10 \text{ keV}$. Intensity uncertainties are not shown for better visualization.

one order of magnitude from the lowest to the highest intensity, analogously to the monoenergetic model (cf. section 7.2.3).

Fig. 7.15b shows our results of the fast electron conversion efficiency when scaling with the HOPG data. Concerning the shot dependent temperatures, the trend of increasing conversion efficiency with laser intensity can be observed when neglecting the uncertainties, similar to the HXRD scaling. The intensity dependence of the conversion efficiencies from both scalings is alike. Comparing the absolute values between the HXRD and HOPG scaling for the fixed fast electron temperature, we observe that the latter are around one order of magnitude larger, as in the case of the monoenergetic model. The maximum conversion efficiency $E_{\text{Electrons}}^{\text{HOPG,T}^{\text{fix}}} / E_{\text{Laser}} = (0.422 \pm 0.052) \%$ for the shot at highest intensity (ID 19723) is similar to the maximum value $E_{\text{Electrons}}^{\text{HOPG,T}^{\text{fix}}} / E_{\text{Laser}} = (0.626 \pm 0.077) \%$ at best focus (ID 19612). The reader should be reminded that the scaling from K_α yield to fast electron numbers actually depends only on the simulations (cf. section 7.1.8). Since we considered the same fixed temperature for both settings, the similarity of conversion efficiencies is directly related to the fact that the same observation was made for the K_α conversion efficiency (cf. section 7.2.2). This explanation holds true for the similarities of the results from the monoenergetic model between the two laser settings (cf. section 7.2.3), too. Furthermore, it is the explanation for the fact that the increase of the conversion efficiency from the monoenergetic to the temperature distributed model is the same for both laser settings.

To conclude, the phase plate did not result in an increase of the fast electron temperature or conversion efficiency compared to the best focus setting. The resulting K_α strengths were observed to be similar. The results of Froula *et al.* [35] and Yaakobi *et al.* [32] might indicate that higher fast electron temperatures can be reached by larger intensities depending on the comparability of their experiments and our study.

8. Conclusion and Outlook

In this last chapter, I summarize the most important results from our experiment and the reason why we observed much less conversion efficiency from laser energy into K_α emission than the value $\frac{E(K_\alpha)(\text{mJ})}{E_{\text{Laser}}(\text{kJ})} \gtrsim 10$ reported by Yaakobi *et al.* [32]. Based on that, I will give an outlook on future work to increase the K_α conversion efficiency and on the application of X-ray sources for X-ray diffraction.

During our experiment, we proved that TPD was enhanced by the low-Z coating through the increased $3/2 \omega_0$ emission, the TPD signature. For coated targets, the similar intensity dependence of TPD strength, K_α photon and fast electron numbers is evidence for the fact that fast electrons from TPD caused the K_α emission. This was observed for both, the best focus and phase plate setting. We found out that the K_α conversion efficiency is similar for coated Cu, Mo and Ag which proved that electrons from TPD can be exploited for the production of line emission in high-Z materials.

However, the K_α yield from coated targets did not increase compared to bare targets. Our analysis showed that our maximum K_α conversion efficiency with a coated target in the best focus setting, $\frac{E(K_\alpha)(\text{mJ})}{E_{\text{Laser}}(\text{kJ})} = 0.085 \pm 0.011$, was over two orders magnitude below the value of Yaakobi *et al.* [32]. Using the phase plate resulted in very different laser conditions corresponding to a different TPD regime, but the K_α conversion efficiency did not increase. This behavior is summarized in Fig. 8.1 where data from both TPD regimes are shown.

An important parameter influencing the K_α conversion efficiency is the fast electron temperature. The quantitative implications depend on the substrate material and thickness, but generally a higher temperature is beneficial for K_α production. The analysis of our hard X-ray detector data implies electron temperatures around 10 keV for both, the best focus and the phase plate setting. This is below the fast electron temperatures reported by Froula *et al.* [35] and Yaakobi *et al.* [32] who observed an increase from 20 keV up to 90 keV in the intensity range from $2 \cdot 10^{14} \text{ W cm}^{-2}$ to $7 \cdot 10^{14} \text{ W cm}^{-2}$.

The effect that their higher temperatures enable larger K_α conversion efficiencies is depicted in Fig. 8.1 by a curve that was fitted to the data of Yaakobi *et al.* If the intensity and thus the temperature in our phase plate setting could be increased to the range of Yaakobi *et al.*, larger K_α conversion efficiencies are expected. However, we have already used the maximum PHELIX laser energy such that a higher intensity can only be reached by a phase plate producing a smaller laser spot. It should be noted that we chose coated Cu for the comparison to provide results at the two different TPD regimes. The comparison with coated Mo targets of Yaakobi *et al.* is still justified because our results did not differ largely between coated Cu and coated Mo.

The effect of decreasing the laser spot size, compared to our phase plate setting, needs to be investigated in the future, since a smaller spot is expected to influence the fast electron generation by TPD detrimentally [89]. A trade-off between laser intensity and spot size must be carried out for the specific PHELIX parameters. If an optimum is found, the full benefit of potentially higher temperatures is only obtained

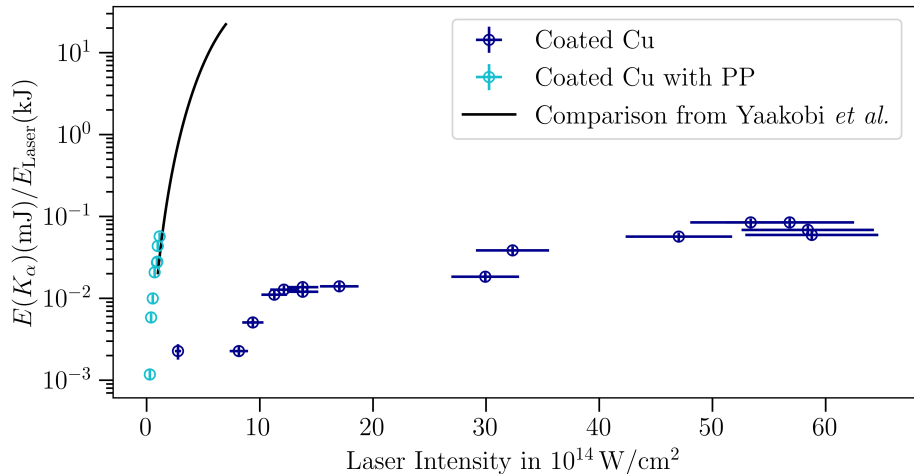


Figure 8.1.: K_α conversion efficiency for shots on $12.7 \mu\text{m}$ Cu with $10 \mu\text{m}$ coating at best focus and with phase plate (PP). Additionally, a fit to the data from [32] is shown for comparison.

when using a target design with a thicker substrate layer than in the experiment conducted in the context of this master thesis.

In order to validate the hypotheses I have presented in this work, 2D or 3D hydro simulations need to be carried out for our best focus and phase plate setting. This enables estimations of the scale length, thermal electron temperature and intensity at quarter critical density. The effects of the different quantities on TPD should not only be analyzed by analytical models, such as the TPD gain, but also be investigated by dedicated TPD simulation tools [57, 58] or particle-in-cell simulations [34]. This might also allow to draw conclusions on the trade-off between intensity and spot size for the PHELIX parameters, in particular when compared to simulations of phase plates producing smaller spot sizes than in our experiment.

Concerning our hard X-ray detector, a more thorough comparison between our method of the temperature determination and that of Froula *et al.* [35] and Yaakobi *et al.* [32] needs to be carried out to confirm the results of our temperature calculation. With the prospect of conducting a future experiment concerning TPD, it should be emphasized that an improvement of the diagnostic capabilities of the hard X-ray detector is necessary in order to obtain smaller temperature uncertainties. The design must be revised, the number of channels increased and filters with smaller transmission added. Potentially, the detection method should be changed from using imaging plates to scintillators. For a future experiment, I additionally suggest to measure the scale length on-shot, e.g., by interferometric methods, since this parameter is essential for estimating the TPD gain and simulating the electron acceleration by TPD.

The motivation for our work was to enhance X-ray diffraction capabilities, therefore, I will give an assessment of which laser targets are most suitable for that application. In the following, I will first consider only the possibilities of using PHELIX at the conditions investigated during our experiment: at best focus and with the $d = 500 \mu\text{m}$ phase plate. Second, I will assume that an optimized phase plate enhancing TPD was designed and successfully implemented.

At best focus, K_α conversion efficiencies at highest laser energies were calculated to be in the same order of magnitude for all tested target types, namely Cu, Mo and Ag, with and without coating. However, a major difference between coated and uncoated targets occurs in the case of Cu, since in bare Cu targets strong line emission from highly charged ions is produced with conversion efficiencies over two orders of

magnitude above the K_{α} conversion efficiencies [44]. This makes uncoated Cu targets superior to coated ones. On the other hand, line emission from higher charged ions was much weaker for bare Mo and Ag targets so that in terms of the applicability for X-ray diffraction both coated and uncoated Mo and Ag targets are expected to perform in a similar way.

The comparison between our results obtained at best focus and with phase plate showed similar but slightly smaller K_{α} conversion efficiencies when using the phase plate. Therefore, the specific phase plate with $d = 500 \mu\text{m}$ is not advantageous for producing X-ray sources for X-ray diffraction. The larger source size constitutes, potentially, even a drawback.

From our previous considerations, we have the two largely different options of target choice for X-ray diffraction: First using bare Cu and second using bare/coated Mo/Ag, both at best focus. With the first option larger conversion efficiencies from laser energy into line emission and with the second option higher photon energies can be obtained. A first guess could be that bare Cu targets are always preferable because the enhancement in line emission conversion efficiency by a factor of over 100 is much larger than the enhancement in photon energy by a factor of 2 to 2.6. However, the trade-off strongly depends on the sample to be investigated, in terms of its attenuation lengths for Cu He $_{\alpha}$ and Mo/Ag K_{α} , and its thickness in X-ray propagation direction. When using Cu and the resulting lower photon energies, it has to be ensured that diffraction rings still have Bragg angles that are covered by the detector. A further drawback of bare Cu is that the Bragg angle resolution decreases due to the increased spectral broadness of emission from highly charged ions compared to K_{α} emission from cold material.

Now, let us assume we have successfully increased the K_{α} conversion efficiency by two orders of magnitude using a phase plate with an optimal spot size. Owing to highest K_{α} photon energies, we would recommend to use coated Ag. Another advantage of using a phase plate is the reduction of shot-to-shot variations which results in better reproducibility of the X-ray source compared to the best focus. The optimal phase plate spot size will be smaller than the tested $500 \mu\text{m}$, therefore increasing the Bragg angle resolution. However, the source size will still be larger than at the best focus setting which is critical for some applications.

A. Intensity Calculation From Focus Images

In this chapter, I describe our method to calculate a calibrated laser intensity I at the target position based on the laser energy E_{Laser} at $\lambda_{\text{vac}} = 527 \text{ nm}$ whose measurement is provided by the PHELIX system. In section A.1, I present the measurements of the laser focus intensity distributions we carried out with low-energy pulses of the PHELIX ns-frontend and how we rescaled them to higher energies. Sections A.2 and A.3 describe the procedure of averaging the spatial intensity distributions at best focus and with the phase plate, respectively.

A.1. Measurements of the Spatial Intensity Distribution

In the scope of our experiment, we measured the spatial intensity distribution of low-energy pulses from the PHELIX ns-frontend with a CCD camera at target position. This was necessary since intensity measurements at target position at full energy or even during a shot on a target were not possible. We carried out the intensity distribution measurements with the $d = 500 \mu\text{m}$ phase plate and without it at best focus corresponding to the two settings used during our experiment. A cutout of a typical CCD camera image containing all relevant features of the laser spot is shown in Fig. A.1 for the best focus and in Fig. A.2 for the phase plate. It should be noted that a frame of a thickness of five pixels within the cutout area has been used to calculate and subtract the background. Furthermore, the CCD signal is rescaled to a potential intensity distribution at $E_{\text{Laser}} = 200 \text{ J}$ by

$$I_i = \frac{S_i^{\text{norm}} \cdot E_{\text{Laser}}}{t_{\text{Laser}} \cdot l_{\text{pixel}}^2}. \quad (\text{A.1})$$

In Eq. A.1, S_i^{norm} denotes the normalized signal strength measured with the CCD camera in pixel i . The normalization was carried out in the way that the sum of S_i over all pixels i within each cutout area equals 1. By this, we assumed that all laser energy must be contained within the respective cutout area. Furthermore, $t_{\text{Laser}} = 1.5 \text{ ns}$ denotes the laser pulse duration and $l_{\text{pixel}} = 2.2 \mu\text{m}$ the CCD camera pixel size.

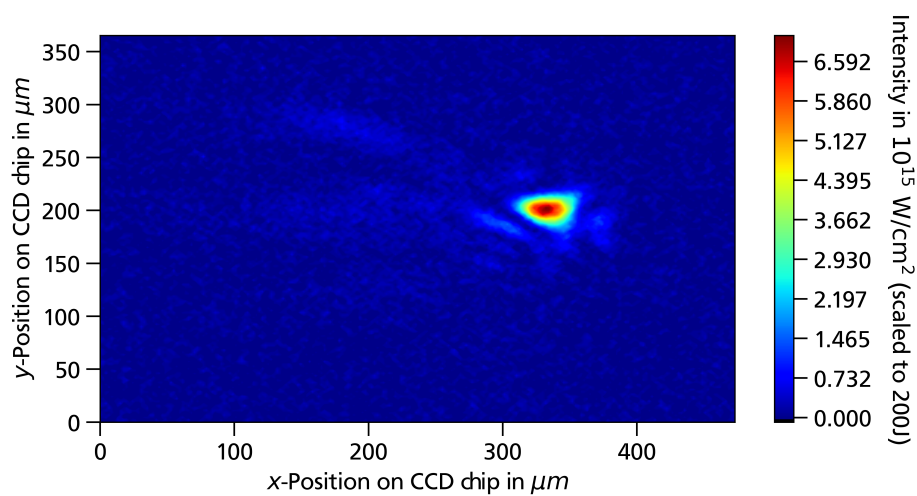


Figure A.1.: Intensity distribution of a low-energy pulse from the PHELIX ns-frontend on the CCD Chip for the best focus setting.

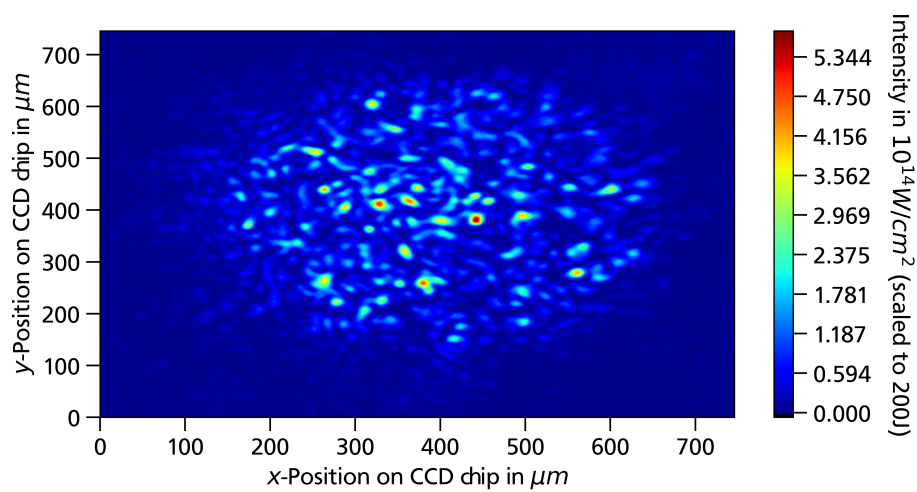


Figure A.2.: Intensity distribution of a PHELIX ns-frontend pulse on the CCD Chip when using the phase plate.

A.2. Calculation of the Spatial Average of the Intensity Distribution at Best Focus

In this section, I describe how we calculated the spatial average of the intensity distribution for the best focus setting. During this procedure, we also determined the laser spot size.

At best focus, the spatial intensity distribution is clearly peaked. Higher intensities are more relevant for laser-matter interactions and especially TPD (cf. sections 4.5.1 and 4.7.1). Therefore, we had to define a measure of how to average the intensity distribution with a stronger weight of higher intensities. For this purpose, we first calculated the FWHM of horizontal and vertical line-outs through the pixel with strongest CCD signal. Note that the line-outs were averaged over a width of three pixels to reduce signal noise. Then, we defined an ellipse with width and height corresponding to horizontal and vertical FWHM and considered data points within this ellipse for the further intensity calculation. This considers on the one hand that high intensities are more relevant. On the other hand, the ellipse has a certain extension including intensities lower than the peak value. From the CCD signal strength S_i of the pixels i within the ellipse A , we calculated the signal weighted average

$$S^{\text{average}} = \frac{\sum_{i \in A} S_i^{\text{norm}2}}{\sum_{i \in A} S_i^{\text{norm}}} \quad (\text{A.2})$$

In total, we recorded four images of the laser intensity distribution at best focus with the CCD camera each corresponding to a different PHELIX pulse from the ns-frontend. We carried out the procedure described above for each of them. We calculated the average S_{mean} and standard deviation S_{std} of S_k^{average} where k denotes the different pulses. During this process, we noticed big variations between different values of S_k^{average} so that S_{std} was rather large. We calculated an averaged laser intensity of

$$I(200 \text{ J}) = I_{\text{mean}} \pm I_{\text{std}} = (5.9 \pm 2.6) \cdot 10^{15} \text{ W cm}^{-2} \quad (\text{A.3})$$

for an exemplarily laser energy of $E_{\text{laser}} = 200 \text{ J}$ using Eq. A.1 for rescaling S_{mean} and S_{std} to I_{mean} and I_{std} . A possible explanation for the strong variations between different PHELIX-frontend pulses is the fact that the last part of the PHELIX laser beamline had to be vented for our measurements with the CCD camera. This might result in enhanced air turbulences that disturb the laser focus. When using PHELIX at high energy shots during our experiment, the beamline was again fully under vacuum so that we expect shot-to-shot variations to strongly decrease.

For converting the specific value of E_{laser} of each shot at best focus into laser intensity I , we linearly scaled the intensity with energy by

$$I(E_{\text{laser}}) = I(200 \text{ J}) \cdot \frac{E_{\text{laser}}}{200 \text{ J}} \quad (\text{A.4})$$

Because of the high value of I_{std} , this energy to intensity calibration has a large error. However, this error affects all data points in our data set in the same way, since it represents an error in the calibration itself. Therefore, the huge uncertainty of the calibration is a systematic uncertainty and does not alter conclusions drawn from comparisons between different shots. Based on this line of argument, we did not take the calibration uncertainty into account for intensity error bars in chapter 7. On the other hand, the stochastic error of I is mainly based on two effects, the stochastic error of the E_{laser} measurement and the shot-to-shot variation of the spatial intensity distribution even if the complete beamline is under vacuum. The latter is due to variations in the wavefront of the laser pulse resulting in different intensity distributions at the focal position. For this work, a stochastic error of 10 % is assumed.

Within our intensity analysis, we also determined the horizontal and vertical laser spot size for each of the four CCD images. By determining the mean and the standard deviation of these eight values in total, we obtained the PHELIX laser spot size of $d_{\text{FWHM}} = (25 \pm 5) \mu\text{m}$ at best focus.

A.3. Calculation of the Spatial Average of the Intensity Distribution With the Phase Plate

In this section, the procedure of averaging the spatial intensity distribution is described for the phase plate setting.

In that case, the intensity distribution extends over a much larger area than at the best focus setting and cannot be characterized by a single peak (see Fig. A.2). Hot spots caused by the phase plate contain only a small ratio of the total laser energy so that all pixels containing laser energy need to be considered for determining a spatially averaged intensity value with phase plate.

To account for the larger relevance of higher intensities, we calculated a signal weighted average by

$$\tilde{S}^{\text{average}} = \frac{\sum S_i^{\text{norm}2}}{\sum S_i^{\text{norm}}}, \quad (\text{A.5})$$

similar to Eq. A.2, but in this case we considered all pixels of the cutoff image. In Eq. A.5, the tilde denotes that the calculation is now carried out for the phase plate.

With the CCD camera, we took a total of five images while the phase plate was used. Similar to section A.2, we calculated \tilde{S}_{mean} and \tilde{S}_{std} and concluded

$$\tilde{I}(200 \text{ J}) = (1.07 \pm 0.02) \cdot 10^{14} \text{ W cm}^{-2} \quad (\text{A.6})$$

for an exemplary laser energy of $E_{\text{Laser}} = 200 \text{ J}$. The standard deviation of $\tilde{S}_k^{\text{average}}$ is much smaller than for the best focus setting. This is due to the fact that the phase plate induces random phases to the laser beam so that air turbulences play a less important role.

In the same manner as for the best focus setting (cf. section A.2), we used the obtained value $\tilde{I}(200 \text{ J})$ to linearly scale the laser energy to intensity for each high energy shot with the phase plate.

One could argue that the small error in the calibrated intensity indicates smaller stochastic errors than at the best focus setting. In contrast, the intensity calibration does not take the uncertainty of the measured laser energy into account. Furthermore, it cannot be predicted how a variation of the spatial intensity distribution, in particular with regard to the speckles, influences TPD. Typical speckles in the laser spot are around 3 to 5 times larger than the determined calibrated intensity (see Fig. A.2), but their spatial and intensity distribution varies between different shots. To account for this uncertainty, a stochastic error of 10 % in the calibrated intensity is assumed for this work, similarly to the best focus setting.

B. Identification of Lines for Uncoated Mo Targets

This chapter is about the identification of the line emission close to K_α energy observed for uncoated Mo. Our hypothesis that this detected K_α line is an overlap of a K_α line from cold material and emission from L → K-shell transitions in higher charged Mo will be supported in the following. To do so, the detected K_α and K_β line positions and ratios of their strengths will be compared between coated and uncoated Mo targets. The identification of the contributions to the detected K_α line is of interest because on the one hand K_α emission from fast electrons penetrating cold material and on the other hand emission from higher charged ions depend on different processes (cf. section 6.2.2).

In Fig. B.1a, the ratio of the strengths of the detected K_α and K_β lines is shown for uncoated Mo. For comparison, the ratio of K_α to K_β strengths is shown for coated targets where we expect to observe only emission from cold matter which would mean that no contribution of emission from higher charged ions occurs (cf. section 6.2.2). This is confirmed, since the line strength ratio of coated Mo is in agreement with the expectation for singly charged Mo (with the only hole in the K-shell, data from [52]). It is clearly visible that the ratio of the detected K_α to K_β line strengths is much stronger in uncoated Mo which indicates that the detected K_α line includes an additional component caused by emission from higher charged ions.

In Fig. B.1b, the energy distance between the detected K_α and K_β lines of uncoated Mo is compared to the energy distance of K_α and K_β lines of coated Mo. Again, coated Mo is in good agreement with the expectation for singly charged Mo (with the hole in the K-shell). On the other side, the line distance is decreased in the case of uncoated Mo which could be explained again by L → K-shell emission from higher charged ions. This emission would shift the detected K_α line to higher energies.

Altogether, the observations for uncoated Mo targets described above could be replicated if the detected K_α line is the superposition of a K_α line from cold material and emission from higher charged ions, and if the line at K_β photon energy does not include emission from higher charged ions. This would mean that K_α and K_β emission would be caused by fast electrons penetrating cold material. On the other hand, the $T_e = 1 - 2 \text{ keV}$ hot Mo plasma would produce L → K-shell emission, but (almost) no M → K-shell emission.

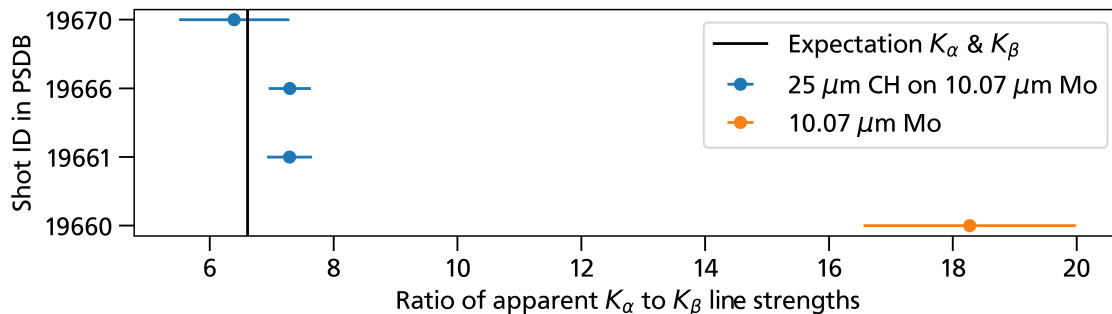
To confirm or contradict this hypothesis, we performed simulations of the hot Mo plasma with FLYCHK [73], which is a tool to calculate ionization level population and the resulting line emission, for thermal electron temperatures from $T_e = 0.5 \text{ keV}$ to $T_e = 3 \text{ keV}$. The calculated emission spectra are shown in Fig. B.2. For each simulation, the density was set to $n_e = 4 \cdot 10^{21}$, i.e., critical density at $\lambda_{\text{vac}} = 527 \text{ nm}$. The simulations show emission from higher charged ions at energies slightly higher than $E^{\text{ph}}(K_\alpha)$, but no K_β emission. This is in agreement with our hypothesis stated above. The reduction of M → K-shell transitions is due to the fact that many electrons in the M-shell are ionized in the hot Mo plasma. Even though discrete lines can be seen in the FLYCHK simulations, this is not necessarily expected for our HOPG spectrometer data due to the HOPG crystal's mosaic structure decreasing energy resolution. We conclude that the expected thermal electron temperature of $T_e = 1 - 2 \text{ keV}$ [44] could explain the contribution of emission from higher charged ions to the detected K_α emission line of uncoated Mo targets. Future work might include a replication of the detected lines by a superposition of K_α emission from cold material and

emission from higher charged ions. Possibly, various temperatures and densities need to be considered and superimposed, since those properties are time and space dependent in a laser produced plasma.

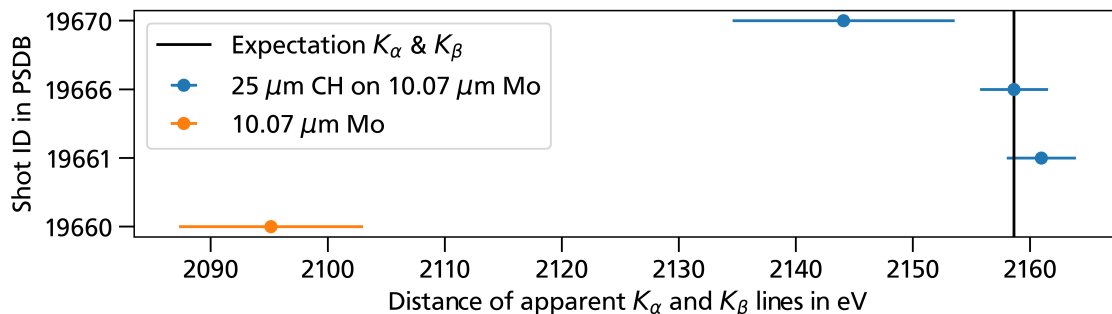
It should be noted that we did not directly compare the positions of the detected K_α lines of coated and uncoated Mo because there were some uncertainties with the energy calibration of the HOPG spectrometer data. This was due to variations in the HOPG spectrometer IP position that changes by few mm from shot to shot. At the energy of Mo K_α , this corresponded to variations of over 100 eV which is larger than the actual deviation we tried to identify between coated and uncoated Mo. Therefore, we used the K_β emission as shot independent calibration and considered the energy difference from the detected K_α to K_β lines.

It is important to point out that the ratio of the line emission strengths in uncoated Mo is about two to three times the ratio in coated Mo. This indicates that the previously described contribution from higher charged ions in uncoated targets is comparably strong to or even a bit stronger than the contribution from cold material. For this work, no separation of the two contributions was carried out, but the whole detected K_α line was used for the calculation of the K_α strength in uncoated Mo. In the future, a quantitative separation might be carried out in order to better distinguish the different contributions to the line.

I would like to add one further remark. If the detected K_α line in uncoated Mo is a superposition of K_α emission from cold material and emission from higher charged ions, we would also expect the line width to increase. However, we could not identify significant differences between coated and uncoated targets due to large variations from shot to shot. This is attributable to the line broadening caused by the HOPG crystal that strongly depends on the crystal's microscopic shape at the specific reflection location.



(a) For uncoated Mo, the detected K_α line is stronger compared to K_β than for coated Mo.



(b) For uncoated Mo, the detected K_α line has a decreased energy distance to the K_β line compared to coated Mo.

Figure B.1.: Comparison of the detected K_α and K_β lines for coated and uncoated Mo. In (a) the ratio of line strengths and in (b) the distance of photon energies is compared.

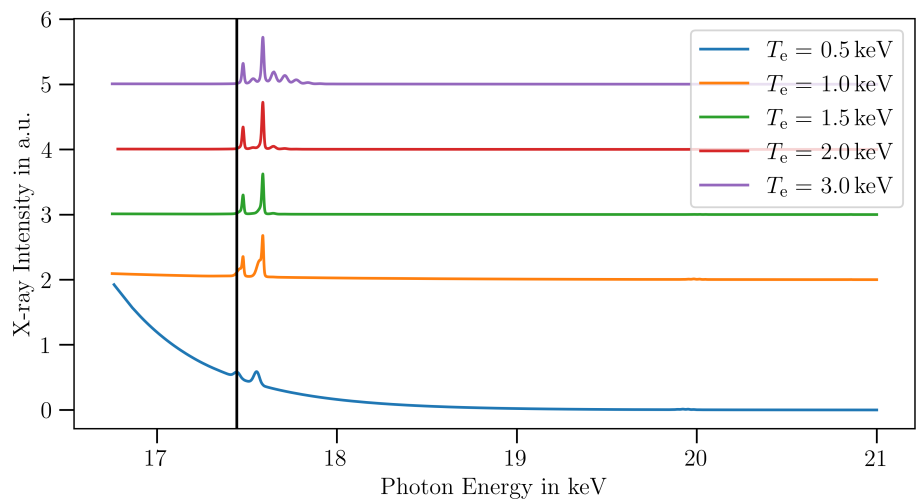


Figure B.2.: Intensity of X-ray emission of Mo simulated with FLYCHK. The different spectra were scaled and vertically shifted for ease of comparison.

Bibliography

- [1] F. Graziani, M. Desjarlais, R. Redmer *et al.*, Frontiers and Challenges in Warm Dense Matter, 2014, doi:10.1007/978-3-319-04912-0.
- [2] A. Ng, T. Ao, F. Perrot *et al.*, Idealized slab plasma approach for the study of warm dense matter, *Laser Part. Beams*, **23**(4):527–537, 2005, doi:10.1017/S0263034605050718.
- [3] R. P. Drake, High-Energy-Density Physics: Foundation of Inertial Fusion and Experimental Astrophysics, Springer International Publishing AG Switzerland, Cham, 2018.
- [4] N. Nettelmann, R. Redmer and D. Blaschke, Warm dense matter in giant planets and exoplanets, *Phys. Part. Nucl.*, **39**(7):1122–1127, 2008, doi:10.1134/S1063779608070277.
- [5] M. Koenig, A. Benuzzi-Mounaix, A. Ravasio *et al.*, Progress in the study of warm dense matter, *Plasma Phys. Controlled Fusion*, **47**(12B):B441–B449, 2005, doi:10.1088/0741-3335/47/12b/s31.
- [6] M. S. Murillo, Viscosity estimates of liquid metals and warm dense matter using the Yukawa reference system, *High Energy Density Phys.*, **4**(1):49–57, 2008, doi:<https://doi.org/10.1016/j.hedp.2007.11.001>.
- [7] S. X. Hu, L. A. Collins, T. R. Boehly *et al.*, First-principles thermal conductivity of warm-dense deuterium plasmas for inertial confinement fusion applications, *Phys. Rev. E*, **89**(4):043105, 2014, doi:10.1103/PhysRevE.89.043105.
- [8] S. B. Hansen, E. C. Harding, P. F. Knapp *et al.*, Fluorescence and absorption spectroscopy for warm dense matter studies and ICF plasma diagnostics, *Phys. Plasmas*, **25**(5):056301, 2018, doi:10.1063/1.5018580.
- [9] N. A. Tahir, C. Deutsch, V. E. Fortov *et al.*, Proposal for the Study of Thermophysical Properties of High-Energy-Density Matter Using Current and Future Heavy-Ion Accelerator Facilities at GSI Darmstadt, *Phys. Rev. Lett.*, **95**(3):035001, 2005, doi:10.1103/PhysRevLett.95.035001.
- [10] M. Altarelli, The European X-ray free-electron laser facility in Hamburg, *Nucl. Instrum. Methods Phys. Res., Sect. B*, **269**(24):2845 – 2849, 2011, doi:10.1016/j.nimb.2011.04.034.
- [11] G. H. Miller, E. I. Moses and C. R. Wuest, The National Ignition Facility: enabling fusion ignition for the 21st century, *Nucl. Fusion*, **44**(12):228–238, 2004, doi:10.1088/0029-5515/44/12/s14.
- [12] E. I. Moses, Ignition on the National Ignition Facility: a path towards inertial fusion energy, *Nucl. Fusion*, **49**(10):104022, 2009, doi:10.1088/0029-5515/49/10/104022.
- [13] S. Root, K. R. Cochrane, J. H. Carpenter *et al.*, Carbon dioxide shock and reshock equation of state data to 8 Mbar: Experiments and simulations, *Phys. Rev. B*, **87**(22):224102, 2013, doi:10.1103/PhysRevB.87.224102.

- [14] K. Falk, Experimental methods for warm dense matter research, *High Power Laser Sci. Eng.*, **6**:e59, 2018, doi:10.1017/hpl.2018.53.
- [15] A. Lévy, F. Dorchies, M. Harmand *et al.*, X-ray absorption for the study of warm dense matter, *Plasma Phys. Controlled Fusion*, **51**(12):124021, 2009, doi:10.1088/0741-3335/51/12/124021.
- [16] A. Benuzzi-Mounaix, S. Mazevet, A. Ravasio *et al.*, Progress in warm dense matter study with applications to planetology, *Phys. Scr.*, **T161**:014060, 2014, doi:10.1088/0031-8949/2014/t161/014060.
- [17] S. Zhang, S. Zhao, W. Kang *et al.*, Link between K absorption edges and thermodynamic properties of warm dense plasmas established by an improved first-principles method, *Phys. Rev. B*, **93**(11):115114, 2016, doi:10.1103/PhysRevB.93.115114.
- [18] A. Höll, R. Redmer, G. Röpke *et al.*, X-ray Thomson scattering in warm dense matter, *Eur. Phys. J. D*, **29**(2):159–162, 2004, doi:10.1140/epjd/e2004-00059-5.
- [19] S. H. Glenzer and R. Redmer, X-ray Thomson scattering in high energy density plasmas, *Rev. Mod. Phys.*, **81**(4):1625–1663, 2009, doi:10.1103/RevModPhys.81.1625.
- [20] T. Döppner, P. F. Davis, A. L. Kritcher *et al.*, Using collective x-ray Thomson scattering to measure temperature and density of warm dense matter, in J. Dunn and G. J. Tallents (Editors), *Soft X-Ray Lasers and Applications VIII*, volume 7451, S. 110 – 118, International Society for Optics and Photonics, SPIE, 2009, doi:10.1117/12.825395.
- [21] B. Cullity, *Elements of X-Ray Diffraction*, Addison-Wesley Publishing Company, Reading, Massachusetts, 1956.
- [22] N. Medvedev and B. Ziaja, Multistep transition of diamond to warm dense matter state revealed by femtosecond X-ray diffraction, *Sci. Rep.*, **8**(1):5284, 2018, doi:10.1038/s41598-018-23632-8.
- [23] S. Götte, PHELIX Lasersystem, URL <https://www.gsi.de/work/forschung/appamml/plasmaphysikphelix/phelix.htm>, accessed 2021-10-14.
- [24] A. Blazevic, Z6 – eine einzigartige Anlage für kombinierte Ionen- und Laserstrahlexperimente, URL https://www.gsi.de/work/forschung/appamml/plasmaphysikphelix/anlagen_in_der_experimenthalle_z6.htm, accessed 2021-10-14.
- [25] S. Le Pape, L. Divol, A. Macphee *et al.*, Optimization of high energy x ray production through laser plasma interaction, *High Energy Density Phys.*, **31**:13–18, 2019, doi:10.1016/j.hedp.2019.01.002.
- [26] M. V. Goldman, Parametric plasmon-photon interactions: Part II. Analysis of plasmon propagator and correlation functions, *Ann. Phys.*, **38**(1):117–169, 1966, doi:10.1016/0003-4916(66)90253-3.
- [27] M. N. Rosenbluth, Parametric Instabilities in Inhomogeneous Media, *Phys. Rev. Lett.*, **29**(9):565–567, 1972, doi:10.1103/PhysRevLett.29.565.
- [28] C. S. Liu and M. N. Rosenbluth, Parametric decay of electromagnetic waves into two plasmons and its consequences, *Phys. Fluids*, **19**(7):967–971, 1976, doi:10.1063/1.861591.
- [29] A. Simon, R. W. Short, E. A. Williams *et al.*, On the inhomogeneous two-plasmon instability, *Phys. Fluids*, **26**(10):3107–3118, 1983, doi:10.1063/1.864037.
- [30] P. Mulser and D. Bauer, *High Power Laser-Matter Interaction*, Springer-Verlag, Berlin and Heidelberg, 2010, doi:10.1007/978-3-540-46065-7.

- [31] W. L. Kruer, *The Physics of Laser Plasma Interactions*, CRC Press, Boca Raton, 2018.
- [32] B. Yaakobi, P.-Y. Chang, A. Solodov *et al.*, Fast-electron generation in long-scalelength plasmas, *Phys. Plasmas*, **19**(1):012704, 2012, doi:10.1063/1.3676153.
- [33] W. Seka, D. H. Edgell, J. F. Myatt *et al.*, Two-plasmon-decay instability in direct-drive inertial confinement fusion experiments, *Phys. Plasmas*, **16**(5):052701, 2009, doi:10.1063/1.3125242.
- [34] R. Yan, C. Ren, J. Li *et al.*, Generating energetic electrons through staged acceleration in the two-plasmon-decay instability in inertial confinement fusion, *Phys. Rev. Lett.*, **108**:175002, 2012, doi:10.1103/PhysRevLett.108.175002.
- [35] D. H. Froula, B. Yaakobi, S. X. Hu *et al.*, Saturation of the Two-Plasmon Decay Instability in Long-Scale-Length Plasmas Relevant to Direct-Drive Inertial Confinement Fusion, *Phys. Rev. Lett.*, **108**(16):165003, 2012, doi:10.1103/PhysRevLett.108.165003.
- [36] D. T. Michel, A. V. Maximov, R. W. Short *et al.*, Measured hot-electron intensity thresholds quantified by a two-plasmon-decay resonant common-wave gain in various experimental configurations, *Phys. Plasmas*, **20**(5):055703, 2013, doi:10.1063/1.4803090.
- [37] D. Turnbull, A. V. Maximov, D. H. Edgell *et al.*, Anomalous Absorption by the Two-Plasmon Decay Instability, *Phys. Rev. Lett.*, **124**(18):185001, 2020, doi:10.1103/PhysRevLett.124.185001.
- [38] D. Varentsov, HHT Experimental Area, URL https://www.gsi.de/work/forschung/appamml/plasmaphysikphelix/anlagen_beि_sis18_hht.htm, accessed 2021-10-14.
- [39] D. H. H. Hoffmann, A. Blazevic, O. N. Rosmej *et al.*, Frontiers of dense plasma physics with intense ion and laser beams and accelerator technology, *Phys. Scr.*, **2006**(T123):1–7, 2006, doi:10.1088/0031-8949/2006/t123/001.
- [40] Ringbeschleuniger SIS18 – der Rekordhalter, URL <https://www.gsi.de/forschungbeschleuniger/beschleunigeranlage/ringbeschleuniger.htm>, accessed 2021-10-14.
- [41] V. Bagnoud, B. Aurand, A. Blazevic *et al.*, Commissioning and early experiments of the PHELIX facility, *Appl. Phys. B: Lasers Opt.*, **100**(1):137–150, 2010, doi:10.1007/s00340-009-3855-7.
- [42] K. Schoenberg, V. Bagnoud, A. Blazevic *et al.*, High-energy-density-science capabilities at the Facility for Antiproton and Ion Research, *Phys. Plasmas*, **27**(4):043103, 2020, doi:10.1063/1.5134846.
- [43] Specialised Imaging Pulserad Flash X-Ray Systems, URL <https://www.specialised-imaging.com/products/intensifiers/flash-x-ray>, accessed 2021-10-14.
- [44] L. Geiger, Durch Nanosekundenlaser erzeugte Röntgenquellen zur Diagnostik dichter Plasmen bei FAIR, Master's thesis, Goethe-Universität Frankfurt, 2020.
- [45] S. White, B. Kettle, J. Vorberger *et al.*, Time-dependent effects in melting and phase change for laser-shocked iron, *Phys. Rev. Res.*, **2**(3):033366, 2020, doi:10.1103/PhysRevResearch.2.033366.
- [46] M. Millot, F. Coppari, J. Rygg *et al.*, Nanosecond X-ray diffraction of shock-compressed superionic water ice, *Nature*, **569**(7755):251–255, 2019, doi:10.1038/s41586-019-1114-6.
- [47] S. Hunklinger, *Festkörperphysik*, Oldenbourg Verlag, München, 2011.
- [48] B. L. Henke, E. M. Gullikson and J. C. Davis, X-Ray Interactions: Photoabsorption, Scattering, Transmission, and Reflection at $E = 50\text{--}30,000 \text{ eV}$, $Z = 1\text{--}92$, *At. Data Nucl. Data Tables*, **54**(2):181 – 342, 1993, doi:10.1006/1993.1013.

- [49] D. Giulietti and L. A. Gizzi, X-ray emission from laser-produced plasmas, *Riv. del Nuovo Cim.*, **21**(10):1–93, 1998, doi:10.1007/BF02874624.
- [50] A. Piel, *Plasma Physics: An Introduction to Laboratory, Space, and Fusion Plasmas*, Springer International Publishing AG Switzerland, Cham, 2017, doi:10.1007/978-3-319-63427-2.
- [51] W. L. Wiese, Transition Probabilities and Atomic Lifetimes, in R. A. Meyers (Editor), *Encyclopedia of Physical Science and Technology* (Third Edition), S. 21–30, Academic Press, New York, third edition Edition, 2002, doi:10.1016/B0-12-227410-5/00787-0.
- [52] A. C. Thompson, D. Vaughan, D. T. Attwood *et al.*, *X-Ray Data Booklet*, Lawrence Berkeley National Laboratory, Berkeley, 2001.
- [53] W. Lotz, Electron Binding Energies in Free Atoms, *J. Opt. Soc. Am.*, **60**(2):206–210, 1970, doi:10.1364/JOSA.60.000206.
- [54] G. J. Tallents, *An Introduction to the Atomic and Radiation Physics of Plasmas*, Cambridge University Press, 2018.
- [55] R. Ramis, J. M. ter Vehn and J. Ramírez, MULTI2D – a computer code for two-dimensional radiation hydrodynamics, *Comput. Phys. Commun.*, **180**(6):977 – 994, 2009, doi:10.1016/j.cpc.2008.12.033.
- [56] F. F. Chen, *Introduction to Plasma Physics and Controlled Fusion*, Springer International Publishing AG Switzerland, Cham, 2016, doi:10.1007/978-3-319-22309-4.
- [57] J. F. Myatt, J. Zhang, J. A. Delettrez *et al.*, The dynamics of hot-electron heating in direct-drive-implosion experiments caused by two-plasmon-decay instability, *Phys. Plasmas*, **19**(2):022707, 2012, doi:10.1063/1.3683004.
- [58] J. F. Myatt, H. X. Vu, D. F. DuBois *et al.*, Mitigation of two-plasmon decay in direct-drive inertial confinement fusion through the manipulation of ion-acoustic and Langmuir wave damping, *Phys. Plasmas*, **20**(5):052705, 2013, doi:10.1063/1.4807036.
- [59] R. Yan, A. V. Maximov, C. Ren *et al.*, Growth and Saturation of Convective Modes of the Two-Plasmon Decay Instability in Inertial Confinement Fusion, *Phys. Rev. Lett.*, **103**(17):175002, 2009, doi:10.1103/PhysRevLett.103.175002.
- [60] C. Z. Xiao, Z. J. Liu, C. Y. Zheng *et al.*, Competition between stimulated Raman scattering and two-plasmon decay in inhomogeneous plasma, *Phys. Plasmas*, **23**(2):022704, 2016, doi:10.1063/1.4941969.
- [61] E. A. Jackson, Parametric Effects of Radiation on a Plasma, *Phys. Rev.*, **153**(1):235–244, 1967, doi:10.1103/PhysRev.153.235.
- [62] J. F. Drake and Y. C. Lee, Temporally Growing Raman Backscattering Instabilities in an Inhomogeneous Plasma, *Phys. Rev. Lett.*, **31**(19):1197–1200, 1973, doi:10.1103/PhysRevLett.31.1197.
- [63] Y. C. Lee and P. K. Kaw, Temporal Electrostatic Instabilities in Inhomogeneous Plasmas, *Phys. Rev. Lett.*, **32**(4):135–138, 1974, doi:10.1103/PhysRevLett.32.135.
- [64] D. A. Russell and D. F. DuBois, $\frac{3}{2}\omega_0$ Radiation from the Laser-Driven Two-Plasmon Decay Instability in an Inhomogeneous Plasma, *Phys. Rev. Lett.*, **86**(3):428–431, 2001, doi:10.1103/PhysRevLett.86.428.
- [65] S. Jackel, J. Albritton and E. Goldman, Critical-Density Scale-Length Measurements in Laser-Produced Plasmas, *Phys. Rev. Lett.*, **35**(8):514–517, 1975, doi:10.1103/PhysRevLett.35.514.

- [66] H. Pant, K. Eidmann, P. Sachsenmaier *et al.*, Threshold of the $2\omega_{pe}$ instability in a laser produced plasma, *Opt. Commun.*, **16**(3):396–398, 1976, doi:10.1016/0030-4018(76)90026-2.
- [67] H. A. Baldis and C. J. Walsh, Growth and saturation of the two-plasmon decay instability, *Phys. Fluids*, **26**(5):1364–1375, 1983, doi:10.1063/1.864262.
- [68] S. N. Dixit, I. M. Thomas, B. W. Woods *et al.*, Random phase plates for beam smoothing on the Nova laser, *Appl. Opt.*, **32**(14):2543–2554, 1993, doi:10.1364/AO.32.002543.
- [69] Universal streak camera C10910-01, URL <https://www.hamamatsu.com/eu/en/product/type/C10910-01/index.html>, accessed 2021-10-14.
- [70] BAS Storage Phosphor Screens, URL <https://www.cytivalifesciences.com/en/us/shop/molecular-biology/nucleic-acid-electrophoresis--blotting--and-detection/molecular-imaging-for-nucleic-acids/bas-storage-phosphor-screens-p-00108>, accessed 2021-10-14.
- [71] Typhoon Gel and Blot Imaging Systems, URL <https://www.cytivalifesciences.com/en/fi/shop/molecular-biology/nucleic-acid-electrophoresis--blotting--and-detection/molecular-imaging-for-nucleic-acids/amersham-typhoon-gel-and-blot-imaging-systems-p-00192>, accessed 2021-10-14.
- [72] U. Samir, K. H. Wright Jr. and N. H. Stone, The expansion of a plasma into a vacuum: Basic phenomena and processes and applications to space plasma physics, *Reviews of Geophysics*, **21**(7):1631–1646, 1983, doi:10.1029/RG021i007p01631.
- [73] H.-K. Chung, M. H. Chen, W. L. Morgan *et al.*, FLYCHK: generalized population kinetics and spectral model for rapid spectroscopic analysis for all elements, *High Energy Density Phys.*, **1**(1):3–12, 2005, doi:10.1016/j.hedp.2005.07.001.
- [74] X. Llovet, C. J. Powell, F. Salvat *et al.*, Cross Sections for Inner-Shell Ionization by Electron Impact, *J. Phys. Chem. Ref. Data*, **43**(1):013102, 2014, doi:10.1063/1.4832851.
- [75] J. J. MacFarlane, I. E. Golovkin and P. R. Woodruff, HELIOS-CR – A 1-D radiation-magnetohydrodynamics code with inline atomic kinetics modeling, *J. Quant. Spectrosc. Radiat. Transfer*, **99**(1):381 – 397, 2006, doi:10.1016/j.jqsrt.2005.05.031.
- [76] HELIOS Overview, URL <http://www.prism-cs.com/Software/Helios/overview.html>, accessed 2021-10-14.
- [77] T. T. Böhlen, F. Cerutti, M. P. W. Chin *et al.*, The FLUKA Code: Developments and Challenges for High Energy and Medical Applications, *Nucl. Data Sheets*, **120**:211 – 214, 2014, doi:10.1016/j.nds.2014.07.049.
- [78] A. Ferrari, P. R. Sala, A. Fasso *et al.*, FLUKA: A multi-particle transport code (Program version 2005), Technical Report CERN-2005-010, SLAC-R-773, INFN-TC-05-11, 2005, doi:10.2172/877507.
- [79] H. Legall, H. Stiel, P.-V. Nickles *et al.*, Applications of highly oriented pyrolytic graphite (HOPG) for x-ray diagnostics and spectroscopy, in G. A. Kyrala, J.-C. J. Gauthier, C. A. MacDonald *et al.* (Editors), *Laser-Generated, Synchrotron, and Other Laboratory X-Ray and EUV Sources, Optics, and Applications II*, volume 5918, S. 11 – 21, International Society for Optics and Photonics, SPIE, 2005, doi:10.1117/12.614847.
- [80] E. K. Schmal, Untersuchung und Vergleich von Imaging Plates und CMOS basierendem Röntgendetektor, Bachelor's thesis, Goethe-Universität Frankfurt, 2017.
- [81] P. Neumayer, personal communication, January 18, 2021.

- [82] M. J. Berger, J. H. Hubbell, S. M. Seltzer *et al.*, NIST Standard Reference Database 8 (XGAM), URL <https://www.nist.gov/pml/xcom-photon-cross-sections-database>, accessed 2021-10-14.
- [83] T. Döppner, P. Neumayer, F. Girard *et al.*, High order reflectivity of highly oriented pyrolytic graphite crystals for x-ray energies up to 22 keV, Rev. Sci. Instrum., **79**(10):10E311, 2008, doi:10.1063/1.2966378.
- [84] C. Stoeckl, V. Y. Glebov, D. D. Meyerhofer *et al.*, Hard x-ray detectors for OMEGA and NIF, Rev. Sci. Instrum., **72**(1):1197–1200, 2001, doi:10.1063/1.1322621.
- [85] J. W. McDonald, R. L. Kauffman, J. R. Celeste *et al.*, Filter-fluorescer diagnostic system for the National Ignition Facility, Rev. Sci. Instrum., **75**(10):3753–3755, 2004, doi:10.1063/1.1788871.
- [86] G. J. Williams, R. Tommasini, N. Lemos *et al.*, High-energy differential-filtering photon spectrometer for ultraintense laser-matter interactions, Rev. Sci. Instrum., **89**(10):10F116, 2018, doi:10.1063/1.5039383.
- [87] C. D. Chen, J. A. King, M. H. Key *et al.*, A Bremsstrahlung spectrometer using k-edge and differential filters with image plate dosimeters, Rev. Sci. Instrum., **79**(10):10E305, 2008, doi:10.1063/1.2964231.
- [88] M. Hohenberger, N. E. Palmer, G. LaCaille *et al.*, Measuring the hot-electron population using time-resolved hard x-ray detectors on the NIF, in P. M. Bell and G. P. Grim (Editors), Target Diagnostics Physics and Engineering for Inertial Confinement Fusion II, volume 8850, S. 106 – 114, International Society for Optics and Photonics, SPIE, 2013, doi:10.1117/12.2024960.
- [89] C. Stoeckl, R. E. Bahr, B. Yaakobi *et al.*, Multibeam Effects on Fast-Electron Generation from Two-Plasmon-Decay Instability, Phys. Rev. Lett., **90**:235002, 2003, doi:10.1103/PhysRevLett.90.235002.